NUMERICAL ANALYSIS OF SURFACE-DRIVEN NON-ISOTHERMAL VISCOELASTIC FLOW

by

Yalın Kaptan

B.S. in M.E., Cumhuriyet University, 2001

M.Sc. in M.E., Cumhuriyet University, 2003

Submitted to the Institute for Graduate Studies in
Science and Engineering in partial fulfillment of
the requirements for the degree of
Doctor of Philosophy

Graduate Program in Mechanical Engineering
Boğaziçi University
2010

ACKNOWLEDGEMENTS

First of all, I would like to express my gratitude to my advisor Assoc. Prof. Dr. Ali Ecder for his guidance, academic vision and constructive comments throughout my study.

Also I would like to thank to Assoc. Prof. Dr. Kunt Atalik for his patience, motivation and continuous support during this long journey.

Moreover, I would like to express my gratitude to my thesis advisory committee members; Assoc. Prof. Dr. Hasan Bedir, Asist. Prof. Dr. Sami And Kılıç and Prof. Dr. Ertan Buyruk for their help during the process.

I would also like to thank to Prof. Dr. Akın Tezel for his considerable assistance throughout my study.

I also would like to specially thank to all of the past and present FMS LAB members but in particular Erhan Turan.

Finally, I would like to express my special thanks to my parents and my wife, Ayşegül, who provided motivation, support and encouragement throughout my studies.

ABSTRACT

NUMERICAL ANALYSIS OF SURFACE-DRIVEN NON-ISOTHERMAL VISCOELASTIC FLOW

The numerical investigations of the moving edge non-isothermal viscoelastic flows are simulated by using two example problems (lid driven cavity (LDC) and rotating disc in a cylindrical enclosure (RDCE) flows) in this study. The viscoelastic behavior of the fluids is modeled by adopting three differential constitutive relations namely Upper Convected Maxwell (UCM), Oldroyd B and Giesekus models. The comparisons reveal that the Giesekus model is the most realistic one and the maximum Weissenberg number limit is higher compared to the others. Two separate solvers are used in the simulations; PETSc and IN-GMRES solvers. PETSc code is used as a solver for the Newtonian flows and a benchmark tool for the Krylov subspace methods and preconditioners. PETSc analyses reveal that BiCGStab with ILU(5) preconditioning is the most effective solver in the simulations of the Newtonian flows. IN-GMRES solver is used to simulate the non-isothermal viscoelastic flows and it is based on the matrix free preconditioned inexact Newton-Krylov methods. To obtain higher Weissenberg number limits in the simulations, the numerical tools such as the continuation, the upwind differencing scheme, the higher order discretization schemes, the slanted stencils and similar others are implemented in the IN-GMRES algorithm. In the non-isothermal part of the study, besides the advection and diffusion, the viscous dissipation is also included and it is understood that the viscous dissipation is very important in simulations of non-Newtonian flows. The viscosity is modeled as temperature dependent by adopting the approximate Arrhenius formulation and it is realized that the viscosity changes can alter the flow field. The effects of the Reynolds number, the Weissenberg number, the Prandtl number, the Brinkman number, aspect ratio and some of the material parameters are documented within this study.

ÖZET

YÜZEY TAHRİKLİ EŞSICAKLIKLI OLMAYAN VİSKOELASTİK AKIMIN SAYISAL OLARAK İNCELENMESİ

Bu çalışmada kenar tahrikli eş sıcaklıklı ve Newtonyen olmayan akış sayısal olarak iki örnek problem (kenar tahrikli kare oyuk akışı, Silindir içerisinde dönen disk akışı) ile incelenmiştir. Newtonyen olmama durumunu modellemek için Upper Convected Maxwell, Oldroyd B ve Giesekus diferansiyel bünye denklemleri kullanılmıştır. Sonuçların karşılaştırılmasıyla Giesekus denklemin diğerlerine oranla daha gerçekçi sonuçlar verdiği ve bu denklem ile daha yüksek Weissenberg sayılarına çıkılabildiği gözlemlenmiştir. Modellemelerde iki farklı çözücüden yararlanılmıştır; PETSc ve IN-GMRES. PETSc, Newtonyen akım problemlerinin çözümü ile Krylov alt uzay ve öniyileştirme yöntemlerinin performans analizi için kullanılmıştır. PETSc analizleri, Newtonyen akım problemi için ILU(5) öniyileştirmeli BiCGStab çözücüsünün en iyi performansı verdiğini ortaya koymuştur. Matris depolamayan öniyileştirmeli Inexact Newton metoduna dayalı olarak geliştirilen IN-GMRES çözücüsünden eş sıcaklıkta ve Newtonyen olmayan akımların modellemesinde yararlanılmıştır. Yüksek Weissenberg sayılarına ulaşabilmek amacıyla continuation, upwind differencing, yüksek mertebeden ayrıklaştırma, eğik şablonlar ile ayrıklaştırma ve buna benzer sayısal araçlardan IN-GMRES algoritması içerisinde yararlanılmıştır. Eş sıcaklıkta olmayan modellemeler kısmında, taşınım ve yayınımın yanı sıra viskoz ısınma terimi de modellenmiş ve Newtonyen olmayan akımlarda bu terimin çok önemli olduğu anlaşılmıştır. Viskozite, Approximate Arrhenius yasasından yararlanılarak sıcaklığa bağlı olarak modellenmiş ve viskozitedeki değişimlerin akım alanını da etkilediği görülmüştür. Reynolds sayısı, Weissenberg sayısı, Prandtl sayısı, Brinkman sayısı, en-boy oranı ve bazı fiziksel özellikler gibi parametrelerin etkileri de incelenmiştir.

TABLE OF CONTENTS

LIST OF FIGURES

LIST OF TABLES

LIST OF SYMBOLS/ABBREVIATIONS

Br	Brinkman number
C_p	Constant pressure specific heat
D	Rate of deformation tensor
De	Deborah number
El	Elasticity number
H	Height
$H(T)$	Temperature dependent shift factor
$\mathbf{J}$	Jacobian matrix
k	Thermal conductivity
L	Length
$\mathbf{M}_{L,k}$	Left preconditioning matrix at kth iteration
$\mathbf{M}_{R,k}$	Right preconditioning matrix at kth iteration
Pe	Péclet number
Pr	Prandtl number
p	Pressure
R	Radius
Re	Reynolds number
S	Non-Newtonian part of the stress tensor
s_k	Linear step solution at kth iteration
T	Temperature
T_{hot}	Temperature at the hot boundary
T_{cold}	Temperature at the cold boundary
u	u component of the velocity
$\mathbf{V}$	Velocity vector
V	Magnitude of the velocity
v	v component of the velocity
We	Weissenberg number
w	w component of the velocity
α	Mobility factor

α_s	Sensitive coefficient of temperature
β	Viscosity ratio
β_T	Temperature dependent viscosity ratio
Γ	Circulation
δ	Aspect ratio (H/R)
ε	Perturbation parameter
η_k	Inexact Newton parameter
λ	Relaxation time
λ_d	Damping parameter
λ_r	Retardation time
μ	Dynamic viscosity
μ_0	Reference dynamic viscosity
ξ	Vorticity
ρ	Density
ψ	Stream function
Ω	Angular velocity

ASM(m)	Additive Schwarz Preconditioning with Overlaps m
ASPIN	Additive Schwarz Preconditioned Inexact Newton
BiCGStab	Bi-Conjugate Gradient Stabilized
CFD	Computational Fluid Dynamics
CG	Conjugate Gradient Method
CGS	Conjugate Gradient Squared Method
CSR	Compressed Sparse Row
DDDN	Directional Differencing Discrete Newton
FDM	Finite Difference Method
FEM	Finite Element Method
FVM	Finite Volume Method
GMRES(m)	Generalized Minimal Residual Method with Restart
ILU(m)	Incomplete LU Factorization Preconditioner with Fill ins m
IN-GMRES	Inexact Newton-GMRES algorithm

LDC	Lid Driven Cavity
PETSc	Portable Extensible Toolkit for Scientific Computing
PTT	Phan-Thien Tanner constitutive relation
QUICK	Quadratic Upstream Interpolation for Convective Kinetics
RDCE	Rotating Disc in a Cylindrical Enclosure
SFV	Stream function - Vorticity
SIMPLE	Semi-Implicit Method for Pressure-Linked Equations
TFQMR	Transpose Free Quasi Minimal Residual
UCM	Upper Convected Maxwell
UD1	First Order Upwinding Scheme
UD2	Second Order Upwinding Scheme

1. INTRODUCTION

Developing technology brings about an industrial need for different materials such as polymeric liquids and in order to make use of these materials, their characteristics under different physical conditions should be known. As far as fluid mechanics is concerned, there exist two different types of liquids which are Newtonian and non-Newtonian. The shear stress of a Newtonian fluid is linearly proportional to the velocity gradient and the constant of proportionality is known as the viscosity. For a Newtonian fluid, viscosity is mainly a function of temperature, therefore if the problem is isothermal it can be assumed as constant. The examples for Newtonian fluids are air, water, glycerin and all other gases. Low molecular weight liquids, and solutions of low molecular weight substances in liquids are also usually Newtonian.

Even though Newtonian fluids are generally used in the engineering applications, non-Newtonian fluids have been drawing a great deal of attention since 1930's as well. This heated attention is brought about by the development of technology and widely use of rheologic fluids such as polymeric liquids. A non-Newtonian fluid is defined as fluid of which viscosity depends on the shear rate (and sometimes time and temperature as well). These dependencies complicate the mechanical properties of the fluid. The shear stress of a non-Newtonian fluid is defined with constitutive relations. To simulate a non-Newtonian fluid, there are three major choices. The first one is to use a generalized Newtonian type relations which utilizes the idea of describing the viscosity as a function of shear rate. The examples of such models are; the Power Law, the Carreu-Yasuda and the Cross models. The second one is to use a differential type constitutive relation like the Upper Convected Maxwell (UCM), the Oldroyd B, the Giesekus and Phan-Thien Tanner (PTT) models. The third idea to model the non-Newtonian behavior is use of integral type constitutive relations such as Doi-Edwards and KBKZ models. These approaches and constitutive relations are satisfactory up to some point; however, none of them can model the non-Newtonian flow phenomenon thoroughly. That's why scientists have been striving to come up with new constitutive relations to simulate the physical phenomenon in a better way.

The investigation of vortex flows in moving edge problems has always been popular because of their physical applications such as lubrication, ocean circulation, turbo machinery, electronic cooling, coating and rheology in particular. The most investigated problems of such flows are lid driven cavity (LDC) and rotating disc in a cylindrical enclosure problems (RDCE), which are still under consideration by many scientists. These geometries are also used as benchmark problems for Computational Fluid Dynamics (CFD). Although the Newtonian case of these problems has been extensively studied, there is limited information on the non-Newtonian cases. In this study, non-Newtonian phenomenon for both LDC and RDCE problems are investigated where the former is an example of the translational moving edge problems while the latter is an example of the rotational moving edge problems.

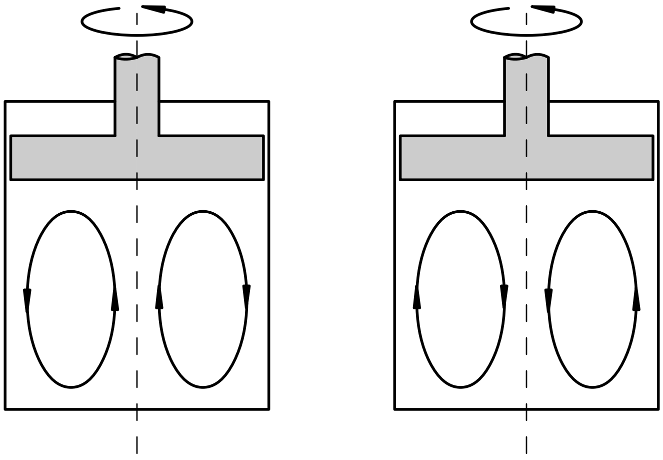

(a) Newtonian fluid (b) Non-Newtonian fluid

Figure 1.1. Secondary flow in a rotating disc in a cylindrical container system

Moreover, RDCE is selected because of a specific flow occurrence distinctive for non-Newtonian fluids within this geometry. This problem has two main fluid motions; the primary rotation in the $r-\theta$ plane and the secondary rotation in the $r-z$ plane. The primary motion, which is the outcome of the rotation of the disc, is always in the tangential direction. The secondary rotation differs according to the type of fluid inside the container. In the case of the Newtonian fluids, the secondary flow rotates radially outward from the disk (Figure 1.1(a)). This motion is triggered by the angular velocity difference between the fluid particles near the rotating disc (large angular velocity) and the fluid particles near the container (small angular velocity). The fluid particles near the rotating disc experience large outward centrifugal forces and the flow rotates radially outward from the disc. For the non-Newtonian fluids, increasing elasticity - increased Weissenberg number in our case - generates growing normal stresses in the opposite direction of the centrifugal force. After a certain point depending on the problem, these stresses counterbalance the centrifugal force and generate a reversed flow field (Figure 1.1(b)).

In the context of this study, in order to investigate the non-isothermal viscoelastic flows within the LDC and RDCE geometries, a preconditioned Inexact Newton-Krylov solver is generated and UCM, Oldroyd B and Giesekus constitutive models are implemented in this algorithm. In addition, continuation in the Weissenberg number is utilized in order to achieve the solutions of the high Elasticity number problems.

The geometries for the lid driven cavity and the rotating disc in a cylindrical enclosure flows can be seen in Figure 1.2(a) and Figure 1.2(b) respectively. The geometry for the lid driven cavity (Figure 1.2(a)) is straightforward. The geometry of the second problem (Figure 1.2(b)) consists of a cylindrical casing and two circular discs at the top and the bottom of the casing. By utilizing the axial symmetry, the computational area is reduced to a rectangle, which can be seen in the same figure with a hatched region. The aspect ratio is defined as $\delta = H/R$ and the moving parts rotate with angular velocity Ω.

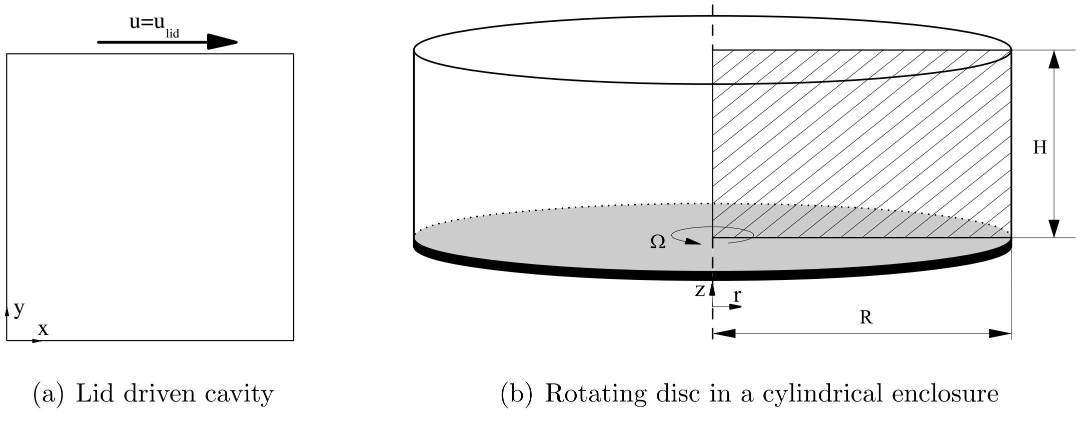

(a) Lid driven cavity

(b) Rotating disc in a cylindrical enclosure

Figure 1.2. Problem geometries

There are many studies concerning the Newtonian flow within a cavity. Ghia *et al.* [1] achieved results for high Reynolds number Newtonian flow using multi grid method where the velocity field within the cavity is computed up to Reynolds number of 10000 by using the Stream Function - Vorticity (SFV) formulation. The data given for the u and v velocity components along the centerlines of the cavity are used for the purpose of comparison in the Newtonian version of the LDC simulations within this study.

Besides the numerous studies of the Newtonian flows within LDC, scientists have also investigated the non-Newtonian flow phenomenon for this geometry. Neofytou [2] worked on the generalized Newtonian type constitutive equations and used Power Law, Quemada, Cason and modified Bingham models for simulation while the Semi-Implicit Method for Pressure-Linked Equations (SIMPLE) method with QUICK upwinding is adopted for the solution.

Griller *et al.* [3] used FENE-CR constitutive relation and modeled leakage at the corners at which the singular points occur. They used Newton-Raphson method with continuation in Weissenberg number and obtained results for Weissenberg number up to 0.24 for fully elastic cavity model. These singular points at the corners have also been investigated by Renardy [4] and numerical values for stresses at the corners in the case of UCM constitutive equation are proposed.

Fattal *et al.* [5] computed solutions for the Oldroyd B fluid up to We = 3 by using log-confirmation representation. Moreover, the functional (Equation 1.1) lid velocity is used to overcome the singularities at the corners within the study of Fattal *et al.* [5].

$$u_{lid}(x,t) = 8\left[1 + tanh8\left(t - 0.5\right)\right]x^2(1-x)^2 \tag{1.1}$$

The singularities at the top corners of the LDC geometry occur because of the velocity differences between the lid and the stationary walls. If the lid velocity is defined as a function which has zero value at its end points, the velocity difference and accordingly the singularities at the corners vanish. Fattal *et al.* [5] defined the lid velocity considering this fact as seen in the Equation 1.1.

Since the steady state solution is searched in this thesis, the time dependence is eliminated from the Equation 1.1 by equating the time to infinity. Thereby, the steady state form of the lid velocity is determined as;

$$u_{lid}(x) = 16x^2(1-x)^2 \tag{1.2}$$

Following Fattal *et al.* [5], Equation 1.1 has extensively been utilized to overcome the singularities at the corners of the lid. For example, Surana *et al.* [6, 7] used this function to analyze the Oldroyd B and UCM flow phenomenon in the LDC geometry. The investigators obtained results up to $De = 0.2$ with Re = 0 in both studies. Moreover, Belblidia *et al.* [8] modeled the same problem by using Oldroyd B constitutive model while the solutions are achieved for the viscosity ratio of 8/9 and Reynolds numbers 0 and 100. The Weissenberg number limit in the study is 0.25.

Pakdel *et al.* [9] have worked on the problem experimentally by using the laser Doppler velocimetry and digital particle image velocimetry. In the study, the aspect ratio is varied from 0.24 to 4 where the range of Deborah number is changed between 0 and 0.35. The study concludes that the symmetry for the zero Reynolds number is disturbed with the increasing elastic effects while it is observed that at the low Deborah numbers, the increasing velocity causes the primary vortex center to move upstream.

Two of the earlier studies about the Newtonian case of rotating disc in a cylindrical enclosure problem are carried out by Pao [10, 11]. In this mentioned study, one of the plates (bottom or top) are made stationary while the other plate and the casing rotate. The solutions are obtained for small Reynolds numbers with the fixed aspect ratio ($\delta = 1$). Similar problems are considered by Lopez [12] and Saci *et al.* [13] in which the results are obtained for the high Reynolds numbers and the various aspect ratios considering the Newtonian fluids. Moreover, Kaptan *et al.* [14] has solved this problem by using the preconditioned Newton-Krylov techniques which are similar to the techniques used in this research.

Moroi *et al.* [15] have investigated the non-Newtonian flow in the RDCE geometry. The scientists numerically acquire the flow patterns for different aspect ratios using the Giesekus constitutive model with the mobility factor $\alpha = 0.1$ and utilized splitting of the stress tensor into the Newtonian and non-Newtonian parts to ease up the solution. The limit of the elasticity number in the numerical part of the research is 0.01. The types of the flow patterns for varying aspect ratios are given in tables considering the Elasticity numbers. In the experimental part, four types of the flow patterns are observed. The first one is the Newtonian like flow which rotates in the same direction with the Newtonian fluids while the second one is the reverse flow which is rotating in the opposite direction of the Newtonian flow. The other two types have a double cell structure. The DC1 is the one which has two vortex cells side by side while the DC2 has two vortex cells, one of which is on the top of the other. What is more, the scientists have tried to simulate the double cell structure with the UCM model; however, they haven't succeeded which emphasizes the importance of the selection of the constitutive relation. Nevertheless, the Newtonian like and the reverse flows can be observed by using the UCM model.

Similar to their previous work, Moroi *et al.* [16] have studied the flow patterns both numerically and experimentally. The v velocity distribution is given at $R = 0.5$ line for constant Elasticity number of 0.0048. In the numerical part, the Giesekus ($\alpha = 0.1$), Phan Thien Tanner (PTT) and Power law models are adopted where in the experimental part particle tracking velocimetry isused. In this cited study, a graph of the Reynolds number versus the Elasticity number which indicates the flow structure is given as well.

Itoh *et al.* [17] numerically and experimentally investigate the non-Newtonian flow in a rotating disc in a cylindrical enclosure geometry with the Reynolds number range of 0.36 to 50. In this study, the laser doppler velocimeter is utilized for the experiments where the scientists applied the Power law and Giesekus ($\alpha = 0.1$) constitutive relations for the numerical computations. In the numerical part of the study, a fixed

Elasticity number ($El = 0.0048$) is used. The scientists give the v velocity versus local height plots for Re = 10 and Re = 50 values. In addition, the high Elasticity number phenomenon is discussed experimentally with the Elasticity numbers of $El = 1.862$ and $El = 38.05$. Periodical oscillations near the axis for the $El = 1.862$ case and reverse flow for $El = 38.05$ case are observed in the experiments.

Additionally, the oscillated flow is experimentally studied by Tamano *et al.* [18, 19]. In the study, it is observed that a vortex ring is shedding away from the rotating disc in the unsteady regime while with the further increase in the Reynolds number, the vortex ring becomes non-axisymmetric. Moreover, the researchers analyze the effects of the aspect ratio and the different surfactant solutions on this unsteady phenomenon.

Stokes *et al.* [20, 21] are also among the ones who worked on the RDCE flow of the non-Newtonian fluids and these studies are about the effects of inertia and elasticity on the flow patterns. The scientists conducted experiments with the particle imaging velocimetry technique by using the Boger fluids and investigated the flow patterns for Reynolds number up to 1600. The observed flow types are similar to Moroi *et al.* [15, 16].

Another numerical study is realized by Xue *et al.* [22]] in which the UCM flow in a 3-D geometry for the different aspect ratios is simulated. The study uses the Finite Volume Method (FVM) for the discretization and the SIMPLE type method for the solution. The scientists give streamlines for Elasticity numbers of $El = 0.0001875$, $El = 0,03125$, $El = 0,0625$ and $El = 0,15625$ ($\delta = 1.0$ case). The flow patterns alter from the Newtonian like to the reverse flow with the increasing Elasticity numbers.

The elastic turbulence, which can be described as a type of turbulence revealed not in high Reynolds numbers but in high Weissenberg numbers (Elasticity number is high), is another hot topic in the area of non-Newtonian fluid mechanics. Groisman *et al.* [23, 24] conducted some experiments on the curvilinear flows and acquire the turbulent flow structures for the high Elasticity number polymer solutions (such as $El = 18.57$). Despite being a very striking phenomenon, the subject of the elastic turbulence can not be simulated with the numerical studies since it is a very high Elasticity number event.

Xianhong and Li [25] studied the non-isothermal version of non-Newtonian flow for 4:1 contraction flow. The Power Law model is used to model the non-Newtonian behavior where the solutions up to Péclet number of 100 are obtained by employing a Crank-Nicolson based implicit algorithm. The effect of viscous dissipation is included in the energy equation while the viscosity is modelled by using a non-isothermal version of Power Law model.

Wachs *et al.* [26] investigated the non-isothermal viscoelastic flow in a 4:1 contraction in which the viscoelastic effects are simulated by using UCM constitutive relation and the temperature dependence of viscosity is modeled by WFL equation and the viscous dissipation is included. The total stresses are splitted into the Newtonian and non-Newtonian parts as in this thesis and the solutions up to Weissenberg number of 10 are reported.

Yesilata [27] studied the non-isothermal viscoelastic flow between two rotating coaxial parallel discs with the aspect ratio of 1/12. The flow is modeled as creeping flow (Re=0) and the Oldroyd B constitutive relation is used to analyse the viscoelastic behavior. The temperature dependence of viscosity is simulated with the Arrhenius Law where the viscous dissipation is taken into consideration in the energy equation. The effect of viscous dissipation on the temperature field is presented up to Deborah number of 5.

As far as the numerical methods are concerned, the researchers mentioned before used time dependent codes to simulate the non-Newtonian phenomenon. They generally used Picard or SIMPLE type algorithms. These and some other solution strategies are explained in detail in the books of Crochet *et al.* [28] and Owens *et al.* [29].

Tasai *et al.* [30] conducted their research by using similar methods to the ones applied in this thesis. They solved the stick-slip and the 4:1 contraction problems of the Oldroyd B fluid with three different solvers. The first solver is the modified Frontal solver which is a type of a direct solution technique. The other two are matrix free Incomplete LU (ILU) preconditioned Newton-Krylov techniques. The linear solvers in these two are the Generalized Minimal Residual Method with Restart (GMRES(m)) and Bi-Conjugate Gradient Stabilized (BiCGStab) methods. From the observation of the convergence rates of the solvers, Frontal solver turns out to be the worst one among the other solvers. In some cases this method fails to converge. The comparison between GMRES(40) and BiCGStab reveals that BiCGStab converges faster than GMRES(40).

The flow past a confined cylinder problem of Oldroyd B fluid is investigated by Kim *et al.* [31]. Similar to Tasai *et al.* [30], the scientists use the ILU preconditioned Newton-BiCGStab technique with the storage format of Compressed Sparse Row (CSR).

Howell [32] worked on the high Weissenberg number phenomenon using simple, natural, and pseudo-arclength continuation methods. He solved 4:1 contraction problem with the Johnson-Segalman model. The researcher used Newton method to linearize the equations where the linearized equations were solved by UMFPACK package.

Baaijens [33] investigated the UCM flow of falling sphere and axisymmetric 4:1 contraction problems with Newton-Krylov methods. The researcher analytically derived the Jacobian and benefited from GMRES and BiCGStab for the linear system solutions. In the study, it is mentioned that the BiCGStab solver frequently stalls when the Weissenberg number is high.

1.1. Objective

In the light of the previous studies, the objective of this study is selected as developing a preconditioned IN-GMRES algorithm that can deal with the high nonlinearities arising from the simulation of the non-isothermal non-Newtonian flows. The most important aspect of this solver is its capability of achieving results for high Weissenberg number problems.

In this thesis the RDCE is the main problem therefore Table 1.1 reveals the limits of the Weissenberg numbers for only RDCE. It will be revealed in the Chapter 4 that the Weissenberg numbers/Elasticity numbers achieved by using the IN-GMRES algorithm of this study are substantially higher than the previous studies (for example El = 130.5 for the Re = 1, $\delta = 0.5$ case of RDCE problem).

Table 1.1. Literature Review for RDCE

Scientist	Model	Aspect Ratio	Problem Parameters
Moroi [16]	Power Law, Giesekus, PTT	0.3, 0.5, 1, 2	up to El = 0.0048
Itoh [17]	Power Law, Giesekus	0.3, 1, 2	up to El = 0.0048
Xue [22]	UCM	1, 2	up to El = 0.15625
Yesilata [27]	Oldroyd B	0.083	up to We = 5.0 Re = 0, Non-isothermal

Moreover, there is a lack of research concerning the non-isothermal RDCE flow in the literature. Only Yesilata [27] studied this problem with the assumption of creeping flow (Re = 0 and therefore Pe = 0). In this thesis, the non-isothermal version of the RDCE problem is investigated considering the effects of the Reynolds number, temperature dependence of the viscosity, viscous dissipation and non-zero Péclet number. Therefore, it can be said that the non-isothermal effects are more realistically modeled.

The effects of the Reynolds number, Weissenberg number, Prandt number, Brinkman number, Péclet number, aspect ratio, selection of the constitutive equation and its parameters such as the mobility factor in the Giesekus relation, temperature sensitive coefficient and many other computational parameters are surveyed as well.

2. MATHEMATICAL MODELING

In this part of the study, derivations of governing equations, non-dimensional parameters and boundary conditions will be explained. Additionally, the foundations behind the constitutive relations will be briefly introduced.

2.1. Governing Equations

2.1.1. Dimensional Equations

Dimensional governing equations for steady and incompressible fluids without body force can be written in vector form as;

$$\nabla.\mathbf{V} = 0 \tag{2.1}$$

$$\rho(\mathbf{V}.\nabla\mathbf{V}) = -\nabla p + \nabla.\tau \tag{2.2}$$

$$\rho C_p(\mathbf{V}.\nabla T) = k\nabla^2 T + \Phi \tag{2.3}$$

In Equation 2.3, Φ is the viscous dissipation term and it can be written as follows;

$$\Phi = \tau\mathbf{:}\nabla\mathbf{V} \tag{2.4}$$

Since we are dealing with non-Newtonian fluids, the stress tensor appearing in Equations 2.2 and 2.3, can be splitted into two parts which are Newtonian and non-Newtonian components as mentioned in Crochet *et al.* [28]. This decomposition changes the type of the vorticity equation to elliptic and improve the convergence of Inexact Newton-GMRES (IN-GMRES) algorithm.

$$\tau = S + 2\mu D \tag{2.5}$$

$$D = \frac{1}{2}\left[\nabla\mathbf{V} + (\nabla\mathbf{V})^T\right] \tag{2.6}$$

Here S is the non-Newtonian part of the stress tensor and D is the rate of deformation tensor, which is related to the Newtonian part of the stress where μ is the Newtonian viscosity. With the system of Equations 2.1 through 2.3, there exist more unknowns than the number of equations. For example, there are four equations for the lid driven cavity problem (continuity, u-momentum, v-momentum and energy equations) where the number of unknowns is seven (u-velocity, v-velocity, pressure, temperature, S_{xx}, S_{xy} and S_{yy}). Therefore, three additional equations are required to close the system. These equations are called constitutive relations and three of these models are studied in this research: Upper Convected Maxwell (UCM), Oldroyd B and Giesekus. These equations are differential type viscoelastic constitutive relations. The differential relations are preferred over generalized Newtonian models such as Power Law model because they can simulate viscoelastic phenomena more realistically than the generalized Newtonian models.

UCM, which is one of the simplest constitutive relations, is the first model implemented in this study. The usage of the UCM is recommended when the information about the fluid is limited. Although the formulation of the UCM model is simple, the numerical computations using this model are difficult in terms of convergence. The UCM constitutive relation is given as follows;

$$\tau + \lambda \overset{\nabla}{\tau} = 2\mu D \tag{2.7}$$

Here $\overset{\nabla}{\tau}$ is the upper convected derivative of the stress tensor and it is formulated as;

$$\overset{\nabla}{\tau} = \frac{\partial \tau}{\partial t} + \mathbf{V}\nabla\tau - (\nabla\mathbf{V})^T.\tau - \tau.\nabla\mathbf{V} \tag{2.8}$$

Oldroyd B is the second constitutive equation used. It is more realistic and has better convergence behavior than UCM model. This equation can be employed when the solvent and polymer viscosities of the non-Newtonian fluid are known explicitly.

Since Oldroyd B relation is applicable for low shear rates, it is not useful for very high Weissenberg number problems. The constitutive equation for Oldroyd B model can be written as follows;

$$\tau + \lambda \overset{\nabla}{\tau} = 2\mu \left(D + \lambda_r \overset{\nabla}{D} \right) \tag{2.9}$$

Where λ_r is the retardation time and the upper convected derivative of the deformation tensor can be obtained similar to Equation 2.8.

The final constitutive relation used is Giesekus which is one of the most realistic differential constitutive relations. This constitutive equation displays shear thinning behavior which has been proved to be useful in our research especially in the viscoelastic simulation of rotating disc in a cylindrical enclosure. The Giesekus constitutive relation is given as;

$$\left(I + \frac{\alpha\lambda}{\mu}\tau \right) . \tau + \lambda \overset{\nabla}{\tau} = 2\mu D \tag{2.10}$$

In Equation 2.10, I is the unit tensor and α is the mobility factor of the Giesekus constitutive equation.

If the flow is non-isothermal, the temperature dependence of the viscosity should be considered. This dependence can be modeled by using relations such as Arrhenius Law, Approximate Arrhenius Law, Fulcher Law, WFL Law, WFL Shear-Stress Law, Mixed-Dependence Law, etc. In this study, Approximate Arrhenius Law is selected to model the temperature dependent viscosity since the temperature differences in the simulations are small. Therefore this law is valid. In this relation, the viscosity can be factorized as follows;

$$\mu = H(T)\mu_0 \tag{2.11}$$

Where μ is the temperature dependent viscosity, $H(T)$ is the temperature dependent shift factor and μ_0 is the reference viscosity. The shift factor can be written as;

$$H(T) = \exp[-\alpha_s(T - T_\alpha)] \tag{2.12}$$

Where α_s is the sensitive coefficient of temperature, T is the local temperature while T_α is the reference temperature where $H(T) = 1$.

In the area of computational fluid dynamics, it is beneficial to model the physical phenomena with the dimensionless equations. This is mainly due to the comparability of the solutions. Since there are two problems with different coordinate systems, both of them need to be nondimensionalized separately. Below the nondimensionalization parameters are given for these problems.

The nondimensionalization parameters for the lid driven cavity problem are;

$$\begin{gathered} x^* = \frac{x}{L}, \qquad y^* = \frac{y}{L}, \qquad u^* = \frac{u}{V}, \qquad v^* = \frac{v}{V} \\ \tau^* = \frac{L}{\mu V}\tau, \qquad p^* = \frac{L}{\mu V}p, \qquad T^* = \frac{T - T_0}{T_{\text{hot}} - T_0} \end{gathered} \tag{2.13}$$

where $(^*)$ indicates the dimensionless parameters and V is the magnitude of the velocity.

For the rotating disc in a cylindrical enclosure problem the nondimensionalization parameters can be given as follows;

$$\begin{gathered} r^* = \frac{r}{R}, \qquad z^* = \frac{z}{R}, \qquad u^* = \frac{u}{R\Omega}, \qquad v^* = \frac{v}{R\Omega}, \qquad w^* = \frac{w}{R\Omega} \\ \tau^* = \frac{\tau}{\rho R^2 \Omega^2}, \qquad p^* = \frac{p}{\rho R^2 \Omega^2}, \qquad T^* = \frac{T - T_0}{T_{\text{hot}} - T_0} \end{gathered} \tag{2.14}$$

The differential equations of UCM, Oldroyd B and Giesekus constitutive relations can be merged into one equation since their mathematical expressions are similar. Subsequently, if they are nondimensionalized with the other governing equations, certain nondimensional numbers will appear. Before proceeding with the nondimensional forms of the governing equations, these numbers and their effects on the flow should be explained.

2.1.2. Nondimensional Numbers

The definitions and effects of the nondimensional numbers are explained below. In the equations,the abbreviation LDC corresponds to the lid driven cavity where the abbreviation RDCE corresponds to the rotating disc in a cylindrical enclosure problems.

2.1.2.1. Reynolds Number. The Reynolds number (Equations 2.15 and 2.16) is defined as the ratio of inertial forces to the viscous forces and it is used for determining whether the flow is laminar or turbulent.

$$\mathrm{Re} = \frac{\rho V L}{\mu_0} \qquad \text{LDC} \tag{2.15}$$

$$\mathrm{Re} = \frac{\rho \Omega R^2}{\mu_0} \qquad \text{RDCE} \tag{2.16}$$

In these equations; ρ is the density of the fluid, V is the magnitude of the velocity, L is the characteristic length, Ω is the angular velocity, R is the radius and μ_0 is the reference dynamic viscosity. It should also be mentioned that since the viscosities of the non-Newtonian fluids are high, the non-Newtonian flow phenomena is generally a low Reynolds number event therefore the elastic effects are more important than the inertial effects.

2.1.2.2. Weissenberg Number. The Weissenberg number, which can be seen in Equations 2.17 and 2.18, provides a measure of viscoelastic effects. The magnitude of the viscoelastic effects of the flow is directly proportional to the Weissenberg number. In the limit of zero Weissenberg number, Newtonian flow is acquired. Here λ is the relaxation time.

$$\mathrm{We} = \lambda \frac{V}{L} \qquad \text{LDC} \tag{2.17}$$

$$\mathrm{We} = \lambda \Omega \qquad \text{RDCE} \tag{2.18}$$

2.1.2.3. Elasticity Number. As far as viscoelastic flow is concerned, Elasticity number is the most critical nondimensional parameter and can be thought as the ratio of the elastic forces to the inertial forces. The numerical simulations of the non-Newtonian problems are mainly limited by this number. The Elasticity number alters the flow patterns in a dramatic way. For example at very high Elasticity numbers, the viscoelastic flows can interestingly reveal turbulent-like behaviors. This phenomenon is called "the elastic turbulence" and it is experimentally investigated by numerous scientists recently [23, 24].

$$\mathrm{El} = \frac{\mathrm{We}}{\mathrm{Re}} \tag{2.19}$$

2.1.2.4. Prandtl Number. The Prandtl number is the ratio of the momentum diffusivity to the thermal diffusivity and provides a measure of relative thickness of momentum and thermal boundary layers. Small Prandtl number points to the fact that the heat is diffusing at a higher rate compared to the momentum (velocity) and that the thermal boundary layer is thicker than the momentum boundary layer. The Prandtl number is written as follows;

$$\mathrm{Pr} = \frac{\mu C_p}{k} \tag{2.20}$$

In the simulation of viscoelastic fluids there are two ways of determining the Prandtl number. The first one is to take this number as a constant in the governing equations by using constant reference viscosity (μ_0) while the second method is to take this number as a variable by using the temperature dependent viscosity (μ). The latter is adapted in this study since the modeling of the physical phenomenon is more realistic in this way. The Prandtl numbers for the viscoelastic fluids are relatively higher than the Newtonian fluids.

2.1.2.5. Péclet Number. The Péclet number, which can be defined as the product of the Reynolds and Prandtl numbers, is a measure of relative strength of advection and diffusion. As the Péclet number approaches to zero, the properties are transported purely with diffusion and as the Péclet number approaches to infinity, the properties are transported via pure convection.

$$\mathrm{Pe} = \mathrm{Re}.\mathrm{Pr} \tag{2.21}$$

2.1.2.6. Brinkman Number. The Brinkman number is a measure of heat conduction from a wall to a flowing viscous fluid which is commonly used in polymer processing. This number appears as a multiplier of the viscous dissipation term of the nondimensional energy equation therefore if the Brinkman number is small then the viscous dissipation can be neglected. In Equations 2.22 and 2.23 T_{hot} is the temperature of the hot boundary where T_{cold} is the temperature of the cold boundary. Similar to the Prandtl number, within the Brinkman number viscosity is modeled as temperature dependent.

$$\mathrm{Br} = \frac{\mu V^2}{k(T_{\text{hot}} - T_{\text{cold}})} \qquad \text{LDC} \tag{2.22}$$

$$\mathrm{Br} = \frac{\mu R^2 \Omega^2}{k(T_{\text{hot}} - T_{\text{cold}})} \qquad \text{RDCE} \tag{2.23}$$

2.1.3. Nondimensional Equations

The dimensionless continuity, momentum, constitutive and energy equations for steady, incompressible and non-isothermal flow without body force can be given in vector form as follows (* are dropped);

$$\nabla.\mathbf{V} = 0 \tag{2.24}$$

$$\mathrm{Re}\,(\mathbf{V}.\nabla)\,\mathbf{V} + \nabla p - \beta_T \nabla^2 \mathbf{V} - (1-\beta_T)\nabla.\tau = 0 \tag{2.25}$$

$$\tau + \mathrm{We}\left[\mathbf{V}.\nabla\tau - (\nabla\mathbf{V})^T.\tau - \tau.\nabla\mathbf{V} + \alpha\tau.\tau\right] - \left[\nabla\mathbf{V} + (\nabla\mathbf{V})^T\right] = 0 \tag{2.26}$$

$$\mathrm{Pe}\,(\mathbf{V}.\nabla)\,T - \nabla^2 T - \mathrm{Br}(\tau\mathbf{:}\nabla\mathbf{V}) = 0 \tag{2.27}$$

Equation 2.26 is the merged version of the UCM, Oldroyd B and Giesekus constitutive relations. In the equations above τ is the viscoelastic stress tensor, p is the pressure, β_T is the temperature dependent viscosity ratio (given that μ_s is solvent viscosity and μ_p is polymer viscosity, $H(T)\mu_s/(\mu_s+\mu_p) = H(T)\beta$) and α is the mobility factor. In the equations above if α and β are zero then UCM constitutive relation is obtained. If β is non-zero and α is zero then Oldroyd B is obtained. Finally, if both α and β are non-zero the constitutive relation turns out to be Giesekus.

Since the coordinate systems are different, the governing equations for lid driven cavity and rotating disc in a cylindrical enclosure are different. As a result, the derivation of these equations will be given in two separate sections.

2.1.3.1. Lid Driven Cavity Problem. In order to eliminate pressure from the momentum equations cross differentiation (differentiate u-momentum with respect to y, v-momentum with respect to x and subtract latter from the first one) is used. Then stream function (ψ) - vorticity (ξ) approach is selected to ease up the solution. If the velocity vector in cartesian coordinates is defined as $\mathbf{V} = (u, v)$ in 2-D (no z dependence), the components of velocity and vorticity are given as;

$$u = \frac{\partial\psi}{\partial y} \tag{2.28}$$

$$v = -\frac{\partial\psi}{\partial x} \tag{2.29}$$

$$\xi = \frac{\partial v}{\partial x} - \frac{\partial u}{\partial y} \tag{2.30}$$

As can be seen in Equation 2.32, the viscoelastic stress tensor (Equation 2.31) is splitted to Newtonian and non-Newtonian parts with the purpose of making the type of the vorticity equation elliptic.

$$\tau = \begin{pmatrix} \tau_{xx} & \tau_{xy} \\ \tau_{xy} & \tau_{yy} \end{pmatrix} \tag{2.31}$$

$$\tau = S + 2D \tag{2.32}$$

Here S is the non-Newtonian part of the stress tensor and D is the rate of deformation tensor, which is related the Newtonian part of the stress, defined in Equation 2.33.

$$D = \frac{1}{2}\left[\nabla\mathbf{V} + (\nabla\mathbf{V})^T\right] \tag{2.33}$$

The velocity gradient tensor appearing in Equation 2.33 is;

$$\nabla\mathbf{V} = \begin{pmatrix} \frac{\partial u}{\partial x} & \frac{\partial v}{\partial x} \\ \frac{\partial u}{\partial y} & \frac{\partial v}{\partial y} \end{pmatrix} \tag{2.34}$$

The remaining terms in Equations 2.25, 2.26 and 2.27 are shown in Appendix A. After splitting the stresses and using Equations 2.28 through 2.34 and Appendix A for arrangements, the governing equations for the lid driven cavity flow is derived as given below;

$$\frac{\partial^2\psi}{\partial x^2} + \frac{\partial^2\psi}{\partial y^2} + \xi = 0 \tag{2.35}$$

$$\begin{aligned} \mathrm{Re}\left(\frac{\partial\psi}{\partial y}\frac{\partial\xi}{\partial x} - \frac{\partial\psi}{\partial x}\frac{\partial\xi}{\partial y}\right) - \left(\frac{\partial^2\xi}{\partial x^2} + \frac{\partial^2\xi}{\partial y^2}\right) \\ -(1-\beta_T)\left[\frac{\partial^2 S_{xy}}{\partial x^2} - \frac{\partial^2 S_{xy}}{\partial y^2} + \frac{\partial^2 S_{yy}}{\partial x\partial y} - \frac{\partial^2 S_{xx}}{\partial x\partial y}\right] = 0 \end{aligned} \tag{2.36}$$

$$\begin{aligned}
&S_{xx}\left(1-2\mathrm{We}\frac{\partial^2\psi}{\partial x\partial y}\right)+\mathrm{We}\left(\frac{\partial\psi}{\partial y}\frac{\partial S_{xx}}{\partial x}-\frac{\partial\psi}{\partial x}\frac{\partial S_{xx}}{\partial y}\right)-2\mathrm{We}\frac{\partial^2\psi}{\partial y^2}S_{xy}\\
&\quad-2\mathrm{We}\left[2\left(\frac{\partial^2\psi}{\partial x\partial y}\right)^2-\frac{\partial\psi}{\partial y}\frac{\partial^3\psi}{\partial x^2\partial y}+\frac{\partial\psi}{\partial x}\frac{\partial^3\psi}{\partial x\partial y^2}+\frac{\partial^2\psi}{\partial y^2}\left(\frac{\partial^2\psi}{\partial y^2}-\frac{\partial^2\psi}{\partial x^2}\right)\right]\\
&\quad+\alpha\mathrm{We}\Bigg[S_{xx}^2+S_{xy}^2+4S_{xx}\frac{\partial^2\psi}{\partial x\partial y}+2S_{xy}\left(\frac{\partial^2\psi}{\partial y^2}-\frac{\partial^2\psi}{\partial x^2}\right)\\
&\qquad\qquad+4\left(\frac{\partial^2\psi}{\partial x\partial y}\right)^2+\left(\frac{\partial^2\psi}{\partial y^2}-\frac{\partial^2\psi}{\partial x^2}\right)\Bigg]=0
\end{aligned}\tag{2.37}$$

$$\begin{aligned}
&S_{xy}+\mathrm{We}\left(\frac{\partial\psi}{\partial y}\frac{\partial S_{xy}}{\partial x}-\frac{\partial\psi}{\partial x}\frac{\partial S_{xy}}{\partial y}\right)+\mathrm{We}\frac{\partial^2\psi}{\partial x^2}S_{xx}-\mathrm{We}\frac{\partial^2\psi}{\partial y^2}S_{yy}\\
&\quad+\mathrm{We}\Bigg[2\frac{\partial^2\psi}{\partial x\partial y}\left(\frac{\partial^2\psi}{\partial x^2}+\frac{\partial^2\psi}{\partial y^2}\right)+\frac{\partial\psi}{\partial y}\left(\frac{\partial^3\psi}{\partial x\partial y^2}-\frac{\partial^3\psi}{\partial x^3}\right)\\
&\qquad\qquad+\frac{\partial\psi}{\partial x}\left(\frac{\partial^3\psi}{\partial x^2\partial y}-\frac{\partial^3\psi}{\partial y^3}\right)\Bigg]\\
&\quad+\alpha\mathrm{We}\left[\left(S_{xx}+S_{yy}\right)\left(S_{xy}+\left(\frac{\partial^2\psi}{\partial y^2}-\frac{\partial^2\psi}{\partial x^2}\right)\right)\right]=0
\end{aligned}\tag{2.38}$$

$$\begin{aligned}
&S_{yy}\left(1+2\mathrm{We}\frac{\partial^2\psi}{\partial x\partial y}\right)+\mathrm{We}\left(\frac{\partial\psi}{\partial y}\frac{\partial S_{yy}}{\partial x}-\frac{\partial\psi}{\partial x}\frac{\partial S_{yy}}{\partial y}\right)+2\mathrm{We}\frac{\partial^2\psi}{\partial x^2}S_{xy}\\
&\quad-2\mathrm{We}\left[2\frac{\partial^2\psi}{\partial x\partial y}^2+\frac{\partial\psi}{\partial y}\frac{\partial^3\psi}{\partial x^2\partial y}-\frac{\partial\psi}{\partial x}\frac{\partial^3\psi}{\partial x\partial y^2}-\frac{\partial^2\psi}{\partial x^2}\left(\frac{\partial^2\psi}{\partial y^2}-\frac{\partial^2\psi}{\partial x^2}\right)\right]\\
&\quad+\alpha\mathrm{We}\Bigg[S_{xy}^2+S_{yy}^2-4S_{yy}\frac{\partial^2\psi}{\partial x\partial y}+2S_{xy}\left(\frac{\partial^2\psi}{\partial y^2}-\frac{\partial^2\psi}{\partial x^2}\right)\\
&\qquad\qquad+4\left(\frac{\partial^2\psi}{\partial x\partial y}\right)^2+\left(\frac{\partial^2\psi}{\partial y^2}-\frac{\partial^2\psi}{\partial x^2}\right)\Bigg]=0
\end{aligned}\tag{2.39}$$

$$\begin{aligned}
&\mathrm{Pe}\left(\frac{\partial\psi}{\partial y}\frac{\partial T}{\partial x}-\frac{\partial\psi}{\partial x}\frac{\partial T}{\partial y}\right)-\left(\frac{\partial^2 T}{\partial x^2}+\frac{\partial^2 T}{\partial y^2}\right)\\
&\quad-\mathrm{Br}\Bigg[\left(S_{xx}-S_{yy}\right)\frac{\partial^2\psi}{\partial x\partial y}+S_{xy}\left(\frac{\partial^2\psi}{\partial y^2}-\frac{\partial^2\psi}{\partial x^2}\right)\\
&\qquad\qquad+4\left(\frac{\partial^2\psi}{\partial x\partial y}\right)^2+\left(\frac{\partial^2\psi}{\partial y^2}-\frac{\partial^2\psi}{\partial x^2}\right)^2\Bigg]=0
\end{aligned}\tag{2.40}$$

2.1.3.2. Rotating Disc in a Cylindrical Enclosure Problem. Additional to the primary rotating motion in the $r-\theta$ plane, another circulation appears in the $r-z$ plane in this problem. As a result, modeling of rotating disc in a cylindrical enclosure can not be carried out in two dimensions. Therefore, in addition to stream function (ψ) and vorticity (ξ), circulation (Γ) is used to model the rotation in the $r-\theta$ plane. This approach is generally used for axisymmetric problems (no θ dependence) while it is generally named as 2.5 dimensional simulation (2.5-D). Similar to lid driven cavity problem, the pressure term appearing in the r and z momentum equations are eliminated with cross differentiation (differentiate r-momentum with respect to z, z-momentum with respect to r and subtract latter from the first one). By defining the velocity vector in cylindrical coordinates as $\mathbf{V} = (u, v, w)$, the components of the velocity vector and the vorticity are defined as;

$$u = \frac{1}{r}\frac{\partial \psi}{\partial z} \tag{2.41}$$

$$v = \frac{\Gamma}{r} \tag{2.42}$$

$$w = -\frac{1}{r}\frac{\partial \psi}{\partial r} \tag{2.43}$$

$$\xi = \frac{\partial u}{\partial z} - \frac{\partial w}{\partial r} \tag{2.44}$$

Analogous to the lid driven cavity problem, splitting of the stresses, which are given in Equation 2.32, is used to ease up the computation. Stress and velocity gradient tensors for the cylindrical coordinates can be given as;

$$\tau = \begin{pmatrix} \tau_{rr} & \tau_{r\theta} & \tau_{rz} \\ \tau_{r\theta} & \tau_{\theta\theta} & \tau_{\theta z} \\ \tau_{rz} & \tau_{\theta z} & \tau_{zz} \end{pmatrix} \tag{2.45}$$

$$\nabla \mathbf{V} = \begin{pmatrix} \frac{\partial u}{\partial r} & \frac{\partial v}{\partial r} & \frac{\partial w}{\partial r} \\ \frac{-v}{r} & \frac{u}{r} & 0 \\ \frac{\partial u}{\partial z} & \frac{\partial v}{\partial z} & \frac{\partial w}{\partial z} \end{pmatrix} \tag{2.46}$$

The remaining terms in Equations 2.25, 2.26 and 2.27 are written in the Appendix B. After splitting the stresses and using Equations 2.41 through 2.46 and Appendix B, the governing equations for the rotating disc in a cylindrical enclosure problem are derived as given below;

$$\frac{\partial^2\psi}{\partial r^2} - \frac{1}{r}\frac{\partial\psi}{\partial r} + \frac{\partial^2\psi}{\partial z^2} - r\xi = 0 \tag{2.47}$$

$$\begin{aligned}
&\mathrm{Re}\left(\frac{\partial\psi}{\partial z}\frac{\partial\xi}{\partial r} - \frac{\partial\psi}{\partial r}\frac{\partial\xi}{\partial z} - \frac{\xi}{r}\frac{\partial\psi}{\partial z} - \frac{2\Gamma}{r^2}\frac{\partial\Gamma}{\partial z}\right) - \left(\frac{\partial^2\xi}{\partial r^2} + \frac{1}{r}\frac{\partial\xi}{\partial r} + \frac{\partial^2\xi}{\partial z^2} - \frac{\xi}{r^2}\right)\\
&\qquad -(1-\beta_T)\left\{\frac{\partial^2 S_{rr}}{\partial r\partial z} - \frac{\partial^2 S_{zz}}{\partial r\partial z} + \frac{\partial^2 S_{rz}}{\partial z^2} - \frac{\partial^2 S_{rz}}{\partial r^2}\right.\\
&\qquad\qquad \left. + \frac{1}{r}\left(\frac{\partial S_{rr}}{\partial z} - \frac{\partial S_{\theta\theta}}{\partial z} - \frac{\partial S_{rz}}{\partial r} + \frac{S_{rz}}{r}\right)\right\} = 0
\end{aligned} \tag{2.48}$$

$$\begin{aligned}
&\mathrm{Re}\left(\frac{\partial\psi}{\partial z}\frac{\partial\Gamma}{\partial r} - \frac{\partial\psi}{\partial r}\frac{\partial\Gamma}{\partial z}\right) - \frac{1}{r}\left(\frac{\partial^2\Gamma}{\partial r^2} - \frac{1}{r}\frac{\partial\Gamma}{\partial r} + \frac{\partial^2\Gamma}{\partial z^2}\right)\\
&\qquad -(1-\beta_T)\left(\frac{\partial S_{r\theta}}{\partial r} + \frac{\partial S_{\theta z}}{\partial z} + \frac{2S_{r\theta}}{r}\right) = 0
\end{aligned} \tag{2.49}$$

$$\begin{aligned}
&S_{rr} + \frac{\mathrm{We}}{r}\left(\frac{\partial\psi}{\partial z}\frac{\partial S_{rr}}{\partial r} - \frac{\partial\psi}{\partial r}\frac{\partial S_{rr}}{\partial z} + \frac{2S_{rr}}{r}\frac{\partial\psi}{\partial z} - 2S_{rr}\frac{\partial^2\psi}{\partial r\partial z} - 2S_{rz}\frac{\partial^2\psi}{\partial z^2}\right)\\
&\quad + \frac{2\mathrm{We}}{r^2}\left[\frac{\partial\psi}{\partial z}\left(\frac{\partial^3\psi}{\partial r^2\partial z} + \frac{2}{r}\frac{\partial^2\psi}{\partial r\partial z}\right) - \frac{\partial\psi}{\partial r}\frac{\partial^3\psi}{\partial r\partial z^2} - 2\left(\frac{\partial^2\psi}{\partial r\partial z}\right)^2\right.\\
&\qquad\qquad \left. - \left(\frac{\partial^2\psi}{\partial z^2}\right)^2 + \frac{\partial^2\psi}{\partial r^2}\frac{\partial^2\psi}{\partial z^2}\right]\\
&\quad + \alpha\mathrm{We}\left[\left(S_{rr} + 2\left(\frac{1}{r}\frac{\partial^2\psi}{\partial r\partial z} - \frac{1}{r^2}\frac{\partial\psi}{\partial z}\right)\right)^2 + \left(S_{r\theta} + \frac{1}{r}\frac{\partial\Gamma}{\partial r} - \frac{2\Gamma}{r^2}\right)^2\right.\\
&\qquad\qquad \left. + \left(S_{rz} + \frac{1}{r}\frac{\partial^2\psi}{\partial z^2} + \frac{1}{r^2}\frac{\partial\psi}{\partial r} - \frac{1}{r}\frac{\partial^2\psi}{\partial r^2}\right)^2\right] = 0
\end{aligned} \tag{2.50}$$

$$\begin{aligned}
S_{r\theta} &+ \frac{\mathrm{We}}{r}\left(\frac{\partial\psi}{\partial z}\frac{\partial S_{r\theta}}{\partial r} - \frac{\partial\psi}{\partial r}\frac{\partial S_{r\theta}}{\partial z} - S_{rr}\left(\frac{\partial\Gamma}{\partial r} - \frac{2\Gamma}{r}\right)\right. \\
&\qquad\qquad \left. - S_{r\theta}\frac{\partial^2\psi}{\partial r\partial z} - S_{rz}\frac{\partial\Gamma}{\partial z} - S_{\theta z}\frac{\partial^2\psi}{\partial z^2}\right) \\
&+ \frac{\mathrm{We}}{r^2}\left[\frac{\partial\psi}{\partial z}\left(\frac{\partial^2\Gamma}{\partial r^2} - \frac{3}{r}\frac{\partial\Gamma}{\partial r} + \frac{4\Gamma}{r^2}\right) - \frac{\partial\psi}{\partial r}\left(\frac{\partial^2\Gamma}{\partial r\partial z} - \frac{2}{r}\frac{\partial\Gamma}{\partial z}\right)\right. \\
&\qquad \left. - \left(\frac{\partial\Gamma}{\partial r} - \frac{2\Gamma}{r}\right)\left(3\frac{\partial^2\psi}{\partial r\partial z} - \frac{2}{r}\frac{\partial\psi}{\partial z}\right) - \frac{\partial\Gamma}{\partial z}\left(2\frac{\partial^2\psi}{\partial z^2} + \frac{1}{r}\frac{\partial\psi}{\partial r} - \frac{\partial^2\psi}{\partial r^2}\right)\right] \\
&+ \alpha\mathrm{We}\left[\left(S_{rr} + 2\left(\frac{1}{r}\frac{\partial^2\psi}{\partial r\partial z} - \frac{1}{r^2}\frac{\partial\psi}{\partial z}\right)\right)\left(S_{r\theta} + \frac{1}{r}\frac{\partial\Gamma}{\partial r} - \frac{2\Gamma}{r^2}\right)\right. \\
&\qquad + \left(S_{r\theta} + \frac{1}{r}\frac{\partial\Gamma}{\partial r} - \frac{2\Gamma}{r^2}\right)\left(S_{\theta\theta} + \frac{2}{r^2}\frac{\partial\psi}{\partial z}\right) \\
&\qquad \left. + \left(S_{rz} + \frac{1}{r}\frac{\partial^2\psi}{\partial z^2} + \frac{1}{r^2}\frac{\partial\psi}{\partial r} - \frac{1}{r}\frac{\partial^2\psi}{\partial r^2}\right)\left(S_{\theta z} + \frac{1}{r}\frac{\partial\Gamma}{\partial z}\right)\right] = 0
\end{aligned} \tag{2.51}$$

$$\begin{aligned}
S_{rz} &+ \frac{\mathrm{We}}{r}\left(\frac{\partial\psi}{\partial z}\frac{\partial S_{rz}}{\partial r} - \frac{\partial\psi}{\partial r}\frac{\partial S_{rz}}{\partial z} - S_{rr}\left(\frac{1}{r}\frac{\partial\psi}{\partial r} - \frac{\partial^2\psi}{\partial r^2}\right) + \frac{S_{rz}}{r}\frac{\partial\psi}{\partial z} - S_{zz}\frac{\partial^2\psi}{\partial z^2}\right) \\
&+ \frac{\mathrm{We}}{r^2}\left[2\frac{\partial^2\psi}{\partial r\partial z}\left(\frac{\partial^2\psi}{\partial z^2} - \frac{1}{r}\frac{\partial\psi}{\partial r} + \frac{\partial^2\psi}{\partial r^2}\right) - \frac{\partial\psi}{\partial r}\left(\frac{\partial^3\psi}{\partial z^3} + \frac{1}{r}\frac{\partial^2\psi}{\partial r\partial z} - \frac{\partial^3\psi}{\partial r^2\partial z}\right)\right. \\
&\qquad\qquad \left. + \frac{\partial\psi}{\partial z}\left(\frac{\partial^3\psi}{\partial r\partial z^2} - \frac{\partial^3\psi}{\partial r^3} + \frac{1}{r^2}\frac{\partial\psi}{\partial r} - \frac{1}{r}\frac{\partial^2\psi}{\partial r^2}\right)\right] \\
&+ \alpha\mathrm{We}\left[\left(S_{rr} + 2\left(\frac{1}{r}\frac{\partial^2\psi}{\partial r\partial z} - \frac{1}{r^2}\frac{\partial\psi}{\partial z}\right)\right)\left(S_{rz} + \frac{1}{r}\frac{\partial^2\psi}{\partial z^2} + \frac{1}{r^2}\frac{\partial\psi}{\partial r} - \frac{1}{r}\frac{\partial^2\psi}{\partial r^2}\right)\right. \\
&\qquad + \left(S_{r\theta} + \frac{1}{r}\frac{\partial\Gamma}{\partial r} - \frac{2\Gamma}{r^2}\right)\left(S_{\theta z} + \frac{1}{r}\frac{\partial\Gamma}{\partial z}\right) \\
&\qquad \left. + \left(S_{rz} + \frac{1}{r}\frac{\partial^2\psi}{\partial z^2} + \frac{1}{r^2}\frac{\partial\psi}{\partial r} - \frac{1}{r}\frac{\partial^2\psi}{\partial r^2}\right)\left(S_{zz} - \frac{2}{r}\frac{\partial^2\psi}{\partial r\partial z}\right)\right] = 0
\end{aligned} \tag{2.52}$$

$$\begin{aligned}
S_{\theta\theta} &+ \frac{\mathrm{We}}{r}\left(\frac{\partial\psi}{\partial z}\frac{\partial S_{\theta\theta}}{\partial r} - \frac{\partial\psi}{\partial r}\frac{\partial S_{\theta\theta}}{\partial z} - 2S_{r\theta}\left(\frac{\partial\Gamma}{\partial r} - \frac{2\Gamma}{r}\right) - \frac{2S_{\theta\theta}}{r}\frac{\partial\psi}{\partial z} - 2S_{\theta z}\frac{\partial\Gamma}{\partial z}\right) \\
&+ \frac{2\mathrm{We}}{r^2}\left[\frac{\partial\psi}{\partial z}\left(\frac{1}{r}\frac{\partial^2\psi}{\partial r\partial z} - \frac{4}{r^2}\frac{\partial\psi}{\partial z}\right) - \frac{1}{r}\frac{\partial\psi}{\partial r}\frac{\partial^2\psi}{\partial z^2} - \left(\frac{\partial\Gamma}{\partial r} - \frac{2\Gamma}{r}\right)^2 - \left(\frac{\partial\Gamma}{\partial z}\right)^2\right] \\
&+ \alpha\mathrm{We}\left[\left(S_{r\theta} + \frac{1}{r}\frac{\partial\Gamma}{\partial r} - \frac{2\Gamma}{r^2}\right)^2 + \left(S_{\theta\theta} + \frac{2}{r^2}\frac{\partial\psi}{\partial z}\right)^2 + \left(S_{\theta z} + \frac{1}{r}\frac{\partial\Gamma}{\partial z}\right)^2\right] = 0
\end{aligned} \tag{2.53}$$

$$\begin{aligned}
S_{\theta z} + \frac{\mathrm{We}}{r}\Bigg(\frac{\partial\psi}{\partial z}\frac{\partial S_{\theta z}}{\partial r} - \frac{\partial\psi}{\partial r}\frac{\partial S_{\theta z}}{\partial z} - S_{rz}\left(\frac{\partial\Gamma}{\partial r} - \frac{2\Gamma}{r}\right) \\
- S_{\theta z}\left(\frac{1}{r}\frac{\partial\psi}{\partial z} - \frac{\partial^2\psi}{\partial r\partial z}\right) - S_{r\theta}\left(\frac{1}{r}\frac{\partial\psi}{\partial r} - \frac{\partial^2\psi}{\partial r^2}\right) - S_{zz}\frac{\partial\Gamma}{\partial z}\Bigg) \\
+\frac{\mathrm{We}}{r^2}\Bigg[\frac{\partial\psi}{\partial z}\left(\frac{\partial^2\Gamma}{\partial r\partial z} - \frac{2}{r}\frac{\partial\Gamma}{\partial z}\right) - \frac{\partial\psi}{\partial r}\frac{\partial^2\Gamma}{\partial z^2} + 3\frac{\partial\Gamma}{\partial z}\frac{\partial^2\psi}{\partial r\partial z} \\
- \left(\frac{\partial\Gamma}{\partial r} - \frac{2\Gamma}{r}\right)\left(\frac{\partial^2\psi}{\partial z^2} + \frac{2}{r}\frac{\partial\psi}{\partial r} - 2\frac{\partial^2\psi}{\partial r^2}\right)\Bigg] \\
+\alpha\mathrm{We}\Bigg[\left(S_{r\theta} + \frac{1}{r}\frac{\partial\Gamma}{\partial r} - \frac{2\Gamma}{r^2}\right)\left(S_{rz} + \frac{1}{r}\frac{\partial^2\psi}{\partial z^2} + \frac{1}{r^2}\frac{\partial\psi}{\partial r} - \frac{1}{r}\frac{\partial^2\psi}{\partial r^2}\right) \\
+ \left(S_{\theta\theta} + \frac{2}{r^2}\frac{\partial\psi}{\partial z}\right)\left(S_{\theta z} + \frac{1}{r}\frac{\partial\Gamma}{\partial z}\right) \\
+ \left(S_{\theta z} + \frac{1}{r}\frac{\partial\Gamma}{\partial z}\right)\left(S_{zz} - \frac{2}{r}\frac{\partial^2\psi}{\partial r\partial z}\right)\Bigg] = 0
\end{aligned} \tag{2.54}$$

$$\begin{aligned}
S_{zz} + \frac{\mathrm{We}}{r}\left(\frac{\partial\psi}{\partial z}\frac{\partial S_{zz}}{\partial r} - \frac{\partial\psi}{\partial r}\frac{\partial S_{zz}}{\partial z} - 2S_{rz}\left(\frac{1}{r}\frac{\partial\psi}{\partial r} - \frac{\partial^2\psi}{\partial r^2}\right) + 2S_{zz}\frac{\partial^2\psi}{\partial r\partial z}\right) \\
+\frac{2\mathrm{We}}{r^2}\Bigg[\frac{\partial\psi}{\partial z}\left(\frac{1}{r}\frac{\partial^2\psi}{\partial r\partial z} - \frac{\partial^3\psi}{\partial r^2\partial z}\right) + \frac{\partial\psi}{\partial r}\frac{\partial^3\psi}{\partial r\partial z^2} - 2\left(\frac{\partial^2\psi}{\partial r\partial z}\right)^2 \\
- \left(\frac{1}{r}\frac{\partial\psi}{\partial r} - \frac{\partial^2\psi}{\partial r^2}\right)\left(\frac{\partial^2\psi}{\partial z^2} + \frac{1}{r}\frac{\partial\psi}{\partial r} - \frac{\partial^2\psi}{\partial r^2}\right)\Bigg] \\
+\alpha\mathrm{We}\Bigg[\left(S_{rz} + \frac{1}{r}\frac{\partial^2\psi}{\partial z^2} + \frac{1}{r^2}\frac{\partial\psi}{\partial r} - \frac{1}{r}\frac{\partial^2\psi}{\partial r^2}\right)^2 + \left(S_{\theta z} + \frac{1}{r}\frac{\partial\Gamma}{\partial z}\right)^2 \\
+ \left(S_{zz} - \frac{2}{r}\frac{\partial^2\psi}{\partial r\partial z}\right)^2\Bigg] = 0
\end{aligned} \tag{2.55}$$

$$\begin{aligned}
\frac{\mathrm{Pe}}{r}\left(\frac{\partial\psi}{\partial z}\frac{\partial T}{\partial r} - \frac{\partial\psi}{\partial r}\frac{\partial T}{\partial z}\right) - \left(\frac{\partial^2 T}{\partial r^2} + \frac{1}{r}\frac{\partial T}{\partial r} + \frac{\partial^2 T}{\partial z^2}\right) \\
-\frac{\mathrm{Br}}{r}\left(1-\beta_T\right)\Bigg[S_{rr}\left(\frac{\partial^2\psi}{\partial r\partial z} - \frac{1}{r}\frac{\partial\psi}{\partial z}\right) + S_{r\theta}\left(\frac{\partial\Gamma}{\partial r} - \frac{2\Gamma}{r}\right) + \frac{S_{\theta\theta}}{r}\frac{\partial\psi}{\partial z} \\
+S_{rz}\left(\frac{1}{r}\frac{\partial\psi}{\partial r} - \frac{\partial^2\psi}{\partial r^2} + \frac{\partial^2\psi}{\partial z^2}\right) + S_{\theta z}\frac{\partial\Gamma}{\partial z} - S_{zz}\frac{\partial^2\psi}{\partial r\partial z}\Bigg] \\
-\frac{\mathrm{Br}}{r^2}\Bigg[2\left(\frac{\partial^2\psi}{\partial r\partial z} - \frac{1}{r}\frac{\partial\psi}{\partial z}\right)^2 + 2\left(\frac{1}{r}\frac{\partial\psi}{\partial z}\right)^2 + 2\left(\frac{\partial^2\psi}{\partial r\partial z}\right)^2 + \left(\frac{\partial\Gamma}{\partial z}\right)^2 \\
+ \left(\frac{\partial\Gamma}{\partial r} - \frac{2\Gamma}{r}\right)^2 + \left(\frac{1}{r}\frac{\partial\psi}{\partial r} - \frac{\partial^2\psi}{\partial r^2} + \frac{\partial^2\psi}{\partial z^2}\right)^2\Bigg] = 0
\end{aligned} \tag{2.56}$$

2.1.4. Boundary Conditions

Similar to the governing equations, the boundary conditions are different for lid driven cavity and rotating disc in a cylindrical enclosure problems. Therefore, separate sections are assigned for both. Since the indexing used for both problems are the same, it should be introduced first.

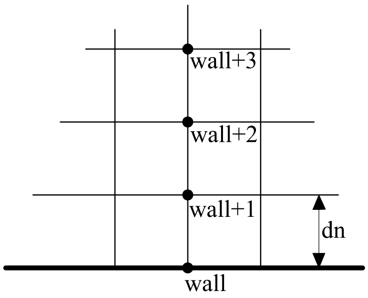

Figure 2.1. Boundary stencil

In the Figure 2.1, the stencil is revealed. Here, the index $wall$ indicates the node at the wall whereas the $wall+1$ refers to the first inner node. Similarly the $wall+2$ is the second inner node from the wall while the index $wall+3$ is the third inner node. Moreover, dn is the distance between the nodes in the normal direction.

2.1.4.1. Lid Driven Cavity Problem . The lid driven cavity problem has three stationary and one moving boundaries. The zero stream function boundary condition is applied for all walls. For vorticity, four different boundary conditions are tested, which are given in Table 2.1. The results of these tests will be revealed in Chapter 4. The wall velocities in the equations of Table 2.1 can be constant ($u_{wall} = 1$) or functional (steady version of Equation 1.1).

The stress boundary conditions are the most challenging part of the viscoelastic simulation problems and two types of these boundary conditions are applied in this study. The first one is to use the constitutive equation as the boundary condition because the boundary conditions themselves should satisfy their equations. This approach is widely used in the simulations of the viscoelastic problems and detailed

Table 2.1. Vorticity boundary conditions

	Equation
Thom's Formulae	$\xi_{wall} = \frac{2}{dn^2}\left(\psi_{wall} - \psi_{wall+1} + u_{wall}dn\right)$
Woods' Formulae	$\xi_{wall} = \frac{3}{dn^2}\left(\psi_{wall} - \psi_{wall+1} + u_{wall}dn\right) - \frac{1}{2}\xi_{wall+1}$
Jensen's Formulae	$\xi_{wall} = \frac{1}{2dn^2}\left(7\psi_{wall} - 8\psi_{wall+1} + \psi_{wall+2} + 6u_{wall}dn\right)$
Briley's Formulae	$\xi_{wall} = \frac{1}{18dn^2}(85\psi_{wall} - 108\psi_{wall+1}$ $+27\psi_{wall+2} - 4\psi_{wall+3} + 66u_{wall}dn)$

information about this boundary condition can be found in the book of Crochet *et al.* [28]. The second approach is introduced in a study by Kawabata *et al.* [34] which is successfully applied by Moroi *et al.* [15, 16] and Itoh *et al.* [17]. The investigators equate the second derivatives of the stresses in the normal direction to zero. Both of these boundary conditions are studied here while the results and discussions chapter includes the comparison of these.

Prescribed temperature at the walls are used as the boundary conditions for the energy equation. In simulations T_{hot} is used on the lid where T_{cold} is used on the rest of the walls.

2.1.4.2. Rotating Disc in a Cylindrical Enclosure Problem .

In the rotating disc problem, which can be seen in Figure 1.2(b), there are three walls and an axisymmetry line. The boundary conditions for the stream function, vorticity and circulation are given as follows;

- on the axis where $r = 0$ and $0 < z < H$; $\psi = 0$, $\xi = 0$, $\Gamma = 0$.
- on the rotating discs where $z = 0$ or $z = H$ and $0 < r < 1$; $\psi = 0$, $\xi = \frac{2}{dz^2 r}(\psi_{wall+1} - \psi_{wall})$, $\Gamma = r^2$.
- on the stationary discs where $z = 0$ or $z = H$ and $0 < r < 1$; $\psi = 0$, $\xi = \frac{2}{dz^2 r}(\psi_{wall+1} - \psi_{wall})$, $\Gamma = 0$.
- on the rotating cylinder where $r = 1$ and $0 < z < H$; $\psi = 0$, $\xi = \frac{2}{dr^2}(\psi_{wall+1} - \psi_{wall})$, $\Gamma = 1$.

- on the stationary cylinder where $r = 1$ and $0 < z < H$; $\psi = 0$, $\xi = \frac{2}{dr^2}(\psi_{wall+1} - \psi_{wall})$, $\Gamma = 0$.

The stress boundary conditions on the walls are similar to the lid driven cavity problem; they can either be the constitutive equations themselves or the boundary condition given by Kawabata *et al.* [34]. For the axis of symmetry, axisymmetric boundary conditions are used for all of the stresses.

Similar to lid driven cavity problem, prescribed temperature at the walls are used as the boundary conditions for the energy equation. At the axis of symmetry, axisymmetric boundary condition which is equating the first normal derivative of the temperature to zero is used for temperature.

3. NUMERICAL METHODS

In this part of the thesis, the solution algorithm will be introduced. First of all, the summary of the algorithm will be revealed and then all components of the solver will be explained in detail.

Two separate algorithms, one of them is utilizing full matrix and vectors for the solution while the other is matrix free, are developed in this study. The first one stores whole matrix and it is the ILU (m) preconditioned Inexact Newton-Krylov solver while the second one is matrix free Jacobi preconditioned Inexact Newton-Krylov solver.

The differential equations and the boundary conditions obtained in the previous section are discretized by using the well known finite difference method. The end-result is a coupled, nonlinear, sparse, large scale system (Equation 3.1) to solve.

$$\mathbf{F}(\mathbf{x}) = 0 \tag{3.1}$$

$$\mathbf{M}_{L,k}^{-1}\mathbf{J}_k\mathbf{M}_{R,k}^{-1}(\mathbf{M}_{R,k}\mathbf{s}_k) = -\mathbf{M}_{L,k}^{-1}\mathbf{F}(\mathbf{x}_k) \tag{3.2}$$

$$\mathbf{x}_{k+1} = \mathbf{x}_k + \lambda_d\mathbf{s}_k \tag{3.3}$$

$$\|\mathbf{F}(\mathbf{x}_k) + \mathbf{J}_k\mathbf{s}_k\|_2 \leq \max\left(\eta_k\|\mathbf{F}(\mathbf{x}_k)\|_2, 1E-8\right) \tag{3.4}$$

In the equations above, $\mathbf{J}$ is the Jacobian matrix, $\mathbf{M}_{L,k}$ is the left preconditioning matrix, $\mathbf{M}_{R,k}$ is the right preconditioning matrix, $\mathbf{s}_k$ is the linear step solution in the kth step, λ_d is the damping value and η_k is the inexact Newton parameter.

For the solution of the system in Equation 3.1, the preconditioned Inexact Newton-Krylov algorithm is used. The linear systems arising in the Inexact Newton part is solved by using preconditioned GMRES(m) (Generalized Minimal Residual method with restart m by Saad *et al.* [35]) or BiCGStab (BiConjugate Gradient Stabilized by Van der Vorst [36]). In each step, Equation 3.1 is linearized by using Newton's method and the obtained system is preconditioned with Jacobi or ILU(m) preconditioners. At the end of this procedure, Equation 3.2 is obtained. Preconditioning can be described as altering the original problem to another with the same solution but with favorable spectral properties to enhance the convergence behavior. Here Jacobi preconditioner is based on the benefits of the diagonal dominance where the ILU (m) preconditioner is utilizing the factorization of preconditioning matrix into the lower and upper triangular matrices. More details of preconditioning will be given in the preconditioning section. Thanks to the preconditioning, the convergence turns out to be faster and what is more, in some cases, the convergence becomes possible only by preconditioning. The system in Equation 3.2 is solved via GMRES(m) and the solution is updated as in Equation 3.3. The solution of the linear system is carried out until the inequality in the Equation 3.4 is satisfied. Sometimes damping is required on the update $\mathbf{s}_k$ to achieve convergence. Since the convergence of the Newton's method is strictly dependent on the initial guess, the continuation method is used. The continuation method is described as using the previous solution as the initial guess.

The reason for preferring GMRES(m) as the linear solver is its superiority over the older methods such as Gauss-Seidel, SOR (Successive Over Relaxation)) with respect to the convergence rate, its non-increasing residual property and easy application of the matrix free versions. Furthermore, as BiCGStab reveals oscillatory convergence behavior, GMRES(m) is selected as the primary linear solver in this study.

Since the computation of the Jacobian matrix is very costly and the matrix itself is sparse, the code is decided to be written as matrix free. In the solution of the linear system, GMRES needs only the products of Jacobian matrix and a vector instead of the Jacobian matrix itself. This operation is carried out by using the formula below and this is called Directional Differencing Discrete Newton (DDDN). For any vector $\mathbf{v}$;

$$\mathbf{J}\mathbf{v} \cong \frac{\mathbf{F}(\mathbf{x}+\varepsilon\mathbf{v})-\mathbf{F}(\mathbf{x})}{\varepsilon} \tag{3.5}$$

The linear solver code is written as matrix free with the aid of Equation 3.5. Here ε is the perturbation parameter, the selection of which has an effect on the robustness of the nonlinear solver. This parameter can be selected either as a variable like in the studies of Brown *et al.* [37] and Qin *et al.* [38] or as a constant. In this study, it is taken as a constant which is equivalent to the square root of the machine epsilon. What is more, in the discretization process, the upwinding is used, which considers the direction of the flow rate to speed up the convergence. Moreover, in order to enhance the accuracy of the results, fourth order difference stencils at the interior points are utilized. The convergence tolerance for the nonlinear system is set to 1E-5 where the linear convergence parameter is taken as 1E-8.

The analysis of performance is carried out with the ILU (m) preconditioned Inexact Newton-Krylov solver which stores whole matrix and vectors and matrix free Jacobi preconditioned Inexact Newton-Krylov solver. Since the former requires a lot of storage in the memory, the grid resolutions for both of the problems turn out to be insufficient. Moreover, the solution time is much longer than the matrix free versions. Under the light of these reasons, the matrix free Jacobi preconditioned Inexact Newton GMRES(m) is selected as the primary solver of the study.

3.1. Newton's Method

The Newton's Method is an efficient solver for the sparse, nonlinear systems arising from the discretization of the nonlinear differential equations. This method is used to linearize the nonlinear system in each step and the linear systems are solved by iterative methods such as Krylov methods. An iteration of Newton's Method can be given as;

$$\mathbf{J}_k\mathbf{s}_k = -\mathbf{F}(\mathbf{x}_k) \tag{3.6}$$

where the updated solution and the Jacobian matrix are;

$$\mathbf{x}_{k+1} = \mathbf{x}_k + \mathbf{s}_k \tag{3.7}$$

$$\mathbf{J}_{i,j} = \frac{\partial \mathbf{F}_i}{\partial \mathbf{x}_j} \tag{3.8}$$

As can be understood from the Equation 3.8, the computation of the Jacobian matrix is very costly in terms of computation time since it requires partial derivatives of the equations with respect to all unknowns.

Newton's Method has its advantages and disadvantages like all numerical procedures.

The advantages can be written as follows:

- Easy Implementation.
- Quadratic convergence rate for a nonsingular Jacobian.
- If the function is affine, the exact solution can be obtained in one iteration.

The disadvantages can be written as follows:

- Not globally convergent.
- Jacobian evaluation is needed for every iteration.
- Each iteration needs linear system solution.
- Can stagnate at a local maxima or minima.

Some drawbacks of the Newton method, such as Jacobian evaluation at every step, can be prevented by using Inexact Newton-Krylov techniques since Krylov methods need only the products of Jacobian matrix and a vector instead of the Jacobian matrix itself. This operation is carried out by using DDDN which is given in Equation 3.5. In addition, when the initial guess x_0 is far away from the solution, the first iterates of the Newton's Method become distant to the solution as well. Therefore in the first iterations of the Newton's method, it is unnecessary to solve the linear systems until the tolerance is satisfied.

Figure 3.1 shows the flowchart of the inexact Newton algorithm. The algorithm starts with initial guessing and residual calculation. After the calculation of the residual, the tolerance is computed for the linear iterations of each Newton step by considering the Equation 3.4. Linear solvers, GMRES(m) or BiCGStab, compute the update and it is added to the previous iterate as in Equation 3.3. Then the new residual is calculated and the convergence is checked. If the convergence is obtained, then the program ends with writing the results. However, if not, then additional Newton steps are required.

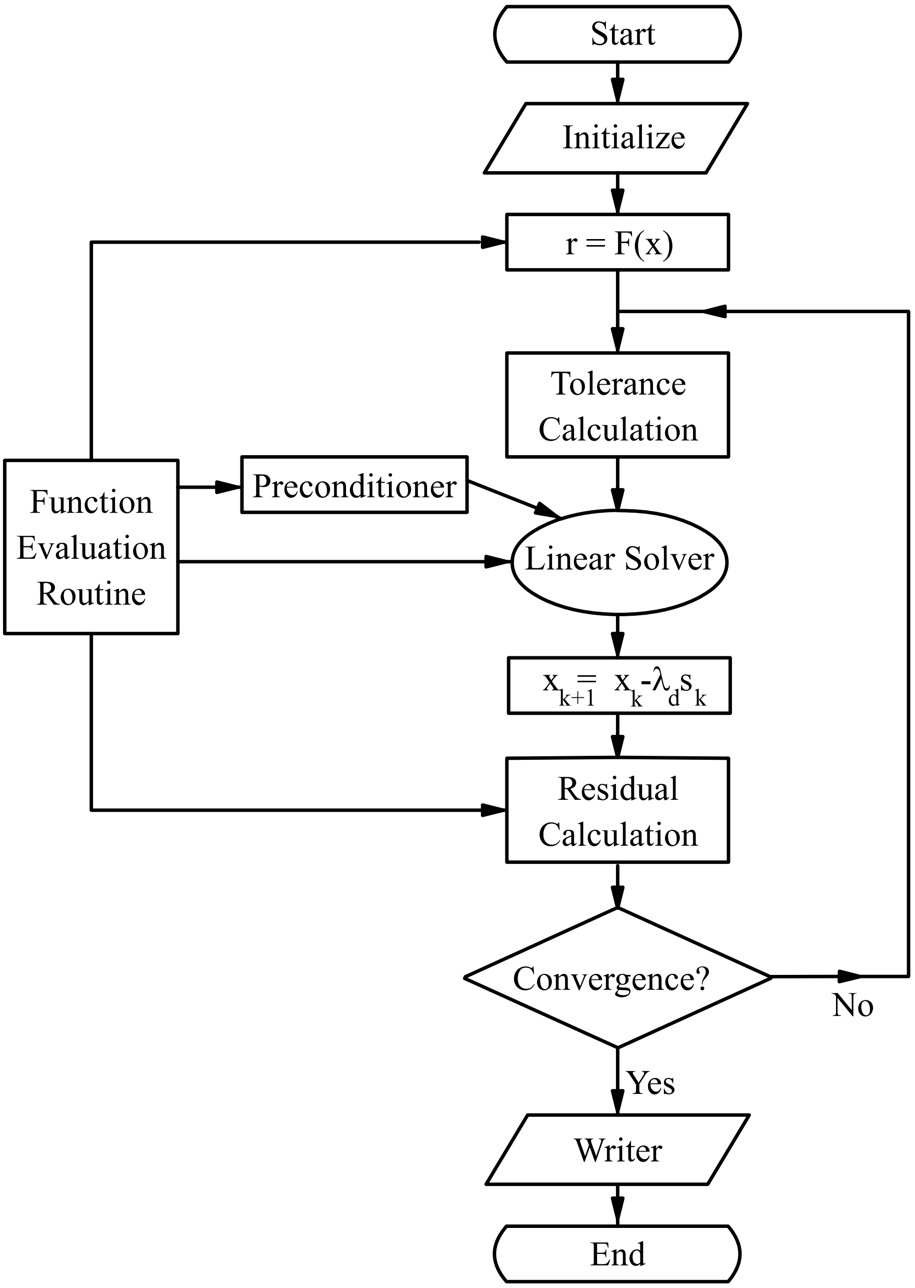

Figure 3.1. Flowchart of the inexact Newton's method

There are some guidelines of selecting the Inexact Newton parameters λ_d and η_k. The theory and implementational issues of the selection is explained in the book of Kelley [41]. In this study, $\eta_k = 1E - 4$ and $\lambda_d = 1.0$ are used.

3.2. Krylov Methods

In each step of the Newton's Method, the linear system shown in Equation 3.2 is required to be solved. The solution can be obtained by direct or iterative methods. Direct methods generally need the inverse of a matrix or a structure that can be solved by back or forward substitution. These processes are very costly in terms of computation and sometimes they are impossible to obtain. For example, inverting a matrix is not always possible. Due to these facts, iterative methods are generally preferred over direct methods. Moreover, iterative methods are separated as the stationary and nonstationary methods. Stationary methods perform same operations on the system independent of the current iterate. Jacobi, Gauss-Seidel, Successive Over Relaxation and Symmetric Successive Over Relaxation methods are four main stationary methods. Nonstationary methods, on the other hand, perform the operations depending on the current iterate, which enables them to converge more rapidly. Due to the better performance, nonstationary Krylov methods GMRES(m), BiCGStab and TFQMR are used in this research.

The idea of the Krylov methods is approximating the problem in a Krylov subspace by generating orthogonal or biorthogonal vectors. Suppose the linear problem of $A\mathbf{x} = \mathbf{b}$ has dimensions of m and the residual vector is $\mathbf{r}_0 = \mathbf{b} - \mathbf{A}\mathbf{x}$, the method seeks the solution in the Krylov subspace ($\mathcal{K}_m$) of;

$$\mathcal{K}_m(\mathbf{A}, \mathbf{r}_0) = \mathbf{r}_0, \mathbf{A}\ \mathbf{r}_0, \mathbf{A}^2\mathbf{r}_0, ..., \mathbf{A}^{m-1}\mathbf{r}_0 \tag{3.9}$$

The Krylov Methods used in the study (GMRES(m), BiCGStab and TFQMR) can be explained as follows.

3.2.1. GMRES

Generalized Minimal Residual Method (GMRES) of Saad *et al.* [35], computes a sequence of orthogonal vectors, and uses least squares to combine these vectors for update. Method generates a sequence of orthogonal vectors in a Krylov subspace of K-independent basis vectors: $v_1 \perp v_2 \perp v_3 ... \perp v_k$. Moreover, this method is applicable to non-symmetric matrices and requires only matrix-vector products with the coefficient matrix. In this way, the matrix free versions of this method can be implemented. The 2-norm residual is non-increasing in every step of the GMRES and the residuals can be monitored without constructing the iterates. As there is no need to compute the residual and Jacobian in GMRES, it reduces computational cost (brings about a 90 % reduction in computational cost in problems).

Due to the fact that this method requires storing whole vectors generated, each new iteration step is more costlier than the previous one. This results in an increase in memory consumption, which is a drawback of this method; that is the reason why the restarted version of GMRES, normally referred as GMRES(m) and/or preconditioning, can be used instead. The iteration is terminated at m^{th} step and the solution will be used as initial guess for the next iteration in the restarted version of GMRES. The difficulty is choosing an appropriate value for m. If m is small, GMRES(m) may have slow convergence, or fail to converge entirely. A value of m that is larger than needed involves excessive work and uses more storage which will ultimately effect the computation time. Unfortunately, there are no definite rules governing the choice of m. In restarted versions obtaining the solution requires little more iteration than unrestarted ones [14].

The pseudo algorithm for left preconditioned GMRES(m) is given with the Figure 3.2.

More information about GMRES(m) and its implementational issues can be found in [35, 43, 44].

```
1. Compute $r_0 = M^{-1}(b - Ax_0)$, $\beta = \|r_0\|_2$, and $v_1 = r_0/\beta$
2. For $j = 1, 2, ..., m$ Do:
3.     Compute $w_j = M^{-1}Av_j$
4.     For $i = 1, ..., j$ Do:
5.         $h_{i,j} = (w_j, v_j)$
6.         $w_j = w_j - h_{i,j}v_j$
7.     End Do
8.     $h_{j+1,j} = \|w_j\|_2$
9.     $v_{j+1} = w_j/h_{j+1,j}$
10. End Do
11. Define $V_m = [v_1, ..., v_m]$, $\overline{H}_m = \{h_{ij}\}_{1\leq i\leq j+1;1\leq j\leq m}$
12. Compute $y_m$=argmin$\|\beta e_1 - \overline{H}_m y\|_2$ and $x_m = x_0 + V_m ym$
13. If satisfied Stop, else set $x_0 := x_m$ and Go To 1
```

Figure 3.2. The pseudo algorithm for left preconditioned GMRES(m)

3.2.2. BiCGStab

The BiConjugate Gradient Stabilized Method (BiCGStab) of Van der Vorst [36], generates two sequences of vectors that are bi-orthogonal. Similar to GMRES(m), non-symmetric systems can be solved by using only matrix-vector products, which enables the matrix free versions of the BiCGStab. The BiCGStab method converged a little faster than GMRES(m) but it can indicate oscillatory convergence behavior which can be seen in Kaptan *et al.* [14]. As a result of the oscillatory convergence behavior of the BiCGStab solver, GMRES (m) is selected as the linear solver in our studies.

The pseudo algorithm for left preconditioned BiCGStab is given with the Figure 3.3.

3.2.3. TFQMR

Transpose Free Quasi Minimal Residual (TFQMR) algorithm of Freund [39] which is derived from the Conjugate Gradient Squared method, is an improved transpose

```
Compute $\mathbf{r}_0 = \mathbf{b} - \mathbf{A}\mathbf{x}_0$
Choose $\tilde{\mathbf{r}}$ (For example, $\tilde{\mathbf{r}} = \mathbf{r}_0$)
For $j = 1, 2, ..., m$ Do:
    $\rho_{i-1} = \tilde{\mathbf{r}}^T \mathbf{r}^{i-1}$
    If $\rho_{i-1} = 0$ Method fails
    If $i = 1$
        $\mathbf{p}_i = \mathbf{r}_{i-1}$
    else
        $\beta_{i-1} = (\rho_{i-1}/\rho_{i-2})(\alpha_{i-1}/\omega_{i-1})$
        $\mathbf{p}_i = \mathbf{r}_{i-1} + \beta_{i-1}(\mathbf{p}_{i-1} - \omega_{i-1}\mathbf{v}_{i-1})$
    end if
    Solve $\mathbf{M}\hat{\mathbf{p}} = \mathbf{p}_i$
    $\mathbf{v}_i = \mathbf{A}\hat{\mathbf{p}}$
    $\alpha_i = \rho_{i-1}/\tilde{\mathbf{r}}^T \mathbf{v}_i$
    $\mathbf{s} = \mathbf{r}_{i-1} - \alpha_i \mathbf{v}_i$
    If $\|\mathbf{s}\|_2 \leq Tol.$, set $\mathbf{x}_i = \mathbf{x}_{i-1} + \alpha_i \hat{\mathbf{p}}$ and stop
    Solve $\mathbf{M}\hat{\mathbf{s}} = \mathbf{s}$
    $\mathbf{t} = \mathbf{A}\hat{\mathbf{s}}$
    $\omega_i = \mathbf{t}^T \mathbf{s}/\mathbf{t}^T \mathbf{t}$
    $\mathbf{x}_i = \mathbf{x}_{i-1} + \alpha_i \hat{\mathbf{p}} + \omega_i \hat{\mathbf{s}}$
    $\mathbf{r}_i = \mathbf{s} - \omega_i \mathbf{t}$
    If $\|\mathbf{r}\|_2 \leq Tol.$ stop
    For continuation it is necessary that $\omega_i \neq 0$
End Do
```

Figure 3.3. The pseudo algorithm for left preconditioned BiCGStab

free version of Quasi Minimal Residual (QMR) algorithm of Freund and Nachtigal [40]. TFQMR can be applied to nonsymmetric matrices and it is designed to overcome the irregular convergence behavior of the Bi-Conjugate Gradient (BiCG) method. In addition, the computational cost and parallelization properties are similar to the BiCG method.

The pseudo algorithm for TFQMR is given with the Figure 3.4. .

```
Compute $w_0 = u_0 = r_0 = b - Ax_0$, $v_0 = Au_0$, $d_0 = 0$
$\tau_0 = \|r_0\|_2$, $\theta_0 = \eta_0 = 0$
Choose $r_0^*$ such that $\rho_0 \equiv (r_0^*, r_0) \neq 0$
For $j = 1, 2, ...$ until convergence, Do:
    If j is even then
        $\alpha_{j+1} = \alpha_j = \rho_j / (v_j, r_0^*)$
        $u_{j+1} = u_j - \alpha_j v_j$
    End If
    $w_{j+1} = w_j - \alpha_j A u_j$
    $d_{j+1} = u_j + (\theta_j^2 / \alpha_j) \eta_j d_j$
    $\theta_{j+1} = \|w_{j+1}\|_2 / \tau_j$, $c_{j+1} = (1 + \theta_{j+1}^2)^{-0.5}$
    $\tau_{j+1} = \tau_j \theta_{j+1} c_{j+1}$, $\eta_{j+1} = c_{j+1}^2 \alpha_j$
    $x_{j+1} = x_j + \eta_{j+1} d_{j+1}$
    If j is odd then
        $\rho_{j+1} = (w_{j+1}, r_0^*)$, $\beta_{j-1} = \rho_{j+1} / \rho_{j-1}$
        $u_{j+1} = w_{j+1} + \beta_{j-1} u_m$
        $v_{m+1} = A u_{j+1} + \beta_{j-1} (A u_j + \beta_{j-1} v_{j-1})$
    End If
End Do
```

Figure 3.4. The pseudo algorithm for TFQMR

3.3. Preconditioning

The preconditioning can be described as altering the original problem to another with the same solution but with favorable spectral properties to enhance the convergence behavior. The preconditioning matrix is an approximation to the Jacobian matrix. It should include same characteristics of the Jacobian so that, $\mathbf{M}^{-1}\mathbf{A}$ should be close to the identity matrix, yet it should be simple enough to invert as well. An example of a preconditioner can be a restricted version of the Jacobian matrix obtained for a coarser grid or by using a low order discretization scheme. The preconditioning step in this study is given by Equation 3.2, which points out the left and right preconditioning cases. If $\mathbf{M}_R$ is taken as the identity tensor $\mathbf{I}$, the left preconditioning takes place and similarly if $\mathbf{M}_L$ is taken as the identity tensor, the right preconditioning takes place. Left preconditioning case of Equation 3.2 can be given as;

$$\mathbf{M}_{L,k}^{-1}\mathbf{J}\mathbf{s}_k = \mathbf{M}_{L,k}^{-1}\mathbf{F}(\mathbf{x}_k) \tag{3.10}$$

The left preconditioning is easy to apply: it is simply the multiplication of both sides of linear systems arising in the Krylov solvers with the inverse of the preconditioning matrices from the left. Additionally it requires the multiplication of the initial residual vector with the preconditioning matrix with the left ($\mathbf{r}_0 \longleftarrow \mathbf{M}_{L,k}^{-1}\mathbf{r}_0$) which brings the disadvantage of this type of preconditioning. Since the residual is scaled, the linear system solvers can converge prematurely and the solution of the linear step leads to an inappropriate Newton direction, which is the reason why Newton's method will fail to converge. To prevent this failure, the tolerance for the linear system can be taken two or three orders less (instead of taking the linear system tolerance 1E-6, 1E-8 should be used).

Right preconditioning case of Equation 3.2 can be formulated as;

$$\mathbf{J}\mathbf{M}_{R,k}^{-1}\mathbf{y}_k = \mathbf{F}(\mathbf{x}_k) \tag{3.11}$$

where;

$$\mathbf{M}_{R,k}\mathbf{s}_k = \mathbf{y} \tag{3.12}$$

In the right preconditioning, the multiplications seen in the Equation 3.11 and Equation 3.12 should be carried out. Additionally, the calculated solution $\mathbf{s}_k$ should be scaled as;

$$\mathbf{s}_k \longleftarrow \mathbf{M}_{R,k}^{-1}\mathbf{s}_k \tag{3.13}$$

The third type of preconditioning is the split preconditioning in which the preconditioning matrix is splitted into two parts which are lower (**L**) and upper (**U**) triangular matrices (**M**=**LU**). This type of preconditioning can be formulated with;

$$\mathbf{L}_k^{-1}\mathbf{J}\mathbf{U}_k^{-1}\mathbf{y}_k = \mathbf{L}_k^{-1}\mathbf{F}(\mathbf{x}_k) \tag{3.14}$$

where;

$$\mathbf{U}_k\mathbf{s}_k = \mathbf{y}_k \tag{3.15}$$

Since the preconditioning matrices are lower and/or upper triangular, the solutions involving them can be obtained by using backward or forward substitution algorithms (for example Equation 3.15 can be solved by backsubstitution).

Besides the preconditioning on the linearized systems, there is also another type of preconditioning which is applied on the non linear system itself. The nonlinear preconditioning obtains the solution of Equation 3.1 by solving a new nonlinear system given in Equation 3.16 which has the same solution with Equation 3.1.

$$\mathcal{F}(\mathbf{x}) = 0 \tag{3.16}$$

There is no restriction on the form of $\mathcal{F}$ since it has the same solution. One way of obtaining $\mathcal{F}$ is carried out by using the additive Schwarz method in which the computational domains are partitioned into several subdomains with or without overlaps. Allowing overlaps improves the communications between the subdomains which results in a better performance. In this case the nonlinear system is represented for N subdomains as;

$$\mathcal{F}(\mathbf{x}) = \sum_{i=1}^{N} T_i(\mathbf{x}) \tag{3.17}$$

where $T_i(\mathbf{x})$ is the solution of the nonlinear system of the i^{th} subdomain. This solution strategy is called as Additive Schwarz Preconditioned Inexact Newton (ASPIN) and the details of this method is explained in the study of Cai *et al.* [42].

The preconditioning algorithms used in this study are Jacobi and ILU(m) preconditioners.

3.3.1. Jacobi Preconditioning

Jacobi preconditioning is the simplest preconditioner which can be expressed as the diagonal of the matrix. It benefits from the fact that the solution of the linear systems which have terms at same order of magnitude is easier. Since this preconditioner is nothing but the diagonal of the matrix, it can be stored as a vector hence the matrix free implementations of Jacobi preconditioners are easy. Furthermore, since the preconditioning matrix has entries only at the diagonal, the inversion is very simple. The Jacobi preconditioner is formulated as follows;

$$\mathbf{M}_{i,j} = \begin{cases} J_{i,i} & \text{if} \quad i = j \\ 0 & \text{otherwise} \end{cases} \tag{3.18}$$

The Jacobi preconditioning is used as the left or right preconditioner in the matrix free codes of this study.

3.3.2. Incomplete LU Factorization Preconditioning

Incomplete LU factorization preconditioning, namely ILU(m) preconditioning, is a type of a split preconditioner which generates sparse lower triangular and upper triangular matrices (**M**=**LU**). These matrices are computed by carrying out the Gaussian elimination and neglecting some of the elements in the specific locations. The (m) in the abbreviation stands for the level of fill in. For example, in the ILU(0) case, the non-zero elements of the computed preconditioning matrices **L** and **U** appear only at the locations where the linear system matrix **A** has non zeroes. Since there are no additional elements, the level of fill in is said to be zero for this situation. The level of fill in can be increased by accepting some additional elements where the linear system matrix **A** has zeroes. Since these additional elements have information about the linear system matrix, increasing the level of fill in results in better preconditioning; however, calculating the additional fill in entries brings some extra cost of computation. Therefore, the preconditioner performance for the computation time of the preconditioner should be optimized. More information about the ILU(m) preconditioners can be found in [43, 44, 45].

In order to demonstrate the change in the preconditioning matrix, the Newtonian LDC problem is solved by utilizing the velocity-vorticity formulation and ILU(m) preconditioning. Figure 3.5 reveals the Jacobian matrix structure for this problem where Figures 3.6, 3.7 and 3.8 demonstrates the preconditioning matrix structures for the level of fill in values of 0, 2 and 5 respectively.

It can be seen from these figures that the preconditioning matrix has the same structure with the Jacobian matrix for the fill in value of zero. Since for the zero fill in value, the non-zero elements of the computed preconditioning matrix appear only at the locations where the Jacobian matrix has non zeroes. For the increasing fill in values it is apparent that the preconditioning matrix has additional non-zero elements. The computation time for generating the preconditioning matrix increases with the increasing level of fill ins. However, increased fill in means that the preconditioning matrix has more information on the Jacobian matrix and the solution of the linear

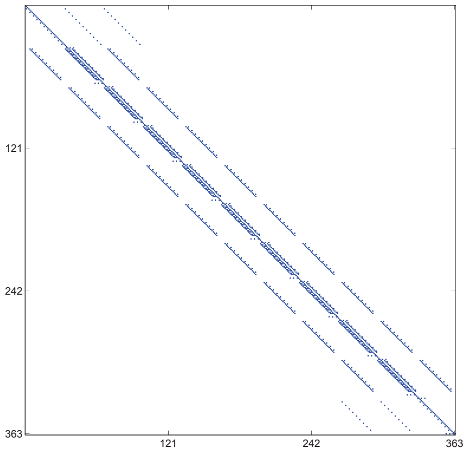

Figure 3.5. The Jacobian matrix structure

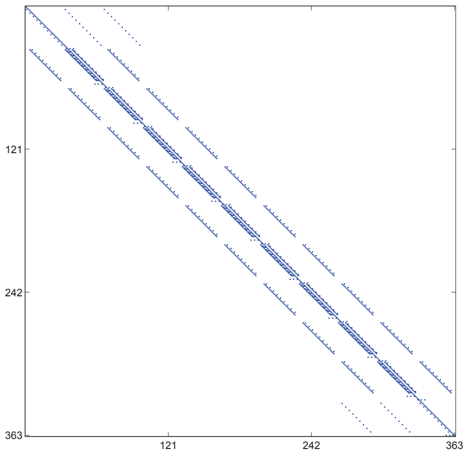

Figure 3.6. The Preconditioning matrix structure for ILU(0)

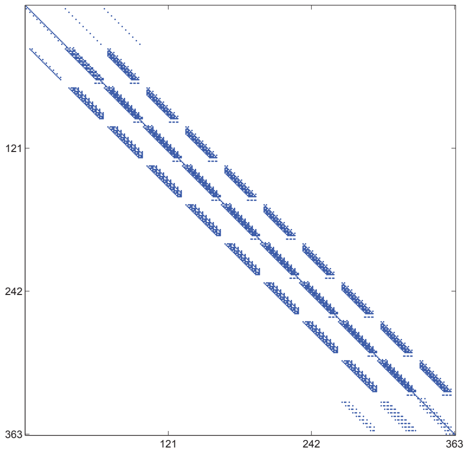

Figure 3.7. The Preconditioning matrix structure for ILU(2)

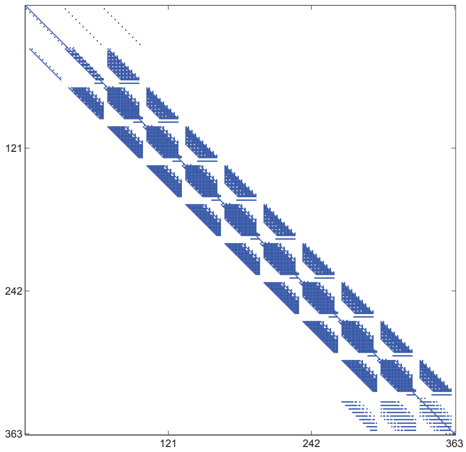

Figure 3.8. The Preconditioning matrix structure for ILU(5)

system will be more easier. One should be optimize the ratio between the generation time of the preconditioning matrix and the solution time of the linear system.

3.4. Upwinding

The upwinding technique gives better results and convergence behavior by identifying the direction of the flow through computing the velocity and modifying the equations with respect to the direction. It is suitable for the problems in which the flow rotates as in the problems of this study and more beneficial for the high Reynolds number flows. To illustrate the upwinding schemes, consider the following term to be discretized in nine point finite difference stencil which can appear in the governing equations.

$$u\frac{\partial \xi}{\partial x} \tag{3.19}$$

Two most popular upwinding schemes have been implemented in the solvers which are the first order upwind scheme (UD1) and the second order upwind scheme (UD2). The comparison between these two is carried out in the results and discussions section.

3.4.1. First Order Upwind Scheme

The first order upwind scheme (UD1) is the simplest upwinding scheme in which the Equation 3.19 is discretized as follows.

$$u\frac{\partial \xi}{\partial x} = \begin{cases} \text{if} \quad u_{i,j} \geq 0 \quad u_{i,j}\frac{\xi_{i,j}-\xi_{i-1,j}}{dx} \\ \text{if} \quad u_{i,j} < 0 \quad u_{i,j}\frac{\xi_{i+1,j}-\xi_{i,j}}{dx} \end{cases} \tag{3.20}$$

Apart from the advantages of the first order upwinding scheme, high numerical diffusion can appear in the case of the large gradients.

3.4.2. Second Order Upwind Scheme

The second Order Upwind Scheme (UD2) is the improved version of the first order scheme in terms of accuracy. However, by using more grid points, it brings extra load to the computation but the numerical diffusion error is less compared to the first order upwinding scheme. The discretization using this scheme is given below;

$$u\frac{\partial \xi}{\partial x} = \begin{cases} \text{if} \quad u_{i,j} \geq 0 \quad u_{i,j}\frac{3\xi_{i,j}-4\xi_{i-1,j}+\xi_{i-2,j}}{2dx} \\ \text{if} \quad u_{i,j} < 0 \quad u_{i,j}\frac{-\xi_{i+2,j}+4\xi_{i+1,j}-3\xi_{i,j}}{2dx} \end{cases} \tag{3.21}$$

3.5. Continuation

Since the convergence of the Newton's method is strictly dependent on the initial guess, the continuation method in Weissenberg number is used. The continuation method is described as using the previous solution as the initial guess. For example, to obtain the solution of the lid driven cavity problem with Weissenberg number of 0.4 with the zero initial guess is impracticable. However, solving the same problem with taking the initial guess as the solution of We = 0.35 is doable.

3.6. PETSc

Portable, Extensible Toolkit for Scientific Computation (PETSc) is a powerful computational tool which is developed in Argonne National Laboratory by Balay *et al.* [46]. It is a program which is designed specifically for the solution of large scale, sparse, nonlinear systems arising from the discretization of the partial differential equations and provides parallel and sequential tools where the solution strategy is based on preconditioned Newton-Krylov methods. The PETSc not only employs the MPI standard for all message-passing communication, but also automatically generates the implementation of MPI as well. That's why the analyst shouldn't have to care about MPI except preparing the nonlinear function or matrices/vectors appropriately.

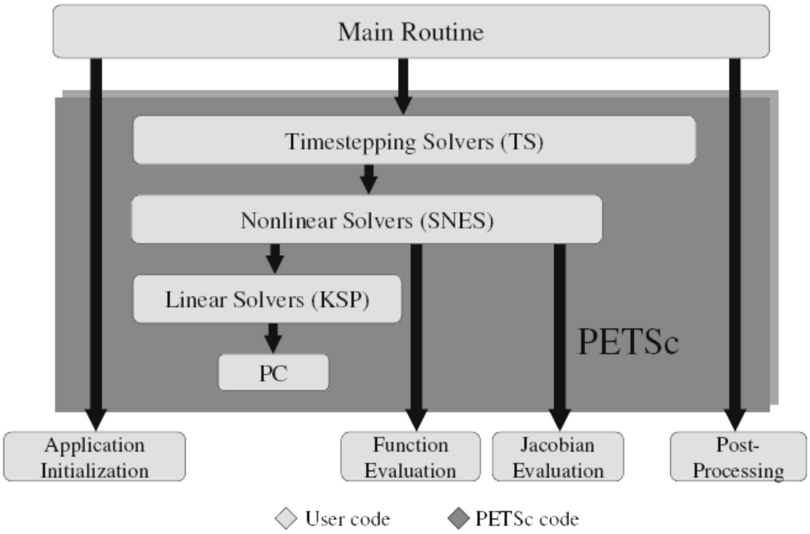

Figure 3.9. PETSc structure [46]

Figure 3.9 shows the structure of a PETSc algorithm. The PETSc code part of the figure indicated with a dark grey region represents the algorithms embedded in PETSc which are unchangeable data structure neutral parts of the PETSc structure. The rest is the user defined parts characterizing the problem. PETSc provides the time evolution methods for the solution of the PDEs and the pseudo-transient continuation techniques for computing the steady-state solutions as the timestepping solvers. The nonlinear systems arising in the discretizations are solved by using the data structure neutral implementations of the Newton methods which include the line search and the trust region techniques. The linear solvers placed within the PETSc are Generalized Minimal Residual (GMRES(m)), Conjugate Gradient (CG), Conjugate Gradient Squared (CGS), Bi-Conjugate Gradient Stabilized (BiCGStab) and two variants of Transpose Free Quasi Minimal Residual (TFQMR) algorithms. The preconditioning of these linear solvers can be carried out by selecting one of the preconditioners embedded inside the PETSc such as Jacobi, Successive Over Relaxation (SOR), Incomplete LU factorization (ILU(m)) or Additive Schwarz (ASM(m)) preconditioners.

The Newtonian case of the rotating disc in a cylindrical enclosure problem is studied by using the PETSc routines and the solutions will be given in the results and discussions chapter.

3.7. POLYFLOW

POLYFLOW is a commercial, finite element based software for simulating non-Newtonian problems emerged in the industry and the academia. The software can model Newtonian, generalized Newtonian, differential and integral viscoelastic models with or without considering the thermal phenomena. POLYFLOW can not work alone, it needs a suite of programs. For example, it imports the mesh from the mesh generators such as GAMBIT, TGRID or ANSYS and the preprocessing of the problem can be carried out by using POLYDATA. After solving the problem with POLYFLOW, the results can be postprocessed with other programs such as ANSYS-CFX Post or TECPLOT.

3.8. Implementational Issues

The partial differential equations representing the problems are discretized by using the well known Finite Difference Method (FDM). The merit of these conversions from the differential equations to the algebraic equations is that the algebraic equations are easier to solve by means of the iterative techniques. Before proceeding with the FDM implementations, the grid should be explained for both of the problems. Since the axisymmetric boundary condition is used for the rotating disc in a cylindrical enclosure problem, both of the problems studied in this research have a rectangular computational domains. Figure 3.10 shows the grid for the lid driven cavity problem. The figure for the rotating disc in a cylindrical enclosure problem is the same while nx is replaced with nr and ny with nz.

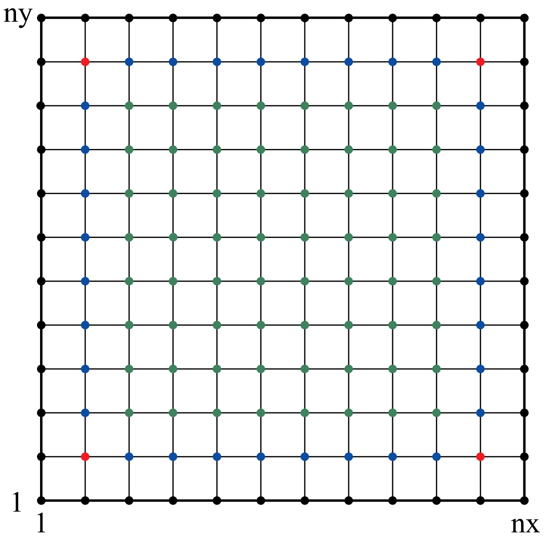

Figure 3.10. Grid

In the discretization of the governing equations, high order schemes for the first and the second derivatives are used in order to increase the accuracy of the results. The green grid points represent the fourth order discretization region which is called the interior. Since the fourth order discretization needs nine point stencil, the lines adjacent to the boundaries, which are illustrated with the blue points, can not be discretized with the fourth order stencil. Instead, the second order discretization is used at the points corresponding to these lines. The second and fourth order discretizations of the first and second order derivatives are trivial; that's why they are not included in this text. More information about these discretizations can be found in the book by Hoffmann *et al.* [47].

The third order derivatives at the interior may be calculated with the following relations.

$$\frac{\partial^3\psi}{\partial x^3} = \frac{\psi_{i+2,j} - 2\psi_{i+1,j} + 2\psi_{i-1,j} - \psi_{i-2,j}}{2dx^3} \tag{3.22}$$

$$\frac{\partial^3\psi}{\partial x^2\partial y} = \frac{\psi_{i+1,j+1} - 2\psi_{i,j+1} + \psi_{i-1,j+1} - \psi_{i+1,j-1} + 2\psi_{i,j-1} - \psi_{i-1,j-1}}{2dx^2dy} \tag{3.23}$$

$$\frac{\partial^3\psi}{\partial x\partial y^2} = \frac{\psi_{i+1,j+1} - 2\psi_{i+1,j} + \psi_{i+1,j-1} - \psi_{i-1,j+1} + 2\psi_{i-1,j} - \psi_{i-1,j-1}}{2dxdy^2} \tag{3.24}$$

$$\frac{\partial^3\psi}{\partial y^3} = \frac{\psi_{i,j+2} - 2\psi_{i,j+1} + 2\psi_{i,j-1} - \psi_{i,j-2}}{2dy^3} \tag{3.25}$$

Since Equation 3.22 and Equation 3.25 need nine point stencil, they are inappropriate for the blue grid points adjacent to the boundary. At these points following difference formulas should be used.

For the adjacent grid points below the lid;

$$\frac{\partial^3\psi}{\partial y^3} = \frac{-2\psi_{i,j+1} + \psi_{i,j} + 2\psi_{i,j-1} - \psi_{i,j-2}}{2dy^3} + \frac{u_{lid@i,j}}{dy^2} \tag{3.26}$$

where $u_{lid@i,j}$ is the tangential velocity of the lid at the point (i, j). The adjacent grid points above the bottom edge can be formulated as;

$$\frac{\partial^3\psi}{\partial y^3} = \frac{\psi_{i,j+2} - 2\psi_{i,j+1} - \psi_{i,j} + 2\psi_{i,j-1}}{2dy^3} \tag{3.27}$$

Similarly, the discretization of the left and right adjacent lines are given in Equation 3.28 and Equation 3.28 respectively.

$$\frac{\partial^3\psi}{\partial x^3} = \frac{\psi_{i+2,j} - 2\psi_{i+1,j} - \psi_{i,j} + 2\psi_{i-1,j}}{2dx^3} \tag{3.28}$$

$$\frac{\partial^3\psi}{\partial x^3} = \frac{-2\psi_{i+1,j} + \psi_{i,j} + 2\psi_{i-1,j} - \psi_{i-2,j}}{2dx^3} \tag{3.29}$$

The stresses at the corners of the geometries are singular, so when these points are included in the discretizations, inaccurate solutions emerge. Due to this fact, the mixed second derivatives of the stresses at the red points of the Figure 3.10 should be

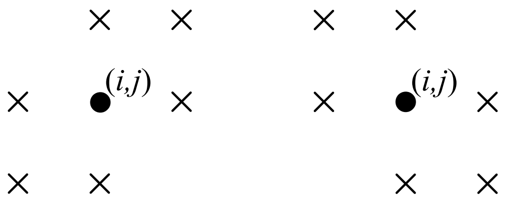

(a) Left slanted (b) Right slanted

Figure 3.11. Computational molecules for the mixed second derivatives [28]

discretized by using one of the following relations.

$$\frac{\partial^2 S_{ij}}{\partial x \partial y} = \frac{S_{i+1,j+1} + 2S_{i,j} + S_{i-1,j-1} - S_{i,j+1} - S_{i+1,j} - S_{i,j-1} - S_{i-1,j}}{2dxdy} \tag{3.30}$$

$$\frac{\partial^2 S_{ij}}{\partial x \partial y} = \frac{S_{i,j+1} + S_{i+1,j} S_{i,j-1} + S_{i-1,j} - S_{i-1,j+1} - 2S_{i,j} - S_{i+1,j-1}}{2dxdy} \tag{3.31}$$

Figure 3.11 points out the grid molecules for the Equation 3.30 and Equation 3.31. Since Equation 3.30, which is illustrated by Figure 3.11(a), doesn't include the top left $(i-1, j+1)$ and bottom right $(i+1, j-1)$ grid points, using this relation in the discretizations is appropriate for the top left and bottom right red points of Figure 3.10. Similarly, Equation 3.31 is appropriate for the discretizations of the top right and the bottom left red points of Figure 3.10.

More information about the discretizations, upwinding, solution strategies and similar processes can be found in the book of Crochet *et al.* [28].

4. RESULTS and DISCUSSIONS

The results and discussions part of this study consists of two sections; lid driven cavity (LDC) flow and rotating disc in a cylindrical enclosure (RDCE) flow. Although the main objective of this research is to investigate the non-Newtonian flow phenomenon of the RDCE geometry, LDC flow is modeled as a step problem. The LDC problem is selected because it is a well known benchmark problem in the area of computational fluid dynamics and consequently there are many studies concerning this flow. In this chapter, both of the problems (LDC and RDCE) have their own subsections such as the validation section (in which grid dependence and comparison is carried out), the Newtonian model section, the UCM model section, the Oldroyd B model section, the Giesekus model section and the non-isothermal viscoelastic flow section. Table 4.1 reveals the corresponding parts for the specific topics.

Table 4.1. Sections of the results

	Lid Driven Cavity	Rotating Disc in a Cylindrical Enclosure
Validation	Section 4.1.1	Section 4.2.1
Newtonian Model	Section 4.1.2	Section 4.2.2
Upper Convected Maxwell Model	Section 4.1.3.1	Section 4.2.3.1
Oldroyd B Model	Section 4.1.3.2	Section 4.2.3.2
Giesekus Model	Section 4.1.3.3	Section 4.2.3.3
Non-isothermal Flow	Section 4.1.3.4	Section 4.2.3.4

4.1. Lid Driven Cavity

The LDC problem is selected as a step problem in order to tune the solver parameters and investigate the efficiency of the solver. The validation subsection for LDC includes the mesh convergence analysis, investigation of the effects of the selection of the upwind scheme, determination of the effects of the selection of the boundary conditions and the examination of the outcomes of the continuation. This section will conclude with the comparison of the data. After tuning the solver parameters, these parameters will be utilized in the following sections of the LDC and RDCE problems.

4.1.1. Validation

In this section; the mesh convergence analysis, the selection of the vorticity and the stress boundary conditions, the upwinding and the comparison with the available data will be carried out in order to justify the results of this study (by considering the isothermal version of non-Newtonian LDC problem). Since the application of the functional lid velocity given in Equation 1.2 is troublesome in POLYFLOW, the velocity of the lid is selected as constant ($U_{lid} = 1.0$) for the POLYFLOW simulations. However, constant lid velocity produces singularities at the top corners of the geometry as mentioned in the Chapter 1. Therefore, the results of the functional lid velocity cases aren't compared with the results of the POLYFLOW simulations. Moreover, it will be clear in the following sections that the inexact Newton-GMRES (IN-GMRES) algorithm developed within this research can achieve higher Weissenberg number limits than POLYFLOW, therefore it is believed that the singularities are modeled better in this research.

4.1.1.1. Mesh convergence analysis. The first step of a numerical study should be the mesh convergence analysis for achieving comparable results. In order to determine the necessary number of the grid, four different sets; 31x31, 41x41, 51x51 and 61x61 are used for LDC. The interior region of the flow domain is discretized by using the fourth order stencil for all sets to achieve better accuracy. The comparisons are carried out between the results of IN-GMRES solver and the results obtained by POLYFLOW simulations. The problem parameters are fixed as; Re = 100, We = 0.04, $U_{lid} = 1.0$ where the UCM constitutive relation is used to simulate the non-Newtonian behavior. Different upwinding schemes are used but they seem to have nearly no effect on the grid resolutions therefore the results of no upwinding cases are given. Comparisons are realized by plotting the u velocity component through the vertical centerline and v velocity component through the horizontal centerline plots. Figures 4.1 and 4.2 show the velocity versus coordinate plots for different grid sets and the corresponding POLYFLOW results. Since the maximum difference between the POLYFLOW solution and the results obtained with IN-GMRES solver is in the limit of 1 %, all of the grids seem suitable for the problem. But small vortexes which are formed at the lower corners of the cavity, seem smoother for the minimum grid number of 51x51; thus it was selected for the grid resolution of the lid driven cavity problem. The reasonable differences between the results of the POLYFLOW and this study are thought to occur because of the dissimilar discretization methods used. To be precise, POLYFLOW used Finite Element Method (FEM) where Finite Difference Method (FDM) is used in the developed algorithm.

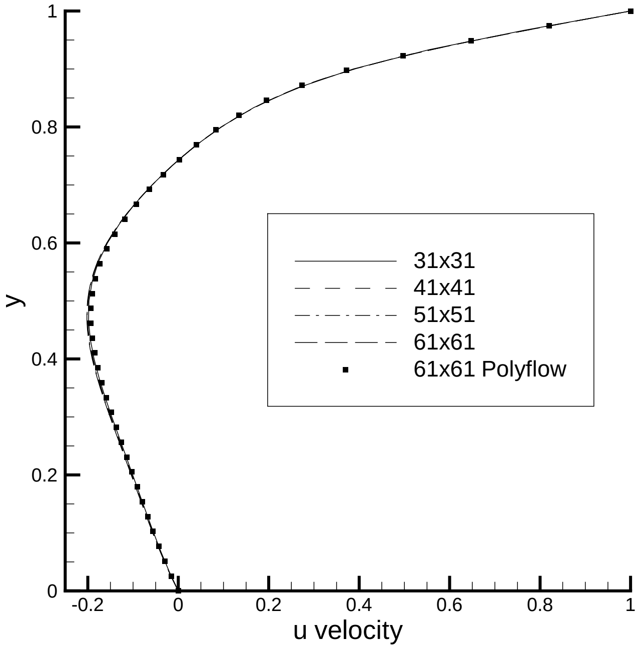

Figure 4.1. u velocity at x=0.5 versus y coordinate plot for Re = 100, We = 0.04, $U_{lid} = 1.0$ and UCM for the constitutive relation

Figures 4.1 and 4.2 also reveal that the developed preconditioned IN-GMRES algorithm gives comparable results for the UCM constitutive relation.

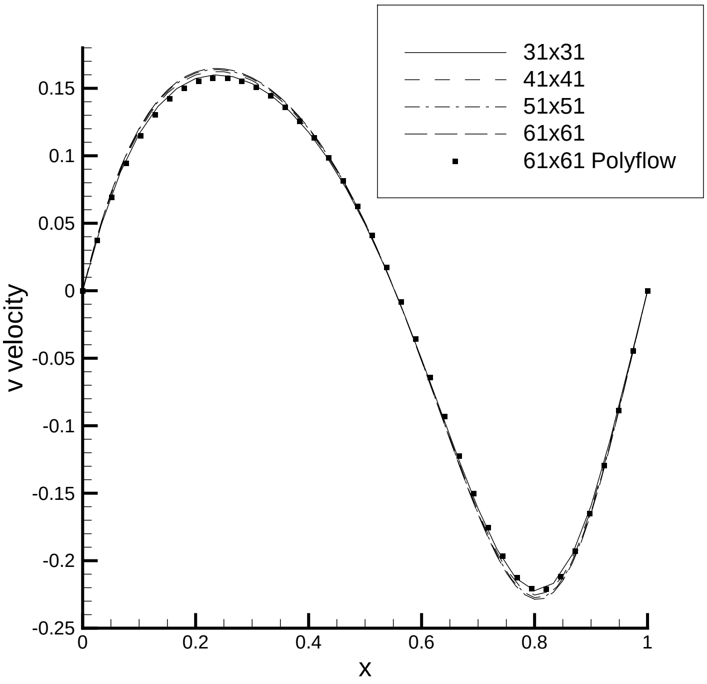

Figure 4.2. v velocity at y=0.5 versus y coordinate plot for Re = 100, We = 0.04, $U_{lid} = 1.0$ and UCM for the constitutive relation

4.1.1.2. Vorticity boundary conditions. In this part of the study, the vorticity boundary conditions which are mentioned in the Subsection 2.1.4.1, are compared with respect to the accuracy of the results and the computational time. The tests are executed for the Oldroyd B model with the parameters; Re = 100, We = 0.05, $\beta = 0.5$ and $U_{lid} = 1.0$. Results are compared with the POLYFLOW simulations as there is no experimental data. Figures 4.3 and 4.4 reveal that the vorticity boundary conditions except the Woods formulae give comparable results. The differences between the results of this study and POLYFLOW are thought to occur because of the dissimilar discretization methods and singularities at the top corners. Moreover, the Weissenberg number limit of the IN-GMRES solver turned out to be higher than POLYFLOW which means that the developed algorithm is more capable than POLYFLOW.

Figure 4.5 shows the nonlinear convergence plots and computation times of different vorticity boundary conditions for the same test problem. The Briley vorticity boundary condition gives the best convergence plot and computation time where the Thom's formula is the second best. But this is a special case where the initial guess

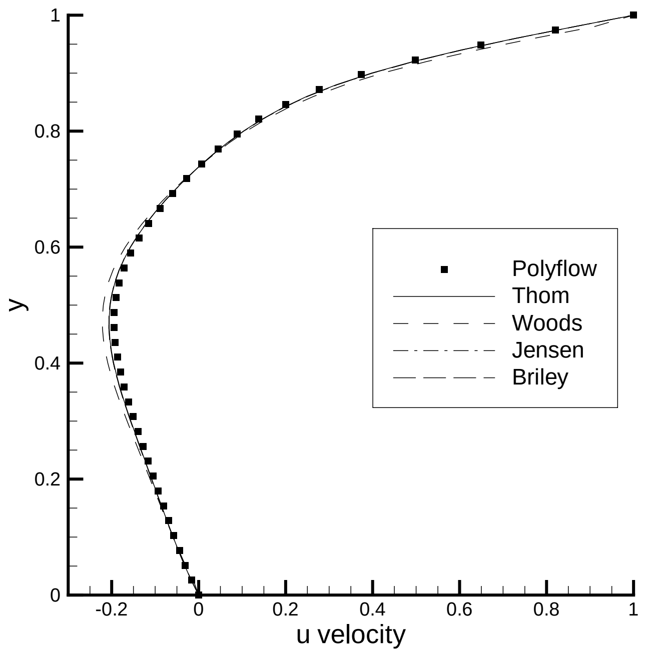

Figure 4.3. u velocity at x=0.5 versus y coordinate plot for Re = 100, We = 0.05, $U_{lid} = 1.0$ and Oldroyd B for the constitutive relation with $\beta = 0.5$

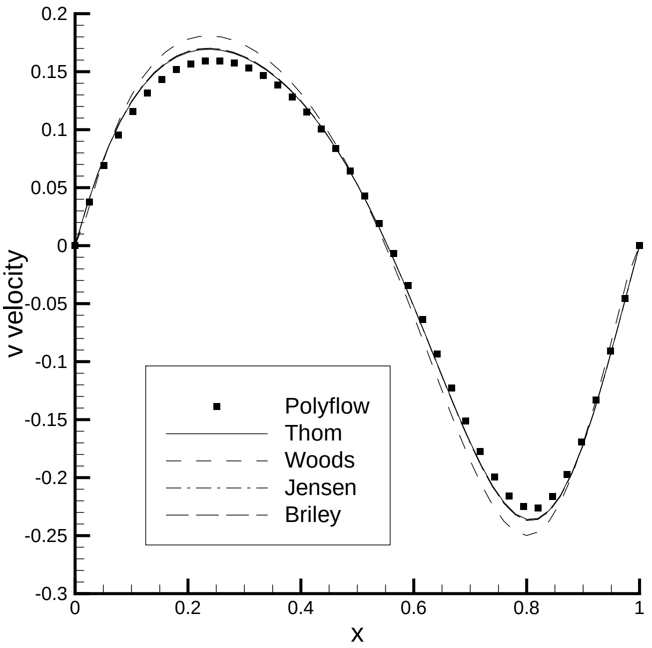

Figure 4.4. v velocity at y=0.5 versus v coordinate for Re = 100, We = 0.05, $U_{lid} = 1.0$ and Oldroyd B for the constitutive relation with $\beta = 0.5$

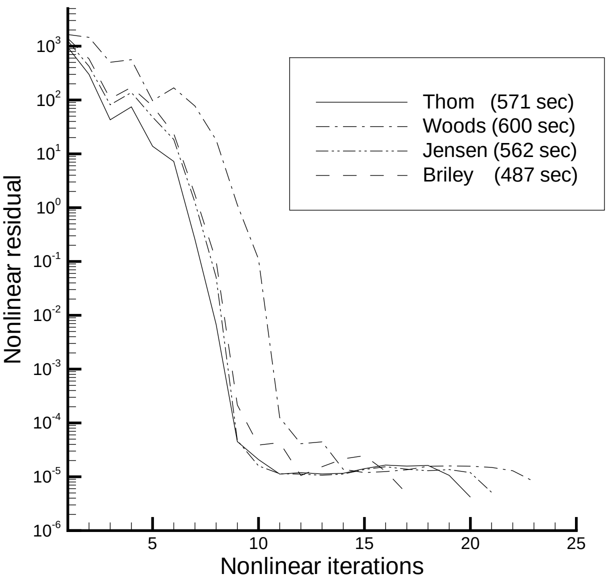

Figure 4.5. Nonlinear convergence graphic of different vorticity boundary conditions for Re = 100, We = 0.05, $U_{lid} = 1.0$, $\beta = 0.5$ and Oldroyd B for the constitutive relation

is zero. Figure 4.6 shows the solution of the same problem, but this time the solution of We = 0.04 case is used as an initial guess. As can be seen from this figure, Thom's formula is the best converging vorticity condition if the continuation method is used. Therefore, it is preferred as the vorticity boundary condition for the rest of the study.

4.1.1.3. Stress boundary conditions. As mentioned in the Subsection 2.1.4.1, two types of boundary conditions can be used for the non-Newtonian parts of the stresses. The first one is the use of the equation as the boundary condition since the boundary conditions themselves should satisfy their governing equations. Detailed information about the derivation of these boundary conditions can be found in the book by Crochet *et al.* [28] and the final forms of them are given as follows;

- Bottom edge;

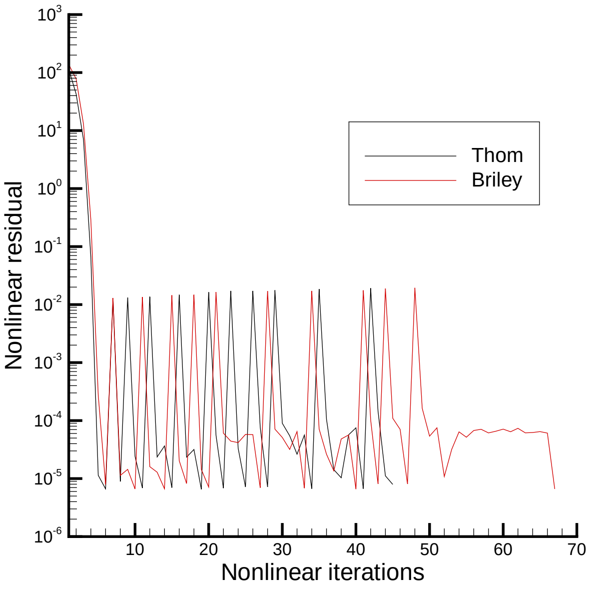

Figure 4.6. Nonlinear convergence graphic of different vorticity boundary conditions for Re = 100, We = 0.05, $U_{lid} = 1.0$, $\beta = 0.5$ and Oldroyd B for the constitutive relation using the solution of We = 0.04 case as an initial guess

$$S_{xx} = 2\text{We}\left(\frac{\partial^2\psi}{\partial y^2}\right)^2, \qquad S_{xy} = \text{We}\left(\frac{\partial^2\psi}{\partial y^2}\right), \qquad S_{yy} = 0 \tag{4.1}$$

- Left and right edges;

$$S_{xx} = 0, \qquad S_{xy} = -\text{We}\left(\frac{\partial^2\psi}{\partial x^2}\right), \qquad S_{yy} = 2\text{We}\left(\frac{\partial^2\psi}{\partial x^2}\right)^2 \tag{4.2}$$

- Lid (discrete form of the equations assuming that $U_{lid} > 0$);

$$(2U_{lid} + dn^2)S_{xx}^{i,j} - 2U_{lid}S_{xx}^{i-1,j} = dn^2\left[2\text{We}\frac{\partial^2\psi}{\partial y^2}S_{xy}^{i,j} + G_1^{i,j}\right] \tag{4.3}$$

$$(2U_{lid} + dn^2)S_{xy}^{i,j} - 2U_{lid}S_{xy}^{i-1,j} = dn^2\left[\text{We}\frac{\partial^2\psi}{\partial y^2}S_{yy}^{i,j} + G_2^{i,j}\right] \tag{4.4}$$

$$(2U_{lid} + dn^2)S_{yy}^{i,j} - 2U_{lid}S_{yy}^{i-1,j} = dn^2 G_3^{i,j} \tag{4.5}$$

where the superscripts i, j correspond to indices and G_1, G_2 and G_3 are;

$$G_1 = 2\mathrm{We}\left[2\left(\frac{\partial^2\psi}{\partial x\partial y}\right)^2 - \frac{\partial\psi}{\partial y}\frac{\partial^3\psi}{\partial x^2\partial y} + \frac{\partial\psi}{\partial x}\frac{\partial^3\psi}{\partial x\partial y^2} + \frac{\partial^2\psi}{\partial y^2}\left(\frac{\partial^2\psi}{\partial y^2} - \frac{\partial^2\psi}{\partial x^2}\right)\right] \tag{4.6}$$

$$G_2 = -\mathrm{We}\left[2\frac{\partial^2\psi}{\partial x\partial y}\left(\frac{\partial^2\psi}{\partial x^2} + \frac{\partial^2\psi}{\partial y^2}\right) + \left(\frac{\partial\psi}{\partial y}\frac{\partial}{\partial x} - \frac{\partial\psi}{\partial x}\frac{\partial}{\partial y}\right)\left(\frac{\partial^2\psi}{\partial y^2} - \frac{\partial^2\psi}{\partial x^2}\right)\right] \tag{4.7}$$

$$G_3 = 2\mathrm{We}\left[2\left(\frac{\partial^2\psi}{\partial x\partial y}\right)^2 + \frac{\partial\psi}{\partial y}\frac{\partial^3\psi}{\partial x^2\partial y} - \frac{\partial\psi}{\partial x}\frac{\partial^3\psi}{\partial x\partial y^2} - \frac{\partial^2\psi}{\partial x^2}\left(\frac{\partial^2\psi}{\partial y^2} - \frac{\partial^2\psi}{\partial x^2}\right)\right] \tag{4.8}$$

The second type of boundary conditions for the stresses is mentioned by Kawabata *et al.* [34] and utilized by Moroi *et al.* [15, 16] and Itoh *et al.* [17]. This boundary condition can be explained as equating the second derivatives of the non-zero stresses to zero (in the normal direction). The boundary conditions applied are given as follows;

- Top and bottom edges;

$$\frac{\partial^2 S_{xx}}{\partial y^2} = 0, \qquad \frac{\partial^2 S_{xy}}{\partial y^2} = 0, \qquad S_{yy} = 0 \tag{4.9}$$

- Left and right edges;

$$S_{xx} = 0, \qquad \frac{\partial^2 S_{xy}}{\partial x^2} = 0, \qquad \frac{\partial^2 S_{yy}}{\partial x^2} = 0 \tag{4.10}$$

The comparison between these two types of boundary conditions is carried out for the UCM flow with the parameters of Re = 100, We = 0.04 and $U_{lid} = 1.0$. Figures 4.7 and 4.8 show the velocity versus coordinate plots for this problem and it is obvious from these figures that the boundary conditions of Kawabata *et al.* [34] gives better results. It can also be understood from the comparison of the equations that the implementation of the boundary conditions of Kawabata *et al.* is much simpler.

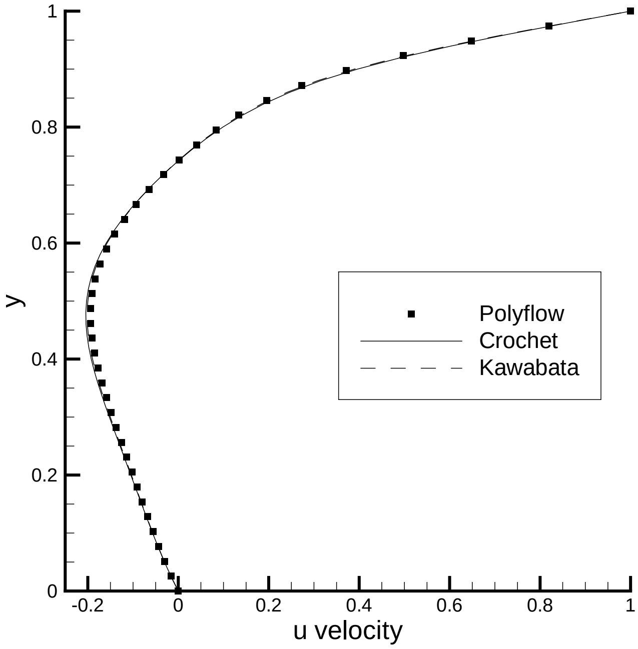

Figure 4.7. u velocity at x=0.5 versus y coordinate plot for Re = 100, We = 0.04, $U_{lid} = 1.0$ and UCM for the constitutive relation

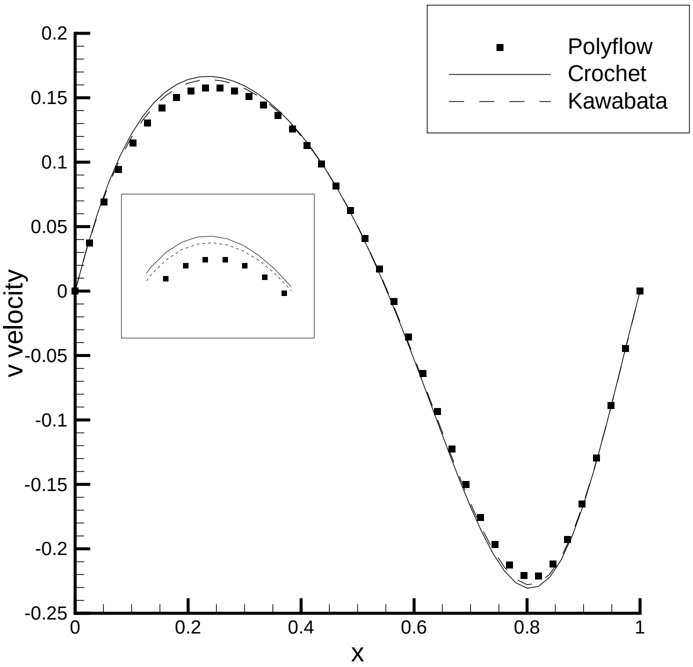

Figure 4.8. v velocity at y=0.5 versus v coordinate for Re = 100, We = 0.05, $U_{lid} = 1.0$ and UCM for the constitutive relation

4.1.1.4. Continuation. Since the convergence of the Newton's method is strictly dependent on the initial guess, continuation method in the Weissenberg number is used. The continuation method can simply be defined as using the previous solution as the initial guess. For example, obtaining the solution of the LDC problem of Weissenberg number 0.05 with the zero initial guess is impracticable. However, solving the same problem by taking the initial guess as the solution of We = 0.04 is doable. Similarly, the solution of We = 0.03 can be utilized for the We = 0.04 case. This goes on until the zero initial guess is applicable. As a result of its benefits, the continuation is used for all of the maximum Weissenberg number limits reached in the previous and latter sections.

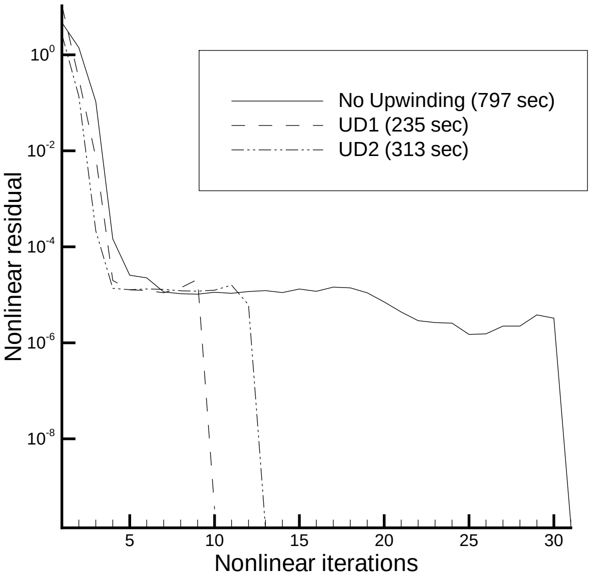

Figure 4.9. Nonlinear convergence graphic of different upwinding schemes for Re = 100, We = 0.05, $U_{lid} = 1.0$, $\beta = 0.5$ and Oldroyd B for the constitutive relation

4.1.1.5. Upwinding. Upwinding gives better results and convergence behavior. In upwinding, the discretizations of the governing equations are modified by identifying the flow direction through computing the velocities. It is particularly suitable for the high Reynolds number flows. In order to examine the effects of upwinding, Oldroyd B flow of LDC with the parameters of Re = 100, We = 0.05, $U_{lid} = 1.0$ and $\beta = 0.5$ is studied as an example. The solutions are obtained using zero initial guesses and the nonlinear residuals for the no-upwinding, the first order upwinding (UD1) and the second order upwinding (UD2) schemes are plotted in Figure 4.9. As can be seen from this figure, UD1 converges faster compared to the others by means of nonlinear iteration number and computation time; thus UD1 should be preferred for the computations of high Reynolds numbers.

The computations for Reynolds numbers lower than 20 reveal different behavior. From that level on, the calculation of the altering of the derivatives takes more computation time than the no-upwinding case and upwinding schemes become less useful.

4.1.2. Newtonian Model

Since the main subject of this thesis is to model the the non-Newtonian flows of the moving edge problems, the Newtonian investigation of this problem is not comprehensively discussed in this section of the study. This part of the work is carried out by using the code generated with the use of PETSc, which is a computational tool for the parallel solution of scientific problems. The Newtonian case of LDC is solved as a step problem for generating a PETSc code for RDCE. Additionally, performance of the linear solvers, performance of the preconditioners, parallel performance and effects of Reynolds number are investigated in this part of the study. The number of the grid is selected similar to the work of Ghia *et al.* [1] (129x129) in order to compare the results accurately (second order stencil is used in the interior).

4.1.2.1. Validation. The lid driven cavity is a well known benchmark problem for computational fluid dynamics codes therefore there are more than one way of comparison. The first way of validating the results is materialized by plotting the velocity versus coordinate plots on some particular lines. Figures 4.10 and 4.11 use this technique for validation. Figure 4.10 reveals the u velocity component through the vertical centerline of the cavity where Figure 4.11 shows the v velocity component through the horizontal centerline. As can be seen from both of these figures, the velocity versus coordinate plots are in well agreement with the results of Ghia *et al.* [1].

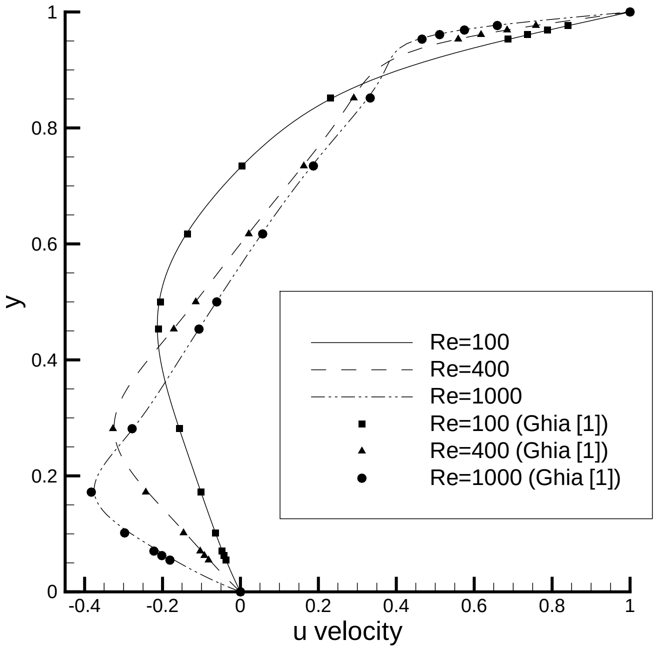

Figure 4.10. u velocity through the vertical centerline

The second way of comparison is carried out by the using the minimum stream function values and their positions which are shown in Table 4.2. As can be seen from this table, the values are comparable with the cited studies of Ghia *et al.* [1], Hou *et al.* [48] and Vanka [49].

4.1.2.2. Performance of the Linear Solvers. For the test of the performance, everything but the linear solver of the problem is fixed. The Reynolds number is selected as 100 and the grid is 129x129. The line search Newton method with backtracing is preferred for the linearization while ILU(5) preconditioning is used to enhance the convergence.

Figure 4.12 shows the required number of linear iterations for different Krylov solvers at the first Newton steps. As can be seen, the best converging method is Bi-Conjugate Gradient Stabilized (BiCSStab) with 20 iterations, where the other methods

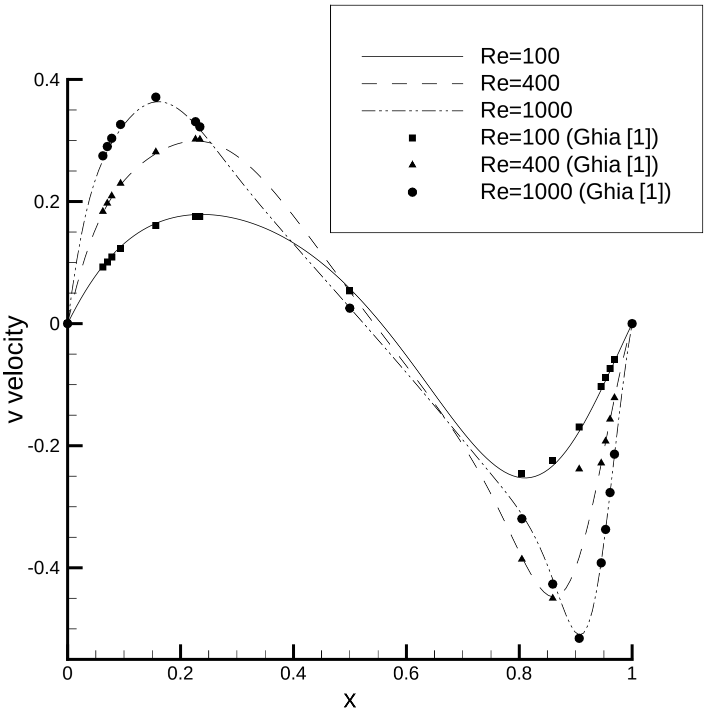

Figure 4.11. v velocity through the horizontal centerline

Table 4.2. Comparison of ψ_{min} with literature

Re	Reference	ψ_{min}	x location	y location
100	[1]	-0.103	0.6172	0.7344
	[49]	-0.103	0.6168	0.7375
	[48]	-0.103	0.6196	0.7373
	present	-0.103	0.6170	0.7355
400	[1]	-0.114	0.5547	0.6055
	[48]	-0.112	0.5608	0.6078
	[49]	-0.114	0.5563	0.6000
	present	-0.113	0.5550	0.6060
1000	[1]	-0.118	0.5313	0.5625
	[48]	-0.118	0.5333	0.5647
	[49]	-0.117	0.5438	0.5625
	present	-0.116	0.5320	0.5650

perform poorly and converge in nearly 24 iterations. Generalized Minimal Residual method (GMRES) with restart 50 (GMRES(50)) converges in the same iteration number with GMRES(30). As there is no restart up to iteration 24, this is an expected behavior. Another important aspect of using GMRES(m) is its non-increasing residual property. The linear residuals for TFQMR, BiCGStab and CGS can fluctuate; however the residual in GMRES is always non-increasing. The significant effects of this property are observed also in the non-isothermal non-Newtonian simulations of IN-GMRES algorithm. Therefore, selecting GMRES(m) as a linear solver in the problems with higher nonlinearities seems to be an appropriate choice.

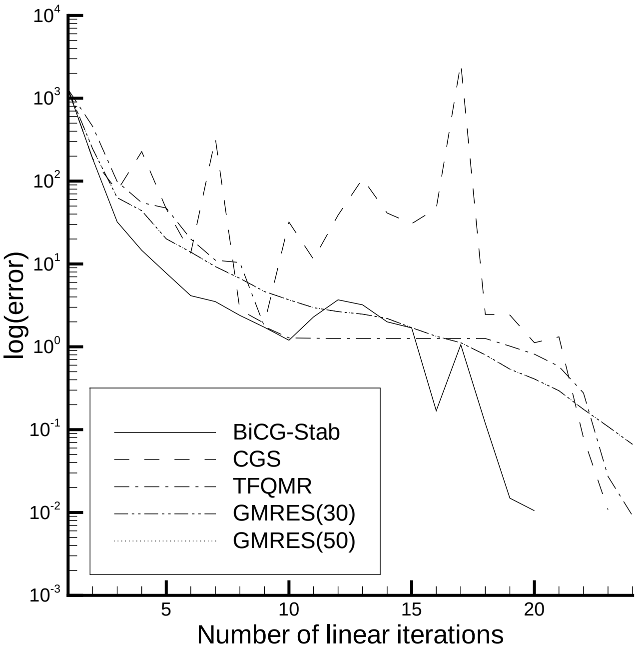

Figure 4.12. Linear solver performances

<u>4.1.2.3. Performance of the Preconditioners.</u> The convergence rate of the iterative methods depends on the spectral properties (eigenvalues) of the coefficient matrix as mentioned earlier. Converting the problem to another with the same solution but favorable spectral properties so that it can converge faster is called preconditioning. Similar to linear solver performance analysis, everything but the preconditioner of the problem is fixed in order to study the performances of the preconditioners and the same problem

is used (the Reynolds number is selected as 100 and the grid is 129x129). The line search Inexact Newton method with backtracing is utilized for the linearization while GMRES(30) is adopted as the linear solver. In addition, linear tolerance is chosen as $1E - 5$.

Figure 4.13 indicates the required number of linear iterations for different preconditioners at the first Newton steps. The no-preconditioning is not presented in this figure because the solver is failed to converge in this case. This figure reveals that the best converging preconditioner is ILU(5) where the convergence is obtained in 27 iterations. The simplest preconditioning method Jacobi makes the problem solvable; however it takes 254 iterations to converge. SOR preconditioning is better than Jacobi while it is obvious that it can not compete with ILU(m) type preconditioners. With increasing fill-in, ILU(m) becomes faster up to ILU(5) with respect to both linear iteration number and computation time. Starting with ILU(6), generating preconditioner matrix takes too much time and the overall efficiency of the code starts to decrease. By this means, the preconditioning becomes less useful.

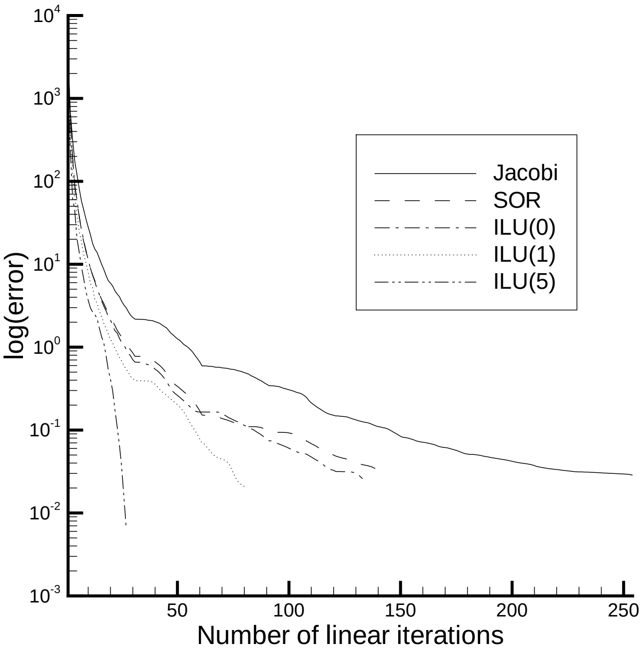

Figure 4.13. Preconditioning performances

4.1.2.4. Effects of Reynolds Number. Figures 4.14, 4.15 and 4.16 show the stream function contours of lid driven cavity flow for different values of Reynolds numbers. These three figures indicate that the core of the primary vortex is moving towards the center of the flow domain with the increasing Reynolds number. What is more, the counter rotating corner vortexes at the left and right bottom corners of the cavity (secondary vortexes) expand into the flow domain with the increase in Reynolds number. Above a certain limit of Reynolds number, there appears an additional vortex near the upper half of the left edge. This additional vortex appears nearly Re = 1000 and it can be observed in Figure 4.16.

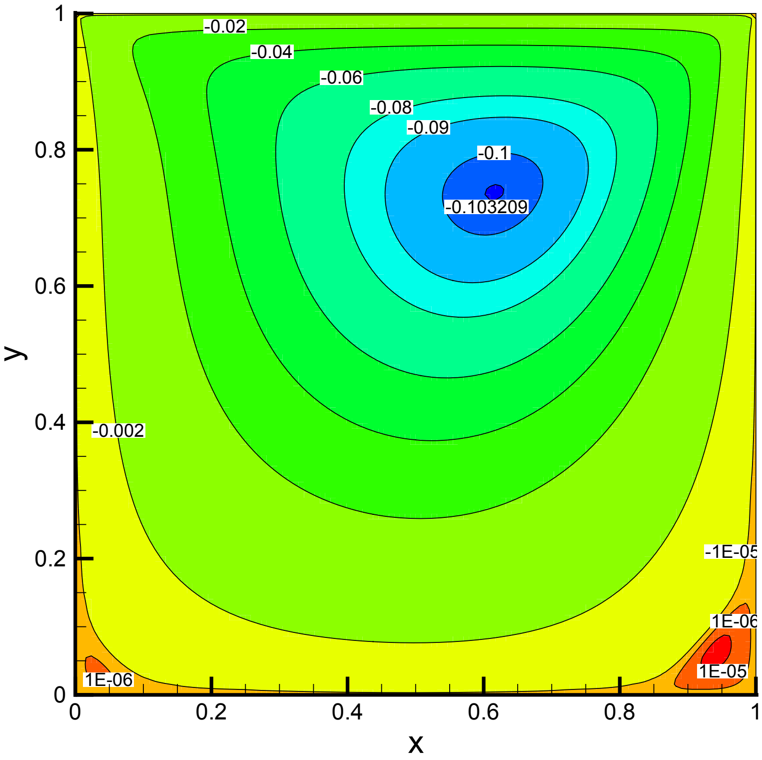

Figure 4.14. Stream function contour of lid driven cavity problem with Re = 100 and 129x129 grid number

Moreover, in Figure 4.16 an extra vortex which rotates in the direction of the primary vortex, is formed below the secondary one at the right corner. This small circulation zone is expected to grow with the increasing Reynolds number similar to the secondary vortexes.

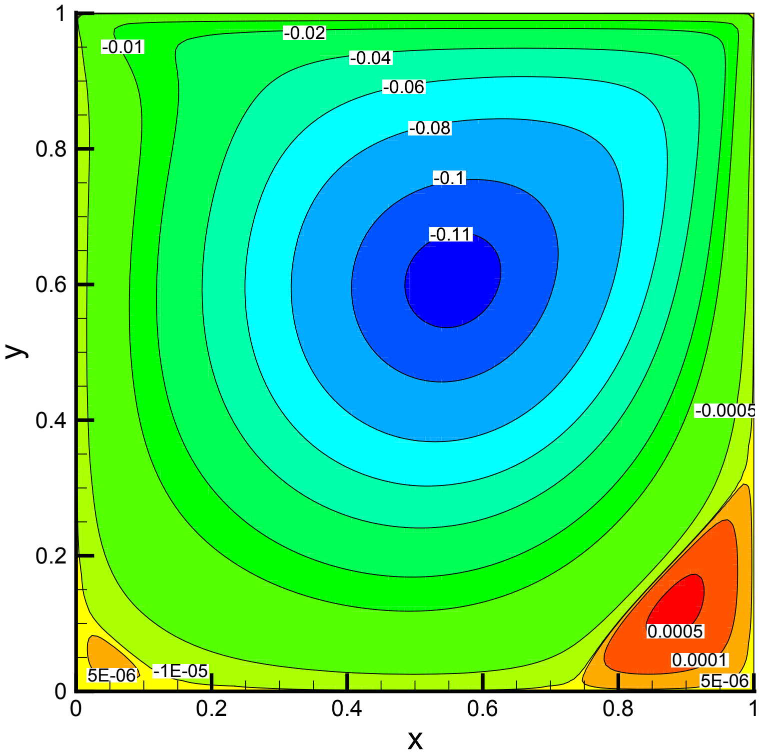

Figure 4.15. Stream function contour of lid driven cavity problem with Re = 400 and 129x129 grid number

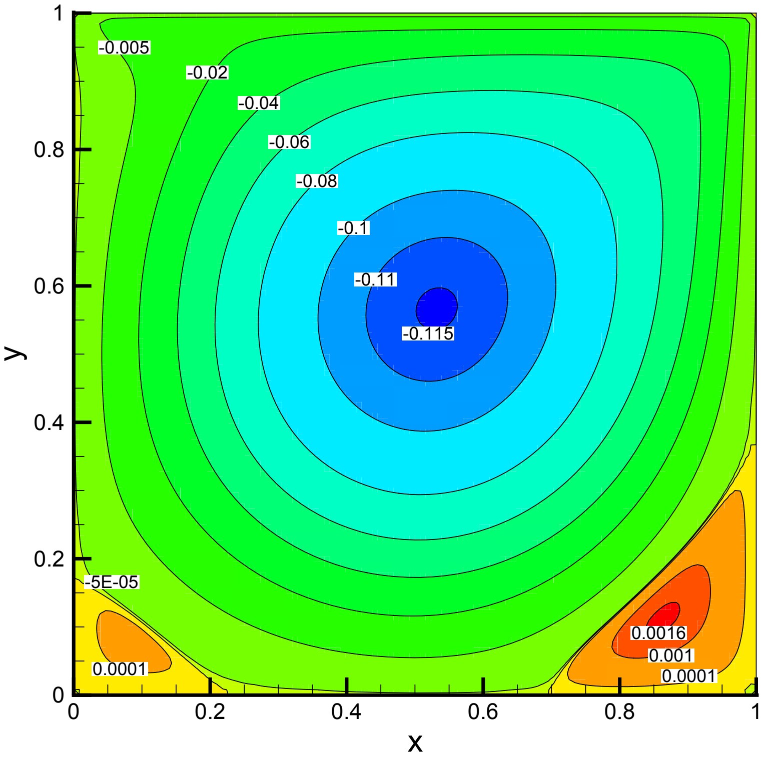

Figure 4.16. Stream function contour of lid driven cavity problem with Re = 1000 and 129x129 grid number

<u>4.1.2.5. Comparison for the Functional Lid Velocity.</u> In the Newtonian flow analyses carried out up to this section constant lid velocity is utilized since there are many comparable data published in the literature. However, in the non-Newtonian flow simulations of this study functional lid velocity is used in order to reduce the corner singularity effects. Therefore, the Newtonian simulations of lid driven cavity flow using the functional lid velocity (Equation 1.2) should also be modeled.

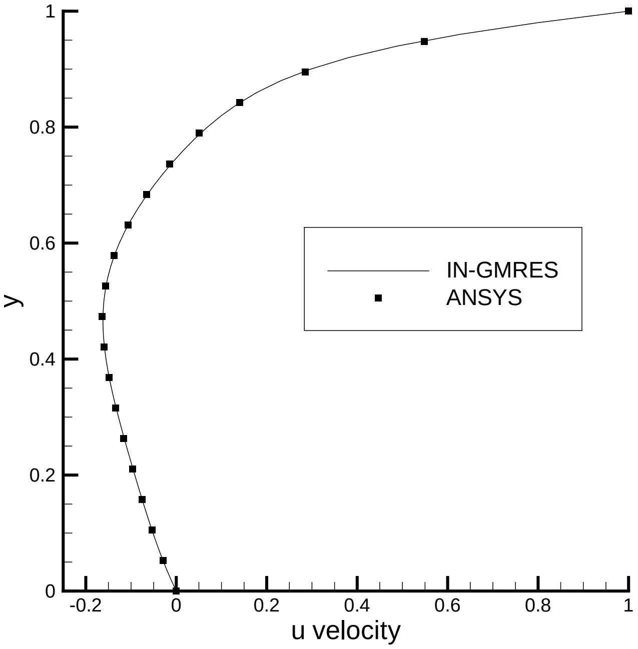

Figure 4.17. Comparison of functional lid velocity Newtonian results for Re = 100

Figure 4.17 shows the u velocity component through the vertical centerline of the cavity. As can be observed from this figure the results of the IN-GMRES solver and the ANSYS simulations are consistent.

4.1.3. Non-Newtonian Models

In this part of the study, the non-Newtonian effects are investigated by adopting three constitutive models; UCM, Oldroyd B and Giesekus. In order to understand the effects of the material properties used in the constitutive relations and non-dimensional numbers, computations are performed for a wide range of these parameters. Moreover, the simulations with constant and functional lid velocities give dissimilar results therefore both are implemented in this part of the study. However, modeling of the functional lid velocity case is troublesome in POLYFLOW, that's why only constant velocity solutions are compared with POLYFLOW simulations in the sense of velocity plots and maximum Weissenberg number limits.

Table 4.3 shows the Weissenberg number limits for constant lid velocity solutions between the IN-GMRES solver and POLYFLOW simulations. In this table the results of constitutive models; UCM, Oldroyd B and Giesekus versus the results of Reynolds numbers of 0, 10 and 100 are revealed. As can be understood from this table, the maximum Weissenberg number limits are higher for our solutions except the Giesekus model. Additionally, the maximum Weissenberg number limits for the Giesekus constitutive relation results show fluctuating values in POLYFLOW simulations and similar variation can be observed in our results. Moreover, the velocity versus coordinate comparisons carried out in the previous and the latter sections reveal that both of the solvers give comparable results. Therefore, it is believed that the corner singularities are sufficiently modeled and the solutions are accurate for the IN-GMRES solver.

Table 4.3. Comparison of maximum Weissenberg numbers between IN-GMRES and POLYFLOW for different constitutive models using constant lid velocity

	UCM		Oldroyd B $\beta = 0.5$		Giesekus $\beta = 0.5$, $\alpha = 0.1$	
	IN-GMRES	Polyflow	IN-GMRES	Polyflow	IN-GMRES	Polyflow
Re = 0	0.052	0.0488	0.085	0.0523	0.122	0.2600
Re = 10	0.053	0.0489	0.094	0.0524	0.120	0.1306
Re = 100	0.050	0.0497	0.090	0.0535	0.101	0.2365

Table 4.4 shows the maximum Weissenberg numbers obtained for different constitutive models using functional lid velocity given in Equation 1.2. The values in this table are consistent with the values in the Table 4.3 since they increase or decrease in

a similar trend. However, the maximum Weissenberg number limits are higher for the functional lid velocity cases as expected. These higher values can be simulated because of the reduced corner singularities of the problem.

Table 4.5 reveals the maximum Weissenberg number limits for various parameters used in the constitutive relations. It is apparent from this table that these parameters have effects on the flow and these effects will be explained in the following section.

Table 4.4. Maximum Weissenberg number limits using functional lid velocity for various constitutive equations and Reynolds numbers

	UCM	Oldroyd B $\beta = 0.5$	Giesekus $\beta = 0.5$, $\alpha = 0.1$
Re = 0	0.241	0.260	0.436
Re = 10	0.245	0.271	0.453
Re = 100	0.250	0.280	0.448

Table 4.5. Maximum Weissenberg number limits using functional lid velocity for various constitutive equations and Re = 100

UCM	Oldroyd B			Giesekus $\beta = 0.5$		
	$\beta = 0.25$	$\beta = 0.5$	$\beta = 0.75$	$\alpha = 0.05$	$\alpha = 0.1$	$\alpha = 0.15$
0.250	0.268	0.280	0.299	0.359	0.448	0.507

<u>4.1.3.1. Upper Convected Maxwell Model.</u> The first differential constitutive relation used in the simulations of LDC is UCM. This equation is one of the simplest constitutive relations and the usage of it is recommended when the information about the fluid is limited. Although the formulation of the UCM model is simple, the numerical computations using this model are difficult in terms of the convergence rate. This difficulty can be observed by comparing the limits of UCM with the limits of Oldroyd B or Giesekus constitutive relations in Tables 4.3, 4.5 and 4.4. Table 4.4 reveals that the maximum Weissenberg number limits of UCM model are between 0.24 and 0.25.

In average, these limits are five times larger than the constant lid velocity solutions which indicates the importance of the implementation of the functional lid velocity and indirectly the effectiveness of the corner singularities.

Figures 4.18 through 4.20 show the effects of increasing Weissenberg numbers on the flow of UCM with Re = 100 where the functional lid velocity is adopted to deal with the corner singularities. The observation of these figures reveals that the maximum value of stream function is decreasing with the increase in the Weissenberg number and the maximum value of the velocity is decreasing accordingly. The slowing down is the result of the increasing elasticity of the fluid with respect to the increasing Weissenberg number.

Moreover, the core of the vortex moves towards the upper left corner of the cavity with the increasing elastic effects. Additionally,the small counter rotating circulations at the right and left bottom corners of the flow domain become smaller with the increasing Weissenberg numbers which means that these vortexes are slowing down similar to the main circulation zone.

Figures 4.21 and 4.22 reveal the velocity versus coordinate plots for the Re = 100 case of the UCM constitutive relation and different Weissenberg numbers. Similar to the stream function contours, the slowing down of the flow can also be observed from these figures.

Figures 4.23, 4.24 and 4.25 show the non-Newtonian stress component through the horizontal centerline for various Weissenberg numbers. As can be observed from these figures the magnitudes of the non-Newtonian parts of the stresses are growing with the increasing Weissenberg numbers as expected. For the We = 0 cases the non-Newtonian parts of the stresses are zero, therefore they are not presented in these figures. Similarly, Figures 4.26, 4.27 and 4.28 reveal the non-Newtonian stress component through the vertical centerline for various Weissenberg numbers. It can be observed from these figures that the values of the stresses are at their peaks close to the lid as expected. These high values are the reasons of the difficulties in the computational simulations.

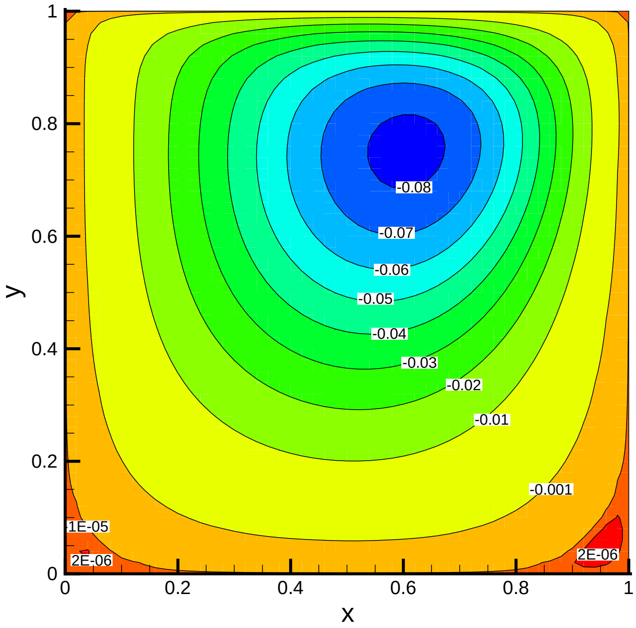

Figure 4.18. Stream function contours for Re = 100, We = 0.0 and UCM for the constitutive relation

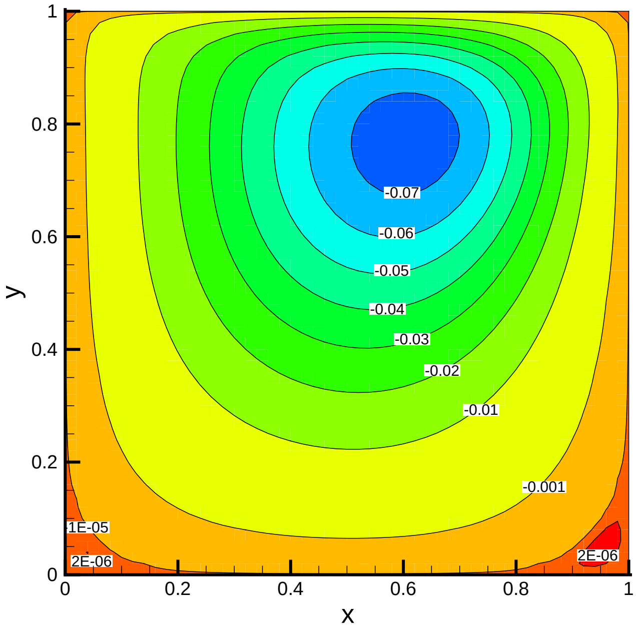

Figure 4.19. Stream function contours for Re = 100, We = 0.1 and UCM for the constitutive relation

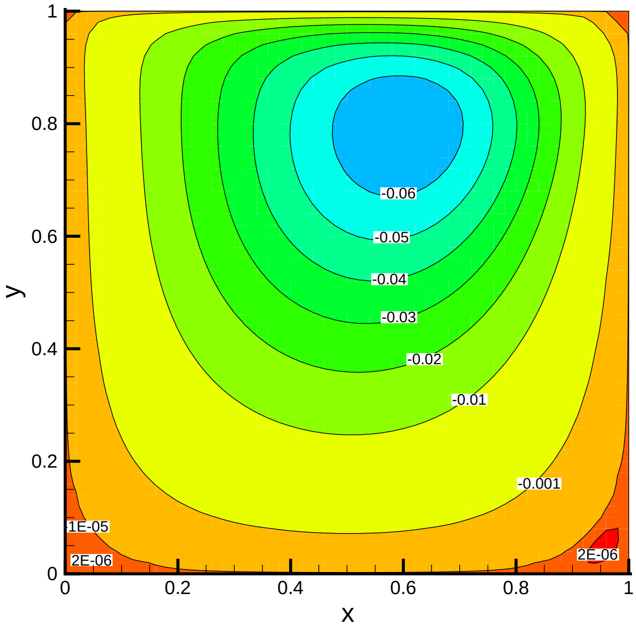

Figure 4.20. Stream function contours for Re = 100, We = 0.2 and UCM for the constitutive relation

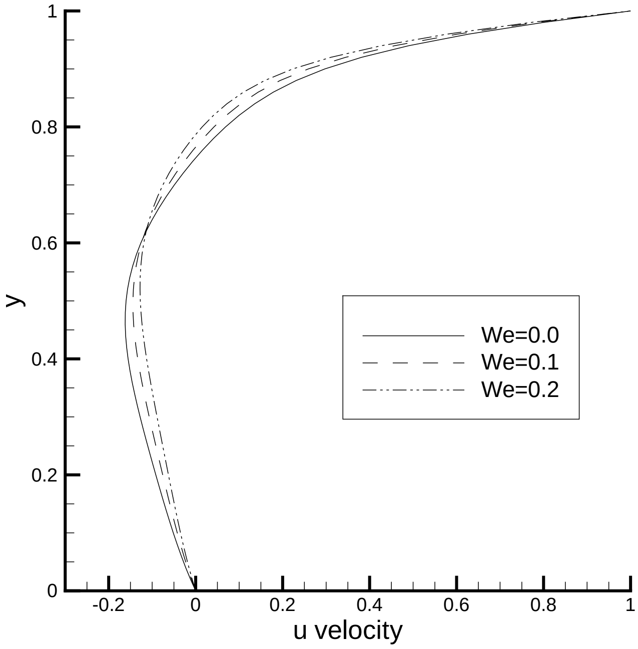

Figure 4.21. u velocity component through the vertical centerline for Re = 100 and UCM for the constitutive relation

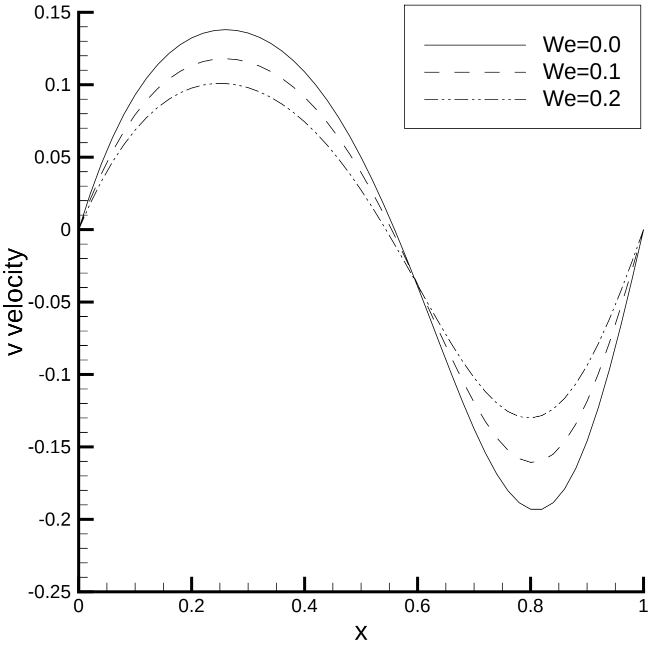

Figure 4.22. u velocity component through the horizontal centerline for Re = 100 and UCM for the constitutive relation

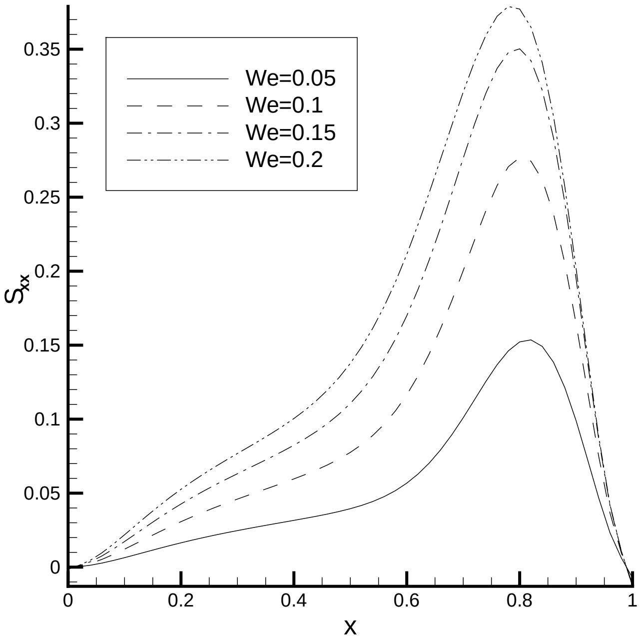

Figure 4.23. The non-Newtonian stress tensor component S_{xx} through the horizontal centerline for Re = 100 and UCM for the constitutive relation

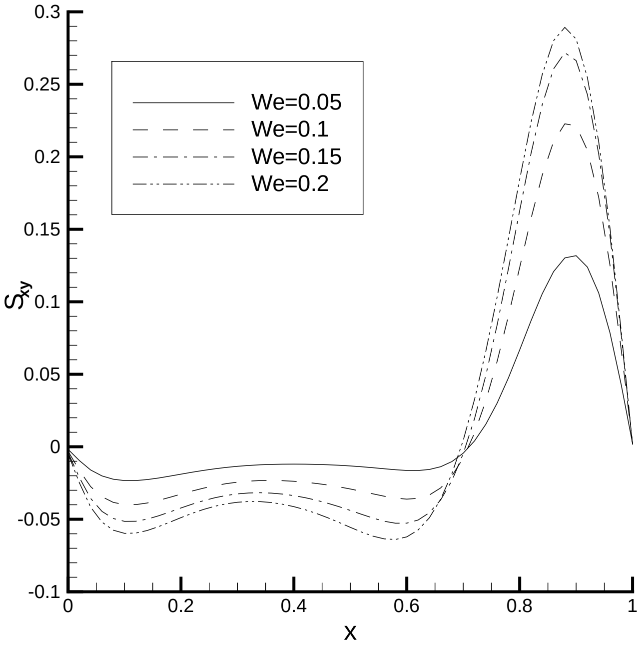

Figure 4.24. The non-Newtonian stress tensor component S_{xy} through the horizontal centerline for Re = 100 and UCM for the constitutive relation

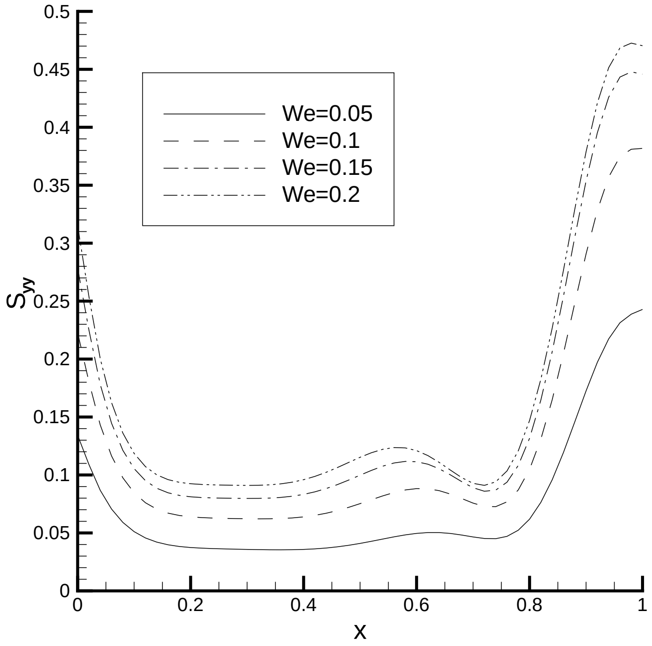

Figure 4.25. The non-Newtonian stress tensor component S_{yy} through the horizontal centerline for Re = 100 and UCM for the constitutive relation

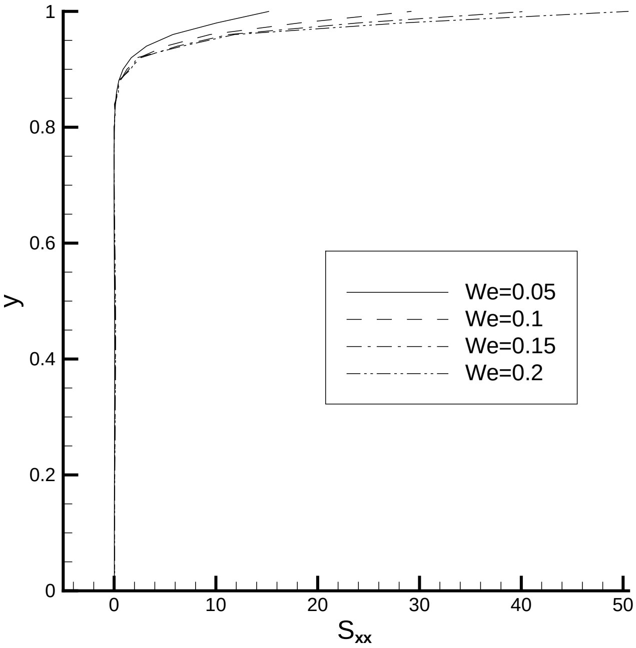

Figure 4.26. The non-Newtonian stress tensor component S_{xx} through the vertical centerline for Re = 100 and UCM for the constitutive relation

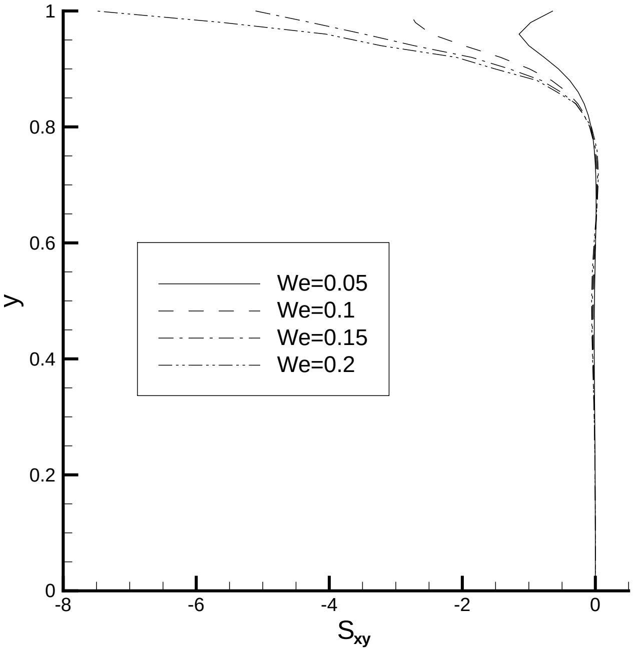

Figure 4.27. The non-Newtonian stress tensor component S_{xy} through the vertical centerline for Re = 100 and UCM for the constitutive relation

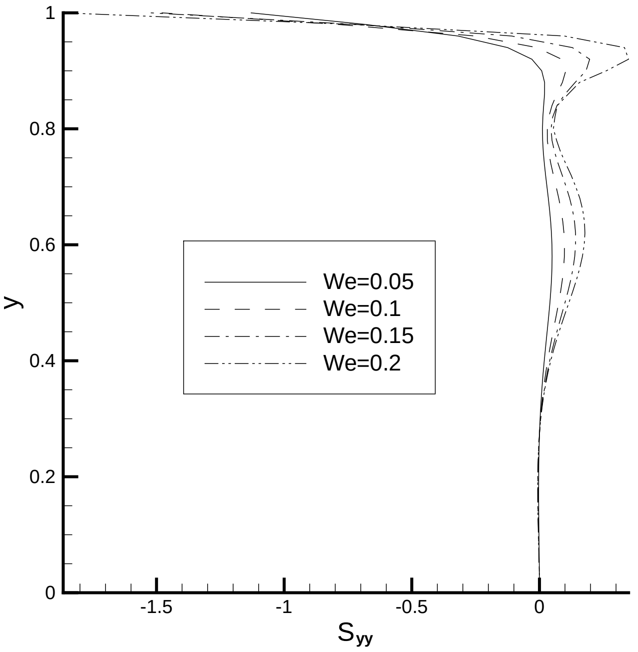

Figure 4.28. The non-Newtonian stress tensor component S_{yy} through the vertical centerline for Re = 100 and UCM for the constitutive relation

The effects of the Reynolds number on the flow of the UCM fluid is similar to the Newtonian cases, that's why they will not be stated in here.

4.1.3.2. Oldroyd B Model. The Oldroyd B model is the second constitutive equation used in the simulations of this study. It is more realistic and has better convergence behavior than the UCM model. This equation can be employed when the solvent and the polymer viscosities of the non-Newtonian fluid are known explicitly. Since the Oldroyd B relation is applicable for low shear rates, it is not useful for very high Weissenberg number problems. The solutions of the Oldroyd B model become easier when the viscosity ratio β is large and they become harder when β is small. The reason for this variance is in the equations of the Oldroyd B constitutive relation itself. For Oldroyd B model, $\beta = 0$ value coincides with the UCM relation where the $\beta = 1$ value coincides with the Newtonian flow. Numerical solutions of Oldroyd B model become easier when viscosity ratio approaches 1 because the elliptic property of the Oldroyd B model increases.

The effects of the viscosity ratio are investigated with a test problem with the parameters of; Re = 100, We = 0.15 and zero initial guess. The flow structures and the convergence ratio are plotted in order to have an insight about this model. Figures 4.29 through 4.31 show the stream function contours for the viscosity ratios of 0.1, 0.5 and 0.9. As can be understood from the minimum value of the stream function, the velocity is the highest for $\beta = 0.9$ case, which is the least elastic one (closest to the Newtonian flow). Since the definition of the viscosity ratio is the ratio of the solvent viscosity to the sum of solvent and polymer viscosities, the polymer amount in the $\beta = 0.9$ case is minimum compared to the others and therefore the least elastic flow is this case. That's why the maximum velocity is appeared for $\beta = 0.9$ value.

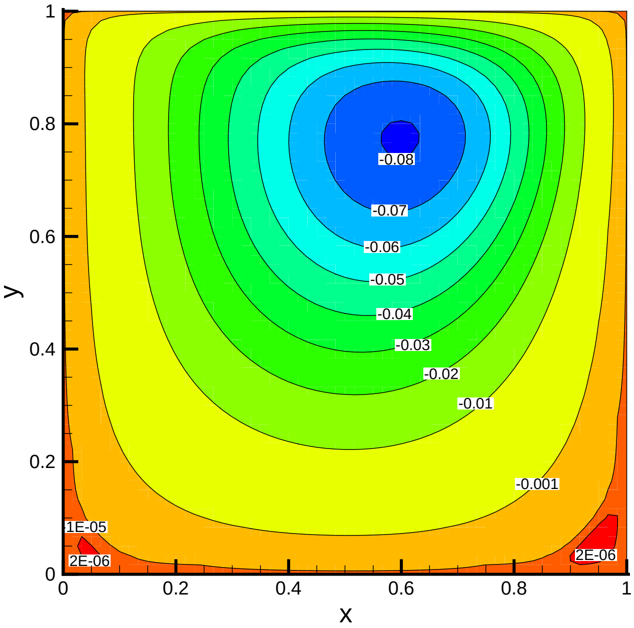

Figure 4.29. Stream function contours of the Oldroyd B fluid with the parameters; Re = 100, We = 0.15 and $\beta = 0.1$

The convergence behavior is plotted in Figure 4.32 and it is obvious that the convergence is harder with the decreasing viscosity ratios as expected. It is also apparent that the computation times are directly proportional to the number of nonlinear iterations and that's why the minimum computation time is observed for the $\beta = 0.9$ case. The optimum value of the viscosity ratio is selected as 0.5 for the rest of the com-

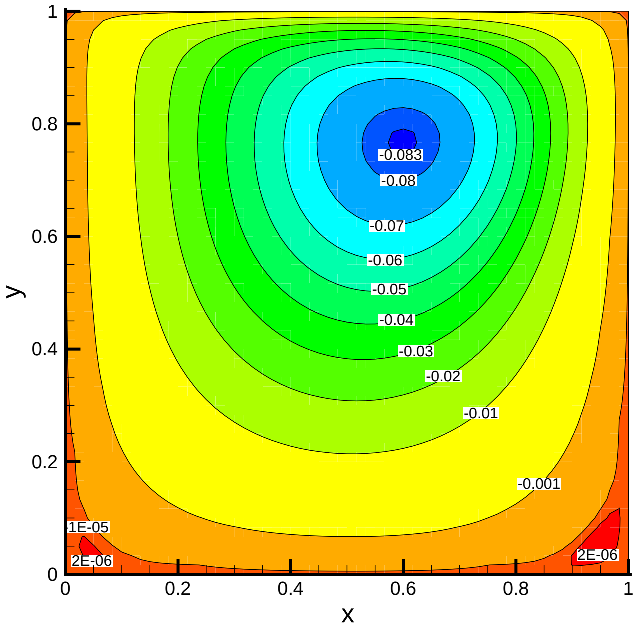

Figure 4.30. Stream function contours of the Oldroyd B fluid with the parameters; Re = 100, We = 0.15 and $\beta = 0.5$

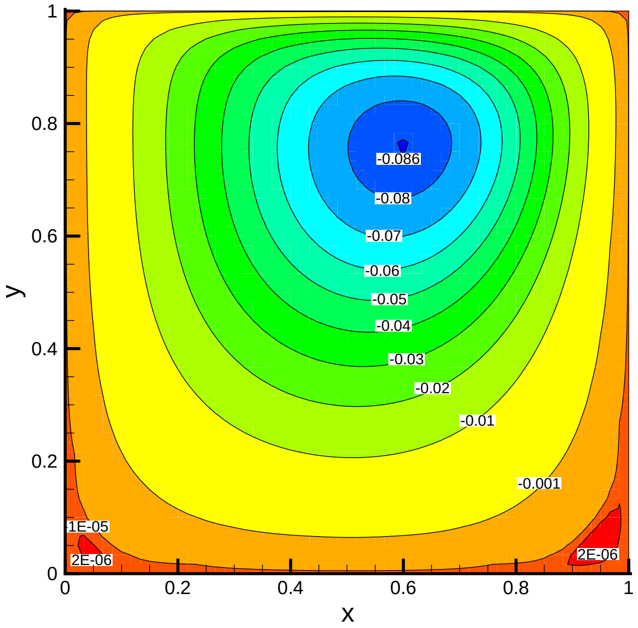

Figure 4.31. Stream function contours of the Oldroyd B fluid with the parameters; Re = 100, We = 0.15 and $\beta = 0.9$

putations since it represents sufficient elasticity and the computations are fast enough.

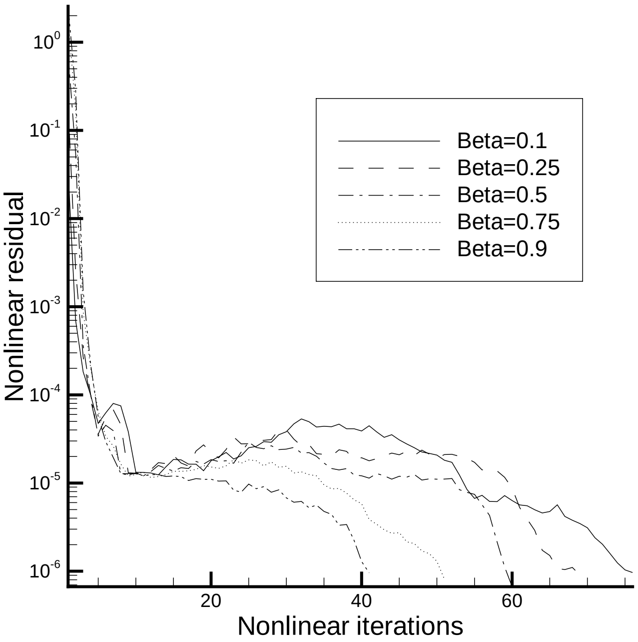

Figure 4.32. Nonlinear convergence graphic of different viscosity ratios for the Oldroyd B flow with the parameters; Re = 100, We = 0.15

The isovorticity lines are given with the Figure 4.33 which reveals the small variations in the vorticity field.

In addition, the most important effect of the viscosity ratio can be grasped in Table 4.5. The increase in the viscosity ratio eases up the solution and the maximum Weissenberg number limits become higher.

4.1.3.3. Giesekus Model. The final constitutive relation used in the simulations of the LDC is the Giesekus model which is one of the most realistic differential constitutive relations. This equation displays shear thinning behavior where the UCM and Oldroyd B models are insufficient for the modeling of the shear thinning fluids. Beneficially, the maximum Weissenberg number limits are higher for Giesekus constitutive relation compared to the UCM and Oldroyd B models (Table 4.4). Since the Giesekus model is the most advantageous one compared with the other two, the simulations carried out

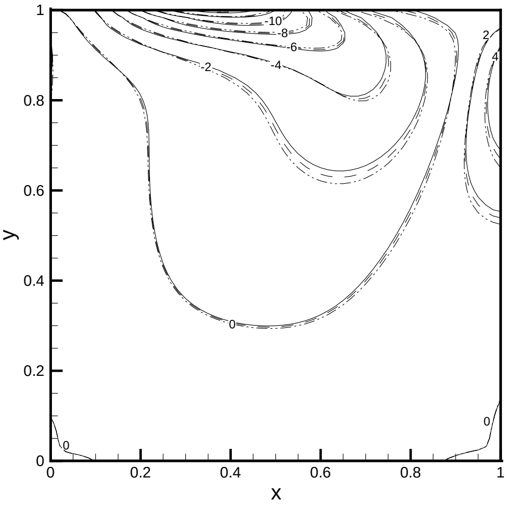

Figure 4.33. Vorticity contours of the Oldroyd B fluid with the parameters; Re = 100, We = 0.1 and varying viscosity ratios (solid line is $\beta = 0.1$ case, dashed line is $\beta = 0.5$ case, dashed and dotted line is $\beta = 0.9$ case)

in the following sections are performed by using the Giesekus constitutive relation.

The material parameter in the Giesekus model is the mobility factor and it should be in the range of 0 and 0.5 in order to obtain realistic solutions (Bird *et al.* [50]). Moreover, the values between 0.05 and 0.15 are preferred in the literature. Therefore, the test problem with the parameters of; Re = 100, $\beta = 0.5$ is used in order to determine the effects of mobility factor. Table 4.5 reveals that the increase in the mobility factor eases up the solution and raises the maximum Weissenberg numbers. The effects of the mobility factor on the stream function can be seen in the Figure 4.34. As can be observed from this figure, the effects are small and since the stream function values are similar for different mobility factors, the velocity fields should also be similar.

The effects of the mobility factor is apparent in the Figures 4.35, 4.36 and 4.37. It can be understood from these and other analyses that the stress values are decreasing with the increase in the mobility factor and this eases up the solution and makes the maximum Weissenberg number limit higher. Similar to the studies in the literature $\alpha = 0.1$ value is selected as the mobility parameter for the rest of the study.

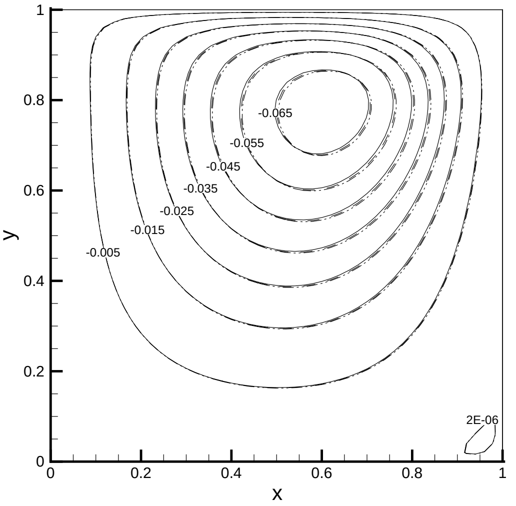

Figure 4.34. Stream function contours of the Giesekus fluid with the parameters; Re = 100, We = 0.3, $\beta = 0.5$ and varying mobility factors (solid line is $\alpha = 0.05$ case, dashed line is $\alpha = 0.1$ case, dashed and dotted line is $\alpha = 0.15$ case)

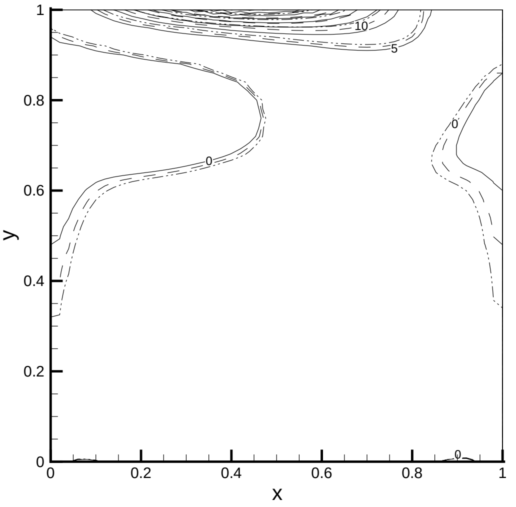

Figure 4.35. Contours of S_{xx} for Giesekus fluid with the parameters; Re = 100, We = 0.3, $\beta = 0.5$ and varying mobility factors (solid line is $\alpha = 0.05$ case, dashed line is $\alpha = 0.1$ case, dashed and dotted line is $\alpha = 0.15$ case)

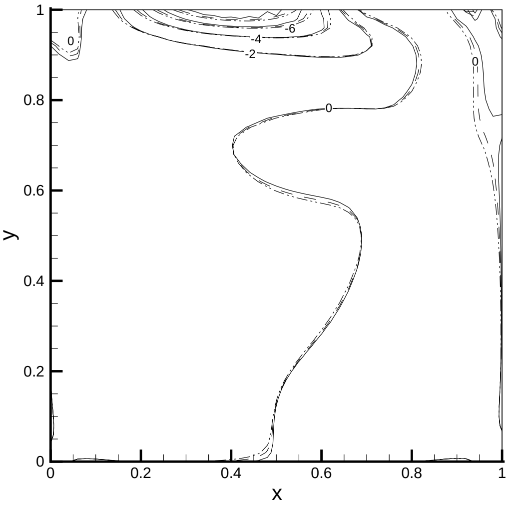

Figure 4.36. Contours of S_{xy} for Giesekus fluid with the parameters; Re $= 100$, We $= 0.3$, $\beta = 0.5$ and varying mobility factors (solid line is $\alpha = 0.05$ case, dashed line is $\alpha = 0.1$ case, dashed and dotted line is $\alpha = 0.15$ case)

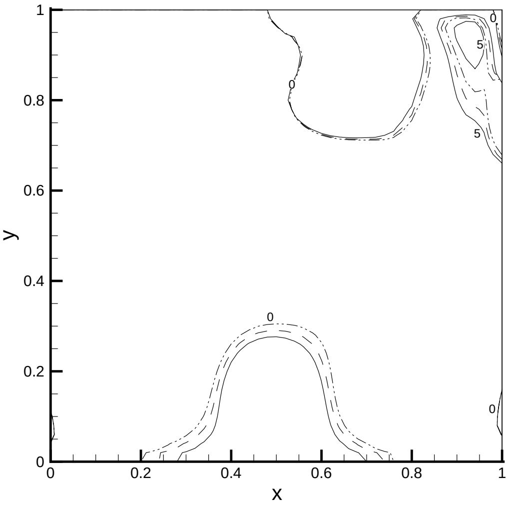

Figure 4.37. Contours of S_{yy} for Giesekus fluid with the parameters; Re $= 100$, We $= 0.3$, $\beta = 0.5$ and varying mobility factors (solid line is $\alpha = 0.05$ case, dashed line is $\alpha = 0.1$ case, dashed and dotted line is $\alpha = 0.15$ case)

It is not advisable to compare the velocity fields or the stress fields of three constitutive relations mentioned above for a fixed Weissenberg number because the different viscosity ratios and mobility factors will result in dissimilar elastic effects and consequently the flow fields will not be similar. However, in order to have an insight, the non-Newtonian stress components are plotted at the centerlines of the cavity for different constitutive relations with Figures 4.38 through 4.43. In these comparisons; Re = 100, We = 0.2, $\beta = 0.5$ and $\alpha = 0.1$ are used as the problems parameters. As can be observed from these figures all of the constitutive relations give dissimilar stress fields with the similar variations.

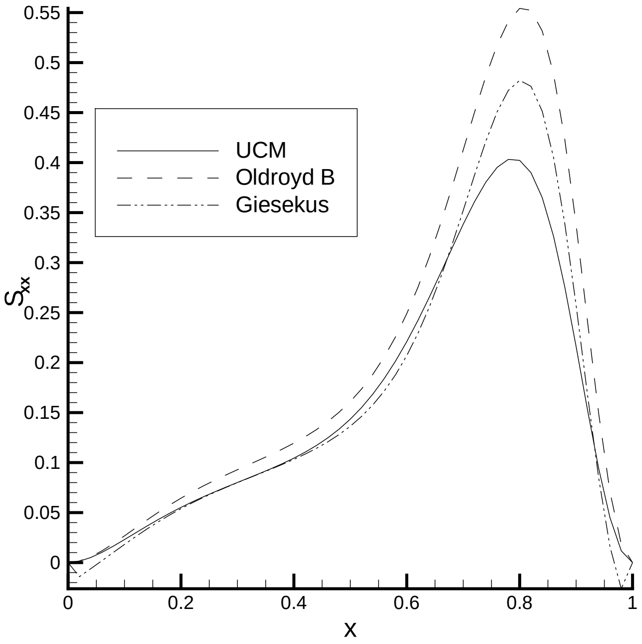

Figure 4.38. The non-Newtonian stress tensor component S_{xx} through the horizontal centerline for various constitutive relations and Re = 100, We = 0.2, $\beta = 0.5$, $\alpha = 0.1$

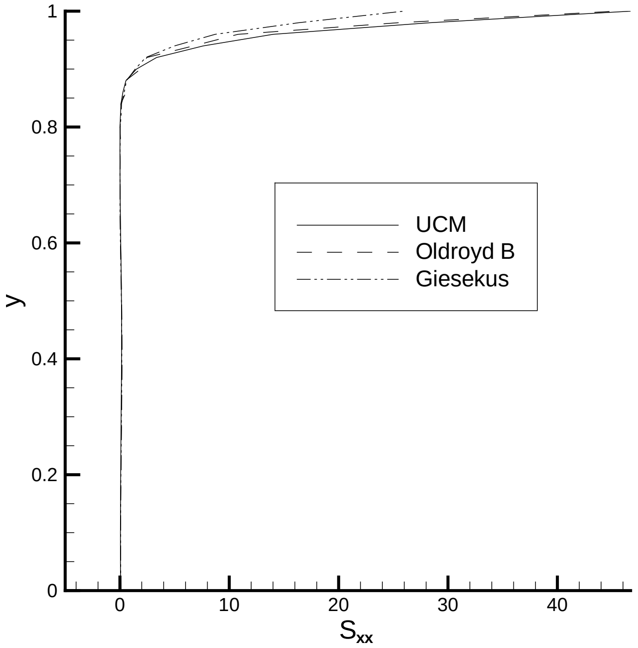

Figure 4.39. The non-Newtonian stress tensor component S_{xx} through the vertical centerline for various constitutive relations and Re = 100, We = 0.2, $\beta = 0.5$, $\alpha = 0.1$

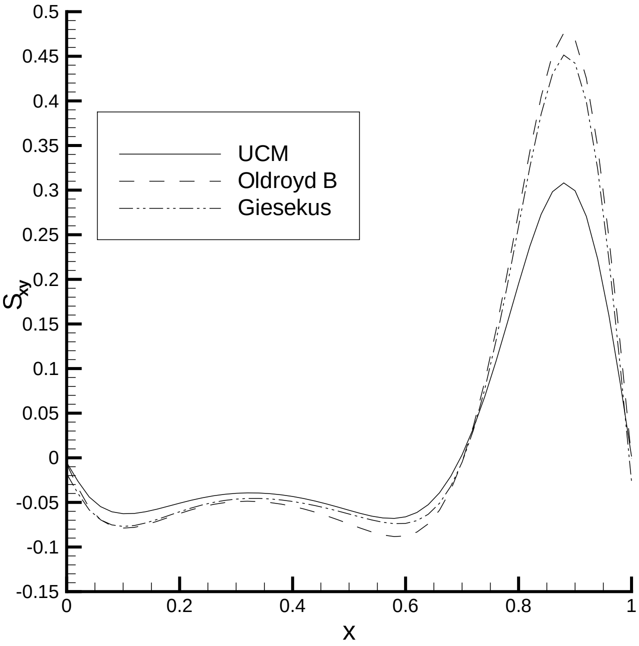

Figure 4.40. The non-Newtonian stress tensor component S_{xy} through the horizontal centerline for various constitutive relations and Re = 100, We = 0.2, $\beta = 0.5$, $\alpha = 0.1$

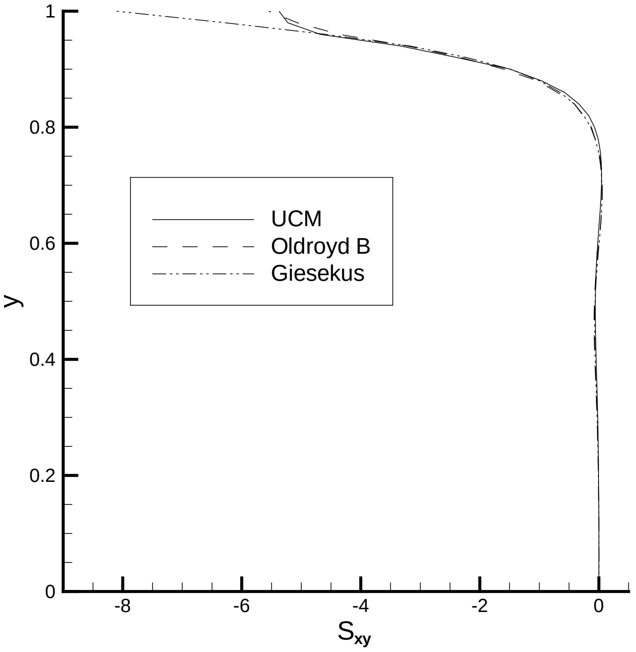

Figure 4.41. The non-Newtonian stress tensor component S_{xy} through the vertical centerline for various constitutive relations and Re = 100, We = 0.2, $\beta = 0.5$, $\alpha = 0.1$

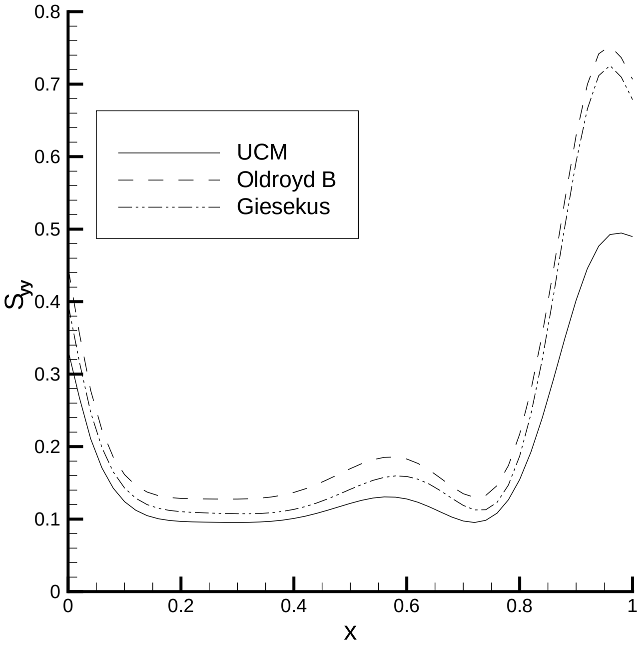

Figure 4.42. The non-Newtonian stress tensor component S_{yy} through the horizontal centerline for various constitutive relations and Re = 100, We = 0.2, $\beta = 0.5$, $\alpha = 0.1$

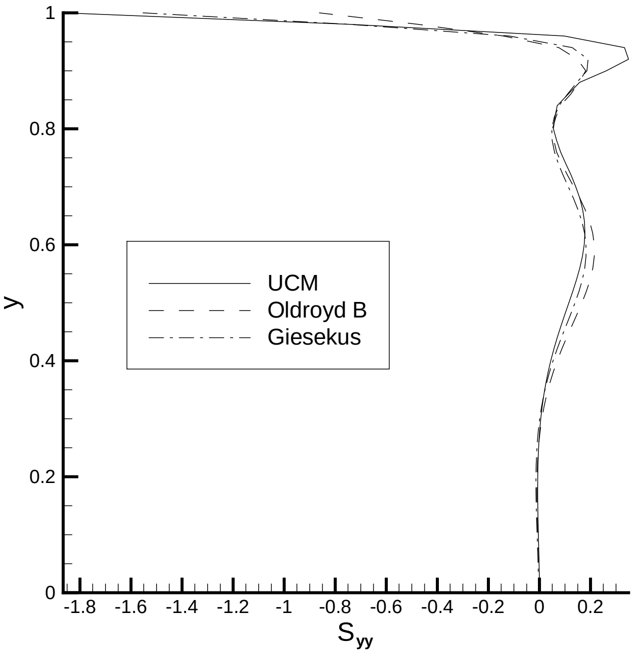

Figure 4.43. The non-Newtonian stress tensor component S_{yy} through the vertical centerline for various constitutive relations and Re = 100, We = 0.2, $\beta = 0.5$, $\alpha = 0.1$

4.1.3.4. Non-isothermal LDC flow. In this part of the study, the thermal effects on the flow of non-Newtonian fluids will be revealed. Since the thermal analyses are connected to many parameters such as the Reynolds number, the Prandtl number (or the Péclet number), the Brinkman number and the temperature sensitive coefficient of the Arrhenius relation, the effects of all of these parameters should separately be studied. In order to simplify the simulations, the Giesekus model with the parameters of $\beta = 0.5$ and $\alpha = 0.1$ is used. This constitutive relation is selected because of its superiority over the UCM and Oldroyd B. In all of the simulations the the lid is at 10^0C where the stationary walls are at 0^0C.

Before proceeding with the effects of the parameters related to the energy equation, the differences between the flow fields of the isothermal and non-isothermal flows should be clarified. In order to achieve this goal, a test problem with the parameters of Re = 100, We = 0.2, $\beta = 0.5$, $\alpha = 0.1$, Pr = 10, Br = 10 and $\alpha_s = 0.01$ is solved. Figures 4.44 and 4.45 reveal the velocity versus coordinate plots for both isothermal and non-isothermal cases of the test problem. Especially the difference in the Figure 4.45 indicate that the effects of temperature may disturb the flow field. This disturbance will gain more and more importance with the increasing energy equation parameters such as the Prandtl number, the Brinkman number and the temperature sensitive coefficient.

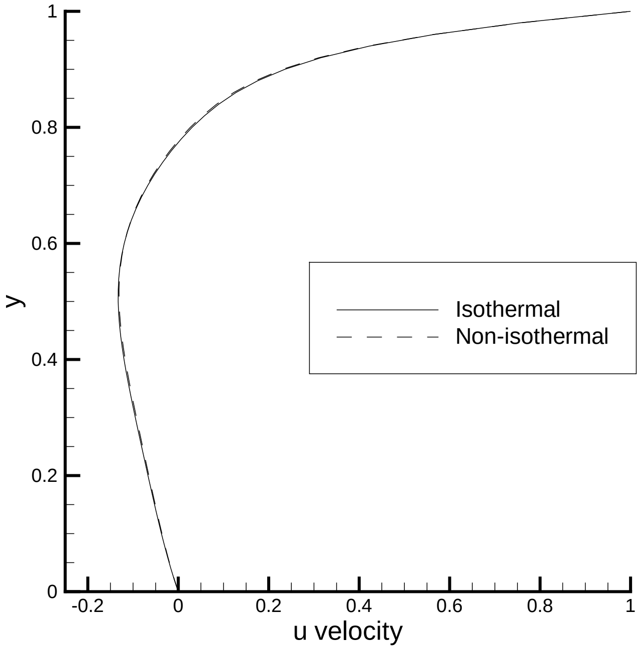

Figure 4.44. u velocity through the vertical centerline

The alteration of the flow field is the result of the variable viscosity, which is simulated by using approximate Arrhenius relation (Equation 2.11). For the test problem above, the temperature dependent shift factor (multiplier of the viscosity) of the approximate Arrhenius relation can be seen in Figure 4.46. As can be observed from this figure the viscosity is decreased at the central domain of the cavity which results in the alteration of the flow field.

Similarly the importance of the effects of the viscous dissipation should also be investigated. For this purpose, the LDC problem is modeled with the parameters; Re = 10, We = 0.4, β = 0.5, α = 0.1, Pr = 10, Br = 20 (since Br $\neq$ 0 viscous dissipation is present) and $\alpha_s = 0.01$. Figure 4.47 reveals that the maximum temperature value within the cavity is 17.0462^0C which is higher than the maximum boundary temperature. This elevation in the temperature is mainly the result of friction within

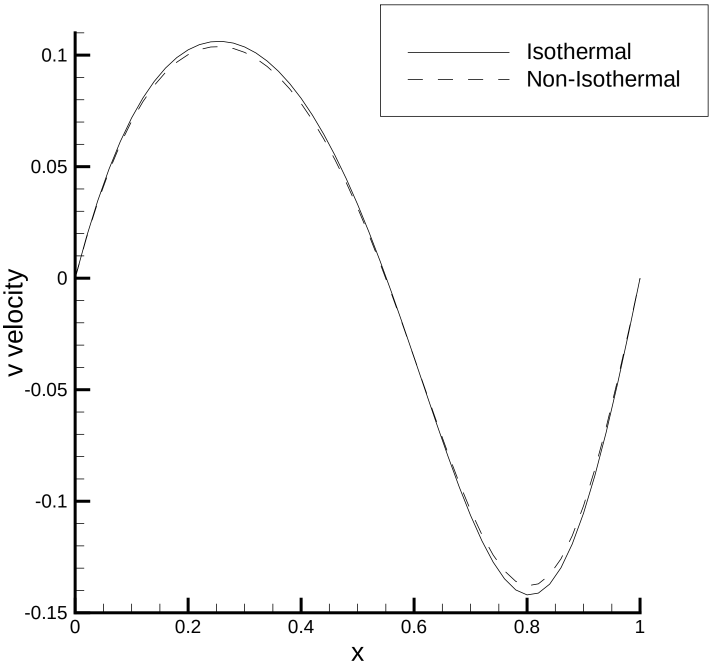

Figure 4.45. v velocity through the horizontal centerline

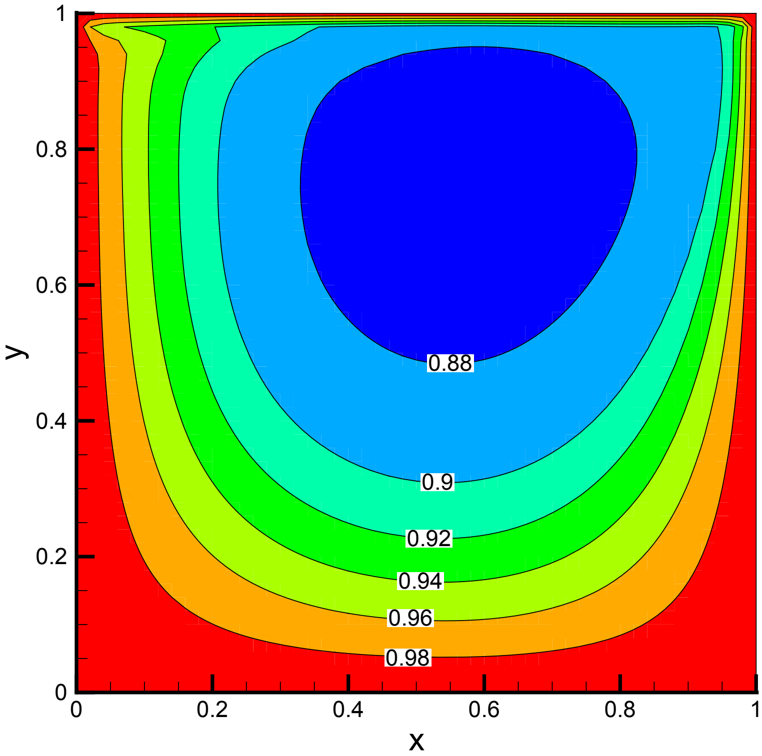

Figure 4.46. The temperature dependent shift factor with the parameters; Re = 100, We = 0.2, $\beta = 0.5$, $\alpha = 0.1$, Pr = 10, Br = 10 and $\alpha_s = 0.01$

the fluid and it can be modeled by viscous dissipation. Given that the viscosity values for the non-Newtonian fluids are high and the friction is proportional to the viscosity, the heating due to viscous dissipation is expected.

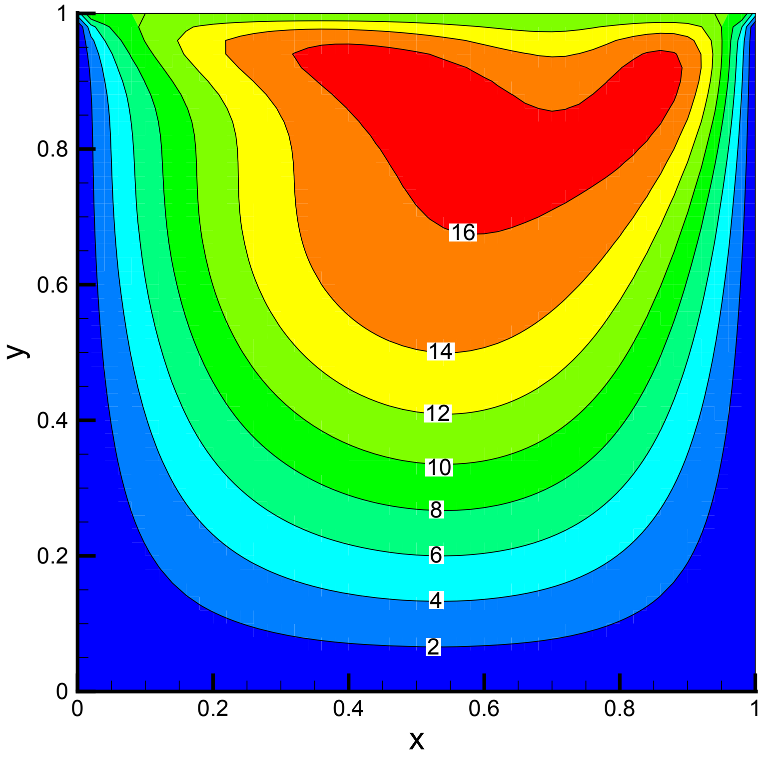

Figure 4.47. The temperature field with the parameters; Re $= 10$, We $= 0.4$, $\beta = 0.5$, $\alpha = 0.1$, Pr $= 10$, Br $= 20$ and $\alpha_s = 0.01$

The energy equation (Equation 2.40) consists of three main parts. The first part is the advection part with the coefficient of the Péclet number, the second part is the diffusion part without any coefficient and the third part is the viscous dissipation part with the coefficient of the Brinkman number. The analyses carried out previously revealed that all of these parts should be considered in order to model the non-isothermal phenomenon accurately.

The effects of the Reynolds number can be seen from Figures 4.48, 4.49 and 4.50. It is observed from these figures that the core of the temperature field is moving to the point between the center of the domain and the right wall with the increasing Reynolds number. The maximum temperatures are 13.58^0C, 13.17^0C, 12.84^0C and 12.77^0C for the Reynolds numbers of 0, 10, 20 and 100 respectively. Therefore, it is understood that with the increasing Reynolds number, the maximum temperature tends to decrease.

This may be explained by the increased mixing effect for higher Reynolds numbers.

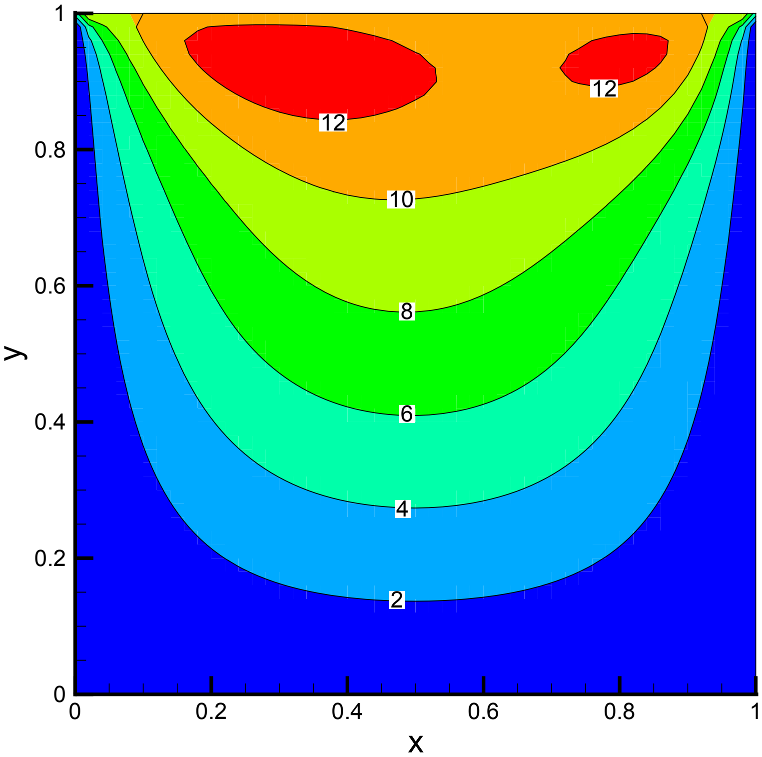

Figure 4.48. The temperature field with the parameters; Re $= 0$, We $= 0.4$, $\beta = 0.5$, $\alpha = 0.1$, Pr $= 10$, Br $= 10$ and $\alpha_s = 0.01$

Figures 4.51 and 4.52 reveal the effect of Reynolds number on the temperature field. Even though the maximum temperatures are lowering with the increasing Reynolds number, the averages of the temperatures are getting higher (5.25^0C, 6.06^0C, 6.57^0C and 7.59^0C for the Reynolds numbers of 0, 10, 20 and 100 respectively). The main reason of the increased average temperature is the friction effect. Increasing Reynolds number results in higher friction which leads to the more heat generation within the flow domain.

Figures 4.53, 4.54 and 4.54 reveal the effects of the Prandtl number on the temperature field for the test problem of; Re $= 10$, We $= 0.4$, $\beta = 0.5$, $\alpha = 0.1$, Br $= 10$ and $\alpha_s = 0.01$. These figures indicate that the core of the temperature field moving through the center of the flow domain. Given that the Péclet number is the multiplication of the Reynolds and the Prandtl numbers, increasing Prandtl and/or Reynolds numbers directly increase the Péclet number of the flow. Since the properties are transported

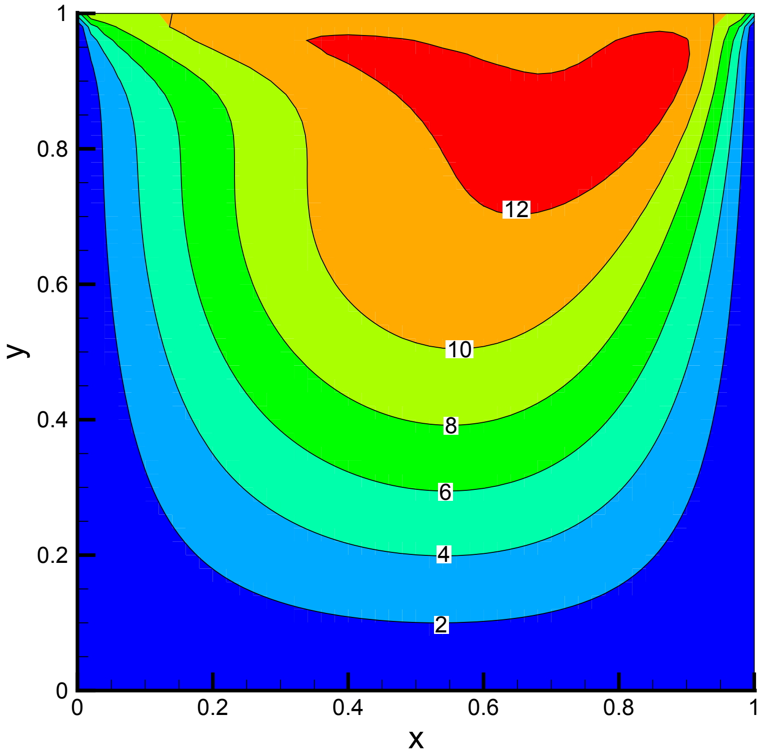

Figure 4.49. The temperature field with the parameters; Re $= 10$, We $= 0.4$, $\beta = 0.5$, $\alpha = 0.1$, Pr $= 10$, Br $= 10$ and $\alpha_s = 0.01$

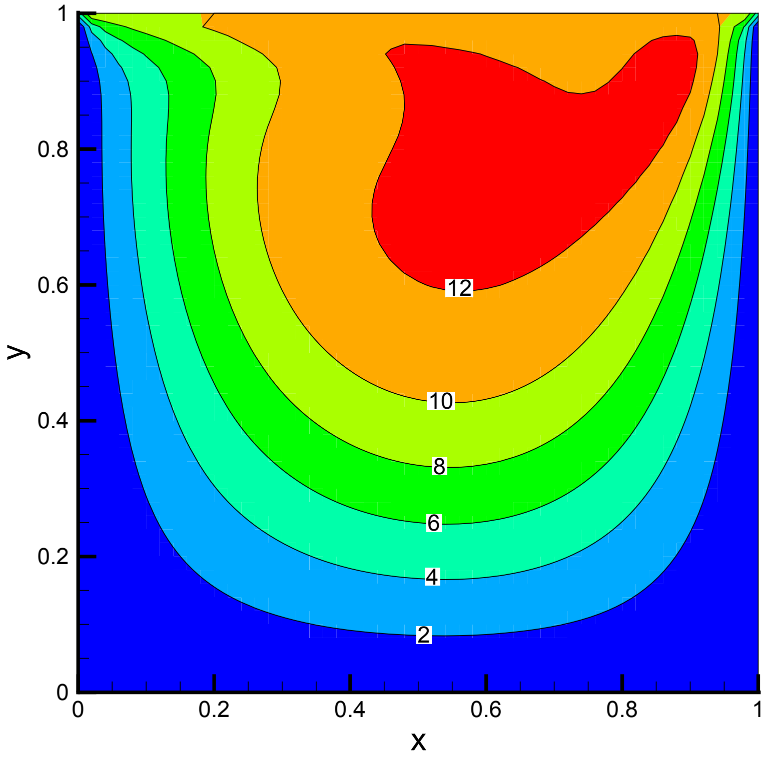

Figure 4.50. The temperature field with the parameters; Re $= 20$, We $= 0.4$, $\beta = 0.5$, $\alpha = 0.1$, Pr $= 10$, Br $= 10$ and $\alpha_s = 0.01$

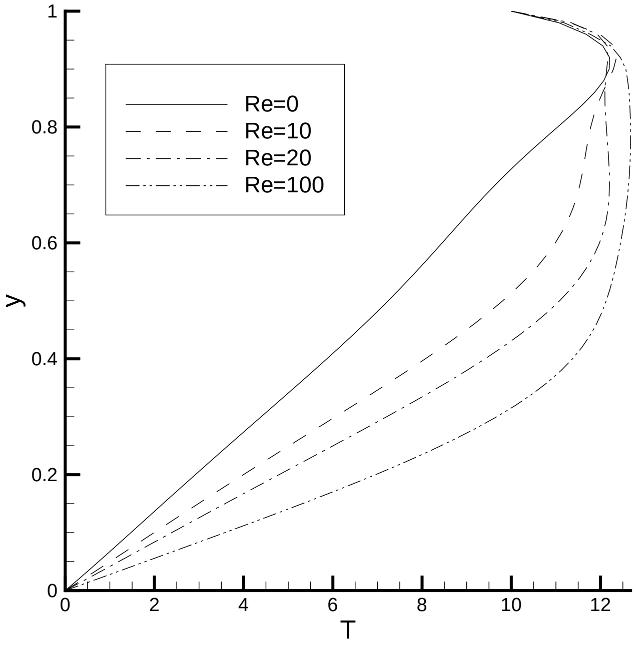

Figure 4.51. Temperature through the vertical centerline with the parameters; We $= 0.4$, $\beta = 0.5$, $\alpha = 0.1$, Pr $= 10$, Br $= 10$ and $\alpha_s = 0.01$

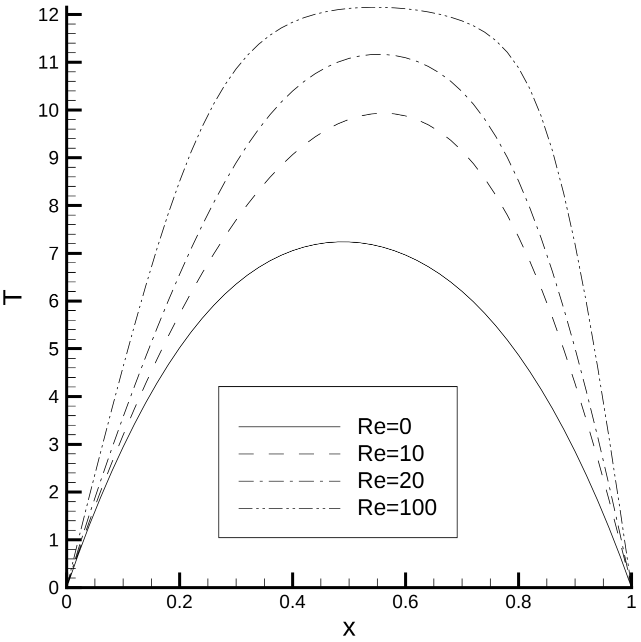

Figure 4.52. Temperature through the horizontal centerline with the parameters; We $= 0.4$, $\beta = 0.5$, $\alpha = 0.1$, Pr $= 10$, Br $= 10$ and $\alpha_s = 0.01$

mostly with advection at high Péclet numbers, the temperature field fluctuates and the simulations get harder. For the creeping flow cases (Re = 0), the Péclet number becomes zero and the fluctuations disappear. The maximum temperatures are calculated as; 13.17^0C, 12.59^0C and 12.53^0C for the Prandtl numbers of 10, 100 and 200 respectively. Therefore, it is safe to say that increasing Prandtl numbers lowers the maximum temperatures.

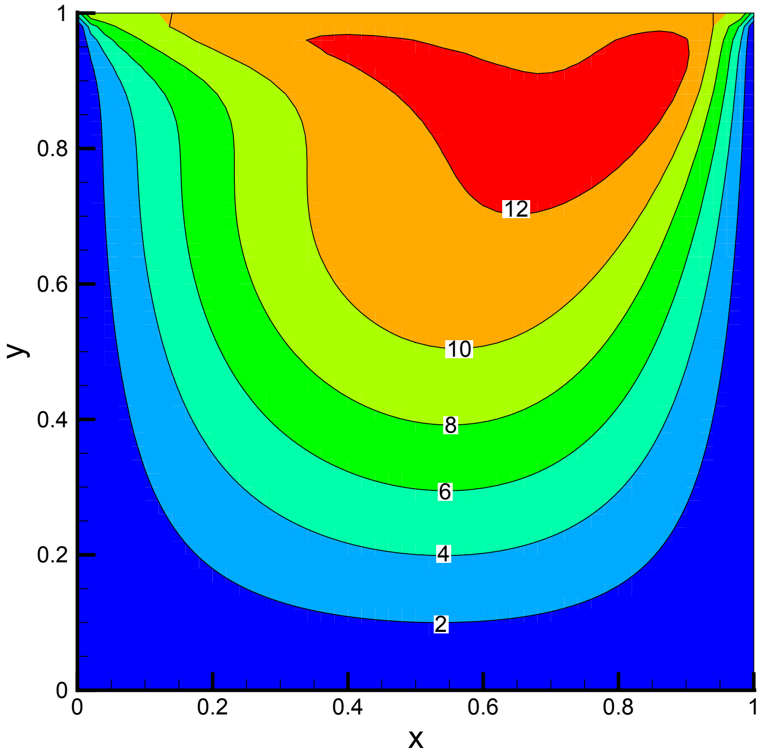

Figure 4.53. The temperature field with the parameters; Re = 10, We = 0.4, $\beta = 0.5$, $\alpha = 0.1$, Pr = 10, Br = 10 and $\alpha_s = 0.01$

Figures 4.56 and 4.57 reveal the temperatures through the centerlines of the cavity for various Prandtl numbers. It can be observed from this and previous figures that the increased Prandtl numbers make the average temperatures higher.

Figures 4.58, 4.59 and 4.60 show the effects of the Brinkman number on the temperature field for the test problem of; Re = 10, Pr = 10, We = 0.4, $\beta = 0.5$, $\alpha = 0.1$ and $\alpha_s = 0.01$. These figures indicate that increased Brinkman numbers result in higher heat generation within the flow domain. Since the Brinkman number is a measure of the viscous dissipation, the higher heat generation is expected.

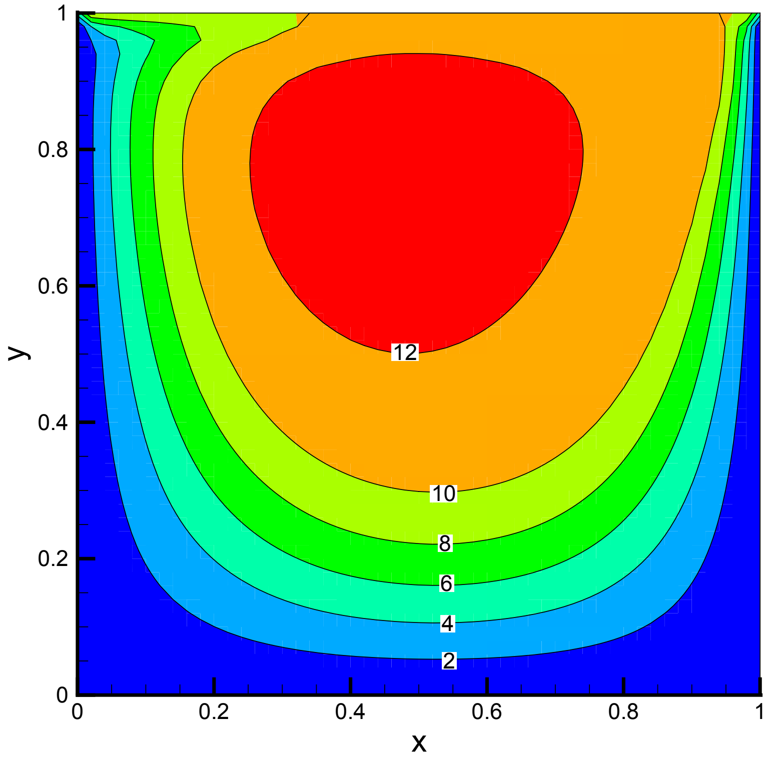

Figure 4.54. The temperature field with the parameters; Re $= 10$, We $= 0.4$, $\beta = 0.5$, $\alpha = 0.1$, Pr $= 100$, Br $= 10$ and $\alpha_s = 0.01$

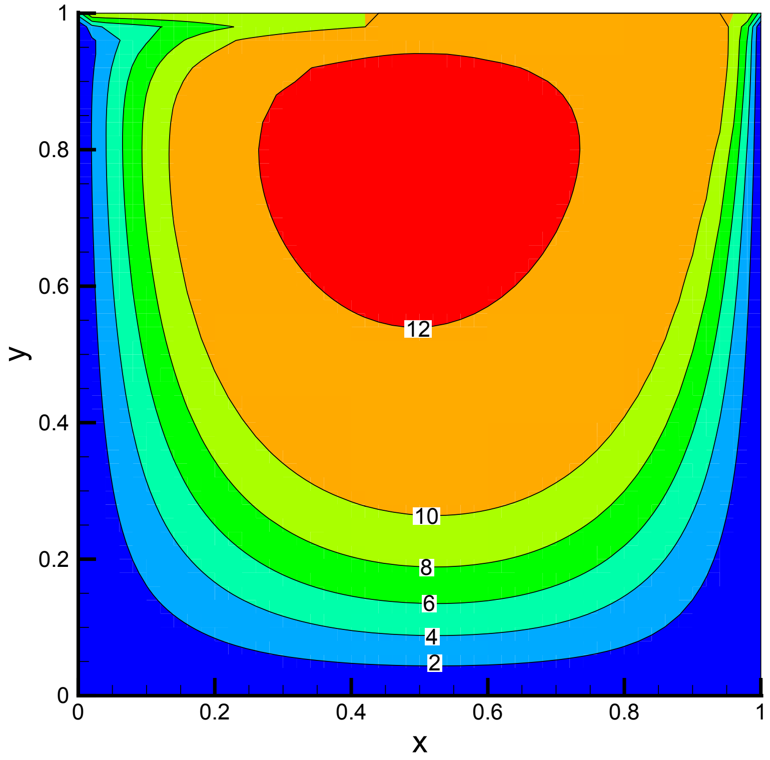

Figure 4.55. The temperature field with the parameters; Re $= 10$, We $= 0.4$, $\beta = 0.5$, $\alpha = 0.1$, Pr $= 200$, Br $= 10$ and $\alpha_s = 0.01$

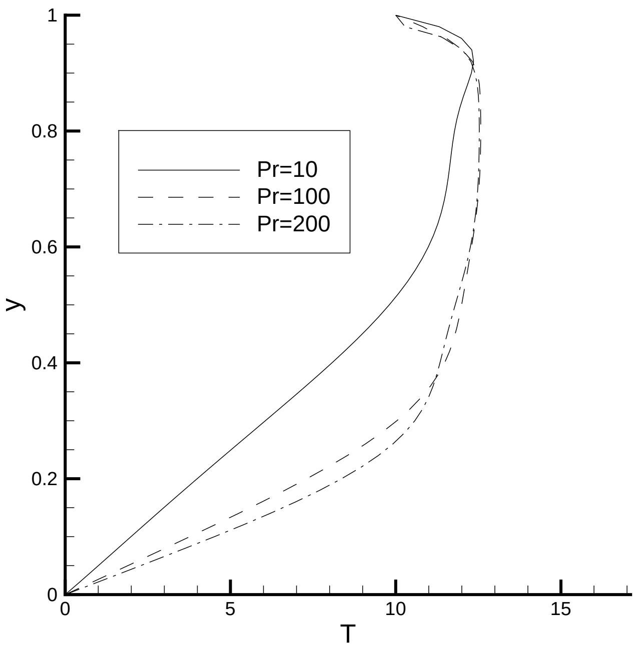

Figure 4.56. Temperature through the vertical centerline with the parameters; Re $= 10$, We $= 0.4$, $\beta = 0.5$, $\alpha = 0.1$, Br $= 10$ and $\alpha_s = 0.01$

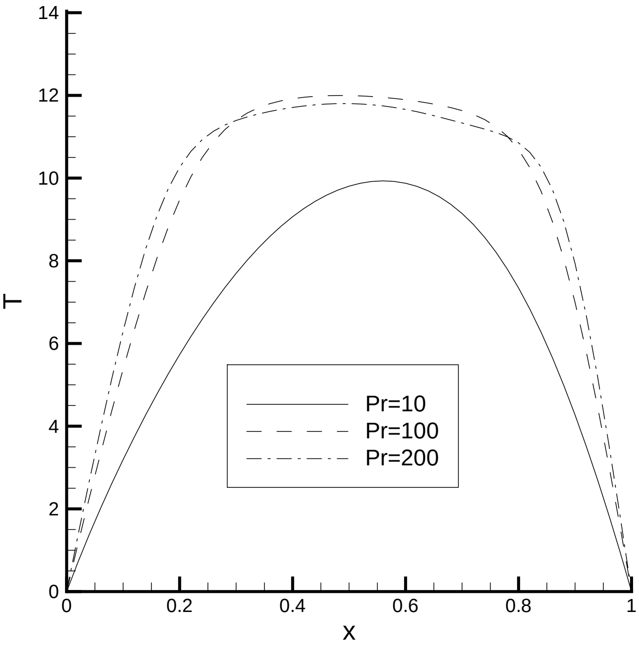

Figure 4.57. Temperature through the horizontal centerline with the parameters; Re $= 10$, We $= 0.4$, $\beta = 0.5$, $\alpha = 0.1$, Br $= 10$ and $\alpha_s = 0.01$

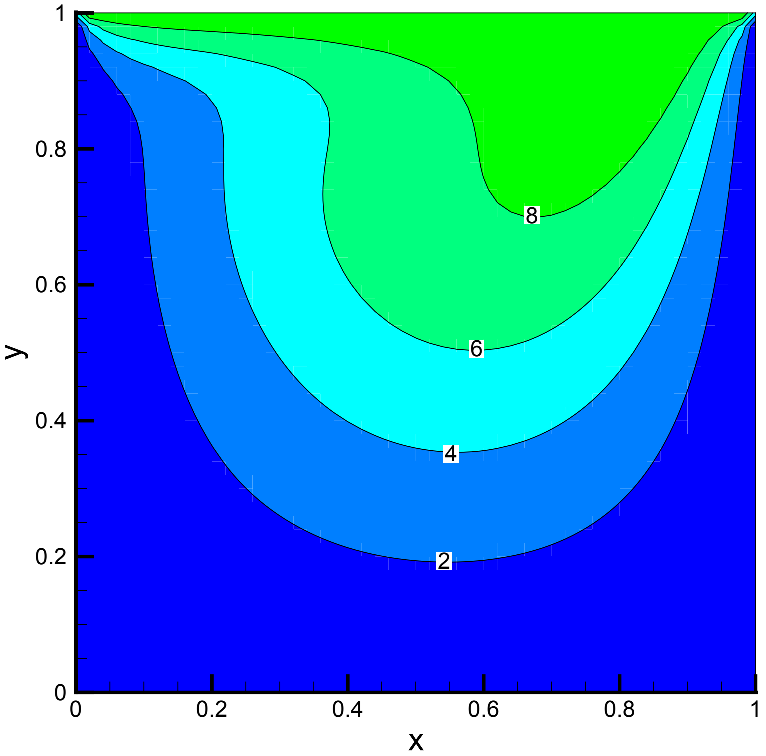

Figure 4.58. The temperature field with the parameters; Re $= 10$, We $= 0.4$, $\beta = 0.5$, $\alpha = 0.1$, Pr $= 10$, Br $= 1$ and $\alpha_s = 0.01$

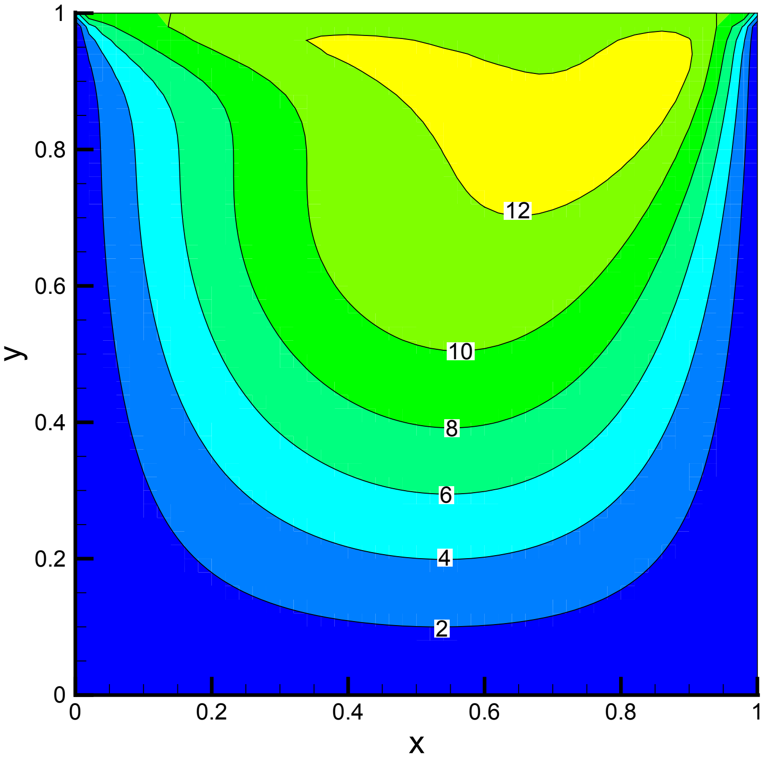

Figure 4.59. The temperature field with the parameters; Re $= 10$, We $= 0.4$, $\beta = 0.5$, $\alpha = 0.1$, Pr $= 10$, Br $= 10$ and $\alpha_s = 0.01$

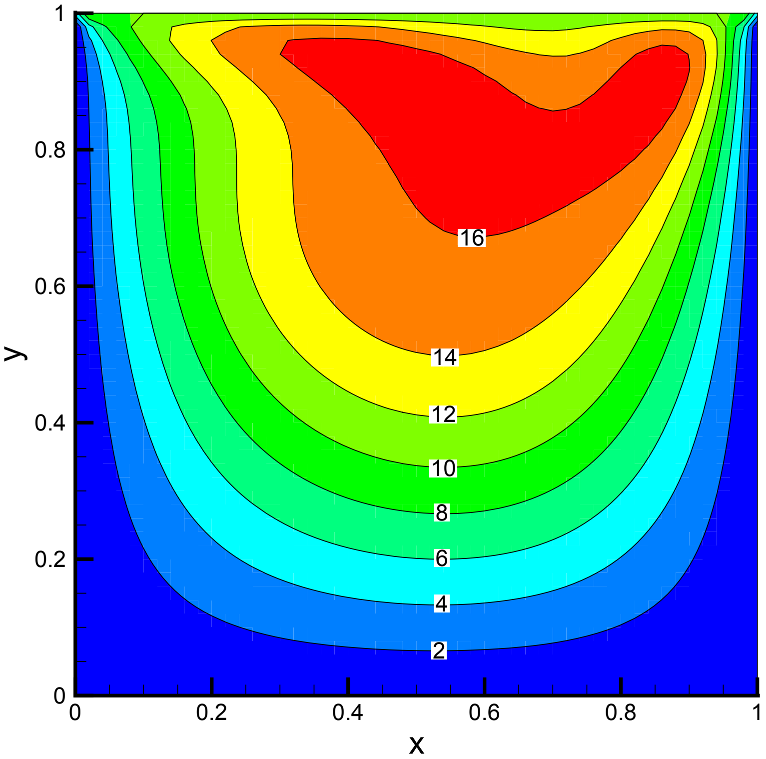

Figure 4.60. The temperature field with the parameters; Re = 10, We = 0.4, $\beta = 0.5$, $\alpha = 0.1$, Pr = 10, Br = 20 and $\alpha_s = 0.01$

The effects of the temperature sensitive coefficient of the approximate Arrhenius relation are determined with the observation of the Figures 4.61, 4.62 and 4.63. Moreover, the maximum temperatures can be found as; 13.4415^0C, 13.1655^0C, 12.9242^0C and the average temperatures can be found as; 6.2189^0C, 6.0586^0C, 5.9143^0C for the temperature sensitive coefficients of 0.005, 0.01 and 0.015 respectively. It can be understood from these values that the increasing temperature sensitive coefficient lowers the maximum and the average temperatures within the flow domain. This decrease is directly related to the viscosity of the fluid. Since the shift factor in the approximate Arrhenius relation is inversely proportional to this constant, the higher temperature sensitive coefficient will result in lower shift factor and consequently lower the viscosity. By this way, the effects of the viscous dissipation and the temperatures will decrease.

In order to investigate the effects of Weissenberg number on the temperature field, a test problem with the parameters of Re = 10, Pr = 10, Br = 20, $\beta = 0.5$, $\alpha = 0.1$ and $\alpha_s = 0.01$ is studied. Figures 4.64, 4.65 and 4.66 reveal the temperature field for the Weissenberg numbers of 0, 0.2 and 0.4 respectively. It is obvious from

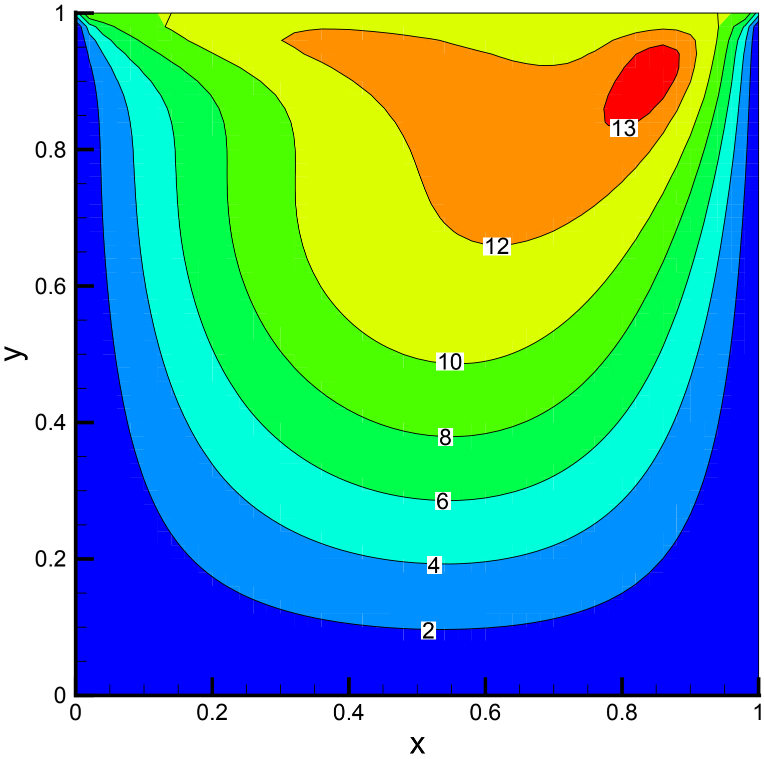

Figure 4.61. The temperature field with the parameters; Re $= 10$, We $= 0.4$, $\beta = 0.5$, $\alpha = 0.1$, Pr $= 10$, Br $= 10$ and $\alpha_s = 0.005$

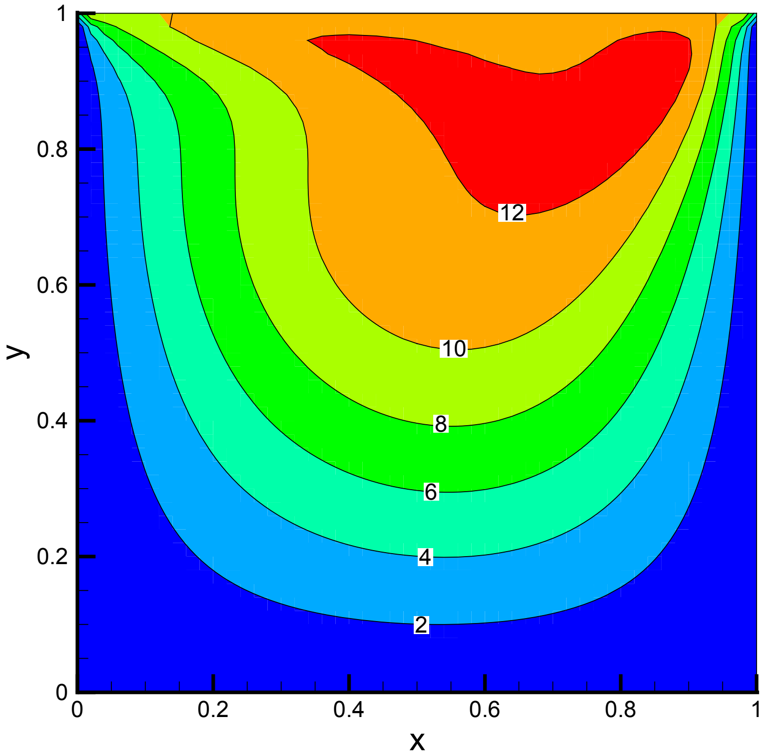

Figure 4.62. The temperature field with the parameters; Re $= 10$, We $= 0.4$, $\beta = 0.5$, $\alpha = 0.1$, Pr $= 10$, Br $= 10$ and $\alpha_s = 0.01$

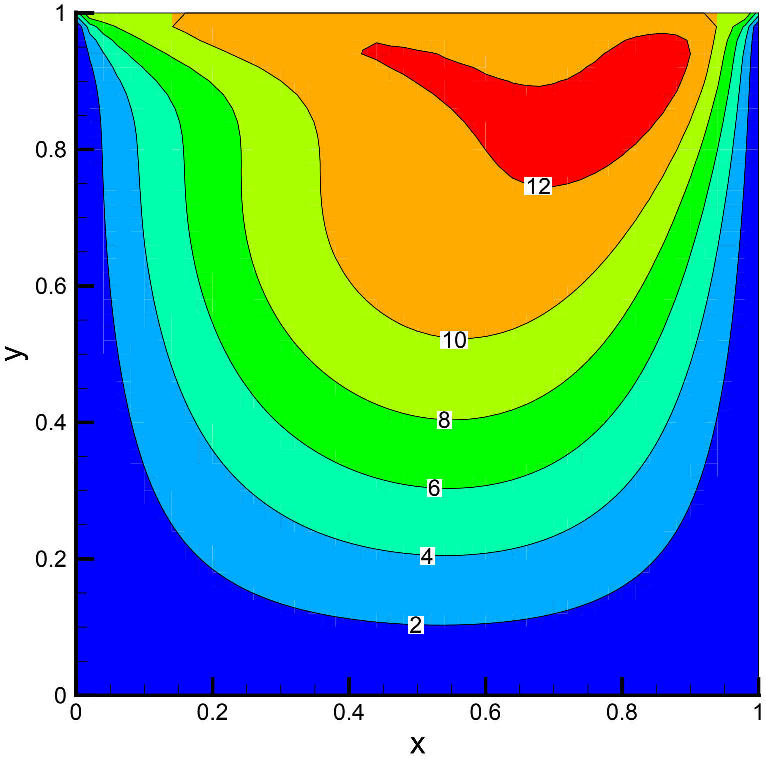

Figure 4.63. The temperature field with the parameters; Re $= 10$, We $= 0.4$, $\beta = 0.5$, $\alpha = 0.1$, Pr $= 10$, Br $= 10$ and $\alpha_s = 0.015$

these figures that the maximum temperature within the flow field is decreased by the increased elasticity of the fluid.

Finally, the maximum Weissenberg number limits for the isothermal and non-isothermal flows of viscoelastic LDC are given with the Table 4.6. The test problem for this table has the parameters of $\beta = 0.5$, $\alpha = 0.1$, Pr $= 10$, Br $= 10$ and $\alpha_s = 0.01$. It can be understood that solving the non-isothermal problem is more difficult. This is generally due to the enhancing of the non-linearity. For example, solving a non-isothermal problem is possible by designating an additional non-linearity arising from the energy equation and this non-linearity can overlap with the ones related to the viscoelasticity.

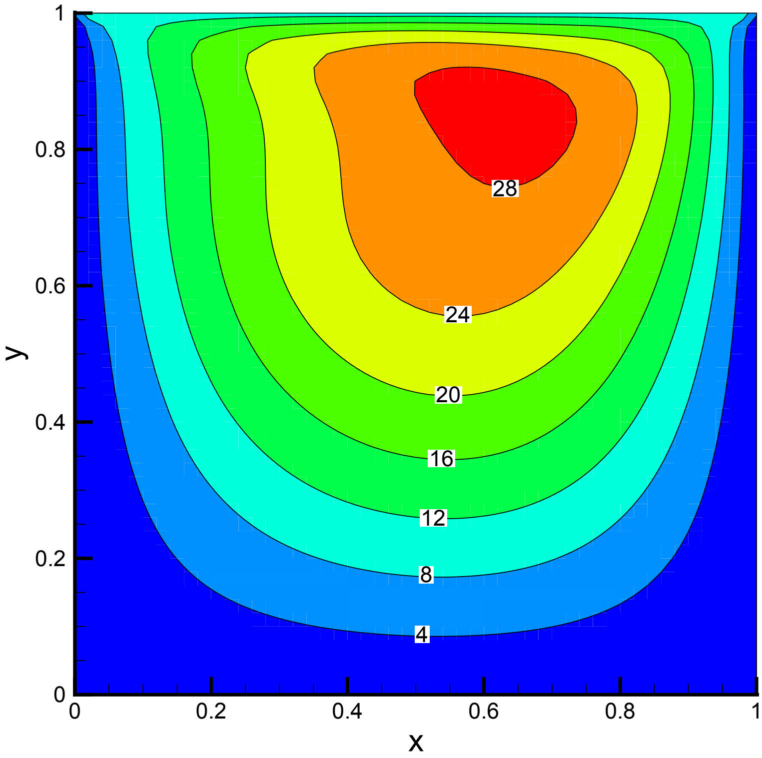

Figure 4.64. The temperature field with the parameters; Re = 10, Pr = 10, Br = 10, We = 0.0, $\beta = 0.5$, $\alpha = 0.1$, and $\alpha_s = 0.01$

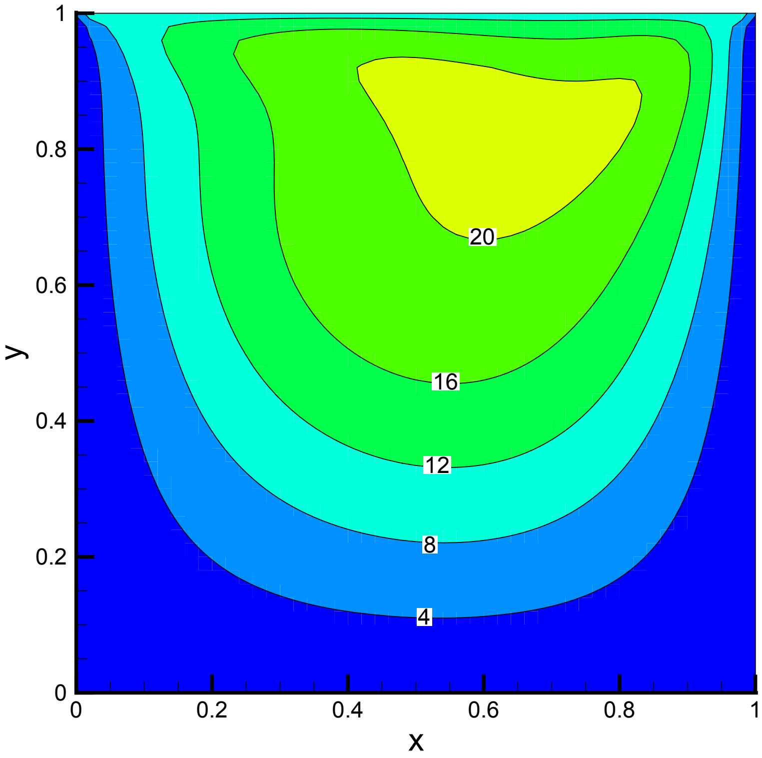

Figure 4.65. The temperature field with the parameters; Re = 10, Pr = 10, Br = 10, We = 0.2, $\beta = 0.5$, $\alpha = 0.1$, and $\alpha_s = 0.01$

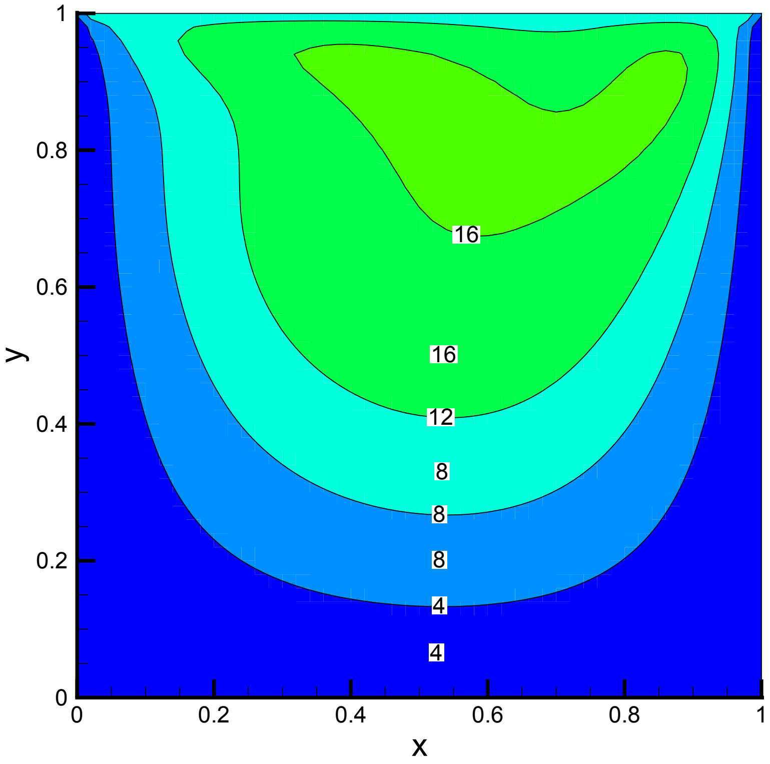

Figure 4.66. The temperature field with the parameters; Re = 10, Pr = 10, Br = 10, We = 0.4, $\beta = 0.5$, $\alpha = 0.1$, and $\alpha_s = 0.01$

Table 4.6. Comparison of maximum Weissenberg numbers of isothermal and non-isothermal LDC flows

	Isothermal	Non-isothermal
Re=0	0.436	0.429
Re=10	0.453	0.436
Re=100	0.448	0.437

4.2. Rotating Disc in a Cylindrical Enclosure

The simulations concerning the RDCE problem will be revealed in this section of the study. Similar to the LDC, the validation of the results will be the first part of this section where the boundary conditions are tested against the POLYFLOW simulations and the literature. The material parameters used in the following parts of this study are selected using the insight obtained from the simulations of the viscoelastic LDC problem. There are three main sections in this part of the study; the Newtonian RDCE subsection, the non-Newtonian RDCE subsection and the non-isothermal and the non-Newtonian RDCE subsection. The Newtonian modeling subsection covers the results obtained by PETSc simulations. In that part, the effects of the Reynolds number and the aspect ratio is investigated. Moreover, the performance of the linear solver, the performance of the preconditioning and the speedup are studied. The non-Newtonian effects for the RDCE are studied in Section 4.2.3 where this section is divided into three parts which are the applications of different constitutive models. Finally, the effects of the Weissenberg number, the Prandtl number, the Brinkman number and the temperature sensitive coefficient will be revealed in the non-isothermal and non-Newtonian flow simulation section.

4.2.1. Validation

Using the knowledge by studying the LDC, the boundary conditions for stream function, vorticity and circulation are selected as explained in the Subsection 2.1.4.2. The boundary conditions for the non-Newtonian parts of the stresses are used similar to the studies of Kawabata *et al.* [34], Moroi *et al.* [15, 16] and Itoh *et al.* [17]. Since the upwinding is effective when the Reynolds number is high (convective terms are dominant) and the non-Newtonian flow is generally a low Reynolds number phenomenon, it is disregarded.

4.2.1.1. Mesh convergence analysis. As mentioned earlier, the first step of a numerical study should be the mesh convergence analysis. In order to determine the necessary number of the grid, three different sets; 31x31, 41x41, 51x51 and 61x61 are used where the first multiplier is the number of grids in the r direction and the second multiplier is the number of grids in the z direction. The comparison is carried out for a fixed problem with the parameters of; Re = 5, We = 2, $\delta = 1.0$, $\beta = 0.5$ and $\alpha = 0.1$. As can be understood from these parameters, the Giesekus constitutive relation is utilized for the test problem.

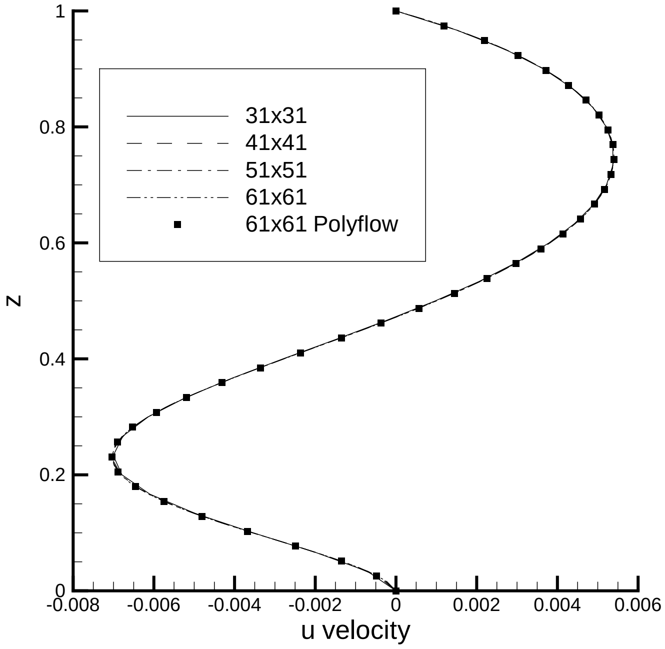

Figure 4.67. u velocity component through the vertical centerline for Re = 5, We = 2, $\delta = 1.0$ and Giesekus constitutive relation with the parameters; $\beta = 0.5$ and $\alpha = 0.1$

Figures 4.67, 4.68 and 4.69 reveal that the results are comparable for all grid sets. The main reason for achieving this accuracy is using the fourth order discretization in the interior points of the domain. The discrepancies between the plots of the different grid sets are higher near the inflection points. It can be clearly observed from the Figure 4.69 that the grid sets of the 51x51 and the 61x61 are both appropriate. Since increasing the number of the mesh brings computational cost, the grid set of 51x51 is selected for the analyses.

Similar to the $\delta = 1.0$ case, Mesh convergence analyses are performed for the aspect ratios of $\delta = 0.25$, $\delta = 0.5$, $\delta = 1.5$ and $\delta = 2$. Consequently, the appropriate

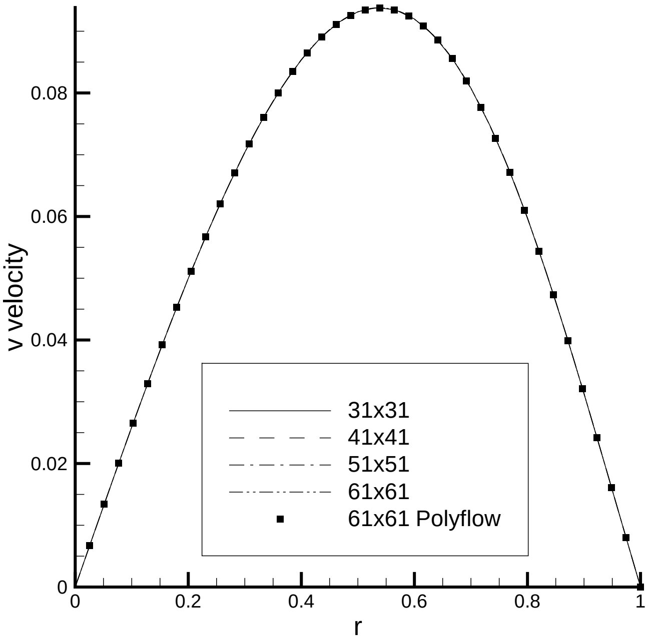

Figure 4.68. v velocity component through the horizontal centerline for Re = 5, We = 2, $\delta = 1.0$ and Giesekus constitutive relation with the parameters; $\beta = 0.5$ and $\alpha = 0.1$

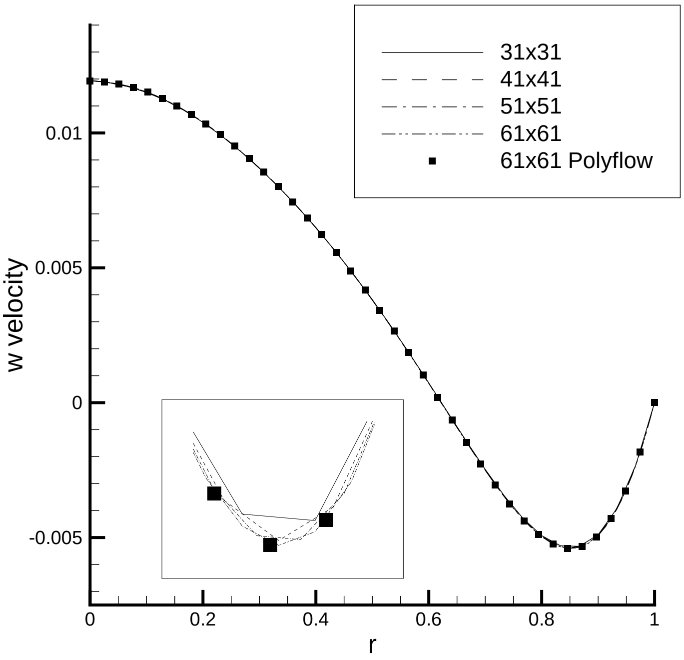

Figure 4.69. w velocity component through the horizontal centerline for Re = 5, We = 2, $\delta = 1.0$ and Giesekus constitutive relation with the parameters; $\beta = 0.5$ and $\alpha = 0.1$

grid numbers for these aspect ratios are selected as 81x21, 51x26, 41x61 and 41x81 respectively.

It is also apparent from the Figures 4.67, 4.68 and 4.69 that the boundary conditions are convenient and the use of no-upwinding is suitable as predicted.

4.2.1.2. Comparison with the POLYFLOW and literature. Unlike LDC, there are some experimental results for the RDCE in the literature. For example, Xue *et al.* [22] investigated the flow structures using Boger fluids for enclosures with $\delta = 1.0$ and $\delta = 2$. For $\delta = 1.0$ case, they obtained streamlines for the Weissenberg numbers of 0.006, 0.013, 0.02 and 0.05. Additionally, Xue *et al.* studied the reversing of the flow which is the result of the balance between the elastic and inertial forces. For a Newtonian fluid, the secondary flow in the r-z plane rotates radially outward from the disk. This is because of the outward centrifugal force applied by the disk. If the fluid inside the container is replaced with a non-Newtonian one, the flow structure changes. The increase in the elasticity of the fluid, in our case Weissenberg number, generates growing normal stresses. After some certain point of elasticity, these stresses counterbalance the outward centrifugal force and reverse the flow field. This reversing process starts from a corner of the flow domain and covers the whole area with the increasing elasticity. This phenomenon can be seen from the Figures 4.70, 4.71, 4.72, 4.73 and 4.74. The Figure 4.70 shows the Newtonian flow for Re = 0.32 and $\delta = 1.0$ case. In this figure the flow is rotating outward from the disk which can be easily understood from the velocity plot given in Figure 4.70(c). Moreover, the direction of the rotation can also be seen from the positive values of stream function.

In the right bottom corner of the Figure 4.71(a) the reversed flow spot appears with a blue core and negative stream function values. Since the elasticity of the fluid is not high, most of the fluid particles are still under the influence of the outward centrifugal force and they are rotating in the direction of the Newtonian flow with the positive stream function values.

Figures 4.72, 4.73 and 4.74 show that the reversed flow grows into the whole flow domain with the increasing elasticity effect (Weissenberg number in our case). Finally, the direction of the flow field is totally reversed with the Weissenberg number of 0.05 (Figure 4.74).

It can also be understood from the figures in this section that the results obtained by using the IN-GMRES solver of this study are in good agreement with the data in the literature and the POLYFLOW simulations.

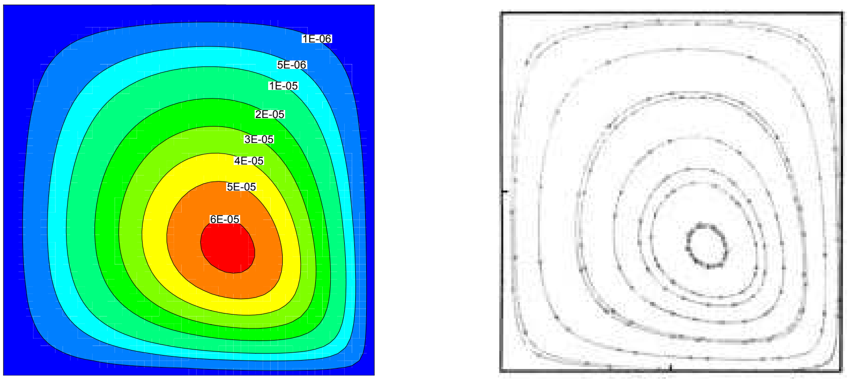

(a) Streamlines computed in this study

(b) Streamlines computed in Xue *et al.* [22]

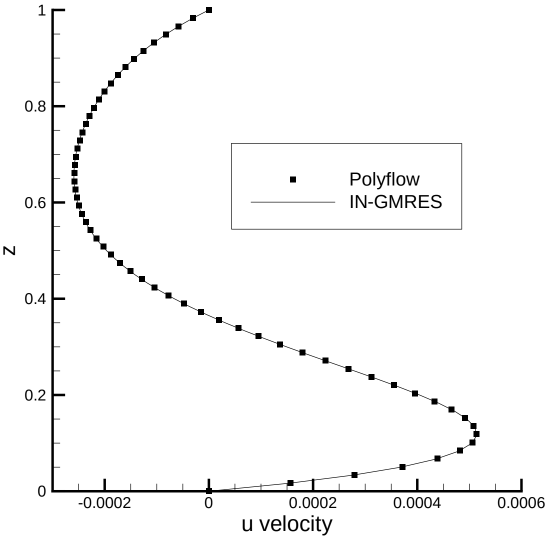

(c) u velocity component through the vertical centerline

Figure 4.70. Comparison of the Newtonian flow with the parameters of Re = 0.32 and $\delta = 1.0$

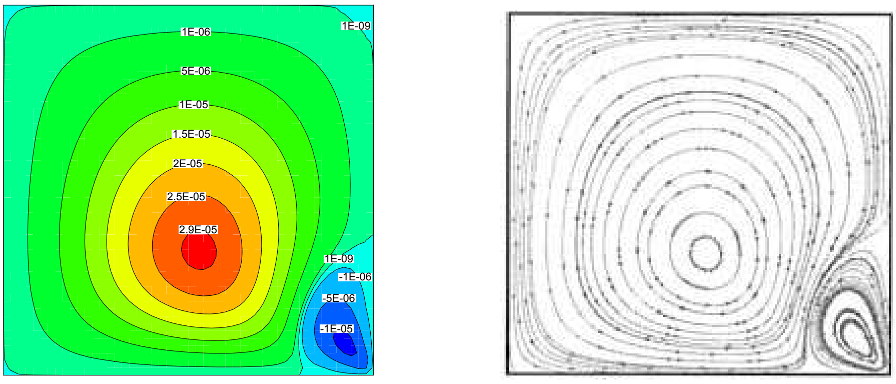

(a) Streamlines computed in this study

(b) Streamlines computed in Xue *et al.* [22]

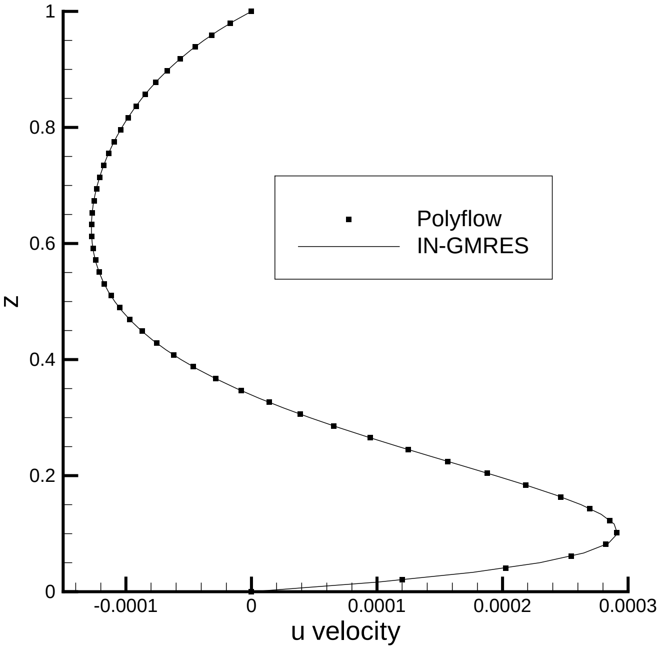

(c) u velocity component through the vertical centerline

Figure 4.71. Comparison of the UCM flow with the parameters of Re = 0.32, We = 0.006 and $\delta = 1.0$

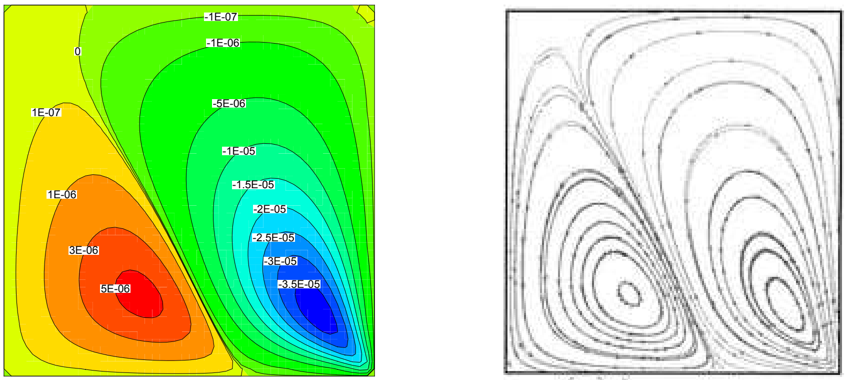

(a) Streamlines computed in this study

(b) Streamlines computed in Xue *et al.* [22]

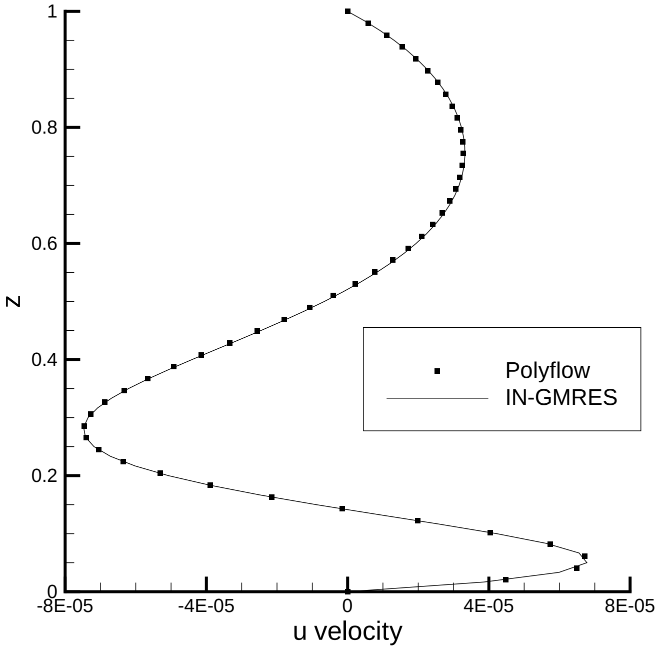

(c) u velocity component through the vertical centerline

Figure 4.72. Comparison of the UCM flow with the parameters of $\mathrm{Re} = 0.32$, $\mathrm{We} = 0.013$ and $\delta = 1.0$

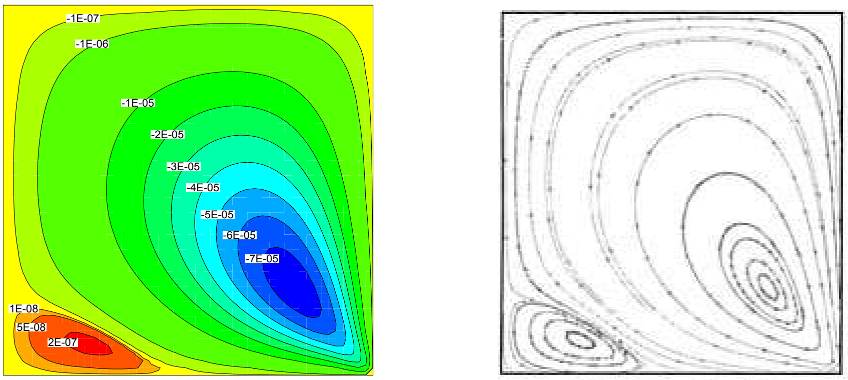

(a) Streamlines computed in this study

(b) Streamlines computed in Xue *et al.* [22]

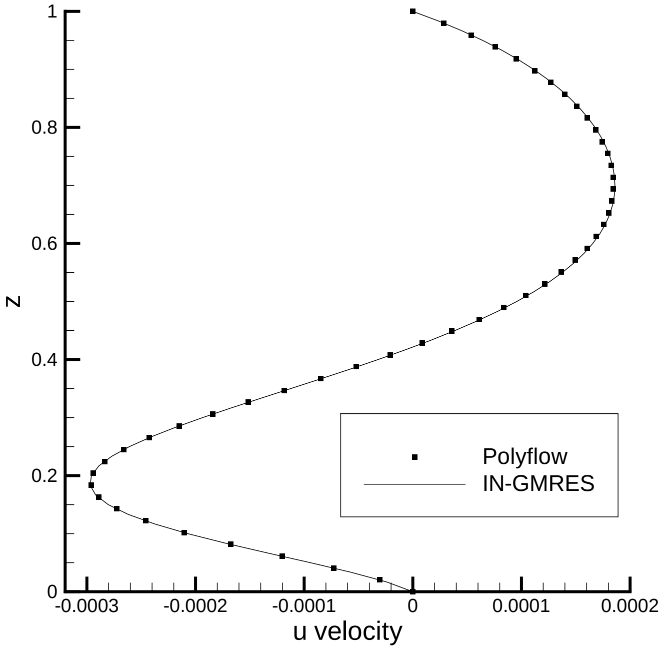

(c) u velocity component through the vertical centerline

Figure 4.73. Comparison of the UCM flow with the parameters of Re = 0.32, We = 0.02 and $\delta = 1.0$

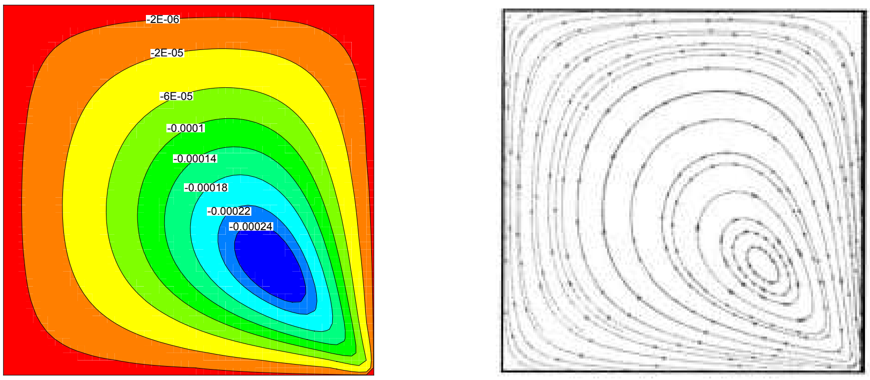

(a) Streamlines computed in this study

(b) Streamlines computed in Xue *et al.* [22]

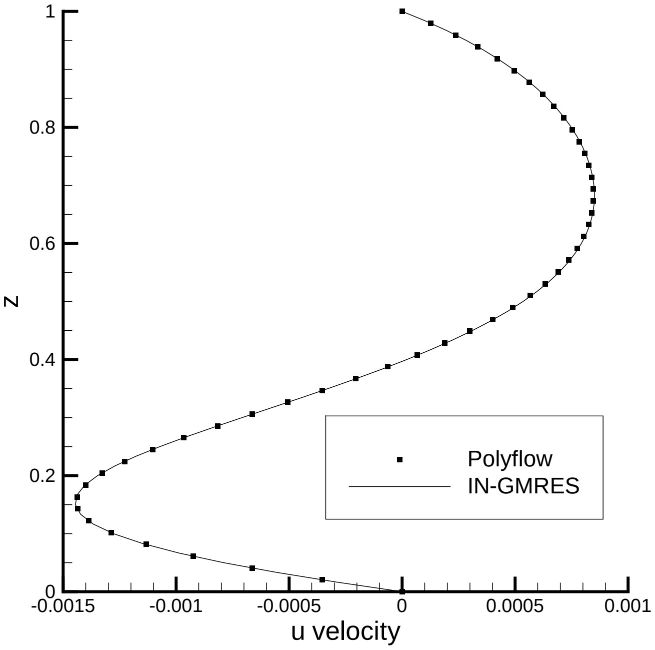

(c) u velocity component through the vertical centerline

Figure 4.74. Comparison of the UCM flow with the parameters of Re = 0.32, We = 0.05 and $\delta = 1.0$

4.2.2. Newtonian Model

Similar to the Newtonian part of the LDC, the Newtonian flow simulations for the RDCE are realized by using PETSc, which is a computational tool for the parallel solution of scientific problems. In this subsection, the linear solvers, preconditioning techniques and number of processors are tested for the performance by keeping the Inexact Newton method as the non-linear solver. What is more, in addition to the computational parameters the effects of some physical parameters such as the Reynolds number, the aspect ratio and altering of the rotating surface are investigated. Recently, the results acquired in this part of the study are published in the JMECH C journal (Proceedings of the Institution of Mechanical Engineers, Part C, Journal of Mechanical Engineering Science) with the title of "Computational Parametric Analysis of Rotating Surface Flow" (Kaptan *et al.* [14]).

4.2.2.1. Validation. Before proceeding with the PETSc solver, the validation with the literature is carried out for the PETSc code. This is achieved by benefiting from the problem in the study of Pao [10]. He used rotating edge boundary conditions for the top disc and the container where the bottom disc is held stationary. The defining parameters of the problem are; Re $= 100$ and $\delta = 1.0$. Figures 4.75, 4.76 and 4.77 reveal the stream function, vorticity and circulation contours for this problem. These figures are generated from the results of the PETSc solver and they are in good agreement with the study of Pao [10]. Moreover, the minimum value of the stream function in the study of Pao is -0.0121 whereas the value of -0.011998 is computed in this thesis.

4.2.2.2. Performance of the Linear Solvers. For the test of performance, everything but the linear solver of the problem is fixed. For the test problem, the bottom disc and the cylindrical enclosure are rotated where top disc is held stationary. The 161x161 grid is used where Re $= 100$, $\delta = 1.0$ and the linear tolerance is $1E-5$. In order to determine the performance of the linear solvers, the line search Newton method with backtracing is preferred for linearization and ILU(5) preconditioning is used to enhance the convergence behavior.

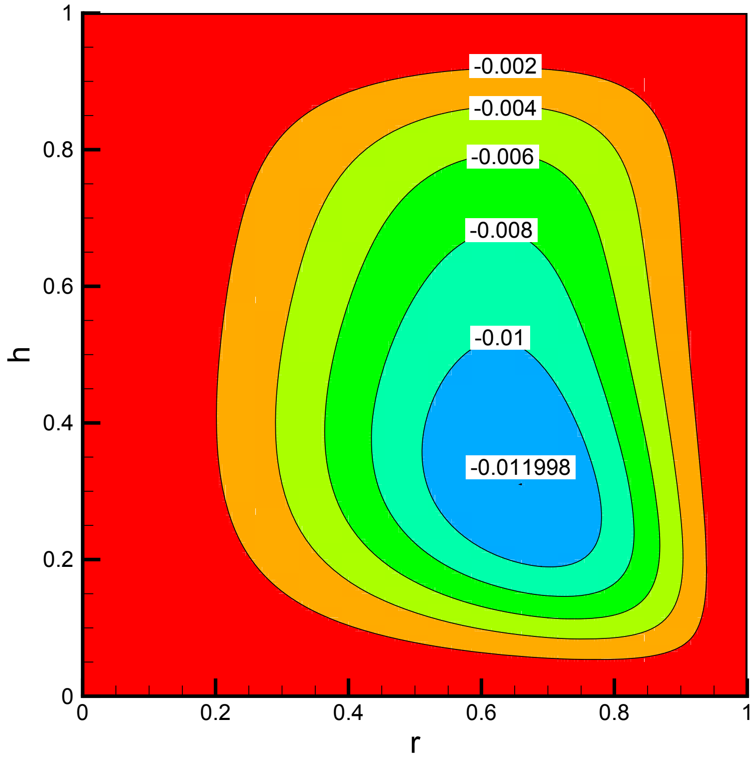

Figure 4.75. Stream function contours for Re = 100 and $\delta = 1.0$

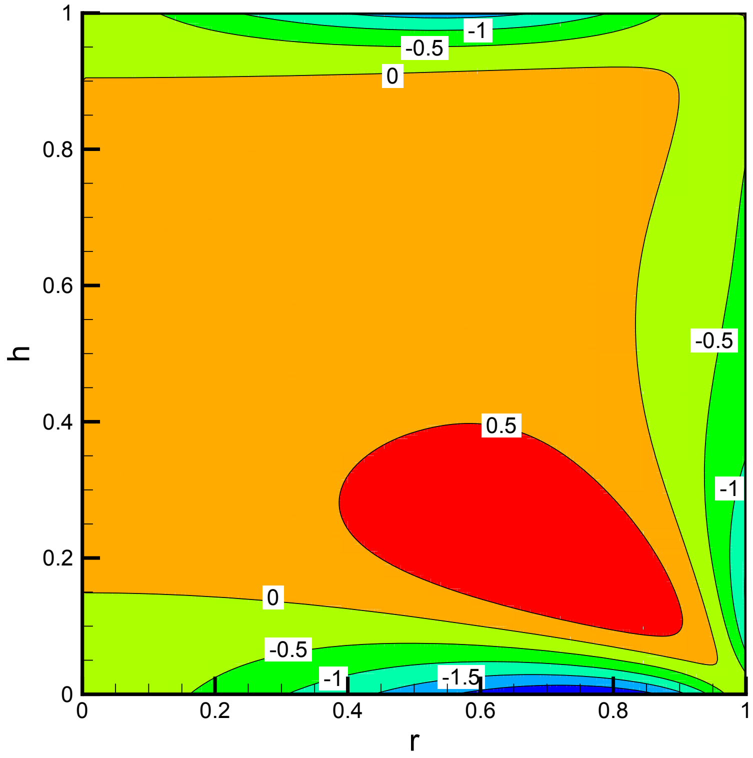

Figure 4.76. Vorticity contours for Re = 100 and $\delta = 1.0$

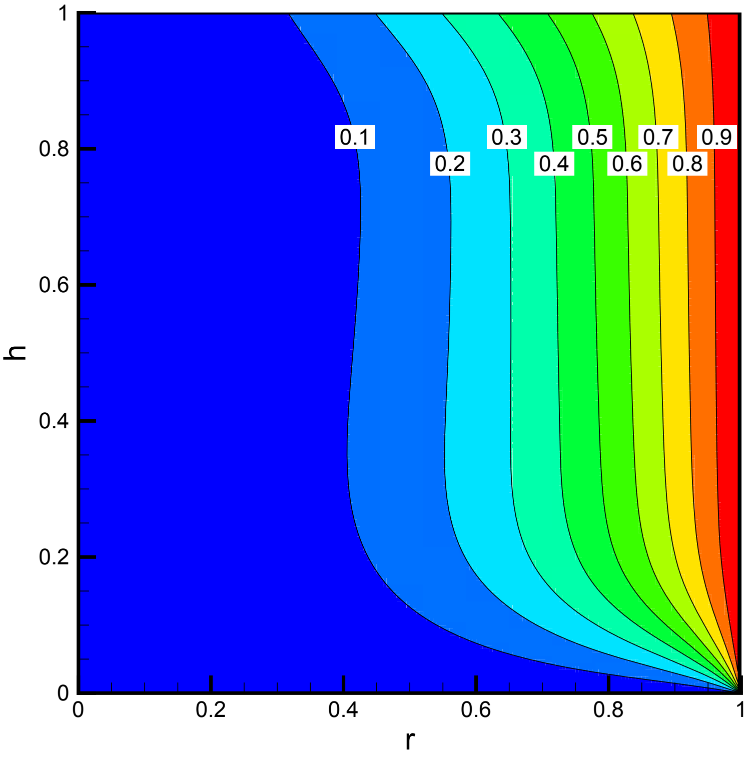

Figure 4.77. Circulation contours for Re $=$ 100 and $\delta = 1.0$

Figure 4.78 shows the required number of linear iterations for different Krylov solvers at the first Newton steps. As can be seen, the best converging method is Bi-Conjugate Gradient Stabilized (BiCSStab) with 31 iterations, where Transpose free Quasi Minimal Residual (TFQMR) performs poorly and converges in 52 iterations. Generalized Minimal Residual method (GMRES) with restart 50 (GMRES(50)) converges faster than GMRES(30) where the iteration numbers are 45 and 59 respectively. This is mainly due to the vector storing property of the GMRES as mentioned earlier. The method generates a sequence of orthogonal vectors, in Krylov subspace of K-independent basis vectors as $v_1 \perp v_2 \perp v_3 ... \perp v_k$. The generation of v_k requires all $v_{k-}1$ vectors. However, the need for storage and the computational cost increase with the additional orthogonalization. To overcome this drawback, storing only (m) of these vectors and restarting with the iterate x(m) as the initial guess are utilized. In this application, restarting is necessary until the convergence is satisfied. On the other hand, storing more vectors decreases the required number of linear iterations. Our case studies revealed that GMRES(30) converges faster than GMRES(50) in terms of computation time although it performs more linear iterations. As can be seen from the Figure 4.78, GMRES(30) and GMRES(50) generate exactly the same linear residual up to 30. Then GMRES(30) restarts and has less information about the previous steps, so it converges in 14 more linear iterations than GMRES(50). Moreover, another important aspect of GMRES(m) is its non-increasing residual property. The linear residuals for TFQMR and BiCGStab can fluctuate but the residual in GMRES is always non-increasing.

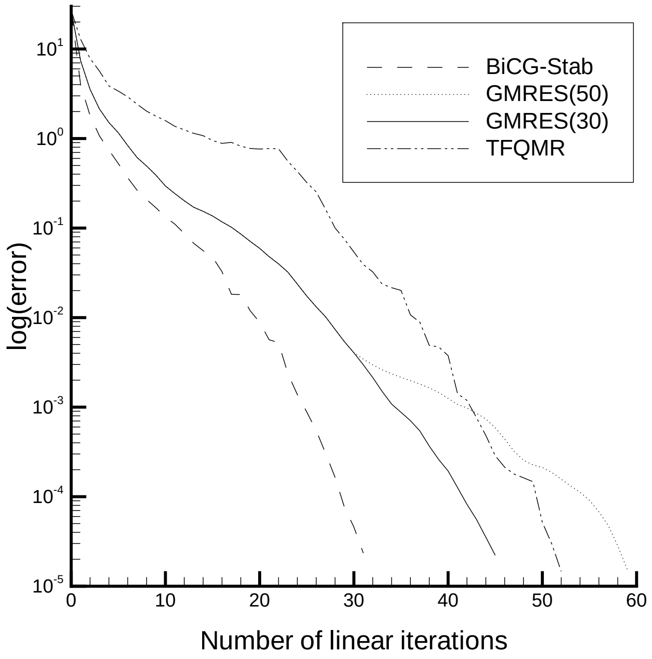

Figure 4.78. Linear solver performances

<u>4.2.2.3. Performance of the Preconditioners.</u> The convergence rate of iterative methods depends on the spectral properties (eigenvalues) of the coefficient matrix. So converting our problem to another with the same solution but favorable spectral properties so that it can converge faster is called preconditioning. In this part of the study, the test problem used in the Section 4.2.2.2 is utilized by adopting the GMRES(30) as the linear solver. As can be seen from the Figure 4.79 the Incomplete LU decomposition with fill in m (ILU(m)) type preconditioners are superior to the other techniques. The no-preconditioning case is not shown in the figure, because it failed to converge. The simplest preconditioning technique Jacobi makes the problem solvable, but it takes

596 iterations to converge. SOR preconditioning is better than Jacobi; however both of these preconditioners can not compete with ILU(m) type preconditioners. With the increasing numbers of fill-in, ILU(m) becomes faster up to ILU(5) by means of both linear iteration number and computation time. Starting with ILU(6), generation of the preconditioner matrix takes too much time in such a way that the overall efficiency of the code starts to decrease and the preconditioning becomes less useful.

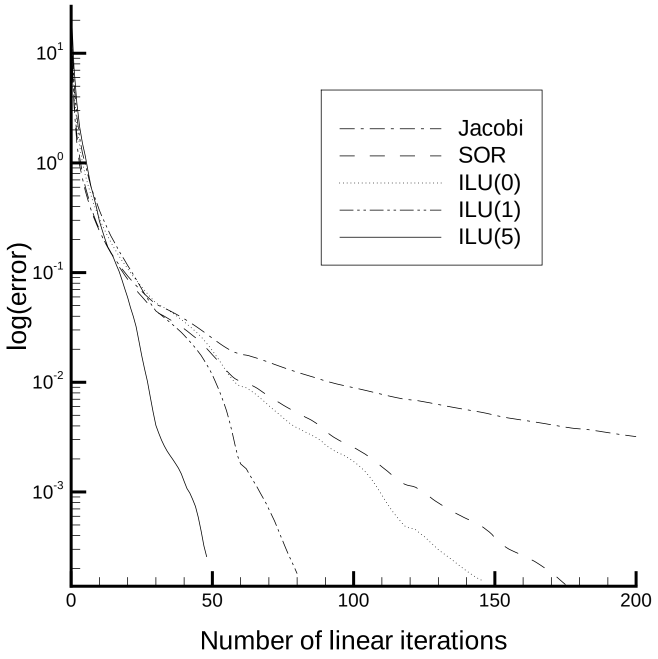

Figure 4.79. Preconditioning performances

4.2.2.4. Effects of Reynolds Number and Aspect Ratio. In this part of the study, the effects of the Reynolds number and the geometry are examined. To investigate these effects the computations for the aspect ratios of $\delta = 0.5$, $\delta = 1.0$ and $\delta = 1.5$ are performed for the Reynolds numbers of Re = 100, Re = 1000 and Re = 2000. Since the main problem of this thesis is to investigate the non-Newtonian flow phenomenon, the plots are reduced. The model problem for this section has a rotating bottom and side edges while the top disc is held stationary. The grid spacing is 0.01 for all of the aspect ratios simulated.

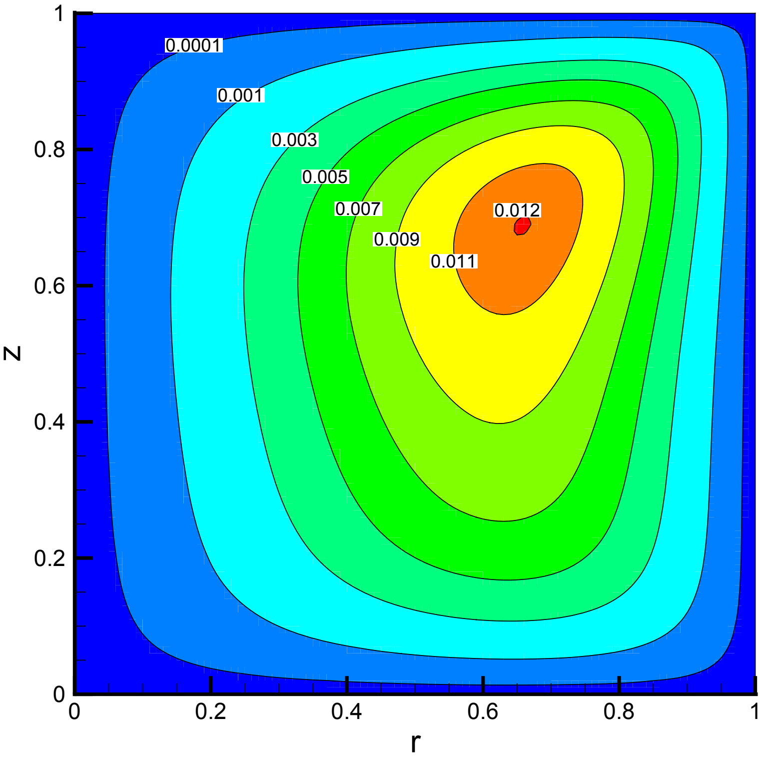

Figure 4.80. Stream function contours for $\delta = 1.0$ and $\mathrm{Re} = 100$

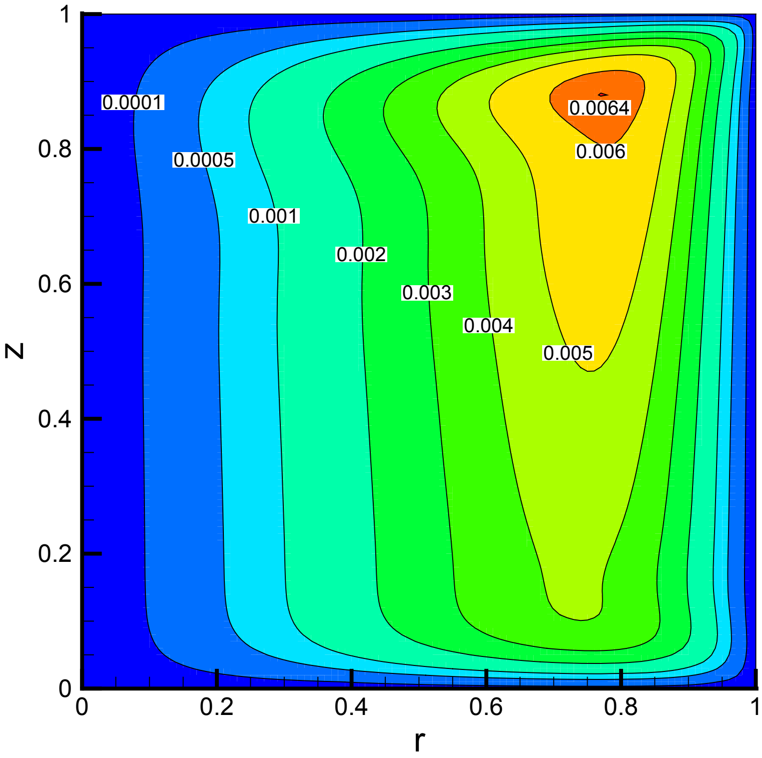

Figure 4.81. Stream function contours for $\delta = 1.0$ and $\mathrm{Re} = 1000$

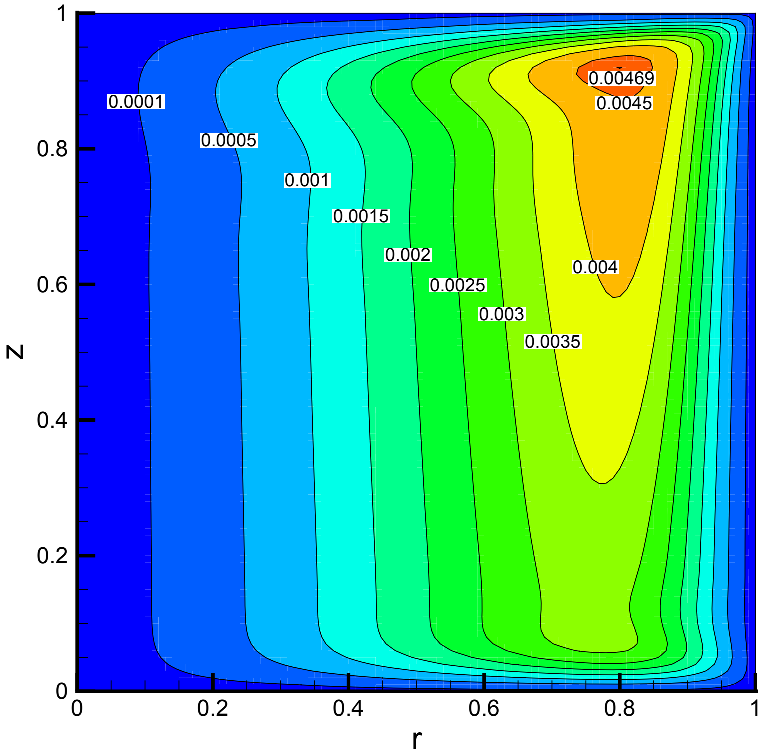

Figure 4.82. Stream function contours for $\delta = 1.0$ and Re = 2000

Figure 4.80, 4.81 and 4.82 show the stream function plots for $\delta = 1.0$ case. Since the stream function contours coincide with the secondary rotations for this geometry, these figures reveal the circulation appearing in the $r - z$ plane. It can be grasped from these figures that the change in the Reynolds number affects the shape and the position of this circulation. When the Reynolds number is small, the core of the rotating region is placed near the center of the computational domain. With the increasing Reynolds numbers this core moves towards the stationary boundaries. This effect can also be seen by comparing the Figure 4.83 with 4.84 and Figure 4.85 with 4.86.

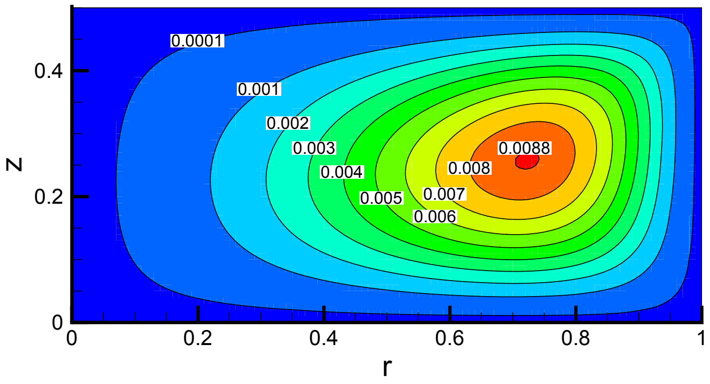

Figure 4.83. Stream function contours for $\delta = 0.5$ and Re = 100

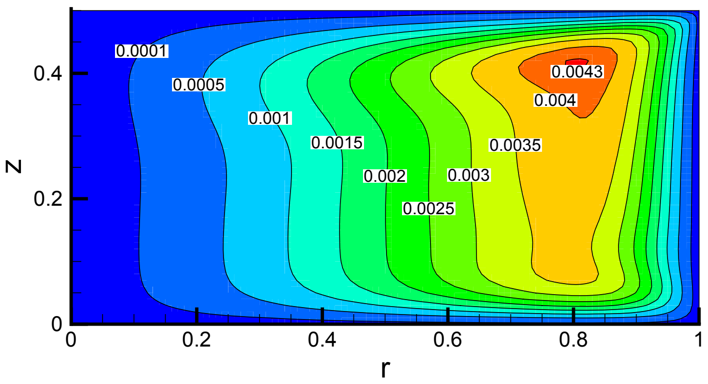

Figure 4.84. Stream function contours for $\delta = 0.5$ and $\mathrm{Re} = 2000$

Although the velocity contours are not given, it can be seen from those figures that the maximum velocity is increasing with the rising Reynolds numbers as expected. The velocity plots also point out that the decreasing aspect ratio lowers the maximum velocities for constant Reynolds numbers. The main reason for this is the effect of the stationary wall. Decreasing the height makes the diffusion harder and lowers the maximum velocities. More information about these effects can be found in the study of Kaptan et.al. [14].

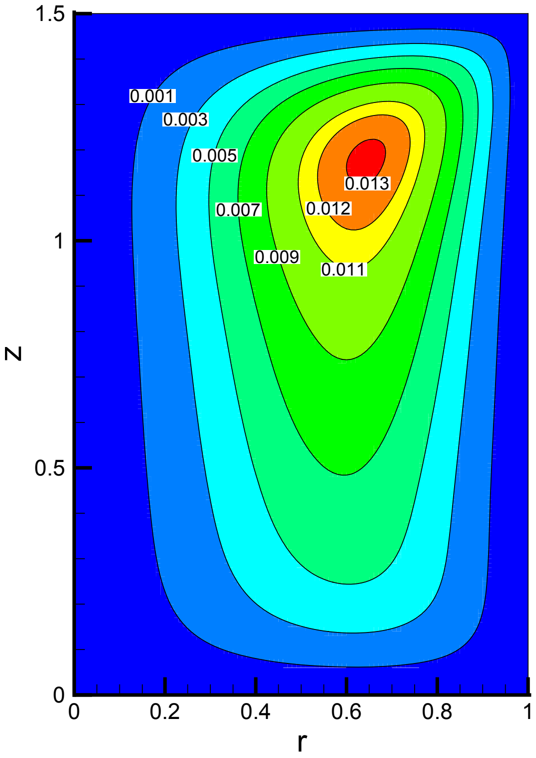

Figure 4.85. Stream function contours for $\delta = 1.5$ and $\mathrm{Re} = 100$

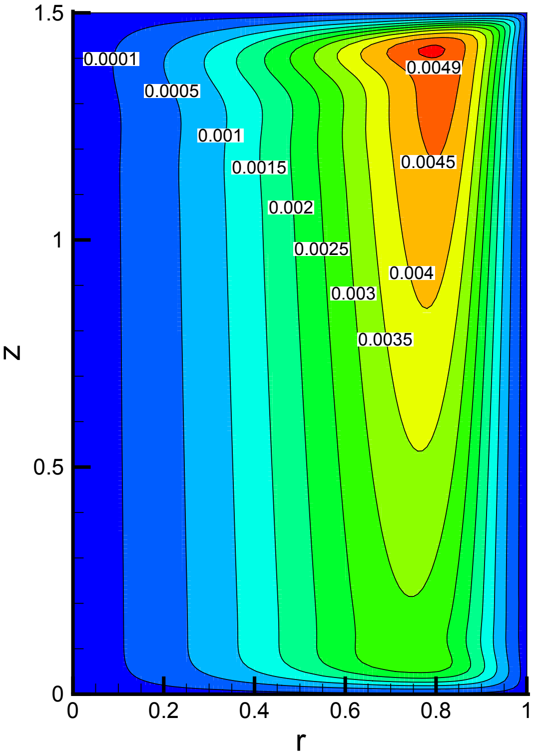

Figure 4.86. Stream function contours for $\delta = 1.5$ and $\mathrm{Re} = 2000$

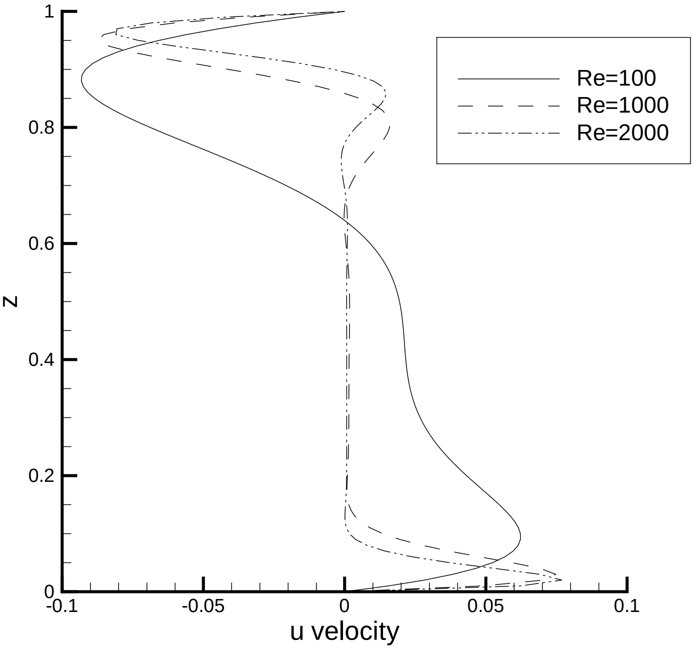

Figure 4.87. u velocity component through the vertical centerline $\delta = 1.0$ geometry

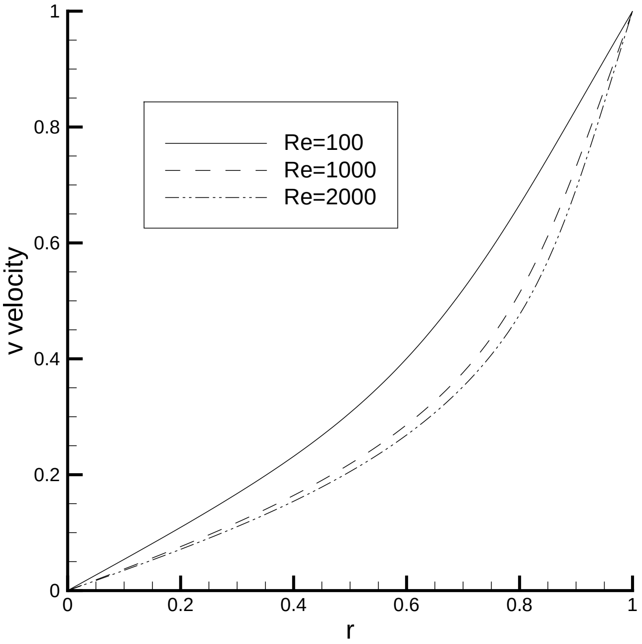

Figure 4.88. v velocity component through the horizontal centerline of $\delta = 1.0$ geometry

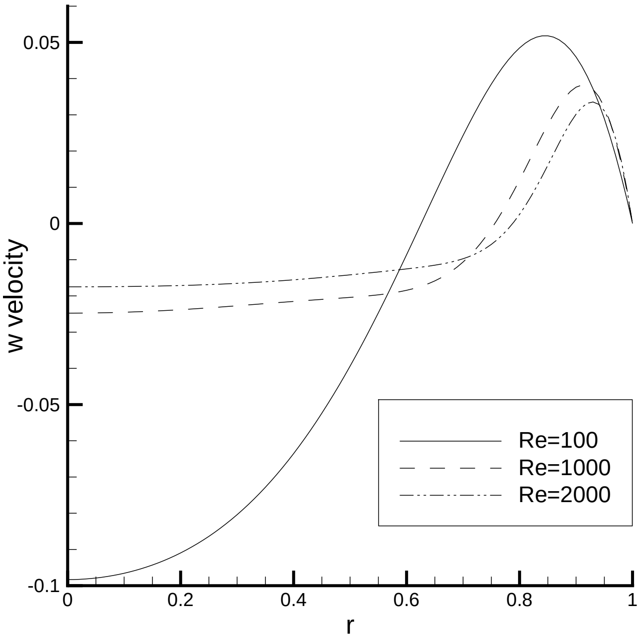

Figure 4.89. w velocity component through the horizontal centerline of $\delta = 1.0$ geometry

Figures 4.87, 4.88 and 4.89 show the velocity versus coordinate plots for $\delta = 1.0$ case. The examination of Figure 4.87 clarifies that the change in the u velocity near the top and the bottom walls occurs rapidly with the increasing Reynolds number. In other words, since the boundary layers at the top and bottom walls are mainly functions of u velocity, the boundary layer thicknesses become smaller when the Reynolds number is high. The similar occurrences can also be observed in the Figure 4.89 (the boundary layers are dependent on w component of the velocity).

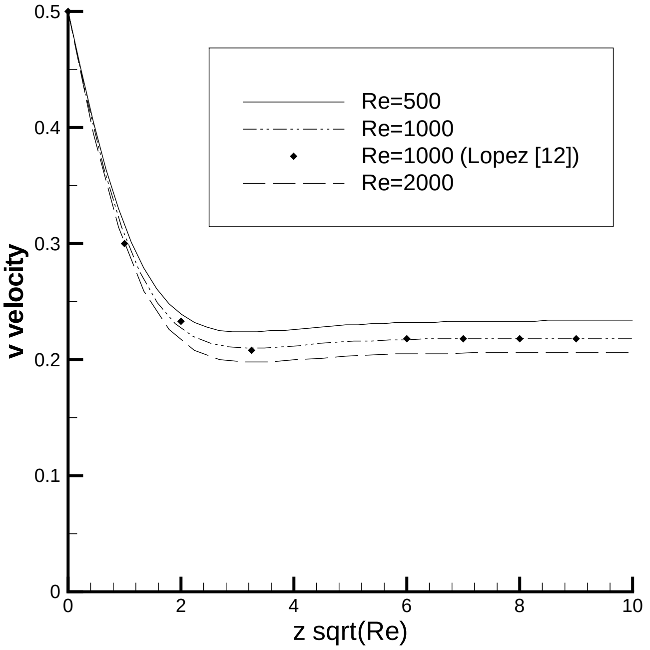

Figure 4.90. Boundary layer profile at the bottom rotating wall for v velocity at $r = 0.5$ for various Reynolds number and $\delta = 1.0$

Figures 4.90 and 4.91 show the boundary layer profiles of the v velocity and comparison of the results with the study of Lopez [12]. It is obvious from these figures that the boundary layer thicknesses are scaling with the square root of the Reynolds number as mentioned by Lopez and the results are comparable. These figures also revealed that the increase in the Reynolds number makes boundary layers thinner as explained before.

Figures 4.92 through 4.95 show the boundary layer profiles of the v velocity for $\delta = 0.5$ and $\delta = 1.5$ cases. When Figures 4.90 and 4.91 are compared with the

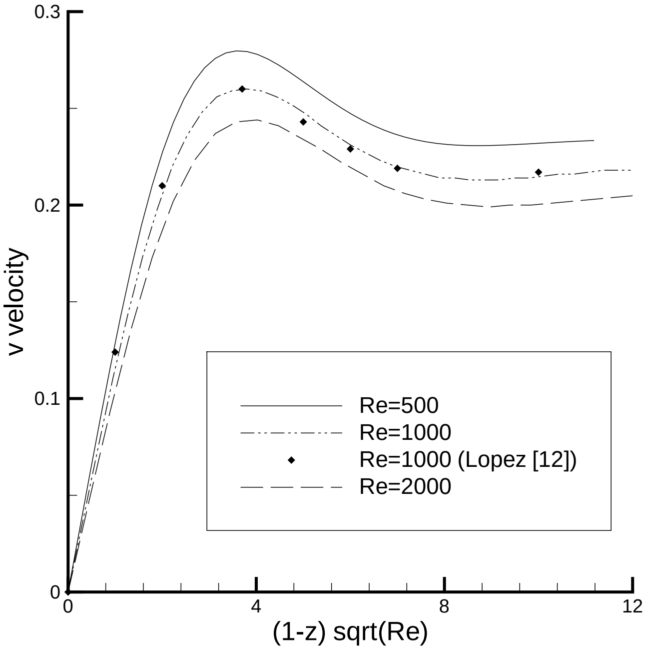

Figure 4.91. Boundary layer profile at the top stationary wall for v velocity at $r = 0.5$ for various Reynolds number and $\delta = 1.0$

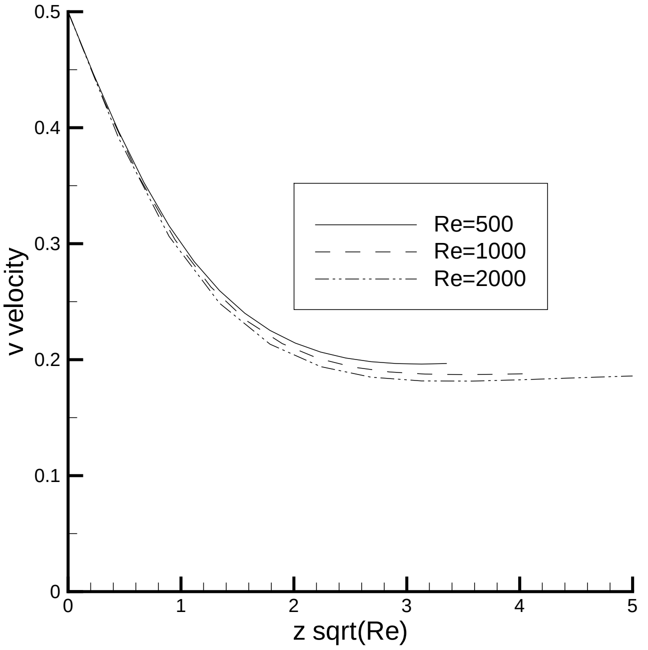

Figure 4.92. Boundary layer profile at the bottom rotating wall for v velocity at $r = 0.5$ for various Reynolds number and $\delta = 0.5$

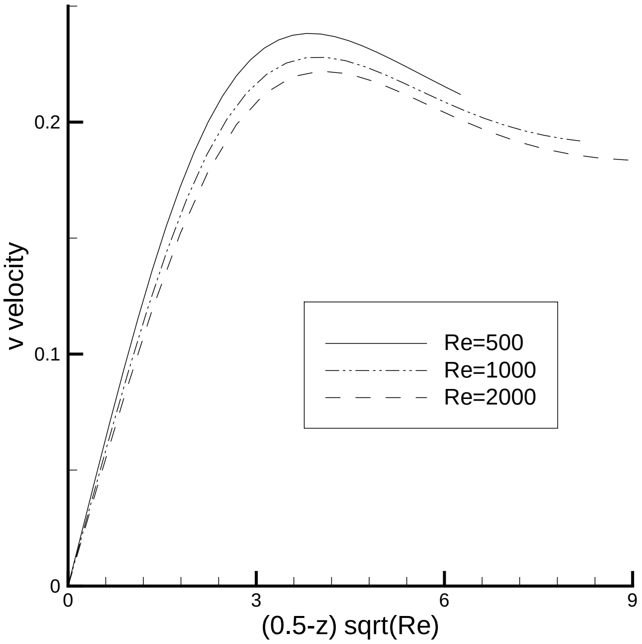

Figure 4.93. Boundary layer profile at the top stationary wall for v velocity at $r = 0.5$ for various Reynolds number and $\delta = 0.5$

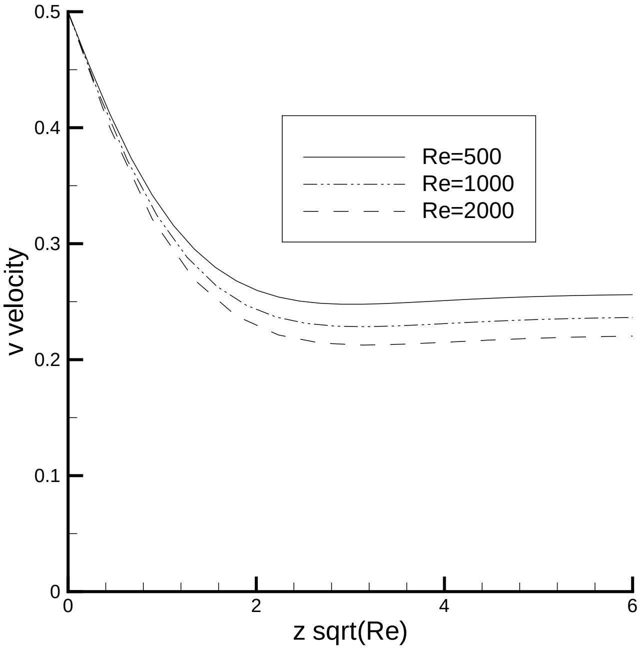

Figure 4.94. Boundary layer profile at the bottom rotating wall for v velocity at $r = 0.5$ for various Reynolds number and $\delta = 1.5$

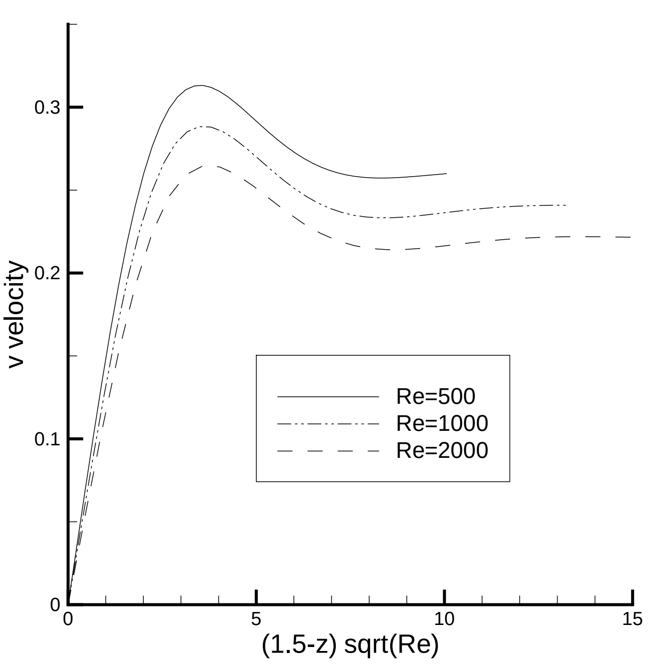

Figure 4.95. Boundary layer profile at the top stationary wall for v velocity at $r = 0.5$ for various Reynolds number and $\delta = 1.5$

Figures 4.92 and 4.93, it can be understood that the thicknesses of the boundary layers are reduced for the $\delta = 0.5$ case because of the effects of walls. As mentioned earlier, decreasing the height makes diffusion harder while it lowers the thickness of the boundary layers. The same conclusions can be attained with the comparison of the Figures 4.90 and 4.91 with Figures 4.94 and 4.95. The shapes of the boundary layers are similar in all of the plots.

4.2.3. Non-Newtonian Models

In this part of the study the non-Newtonian effects are investigated by using three constitutive models; UCM, Oldroyd B and Giesekus. Since the effects for the various Reynolds numbers and aspect ratios are different, the computations should be performed for a wide range of parameters. Table 4.7 shows the comparisons of the Weissenberg number limits between the IN-GMRES solver and the POLYFLOW simulations using the constitutive models of UCM, Oldroyd B and Giesekus for the Reynolds numbers of 0, 1, 5 and 10. The aspect ratio is fixed as $\delta = 0.5$ for the simulations given in this table. The limit of the Reynolds number is appropriate since the non-Newtonian phenomena are generally low Reynolds number occurrences.

Table 4.7. Comparison of the maximum Weissenberg number limits between the IN-GMRES solver and the POLYFLOW simulations

	UCM		Oldroyd B $\beta = 0.5$		Giesekus $\beta = 0.5$, $\alpha = 0.1$	
	IN-GMRES	Polyflow	IN-GMRES	Polyflow	IN-GMRES	Polyflow
Re = 0	1.040	0.19142	2.001	0.27199	56.350	61.800
Re = 1	1.045	0.19142	2.100	0.27198	130.500	92.905
Re = 5	1.061	0.19132	2.151	0.27189	22.130	21.391
Re = 10	0.997	0.19120	2.083	0.27188	11.503	10.174

Table 4.7 reveals that the solver generated in this study is more effective than the steady solver of the POLYFLOW. The maximum Weissenberg number limits of the IN-GMRES are higher than POLYFLOW except the Re = 0 case of the Giesekus model. Similar to the LDC, the Giesekus constitutive relation is proven to be the most useful constitutive relation. In addition to this table, the comparison of the computation times between the IN-GMRES solver and the POLYFLOW is made and the IN-GMRES turned out to be faster than the steady solver of POLYFLOW. For example, the $\delta = 1.0$ case of UCM flow with the parameters; Re = 10, We = 0.2 is solved in 527.32 seconds with the solver of this study where the POLYFLOW solution takes 1027.2 seconds. Figure 4.96 shows the nonlinear convergence plots of the IN-GMRES and POLYFLOW for the first continuation step of the cited problem (We = 0 case). It can also be observed that both solvers have the same convergence behavior but the solver of this study converges more rapidly. Additionally, POLYFLOW needs more continuation steps therefore it requires more computational time.

The similar patterns to the Table 4.7 and Figure 4.96 can be observed for different aspect ratios and Reynolds numbers. However, increasing the node number

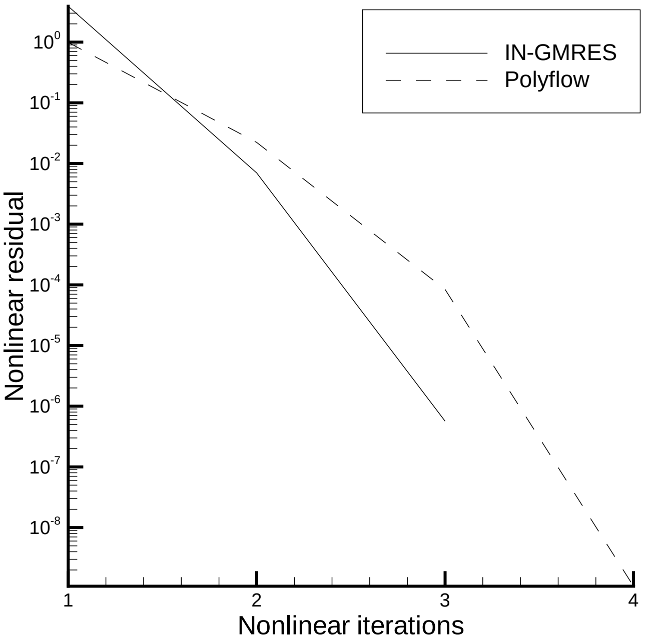

Figure 4.96. Nonlinear residual of the UCM flow with the parameters of Re = 10, We = 0.2 and $\delta = 1.0$

results in computational difficulties since the degree of freedom is ten for a single grid point. To overcome this difficulty, parallelization of the code and better matrix free preconditioners should be applied.

Since the maximum Weissenberg number limit is higher for the Giesekus constitutive relation and it is a more realistic model (it can simulate the shear thinning effect), most of the computations in the following sections are carried out by using this equation. By this means, the realistic flow behavior can be simulated for high Weissenberg numbers.

4.2.3.1. Upper Convected Maxwell Model. The first differential model used in the simulations of RDCE is UCM, which is one of the simplest constitutive relations. The usage of the UCM model is recommended when the information about the fluid is limited. Although the formulation of the UCM model is simple, the numerical computations using this model are difficult in terms of convergence rate and the maximum

Weissenberg number limit. Table 4.7 reveals that the maximum Weissenberg number limit of UCM model is nearly one. This limit is averagely 5.5 times larger than POLYFLOW which proves the capability of the IN-GMRES solver.

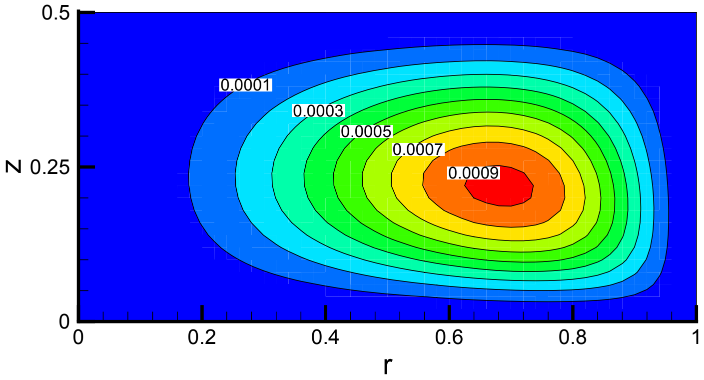

Figure 4.97. Stream function contours for the $\delta = 0.5$ case of UCM flow with the parameters of Re = 10, We = 0.0

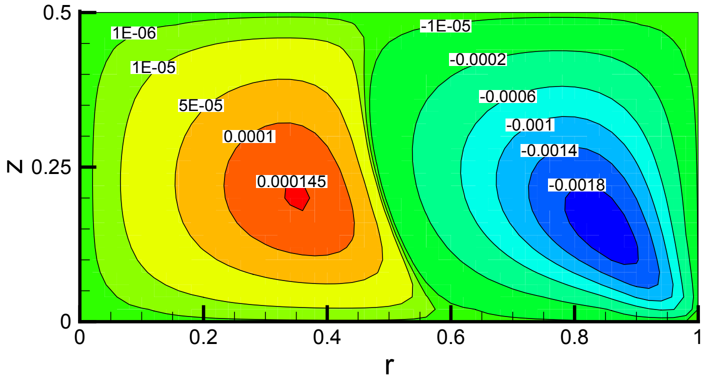

Figure 4.98. Stream function contours for the $\delta = 0.5$ case of UCM flow with the parameters of Re = 10, We = 0.5

Figures 4.97, 4.98 and 4.99 reveal the stream function contours for the Weissenberg numbers of 0, 0.5 and 0.997 respectively. These three figures also demonstrate the reversing of the flow induced by the dominance of the non-Newtonian stresses over the outward centrifugal force. The first one of these figures reveals the Newtonian flow field where the fluid is rotating counterclockwise. With the increasing elasticity of the fluid (Weissenberg number in our case), there appears a reversed rotating spot at the right bottom corner of the flow domain. The reversed spot grows into the whole flow domain with the increasing elasticity.

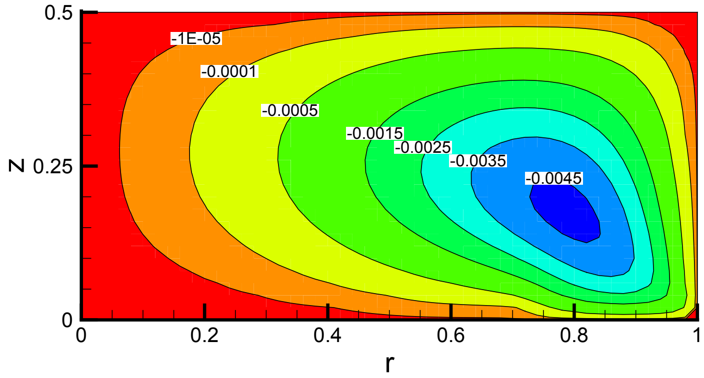

Figure 4.99. Stream function contours for the $\delta = 0.5$ case of UCM flow with the parameters of Re = 10, We = 0.997

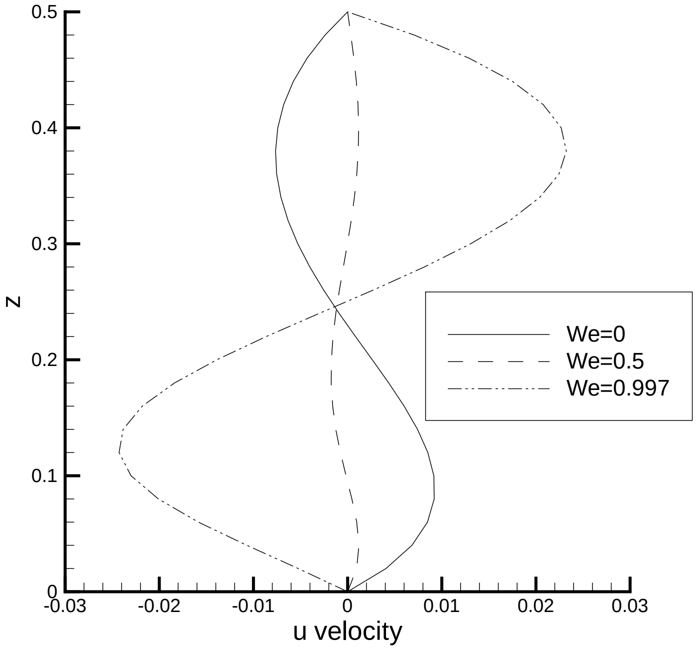

Figure 4.100. u velocity component through the vertical centerline for the UCM flow with the parameters $\delta = 0.5$, Re = 10

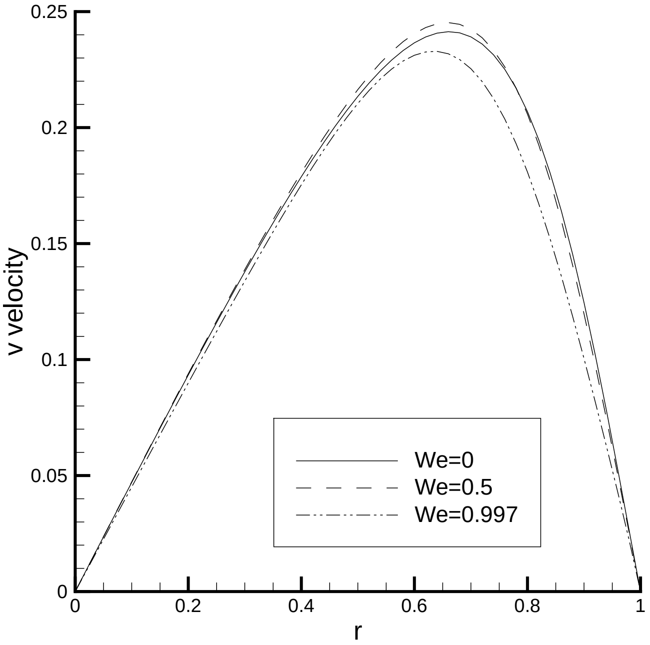

Figure 4.101. v velocity component through the horizontal centerline for the UCM flow with the parameters of $\delta = 0.5$, $\mathrm{Re} = 10$

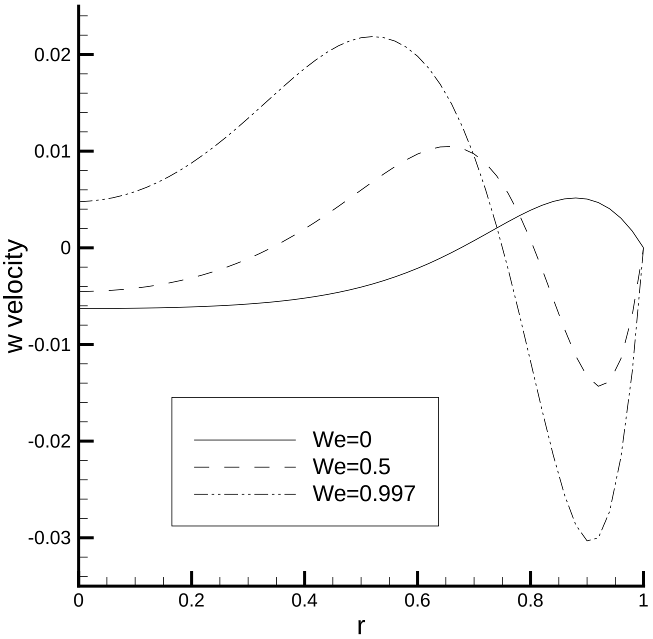

Figure 4.102. w velocity component through the horizontal centerline for the UCM flow with the parameters of $\delta = 0.5$, $\mathrm{Re} = 10$

Figures 4.100, 4.101 and 4.102 show the velocity versus coordinate plots at the centerlines of the flow domain. Because the changes in the velocities are very intense, these three figures also emphasize the reversing of the flow due to the effects of the non-Newtonian parts of the stresses.

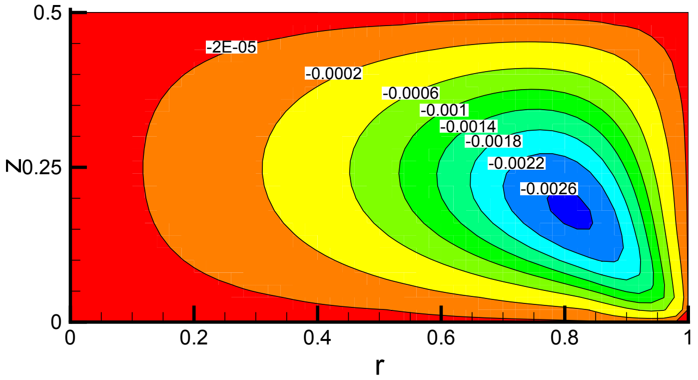

Figure 4.103. Stream function contours for the $\delta = 0.5$ case of UCM flow with the parameters; Re $= 0$, We $= 0.5$

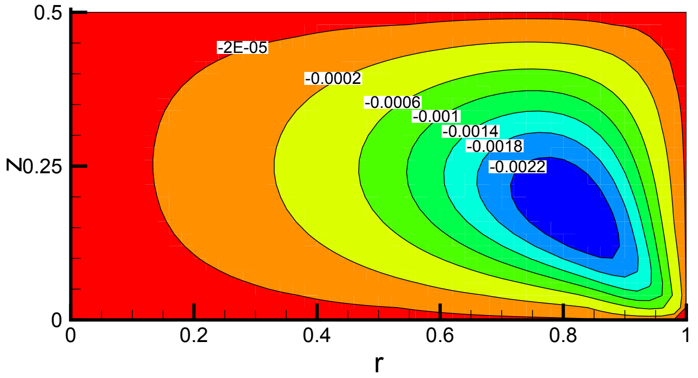

Figure 4.104. Stream function contours for the $\delta = 0.5$ case of UCM flow with the parameters; Re $= 1$, We $= 0.5$

The flow structure of non-Newtonian flows is dependent not only on the Weissenberg number but also on the Reynolds number. Therefore, the combination of these two, which is the Elasticity number (ratio of Weissenberg number to Reynolds number) can be used as a reference point for the flow field.

The effects of the Reynolds number on the UCM flow of RDCE are investigated by comparing the results of $\delta = 0.5$, We $= 0.5$ simulations for various Reynolds numbers. Figures 4.103 through 4.106 show the secondary circulation contours in the $r - z$ plane and it can be grasped from these figures that the flow is fully reversed when

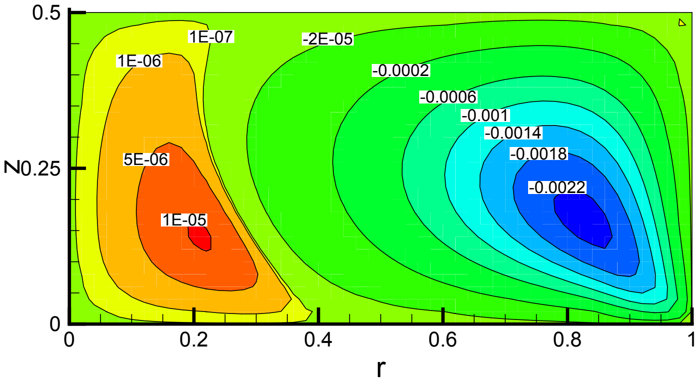

Figure 4.105. Stream function contours for the $\delta = 0.5$ case of UCM flow with the parameters; Re $= 5$, We $= 0.5$

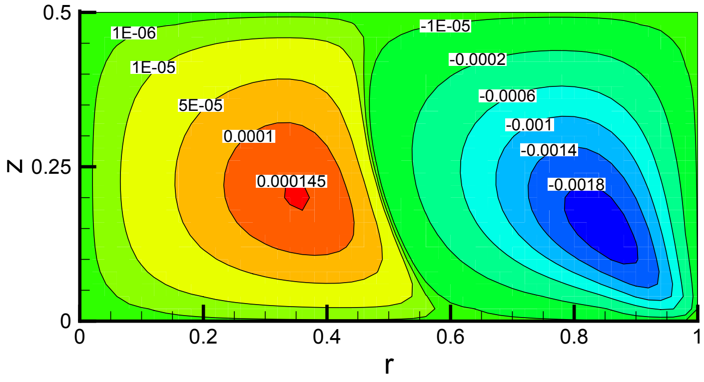

Figure 4.106. Stream function contours for the $\delta = 0.5$ case of UCM flow with the parameters; Re $= 10$, We $= 0.5$

the Elasticity number is high. In other words, since the reversing occurs when the non-Newtonian stresses overpower the outward centrifugal force, the fully reversed flow fields are expected to develop for small Reynolds numbers such as Figures 4.103 and 4.104. In the Figures 4.105 and 4.106, the Reynolds numbers are higher and consequently the Elasticity numbers are lower. Therefore, the inertial forces are more effective on the flow field, thus the non-Newtonian stresses can not totally overcome the centrifugal outward force and the double celled flow structures are formed.

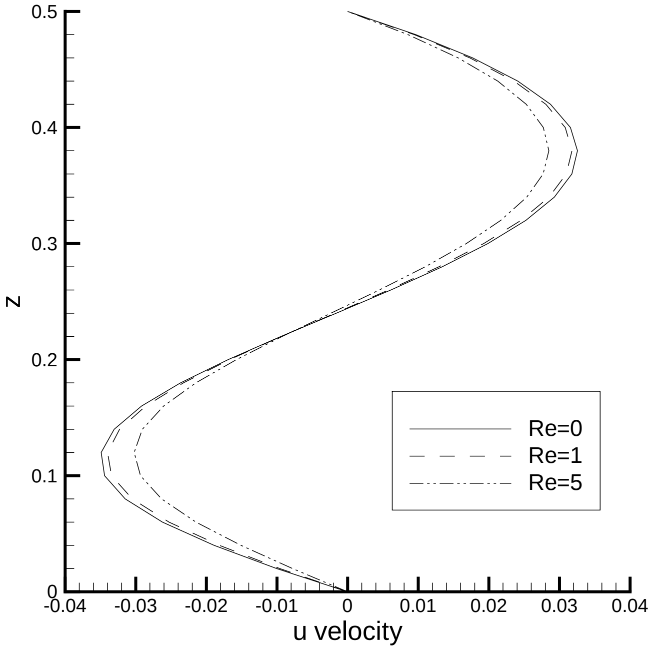

Figure 4.107. u velocity component through the vertical centerline for the UCM flow with the parameters $\delta = 0.5$, We = 1.0

Figures 4.107, 4.108 and 4.109 reveal the velocity distributions on the centerlines of the flow domain. Figure 4.108 shows that the maximum velocity is increasing with the rise in Reynolds number as expected. Figure 4.108 is used to determine the change in the velocity since the main circulation is in the $r - \theta$ plane.

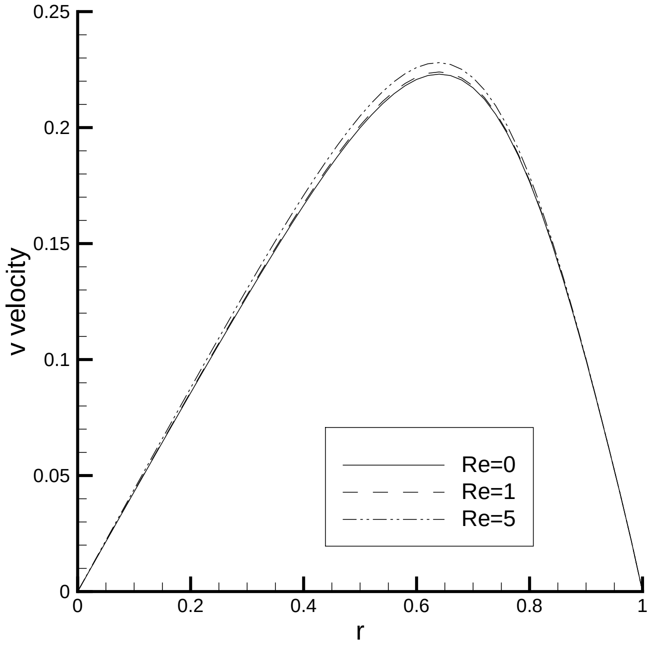

Figure 4.108. v velocity component through the horizontal centerline for the UCM flow with the parameters $\delta = 0.5$, We = 1.0

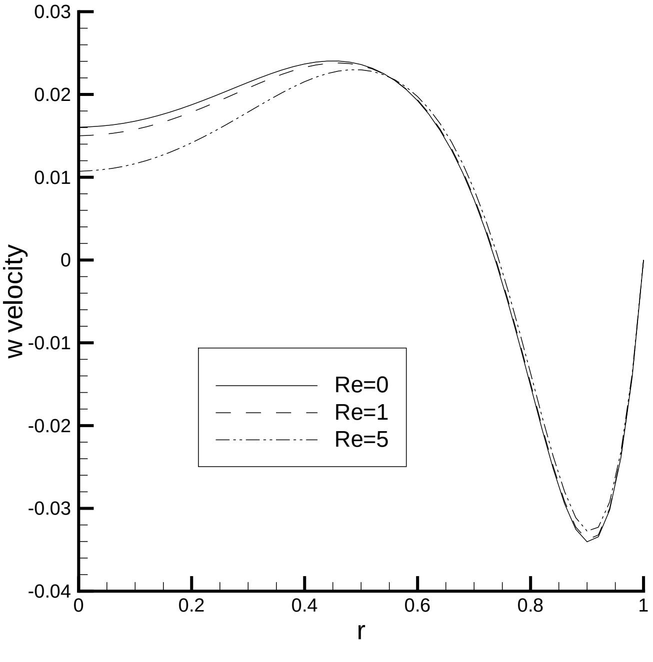

Figure 4.109. w velocity component through the horizontal centerline for the UCM flow with the parameters $\delta = 0.5$, We = 1.0

4.2.3.2. Oldroyd B Model. The Oldroyd B model is the second constitutive equation used in the simulations of this study. It is more realistic and has better convergence behavior than the UCM model. This equation can be employed when the solvent and polymer viscosities of the non-Newtonian fluid are known explicitly. Since Oldroyd B relation is applicable for low shear rates, it is not useful for very high Weissenberg number problems. Table 4.7 reveals that the maximum Weissenberg number limit of the Oldroyd B model is nearly two for the example problem. In average this limit is 7.5 times larger than the limit of the POLYFLOW. The effects of this constitutive relation are studied by using the same problem of the previous subsection; however this time Oldroyd B constitutive relation with $\beta = 0.5$ is adopted to model the viscoelastic behavior.

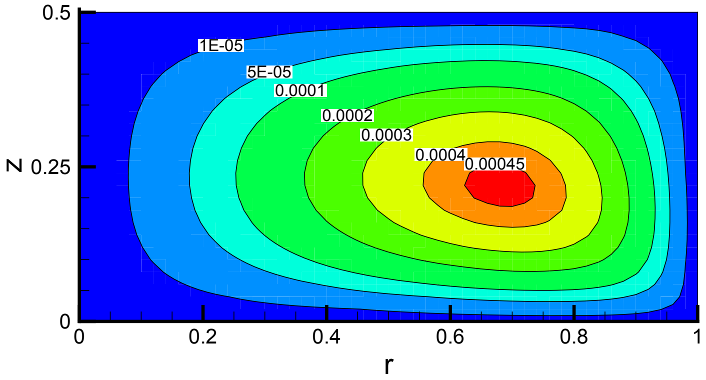

Figure 4.110. Stream function contours for the Oldroyd B flow with the parameters of Re = 5.0, We = 0.0, $\beta = 0.5$ and $\delta = 0.5$

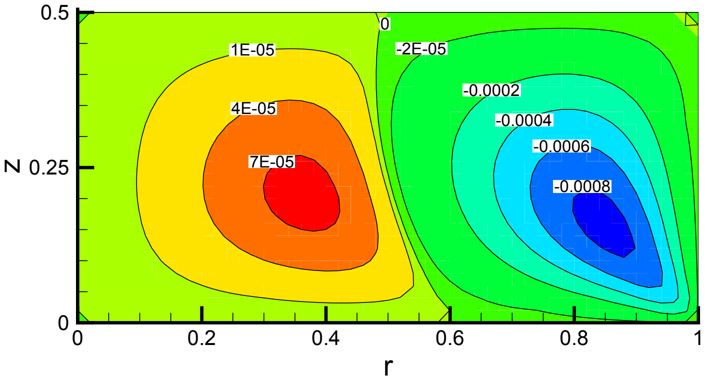

Figure 4.111. Stream function contours for the Oldroyd B flow with the parameters of Re = 5.0, We = 0.5, $\beta = 0.5$ and $\delta = 0.5$

Figures 4.110 through 4.114 reveal the effects of elasticity on the Oldroyd B flow

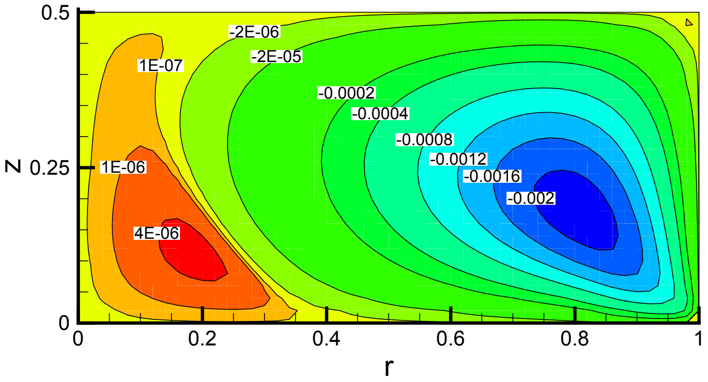

Figure 4.112. Stream function contours for the Oldroyd B flow with the parameters of Re = 5.0, We = 1.0, $\beta = 0.5$ and $\delta = 0.5$

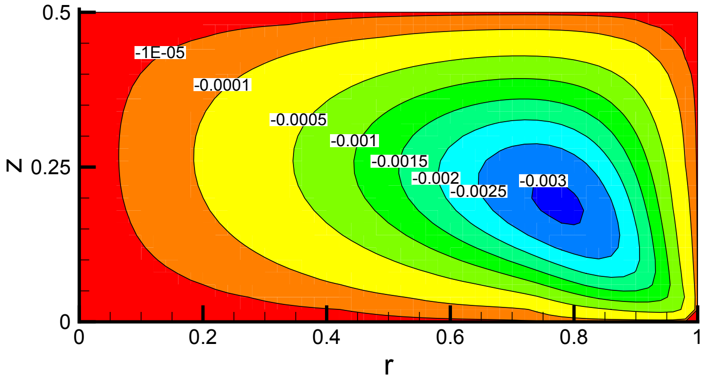

Figure 4.113. Stream function contours for the Oldroyd B flow with the parameters of Re = 5.0, We = 1.5, $\beta = 0.5$ and $\delta = 0.5$

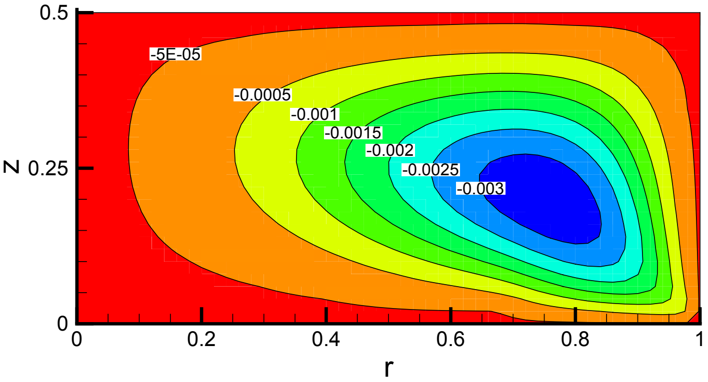

Figure 4.114. Stream function contours for the Oldroyd B flow with the parameters of Re = 5.0, We = 2.0, $\beta = 0.5$ and $\delta = 0.5$

of the RDCE flow with the parameters of $\delta = 0.5$, Re $= 5.0$ and $\beta = 0.5$. Similar to the previous simulations, the flow is reversed with the increase in the elasticity of the fluid. But this time the reversing occurs at higher Weissenberg number which can be observed by comparing stream function figures of UCM and Oldroyd B constitutive relations. For example, the fully reversed flow occurs nearly at We $= 1.0$ for UCM constitutive relation where it occurs nearly at We $= 1.5$ for the Oldroyd B. The main reason for this difference is in the equations of both constitutive relations. Since the elastic stresses in the equations of vorticity and circulation are reduced by $(1 - \beta)$ for the Oldroyd B constitutive relation, the flow of UCM fluid can be thought as more elastic and therefore the non-Newtonian effects are more dominant.

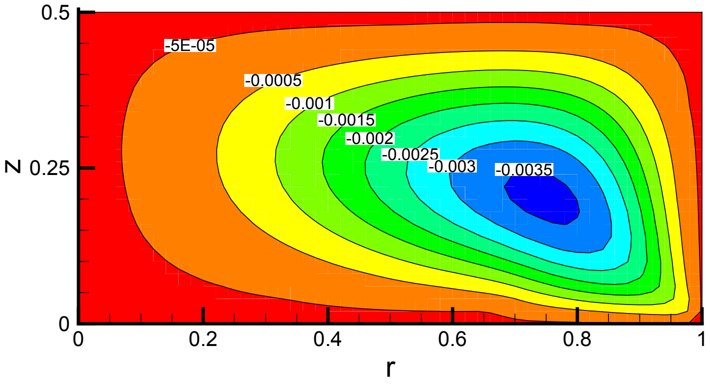

Figure 4.115. Stream function contours for the Oldroyd B flow with the parameters of Re $= 0$, We $= 2.0$, $\beta = 0.5$, $\delta = 0.5$

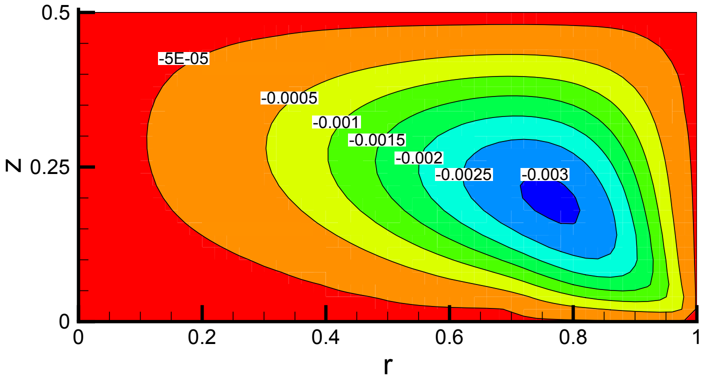

Figure 4.116. Stream function contours for the Oldroyd B flow with the parameters of Re $= 10.0$, We $= 2.0$, $\beta = 0.5$, $\delta = 0.5$

Figures 4.115 and 4.116 demonstrate the stream function contours of the same problem with different Reynolds numbers and since the minimum values are different, these plots show the altered flow fields. The effects of Reynolds number is also clear from the previous stream function figures which are plotted for different Weissenberg numbers.

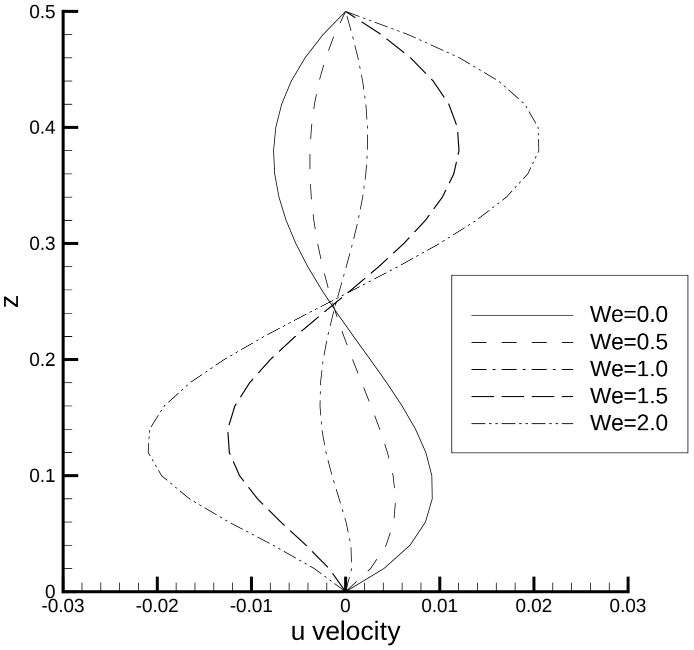

Figure 4.117. u velocity component through the vertical centerline for the Oldroyd B flow with the parameters of Re = 10.0, $\delta = 0.5$, $\beta = 0.5$

Figures 4.117 and 4.118 reveal the velocity versus coordinate plots for different Weissenberg numbers at the centerlines of the flow domain. These plots are generated from the solutions of the flow of Oldroyd B fluid with the parameters Re = 10.0, $\delta = 0.5$, $\beta = 0.5$. Similar to the previous solutions, these figures show the reversing of the flow with the increasing Weissenberg numbers. Unlike UCM, the reversing process occurs more slowly because of the reduced elasticity of the fluid in the Oldroyd B equation. This phenomenon can also be observed in the Figures 4.119 and 4.120 which point out the velocity versus coordinate plots for different Weissenberg numbers at the centerlines of the flow domain. But this time both of the constitutive models are plotted in the same figure. The parameters for the UCM are Re = 5.0, $\delta = 0.5$ where the parameters of the Oldroyd B model are Re = 5.0, $\delta = 0.5$ and $\beta = 0.5$ for these plots. It is obvious from these figures that the flow of UCM model experiences the effects of elasticity more rapidly than Oldroyd B model since the reversing occurred in

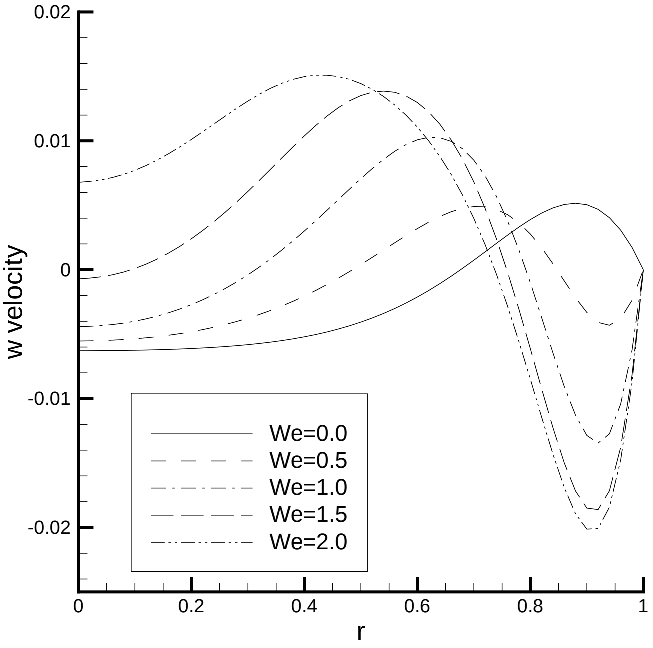

Figure 4.118. w velocity component through the horizontal centerline for the Oldroyd B flow with the parameters of Re = 10.0, $\delta = 0.5$, $\beta = 0.5$

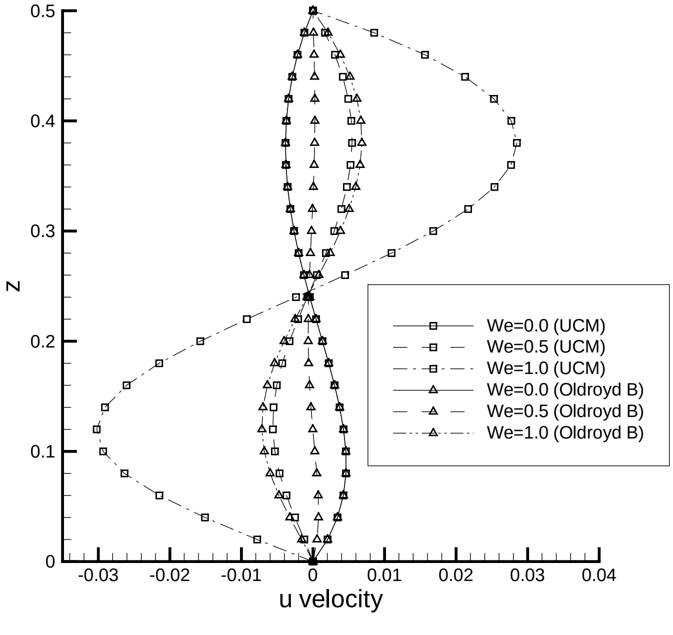

Figure 4.119. Comparison of the u velocity components through the vertical centerline for UCM and Oldroyd B models with the parameters of Re = 5.0, $\delta = 0.5$, $\beta = 0.5$

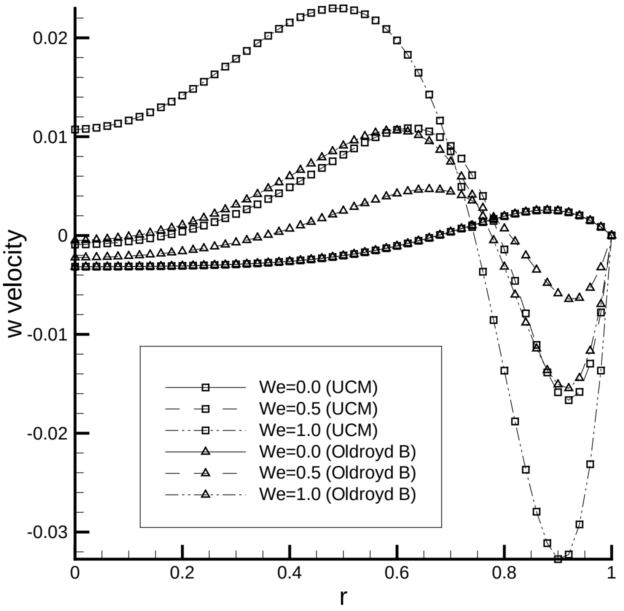

Figure 4.120. Comparison of the w velocity components through the horizontal centerline for UCM and Oldroyd B models with the parameters of Re $= 5.0$, $\delta = 0.5$, $\beta = 0.5$

smaller Weissenberg numbers.

<u>4.2.3.3. Giesekus Model.</u> The final constitutive relation used in this study is the Giesekus model which is one of the most realistic differential constitutive relations. This viscoelastic model displays shear thinning behavior which has been proved to be useful in the modeling of RDCE problem. Table 4.7 reveals that the maximum Weissenberg number limits of Giesekus model are very high compared to the other constitutive relations used in the simulations. Since this relation is the most realistic one and the maximum Weissenberg number limits are higher, the Giesekus model is preferred over UCM and Oldroyd B for the investigations of the effects of the aspect ratio and the reversing process limits. Benefiting from the analyses carried out with the Giesekus model in the LDC section, the viscosity ratio and the mobility parameters of this part of the study are selected as 0.5 and 0.1 respectively ($\beta = 0.5$, $\alpha = 0.1$) unless else is stated.

In order to compare the results of the Giesekus relation with the UCM and Oldroyd B models, the similar problem with the aspect ratio of 0.5 is solved.

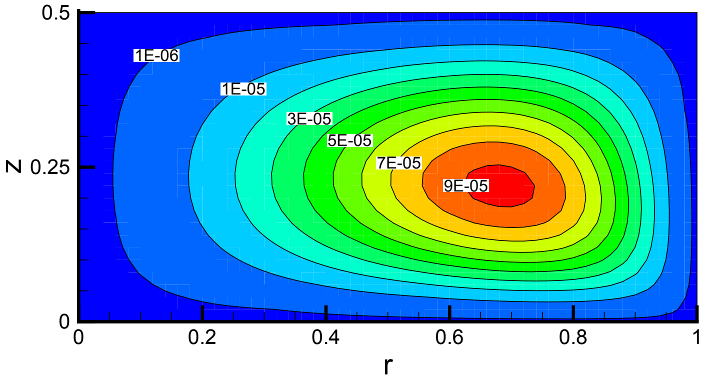

(a) Stream function

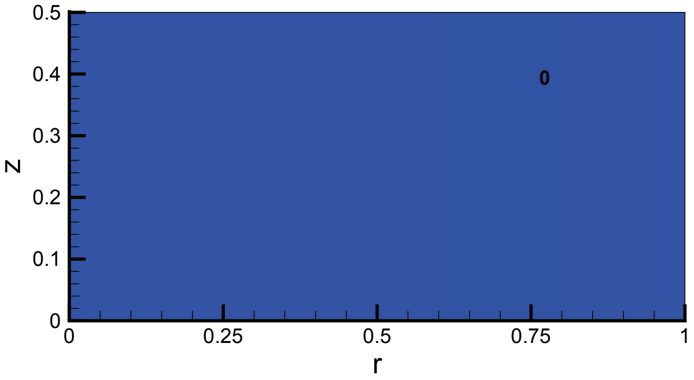

(b) Trace of the non-Newtonian stress tensor

Figure 4.121. Giesekus flow with the parameters of Re = 1.0, We = 0.0, $\beta = 0.5$, $\alpha = 0.1$ and $\delta = 0.5$

Figures 4.121 through 4.131 show the stream function and trace of the non-Newtonian stress tensor ($S_{tr} = S_{rr} + S_{\theta\theta} + S_{zz}$) contours for the flow of the Giesekus constitutive relation where the aspect ratio is 0.5 and the Reynolds number is 1.0. Similar to the previous studies, the reversing of the flow is completed when the Weissenberg number is nearly 0.5. After this Weissenberg number the flow starts to slow down with the increasing elasticity. This slowing process continues and an additional flow spot which rotates in the direction of the Newtonian fluids develops when the Weissenberg number is nearly 25. This spot comes into existence because the outward centrifugal force can now overpower the force of decelerated fluid particles. The further increase in the Weissenberg number enhances the elasticity effects and slows down the flow which results in the growing of the Newtonian like spot into the flow domain. Since

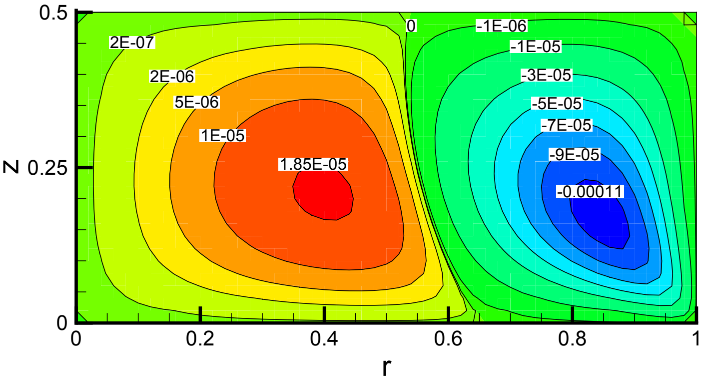

(a) Stream function

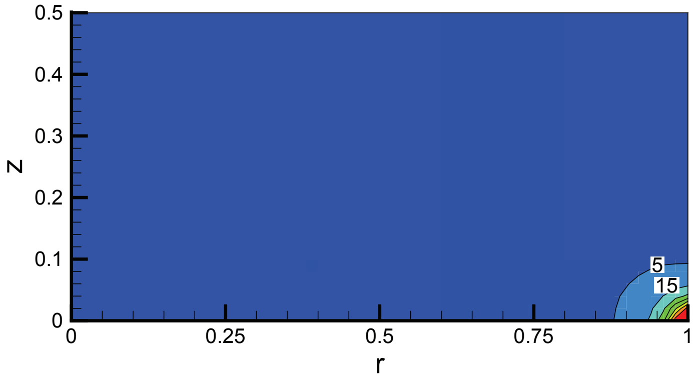

(b) Trace of the non-Newtonian stress tensor

Figure 4.122. Giesekus flow with the parameters of Re = 1.0, We = 0.1, $\beta = 0.5$, $\alpha = 0.1$ and $\delta = 0.5$

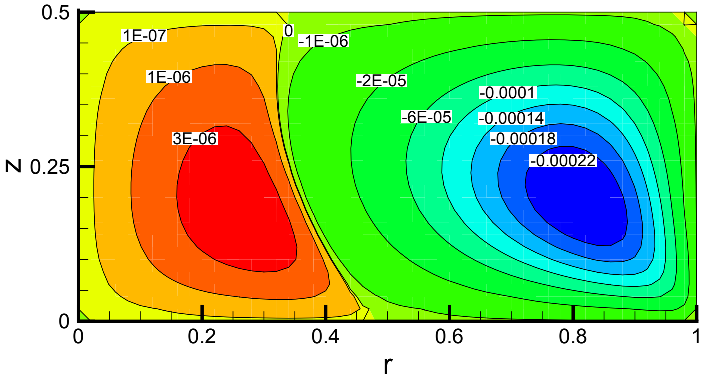

(a) Stream function

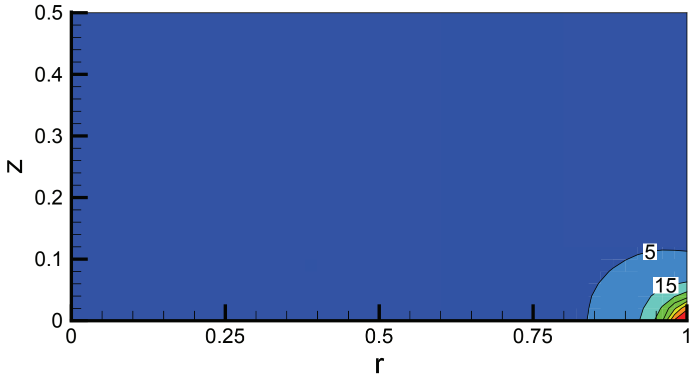

(b) Trace of the non-Newtonian stress tensor

Figure 4.123. Giesekus flow with the parameters of Re = 1.0, We = 0.2, $\beta = 0.5$, $\alpha = 0.1$ and $\delta = 0.5$

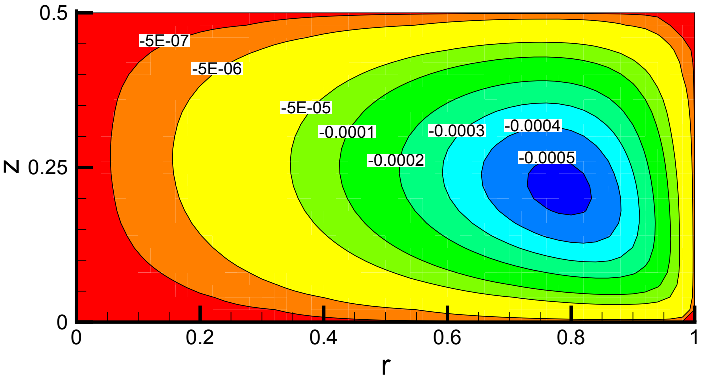

(a) Stream function

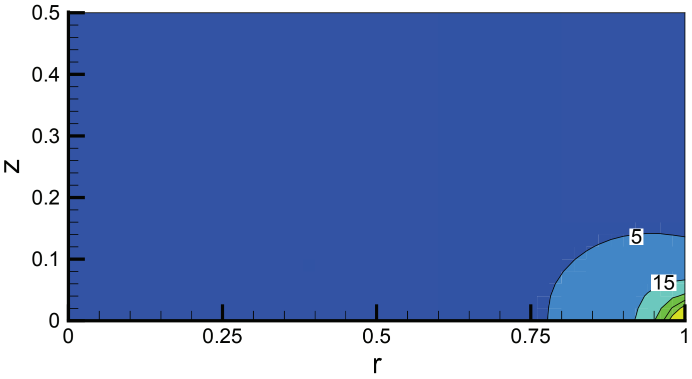

(b) Trace of the non-Newtonian stress tensor

Figure 4.124. Giesekus flow with the parameters of Re = 1.0, We = 0.5, $\beta = 0.5$, $\alpha = 0.1$ and $\delta = 0.5$

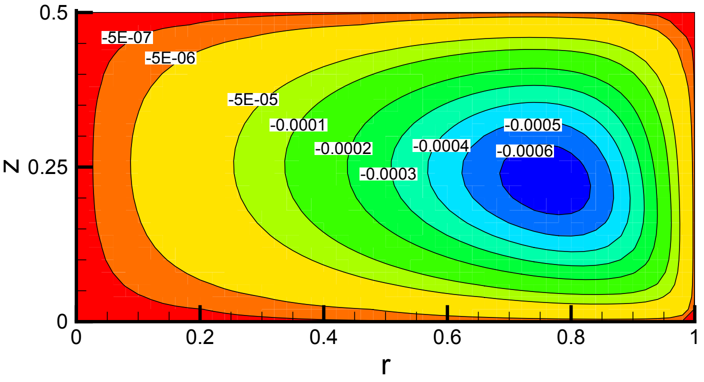

(a) Stream function

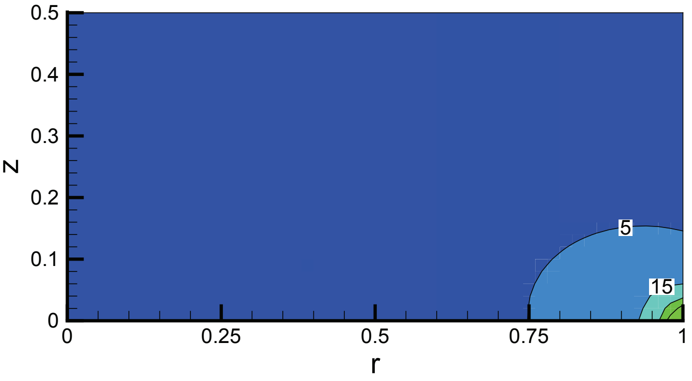

(b) Trace of the non-Newtonian stress tensor

Figure 4.125. Giesekus flow with the parameters of Re = 1.0, We = 1.0, $\beta = 0.5$, $\alpha = 0.1$ and $\delta = 0.5$

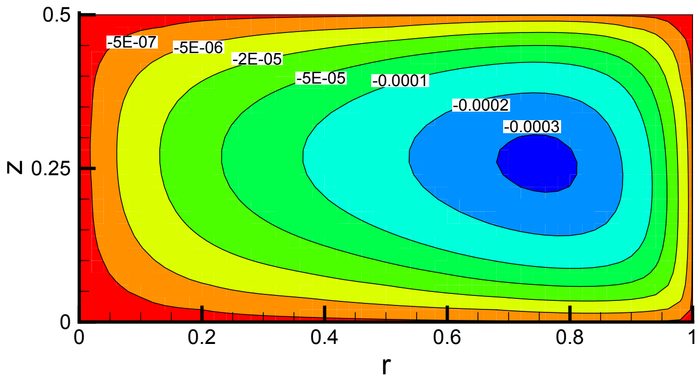

(a) Stream function

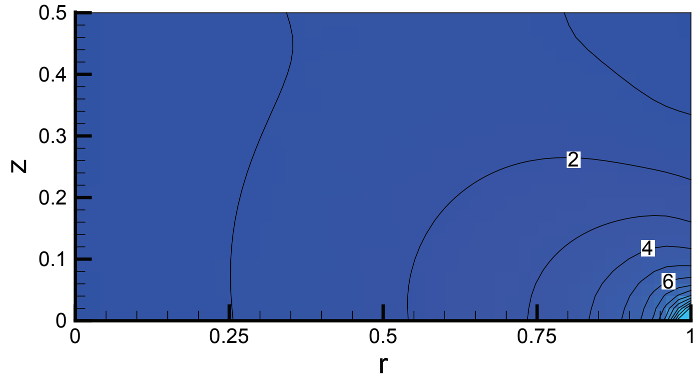

(b) Trace of the non-Newtonian stress tensor

Figure 4.126. Giesekus flow with the parameters of Re = 1.0, We = 10.0, $\beta = 0.5$, $\alpha = 0.1$ and $\delta = 0.5$

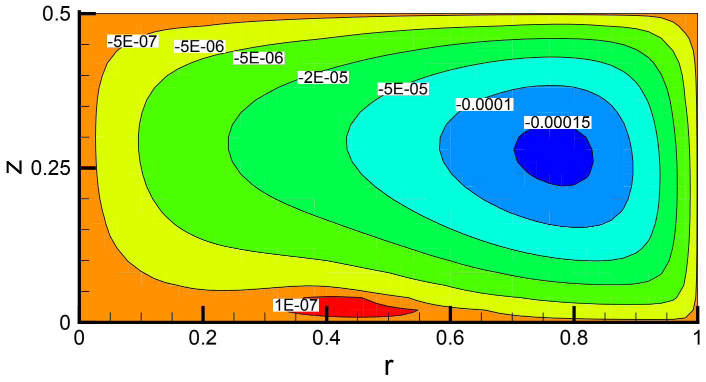

(a) Stream function

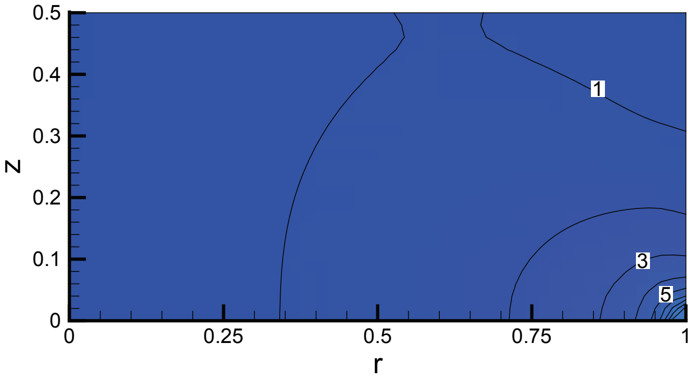

(b) Trace of the non-Newtonian stress tensor

Figure 4.127. Giesekus flow with the parameters of Re = 1.0, We = 25.0, $\beta = 0.5$, $\alpha = 0.1$ and $\delta = 0.5$

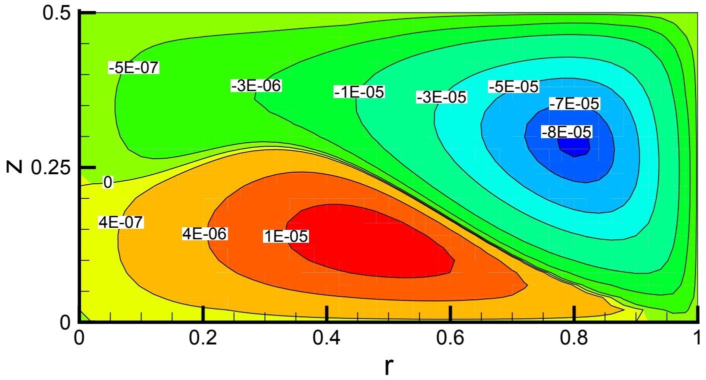

(a) Stream function

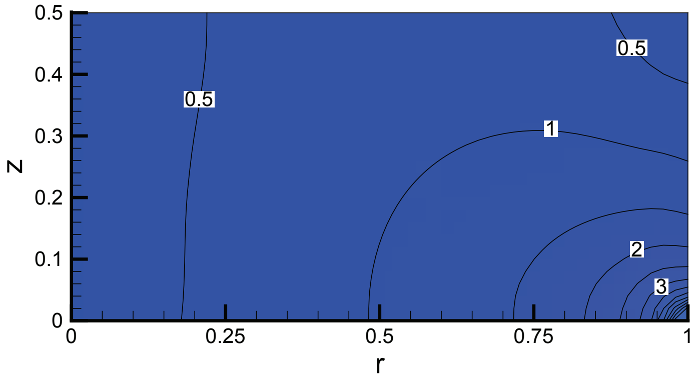

(b) Trace of the non-Newtonian stress tensor

Figure 4.128. Giesekus flow with the parameters of Re = 1.0, We = 50.0, $\beta = 0.5$, $\alpha = 0.1$ and $\delta = 0.5$

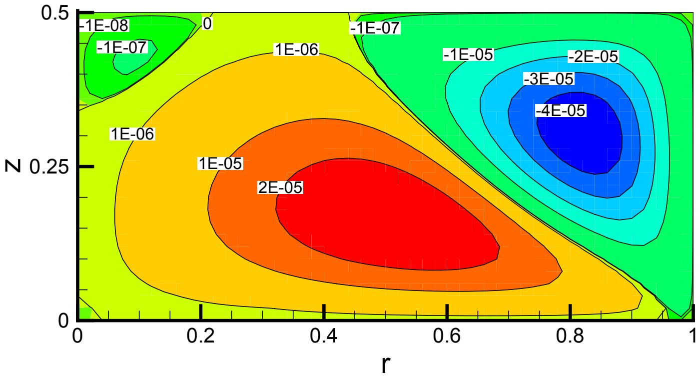

(a) Stream function

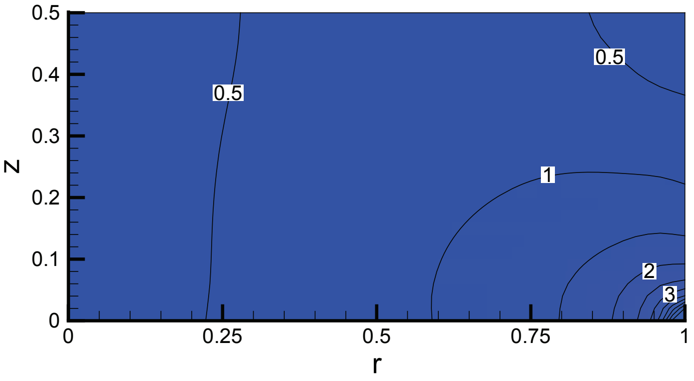

(b) Trace of the non-Newtonian stress tensor

Figure 4.129. Giesekus flow with the parameters of Re $= 1.0$, We $= 75.0$, $\beta = 0.5$, $\alpha = 0.1$ and $\delta = 0.5$

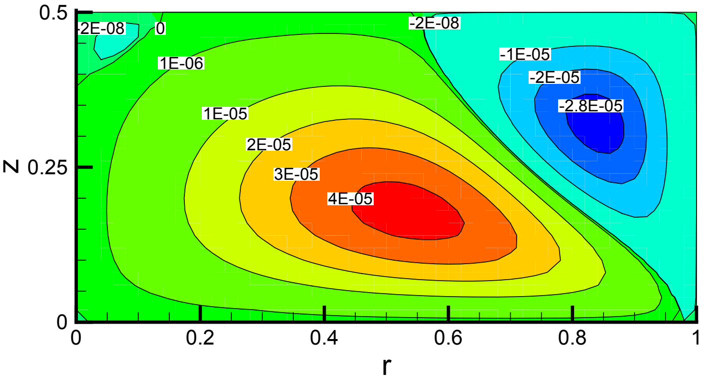

(a) Stream function

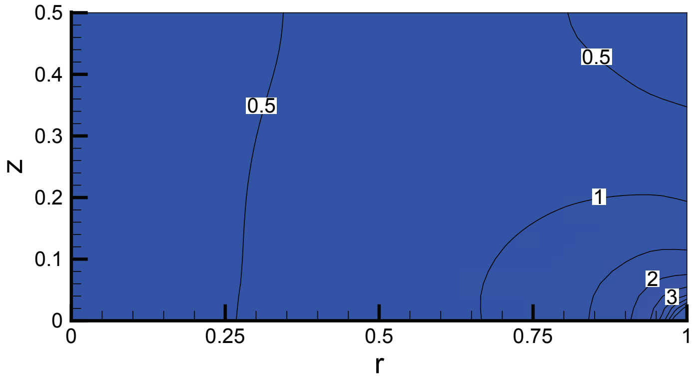

(b) Trace of the non-Newtonian stress tensor

Figure 4.130. Giesekus flow with the parameters of $\mathrm{Re} = 1.0$, $\mathrm{We} = 100.0$, $\beta = 0.5$, $\alpha = 0.1$ and $\delta = 0.5$

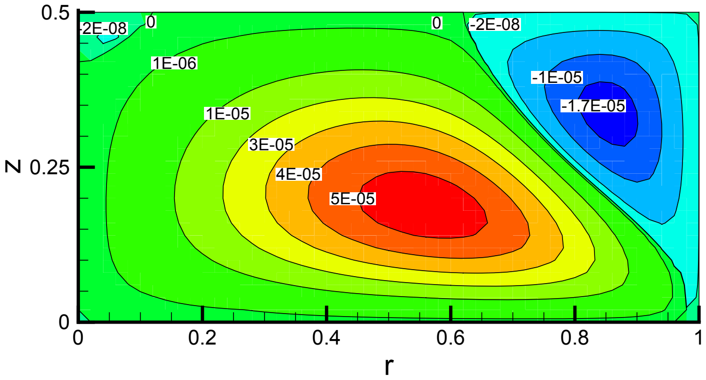

(a) Stream function

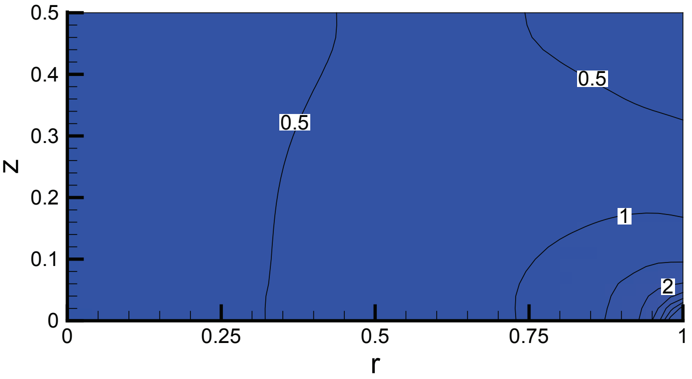

(b) Trace of the non-Newtonian stress tensor

Figure 4.131. Giesekus flow with the parameters of Re = 1.0, We = 130.0, $\beta = 0.5$, $\alpha = 0.1$ and $\delta = 0.5$

this process is dependent on the inertia of the fluid, it can not be observed when the inertia is neglected or in other words when the Reynolds number is zero (creeping flow). Having said that this phenomenon is a high Weissenberg number occurrence, there are no results indicating this type of flows in the literature. The fundamental reason for this deficiency is the limit of the maximum Weissenberg number in the literature. This limit is 4.8 for the numerical simulations (study of Xue *et al.* [22]). As a matter of fact, most of the studies such as Itoh *et al.* [17] and Moroi *et al.* [16] used the Weissenberg numbers less than the order of 1. Additionally, the Weissenberg number limits of our study may be beyond the experimental limits of most of the materials, therefore these results are unique for this research. Moreover, the reliability of the results is proved by the comparison of the solutions with POLYFLOW up to its limits.

The trace of the non-Newtonian stress tensor contours reveal a rapid growth in the right bottom corner with the small Weissenberg numbers and this rapid growth can be explained as the reason of the formation of the reversed flow field near this corner. However with the increasing Weissenberg numbers the trace of the non-Newtonian stress tensor starts to decrease and after some point ($We > 25$ in this case) the centrifugal forces become dominant again.

Figures 4.132 and 4.133 reveal the velocity versus coordinate plots for the same problem. The reversing and slowing processes can also be observed from these figures. For example, the flow is fully reversed and the velocity of the rotation is at its peak value when the Weissenberg number is 1.0. An additional increase in the elasticity slows down the fluid and eventually velocities take similar shapes of the Newtonian flow.

Figures 4.134, 4.135, 4.136 and 4.137 reveal the non-Newtonian stress components on the centerlines of the flow domain. The We = 0.0 case is not presented on these figures since the non-Newtonian stresses are zero for this value. The magnitudes of the stresses are at their peak values for the We = 0.5 case in all of the figures. This means that the stresses increased very rapidly. This peak value can be thought as the reason for the reversing of the flow field. It can be observed from these figures that the

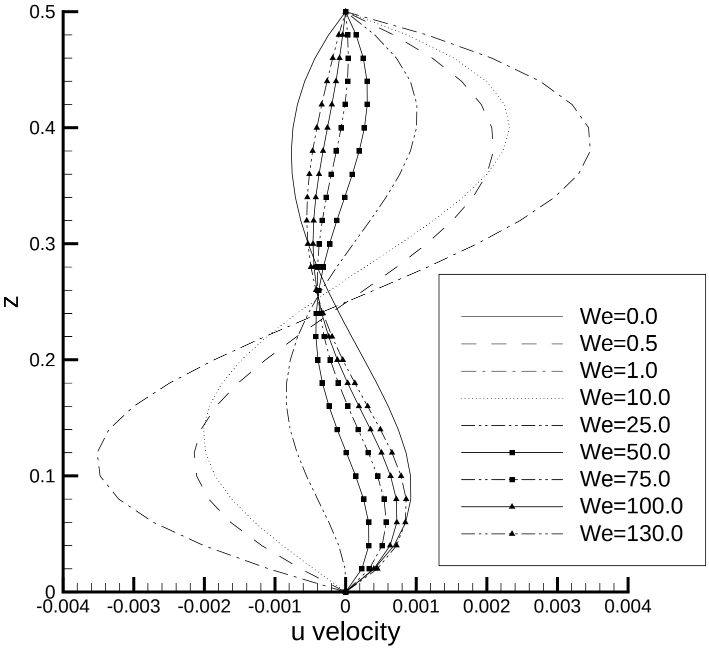

Figure 4.132. u velocity component through the vertical centerline for the Giesekus flow with the parameters of Re = 1.0, $\delta = 0.5$, $\beta = 0.5$ and $\alpha = 0.1$

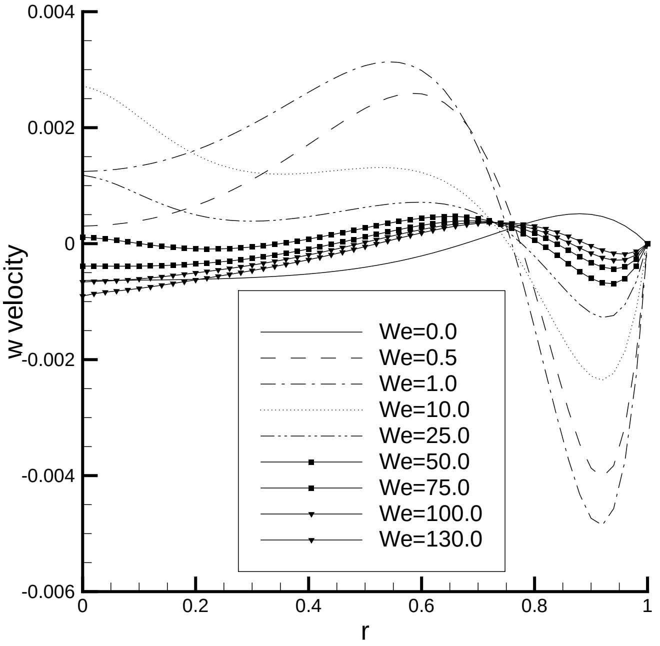

Figure 4.133. w velocity component through the horizontal centerline for the Giesekus flow with the parameters of Re = 1.0, $\delta = 0.5$, $\beta = 0.5$ and $\alpha = 0.1$

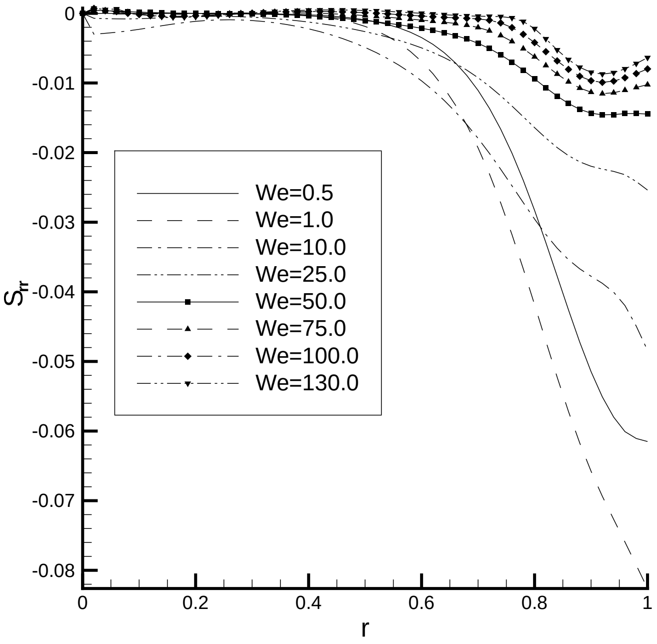

Figure 4.134. The non-Newtonian stress tensor component S_{rr} through the horizontal centerline with the parameters of $\mathrm{Re} = 1.0$, $\delta = 0.5$, $\beta = 0.5$ and $\alpha = 0.1$

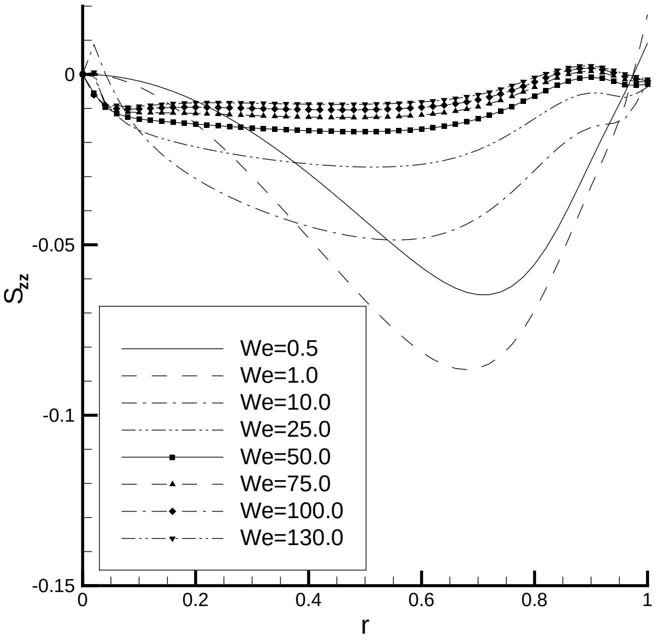

Figure 4.135. The non-Newtonian stress tensor component S_{zz} through the horizontal centerline with the parameters of $\mathrm{Re} = 1.0$, $\delta = 0.5$, $\beta = 0.5$ and $\alpha = 0.1$

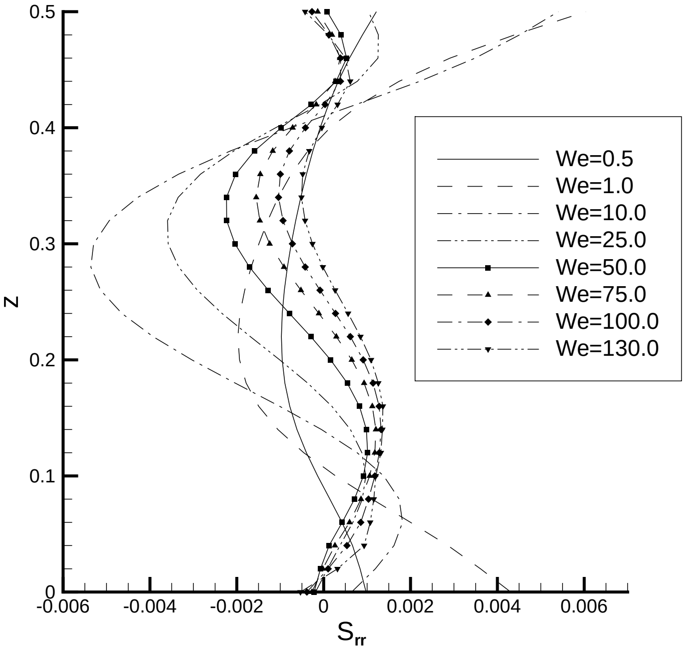

Figure 4.136. The non-Newtonian stress tensor component S_{rr} through the vertical centerline with the parameters of $\mathrm{Re} = 1.0$, $\delta = 0.5$, $\beta = 0.5$ and $\alpha = 0.1$

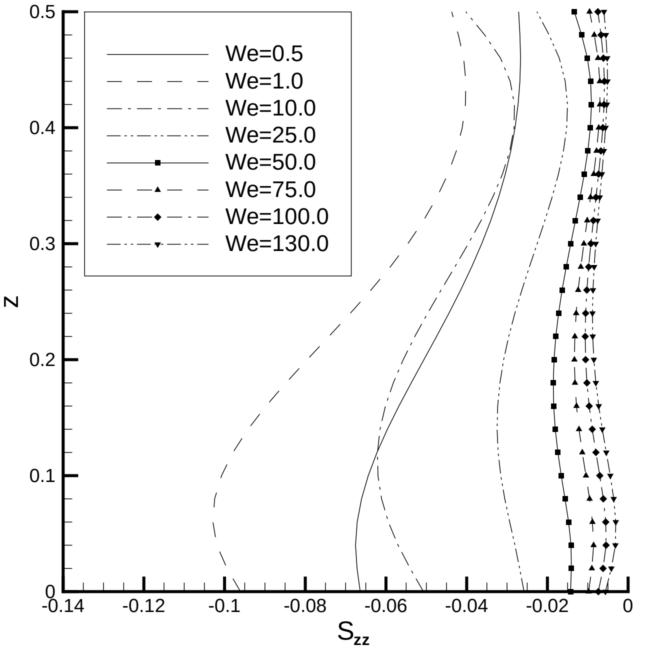

Figure 4.137. The non-Newtonian stress tensor component S_{zz} through the vertical centerline with the parameters of $\mathrm{Re} = 1.0$, $\delta = 0.5$, $\beta = 0.5$ and $\alpha = 0.1$

stresses S_{rr} and S_{zz} are decreasing with the increasing Weissenberg numbers. Since the stresses are proportional to the velocities and the magnitudes of the velocities are declining with the increase in the Weissenberg numbers, the decrease in the magnitudes of the stresses are expected. Moreover, the reformation of the Newtonian like flow can be explained with the decrease in the stress magnitudes.

The regrowth of the Newtonian type vortex is also investigated for different aspect ratios and it is understood that the aspect ratio plays an important role on the formation of the reversed flows. For example, a similar analysis is carried out with the aspect ratio of 0.25 and the stream function contours are plotted in Figures 4.138 through 4.144. It can be observed from these figures that, the formation of the fully reversed flow never takes place. Instead of fully reversed flow, the double cell type flow is developed. This double cell structure is composed of a reversed flow spot (monitored at the right side of the flow domain) and a Newtonian like spot (observed on the left side). For the We = 1.0 value, the reversed spot occupies nearly half of the domain. Afterwards, with the increasing Weissenberg numbers, the flow starts to slow down and this spot starts to shrink while the Newtonian like spot is growing. This process is similar to the reformation of the Newtonian like spot in the $\delta = 0.5$ case. Similarly, the magnitudes of the stresses decrease with the increase in the Weissenberg number which leads to the growing of the Newtonian like spot.

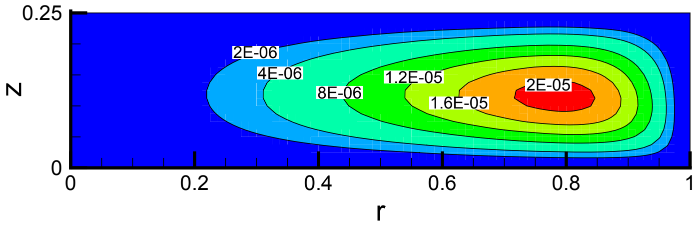

Figure 4.138. Stream function contours for the $\delta = 0.25$ case of Giesekus flow with the parameters; Re = 1.0, We = 0.0, $\beta = 0.5$ and $\alpha = 0.1$

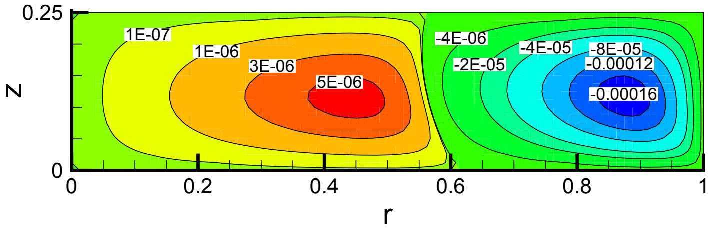

Figure 4.139. Stream function contours for the $\delta = 0.25$ case of Giesekus flow with the parameters; Re = 1.0, We = 0.5, $\beta = 0.5$ and $\alpha = 0.1$

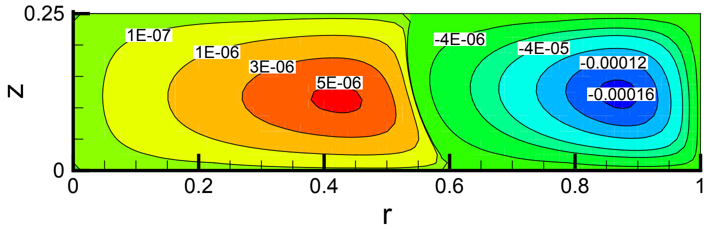

Figure 4.140. Stream function contours for the $\delta = 0.25$ case of Giesekus flow with the parameters; Re = 1.0, We = 1.0, $\beta = 0.5$ and $\alpha = 0.1$

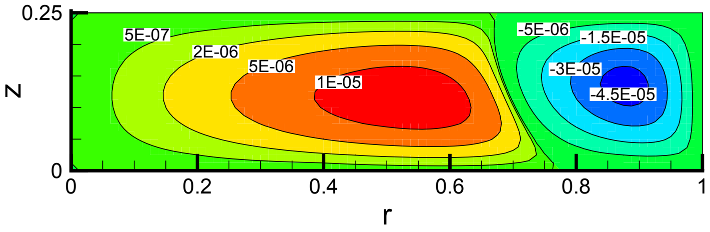

Figure 4.141. Stream function contours for the $\delta = 0.25$ case of Giesekus flow with the parameters; Re = 1.0, We = 10.0, $\beta = 0.5$ and $\alpha = 0.1$

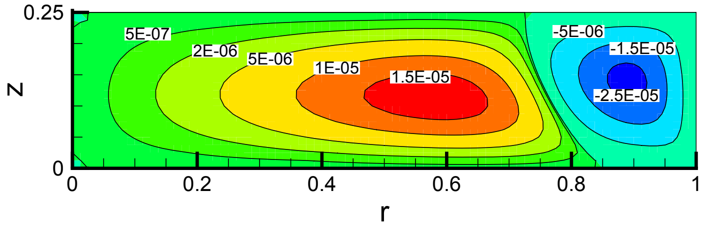

Figure 4.142. Stream function contours for the $\delta = 0.25$ case of Giesekus flow with the parameters; Re = 1.0, We = 20.0, $\beta = 0.5$ and $\alpha = 0.1$

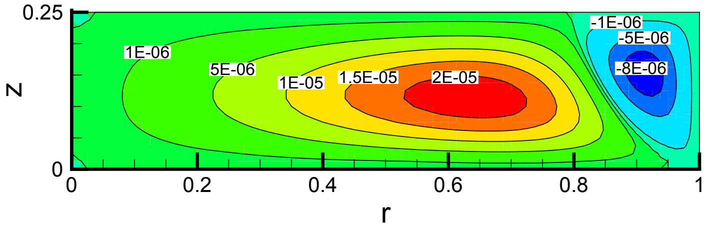

Figure 4.143. Stream function contours for the $\delta = 0.25$ case of Giesekus flow with the parameters; Re = 1.0, We = 50.0, $\beta = 0.5$ and $\alpha = 0.1$

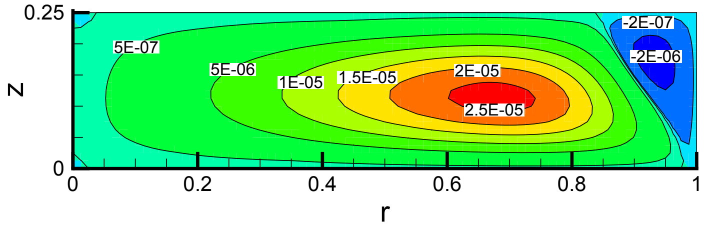

Figure 4.144. Stream function contours for the $\delta = 0.25$ case of Giesekus flow with the parameters; Re = 1.0, We = 100.0, $\beta = 0.5$ and $\alpha = 0.1$

Figures 4.145 and 4.146 point out the velocity versus coordinate plots for the same problem. The slowing down of the velocity and regrowth of the Newtonian like spot can be identified from these figures.

Additional to the aspect ratio, Reynolds number has an effect on the growing of the Newtonian like spot process. These effects are investigated by modeling the flow of the Giesekus constitutive relation with the aspect ratio of 0.5 and the Reynolds number of 5.0.

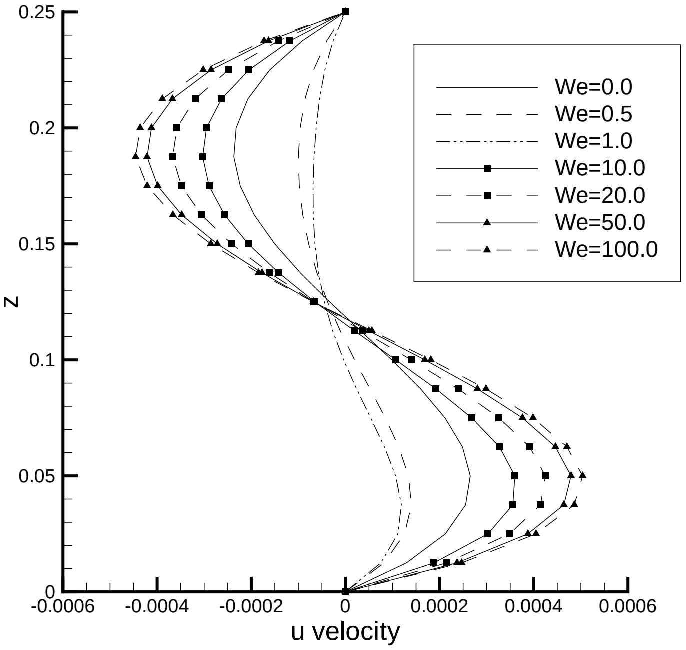

Figure 4.145. u velocity component through the vertical centerline for the Giesekus flow with the parameters Re $= 1.0$, $\delta = 0.25$, $\beta = 0.5$ and $\alpha = 0.1$

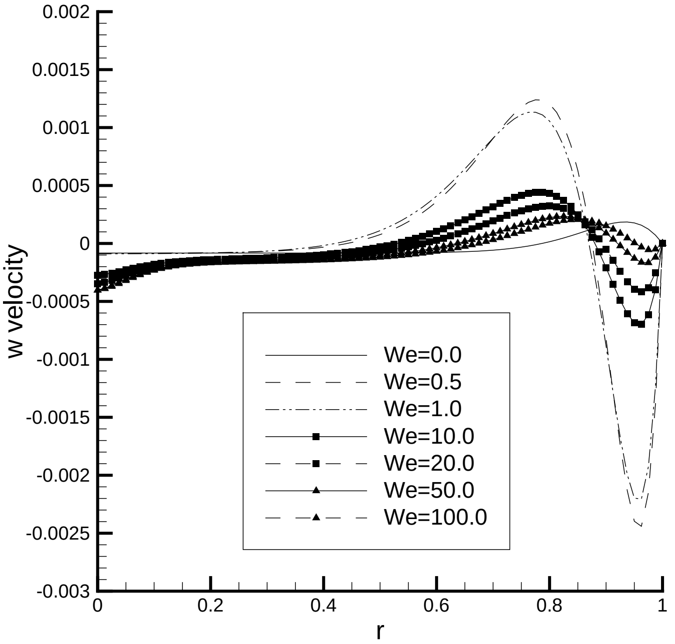

Figure 4.146. w velocity component through the horizontal centerline for the Giesekus flow with the parameters Re $= 1.0$, $\delta = 0.25$, $\beta = 0.5$ and $\alpha = 0.1$

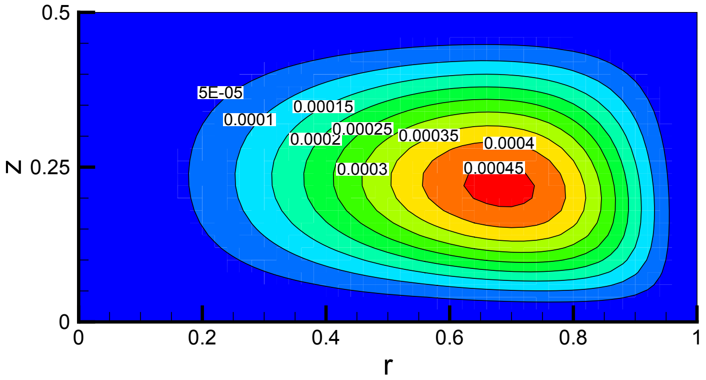

Figure 4.147. Stream function contours for the $\delta = 0.5$ case of Giesekus flow with the parameters; Re $= 5.0$, We $= 0.0$, $\beta = 0.5$ and $\alpha = 0.1$

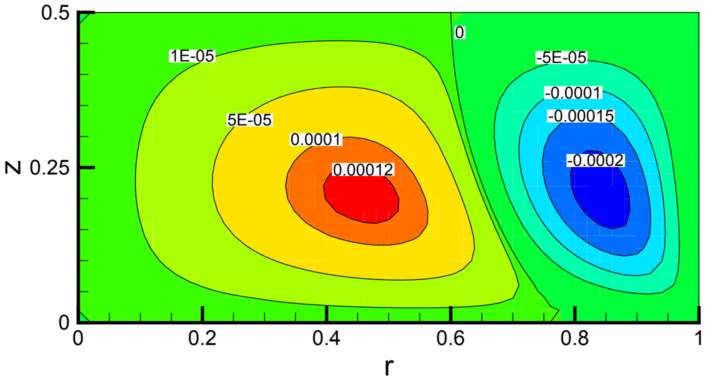

Figure 4.148. Stream function contours for the $\delta = 0.5$ case of Giesekus flow with the parameters; Re $= 5.0$, We $= 0.5$, $\beta = 0.5$ and $\alpha = 0.1$

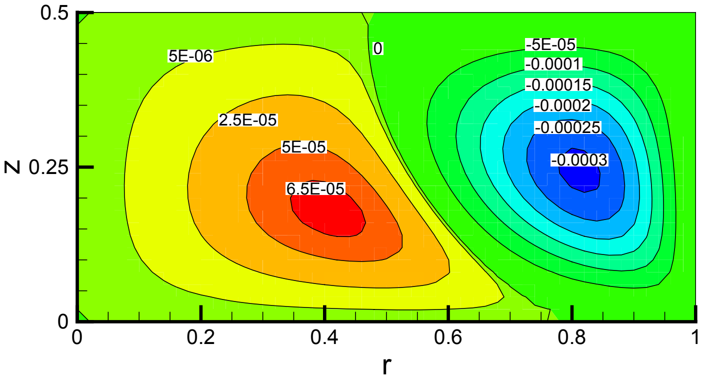

Figure 4.149. Stream function contours for the $\delta = 0.5$ case of Giesekus flow with the parameters; Re $= 5.0$, We $= 1.0$, $\beta = 0.5$ and $\alpha = 0.1$

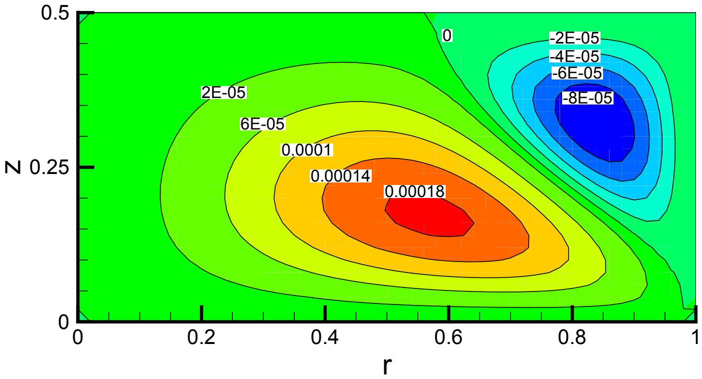

Figure 4.150. Stream function contours for the $\delta = 0.5$ case of Giesekus flow with the parameters; $\mathrm{Re} = 5.0$, $\mathrm{We} = 5.0$, $\beta = 0.5$ and $\alpha = 0.1$

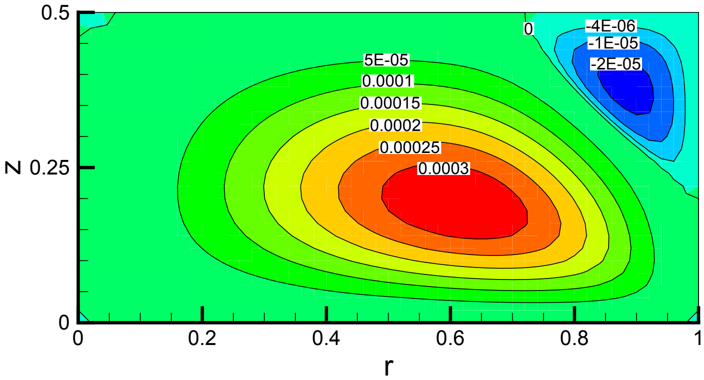

Figure 4.151. Stream function contours for the $\delta = 0.5$ case of Giesekus flow with the parameters; $\mathrm{Re} = 5.0$, $\mathrm{We} = 10.0$, $\beta = 0.5$ and $\alpha = 0.1$

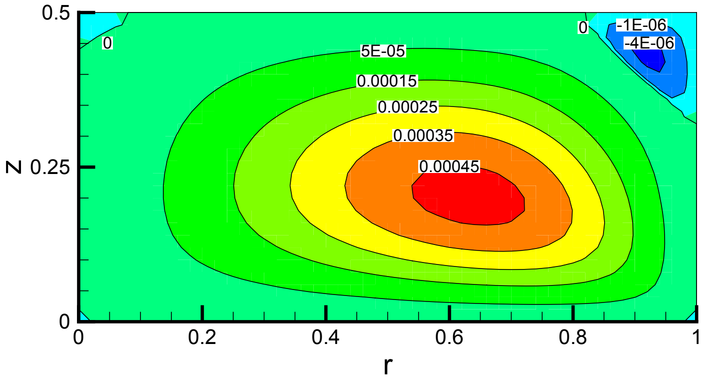

Figure 4.152. Stream function contours for the $\delta = 0.5$ case of Giesekus flow with the parameters; $\mathrm{Re} = 5.0$, $\mathrm{We} = 20.0$, $\beta = 0.5$ and $\alpha = 0.1$

Figures 4.147 through 4.152 show the stream function contours of the flow of Giesekus constitutive relation with the parameters of $\delta = 0.5$, Re $= 5.0$, $\beta = 0.5$ and $\alpha = 0.1$. The difference between this problem and the first test problem of Giesekus constitutive relation is the Reynolds number. The Newtonian flow field transformed into a fully reversed flow with the increasing Weissenberg numbers for Re $= 1.0$ case. Then a Newtonian like spot develops and it grows into the flow domain with the raising elasticity of the fluid. The flow field of Re $= 5.0$ case is different. The Newtonian fluid transforms into a double cell structure similar to the $\delta = 0.25$ case. The reason for not visualization of the fully reversed flow is the increased Reynolds number. As the reversed flow occurs when the non-Newtonian stresses overpower the outward centrifugal force and the centrifugal force is directly proportional to the Reynolds number, the stresses can only drive the fluid particles near the right bottom corner of the geometry. The effects after the development of the double cell are similar to the previous analyses. The Newtonian like spot grows into the flow domain with increasing Weissenberg numbers.

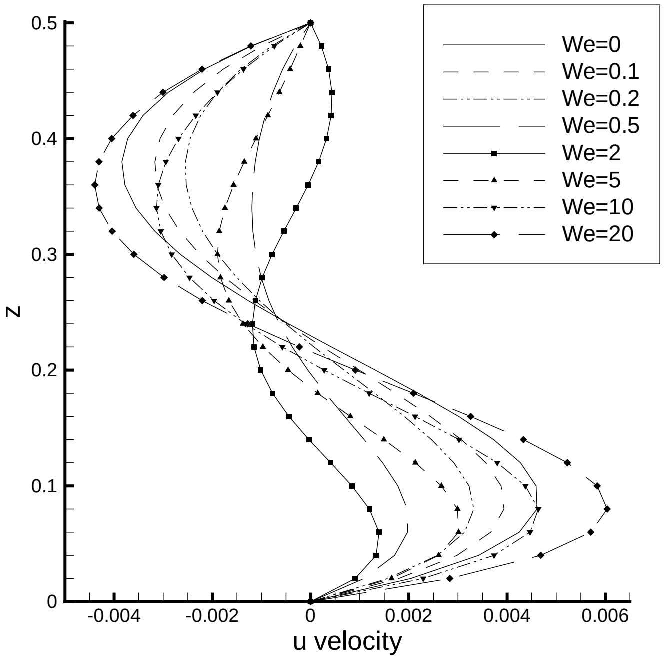

Figure 4.153. u velocity component through the vertical centerline for the Giesekus flow with the parameters Re $= 5.0$, $\delta = 0.5$, $\beta = 0.5$ and $\alpha = 0.1$

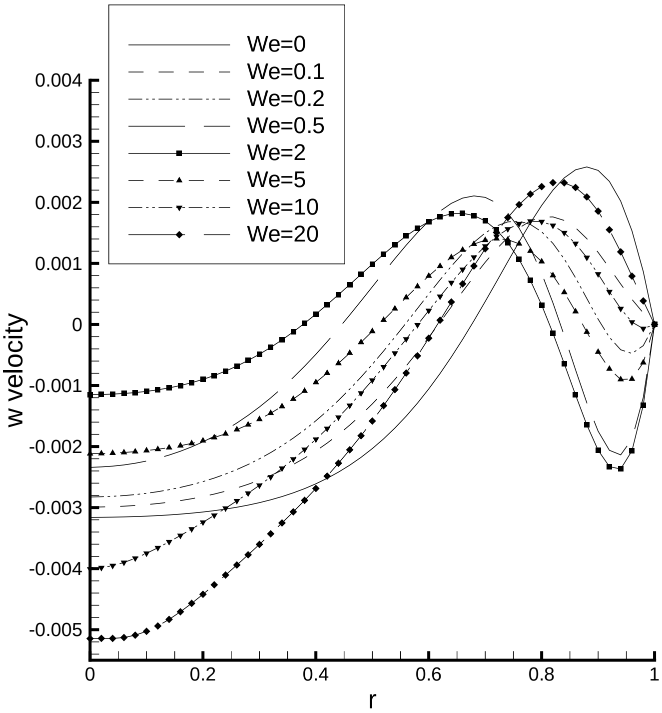

Figure 4.154. w velocity component through the horizontal centerline for the Giesekus flow with the parameters Re $= 5.0$, $\delta = 0.5$, $\beta = 0.5$ and $\alpha = 0.1$

Figures 4.153 and 4.154 reveal the velocity versus coordinate plots on the centerlines of the flow domain. These plots are generated from the solutions of the flow of Giesekus flow with the parameters Re $= 5.0$, $\delta = 0.5$, $\beta = 0.5$ and $\alpha = 0.1$. The slowing down of the flow field can also be grasped from these figures.

The simulations in this section revealed that the emerging of the Newtonian like spot is dependent on the viscoelastic flow field. However, besides the viscoelastic effects, some physical parameters such as the Reynolds number and aspect ratio play an important role on the formation of the flow field. Dependent on these parameters the structure of the flow field can be fully reversed or double cell. Moreover, it is shown that the rise in the Weissenberg number decreases the non-Newtonian parts of the stresses which may lead to the reformation of the Newtonian like flow spot.

Besides the RDCE problem with rotating bottom disc boundary, the RDCE geometry with rotating bottom disc and cylindrical container is also modeled. However, because of the additional inertial forces arising from the rotating cylindrical casing, the reversed flow is not developed. Only the slowing down of the fluid particles is observed and the results of the non-Newtonian flow in this geometry are not presented.

4.2.3.4. Non-isothermal RDCE flow . In this part of the study, the thermal effects on the flow of non-Newtonian RDCE will be revealed. Since the thermal analyses are connected to many parameters, (such as the Brinkman number, the Prandtl number and the Weissenberg number) the effects of all of these individual parameters should be separately studied. In order to simplify the simulations, the Giesekus model with the parameters of $\beta = 0.5$ and $\alpha = 0.1$ is adopted because of its superiority over the UCM and Oldroyd B constitutive relations. Moreover, the non-dimensional temperature of the rotating disc is selected as 1 where the stationary edges are taken as 0 for all of the simulations in this part of the study.

The first non-isothermal simulation is carried out to understand the effects of the intensity of the viscous dissipation and to verify the results of the IN-GMRES solver with the POLYFLOW simulations. For this purpose the non-isothermal flow of Giesekus constitutive relation with the parameters of Re = 10.0, Pr = 100, We = 1.0, $\delta = 0.5$, $\beta = 0.5$ and $\alpha = 0.1$ is simulated for the Brinkman numbers of 0, 10, 20 and 30. Moreover, the temperature dependent viscosity is modeled by using the approximate Arrhenius relation with the coefficient of $\alpha_s = 0.02$. Since the Brinkman number is the multiplier of the viscous dissipation term, the change in this number directly affects the intensity of the viscous dissipation.

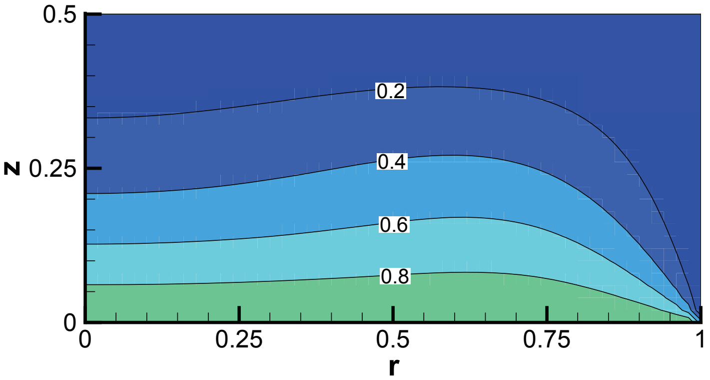

Figure 4.155. Temperature contours for the Giesekus flow with the parameters of Re = 10.0, Pr = 100, We = 1.0, Br = 0.0, $\delta = 0.5$, $\beta = 0.5$, $\alpha = 0.1$ and $\alpha_s = 0.02$

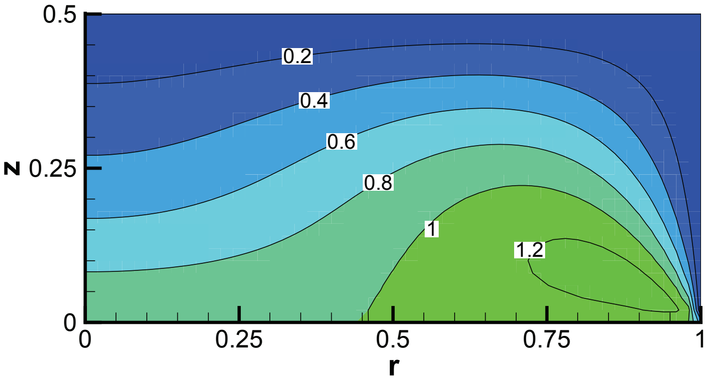

Figure 4.156. Temperature contours for the Giesekus flow with the parameters of Re = 10.0, Pr = 100, We = 1.0, Br = 10.0, $\delta = 0.5$, $\beta = 0.5$, $\alpha = 0.1$ and $\alpha_s = 0.02$

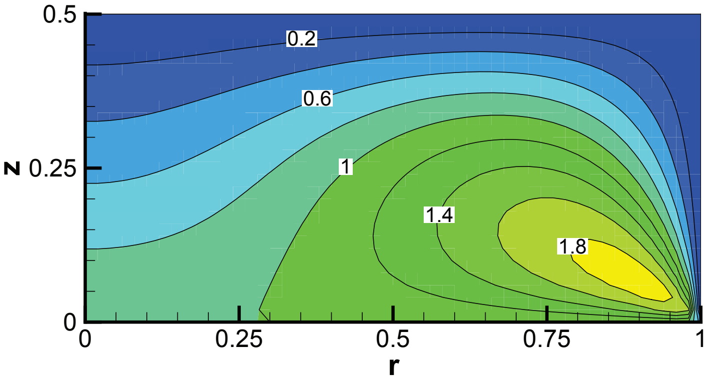

Figure 4.157. Temperature contours for the Giesekus flow with the parameters of Re = 10.0, Pr = 100, We = 1.0, Br = 20.0, $\delta = 0.5$, $\beta = 0.5$, $\alpha = 0.1$ and $\alpha_s = 0.02$

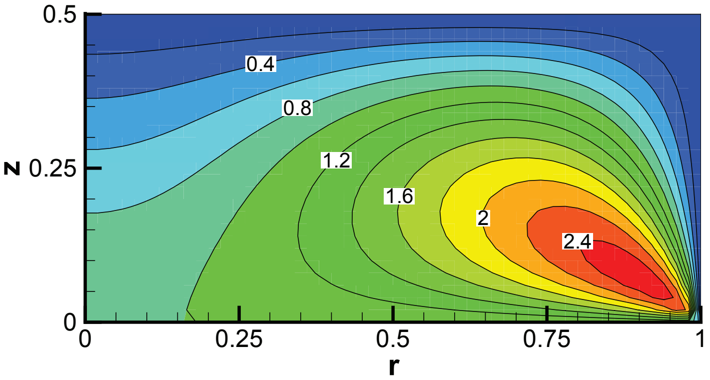

Figure 4.158. Temperature contours for the Giesekus flow with the parameters of Re = 10.0, Pr = 100, We = 1.0, Br = 30.0, $\delta = 0.5$, $\beta = 0.5$, $\alpha = 0.1$ and $\alpha_s = 0.02$

Figures 4.155 through 4.158 reveal the temperature contours for the various Brinkman numbers. The first figure (Figure 4.155) corresponds to the no viscous dissipation case. Therefore, the maximum non-dimensional temperature of this figure is observed as 1 which is the maximum boundary temperature. The Figures 4.156 - 4.158 indicate that with the increasing Brinkman number, the maximum temperatures within the flow domain are increased. Since the Brinkman number is the multiplier of the viscous dissipation term, the increase of this number naturally boosts the heat generation due to viscous dissipation. From the Brinkman number of 3.65, the maximum temperature inside the flow domain exceeds the maximum temperature at the boundary conditions. The Figures 4.160 and 4.159 demonstrate the temperature distributions on the centerlines for both IN-GMRES and POLYFLOW where the results are in good agreement.

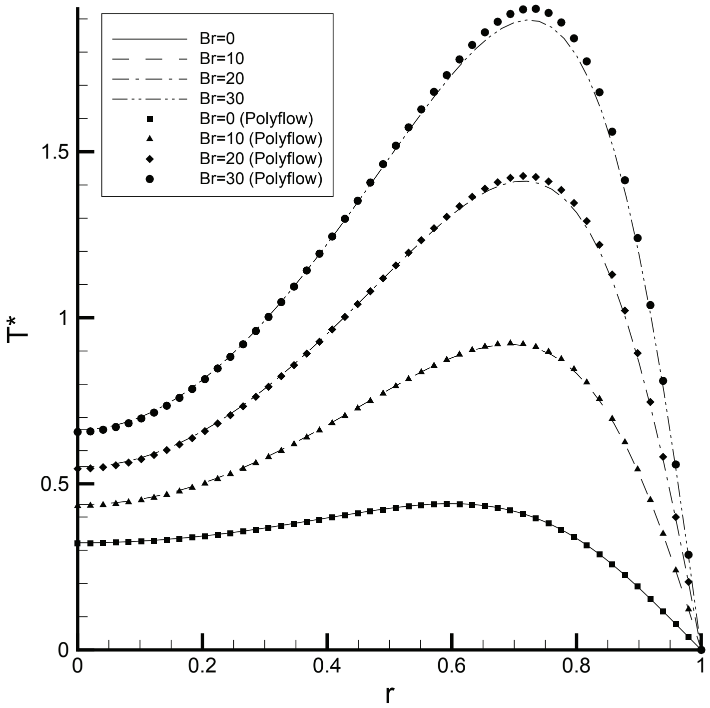

Figure 4.159. Temperature distributions on the horizontal centerline for the Giesekus flow with the parameters of Re = 10.0, Pr = 100, We = 1.0, $\delta = 0.5$, $\beta = 0.5$, $\alpha = 0.1$ and $\alpha_s = 0.02$

Table 4.8 shows the maximum temperatures corresponding to the various Brinkman numbers. It can be observed from this table and Figures 4.155 - 4.158 that the effect of the viscous dissipation is highly prominent since it dramatically alters the temperature

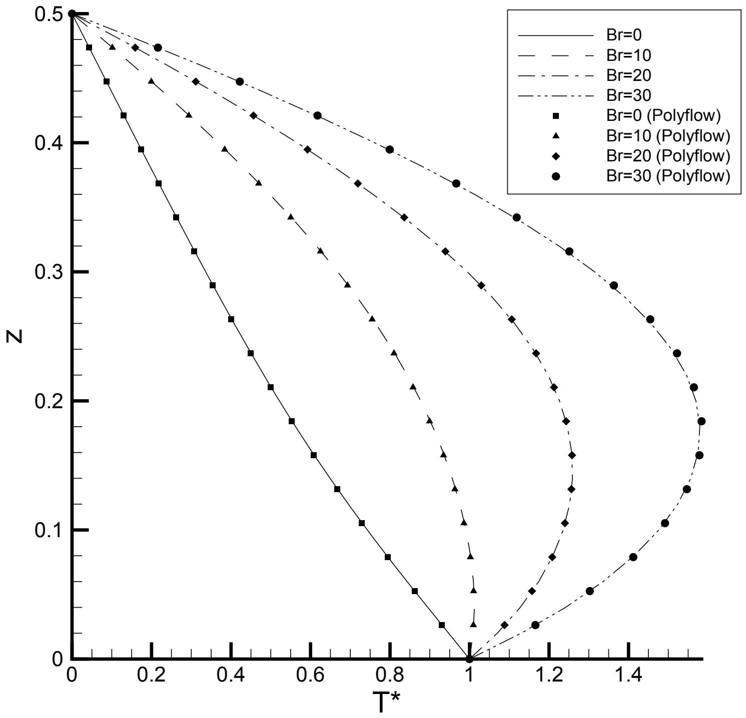

Figure 4.160. Temperature distributions on the vertical centerline for the Giesekus flow with the parameters of Re = 10.0, Pr = 100, We = 1.0, $\delta = 0.5$, $\beta = 0.5$, $\alpha = 0.1$ and $\alpha_s = 0.02$

Table 4.8. Maximum temperature values for different Brinkman numbers.

	Maximum Temperature		r-coordinate		z-coordinate	
	In-Gmres	Polyflow	In-Gmres	Polyflow	In-Gmres	Polyflow
Br = 0	1.000	1.000	On the disc	On the disc	0.000	0.000
Br = 10	1.298	1.303	0.8800	0.8799	0.0600	0.0599
Br = 20	1.931	1.938	0.9100	0.9169	0.0600	0.0599
Br = 30	2.511	2.604	0.9200	0.9198	0.0600	0.0600

field and as a result the viscosity of the fluid. This effect can also be observed from Figures 4.161 and 4.162 which reveal the temperature dependent shift factor $(H(T))$ contours of the Arrhenius relation for the Brinkman numbers of 0 and 30. Since $H(T)$ alters the viscosity in the equations with the help of the Approximate Arrhenius Law, it can be understood that the increase in the Brinkman number affects the viscosity and consequently the flow field.

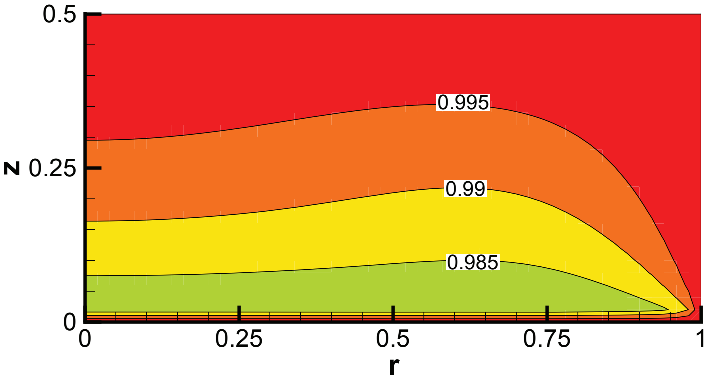

Figure 4.161. Temperature dependent shift factor $(H(T))$ contours for the Giesekus flow with the parameters of $\mathrm{Re} = 10.0$, $\mathrm{Pr} = 100$, $\mathrm{We} = 1.0$, $\mathrm{Br} = 0.0$, $\delta = 0.5$, $\beta = 0.5$, $\alpha = 0.1$ and $\alpha_s = 0.02$

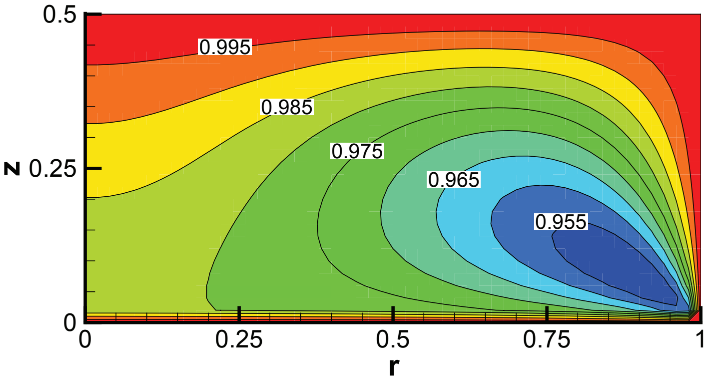

Figure 4.162. Temperature dependent shift factor $(H(T))$ contours for the Giesekus flow with the parameters of $\mathrm{Re} = 10.0$, $\mathrm{Pr} = 100$, $\mathrm{We} = 1.0$, $\mathrm{Br} = 30.0$, $\delta = 0.5$, $\beta = 0.5$, $\alpha = 0.1$ and $\alpha_s = 0.02$

The next analysis is carried out in order to investigate the effects of the Prandtl number. For this purpose, a test problem with the parameters of $\mathrm{Re} = 10.0$, $\mathrm{We} = 1.0$, $\mathrm{Br} = 10$, $\delta = 0.5$, $\beta = 0.5$, $\alpha = 0.1$ and $\alpha_s = 0.02$ is simulated for the Prandtl numbers of 10, 100, 1000 and 10000. The Figures 4.163 through 4.166 show the temperature contours for the Prandtl numbers of 10, 100, 1000 and 10000. As can be understood from these figures when the Prandtl number increases the heat is convected mainly by the fluid motion and for small Prandtl numbers, the diffusion of the heat gains more importance. Therefore it is safe to say that the diffusion of the temperature field is getting harder with the increasing Prandtl number as expected. It should also be noted that the disturbed temperature fields will result in disturbed viscosity fields and consequently altered velocity fields. Figures 4.167 and 4.168 reveal the comparability of the IN-GMRES results with POLYFLOW data similar to the previous analyses.

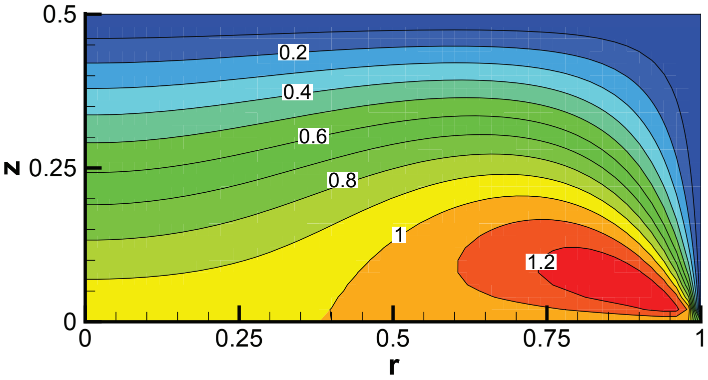

Figure 4.163. Temperature contours for the Giesekus flow with the parameters of Re = 10.0, Pr = 10, We = 1.0, Br = 10.0, $\delta = 0.5$, $\beta = 0.5$, $\alpha = 0.1$ and $\alpha_s = 0.02$

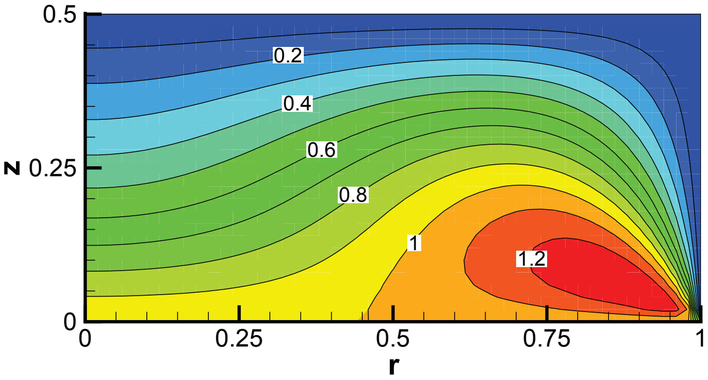

Figure 4.164. Temperature contours for the Giesekus flow with the parameters of Re = 10.0, Pr = 100, We = 1.0, Br = 10.0, $\delta = 0.5$, $\beta = 0.5$, $\alpha = 0.1$ and $\alpha_s = 0.02$

The analyses of Brinkman number and Prandtl number show that the energy equation with the viscous dissipation and the temperature dependent viscosity field should always be modeled alongside with the continuity, momentum and constitutive equations in order to achieve accurate simulations.

The effect of Weissenberg number on the temperature field is studied with an

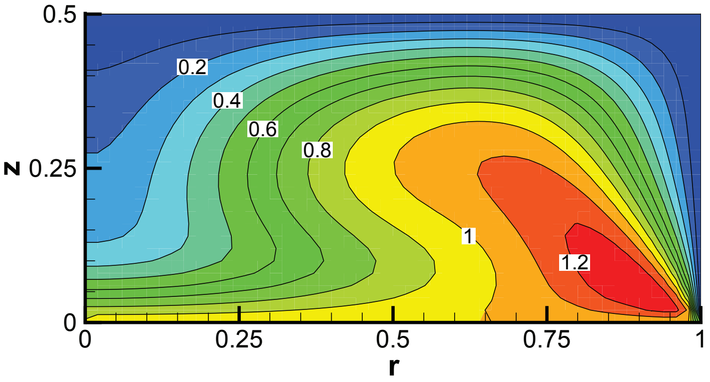

Figure 4.165. Temperature contours for the Giesekus flow with the parameters of $\mathrm{Re} = 10.0$, $\mathrm{Pr} = 1000$, $\mathrm{We} = 1.0$, $\mathrm{Br} = 10.0$, $\delta = 0.5$, $\beta = 0.5$, $\alpha = 0.1$ and $\alpha_s = 0.02$

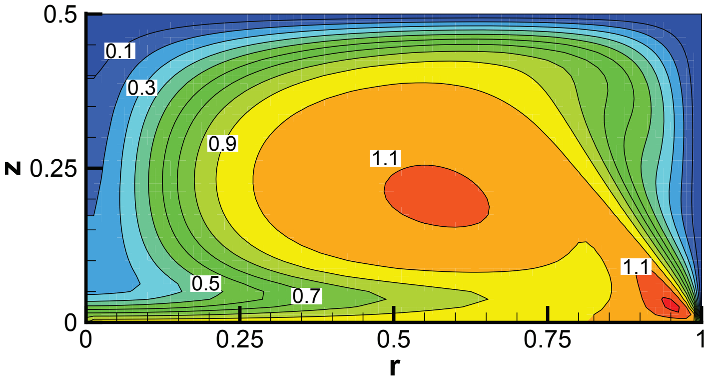

Figure 4.166. Temperature contours for the Giesekus flow with the parameters of $\mathrm{Re} = 10.0$, $\mathrm{Pr} = 10000$, $\mathrm{We} = 1.0$, $\mathrm{Br} = 10.0$, $\delta = 0.5$, $\beta = 0.5$, $\alpha = 0.1$ and $\alpha_s = 0.02$

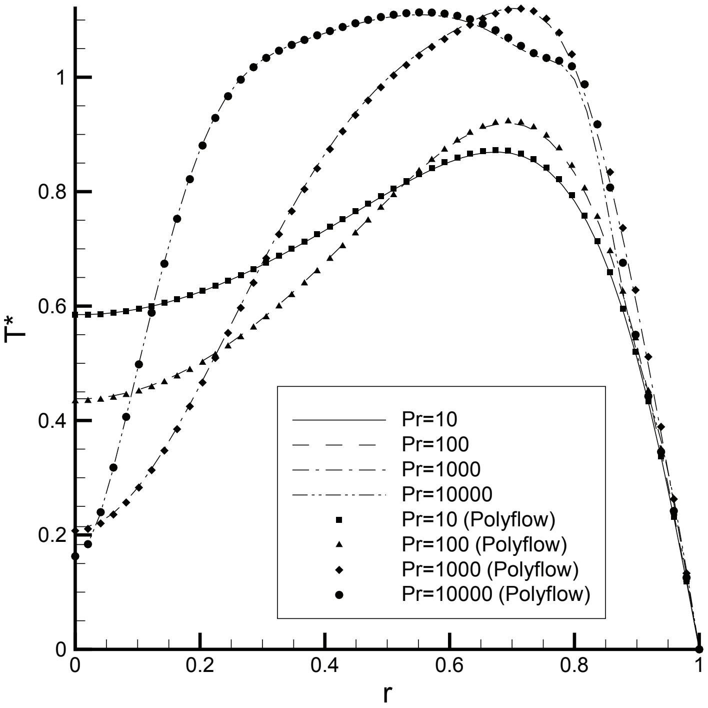

Figure 4.167. Temperature distributions on the horizontal centerline for the Giesekus flow with the parameters of Re = 10.0, Br = 10, We = 1.0, $\delta = 0.5$, $\beta = 0.5$, $\alpha = 0.1$ and $\alpha_s = 0.02$

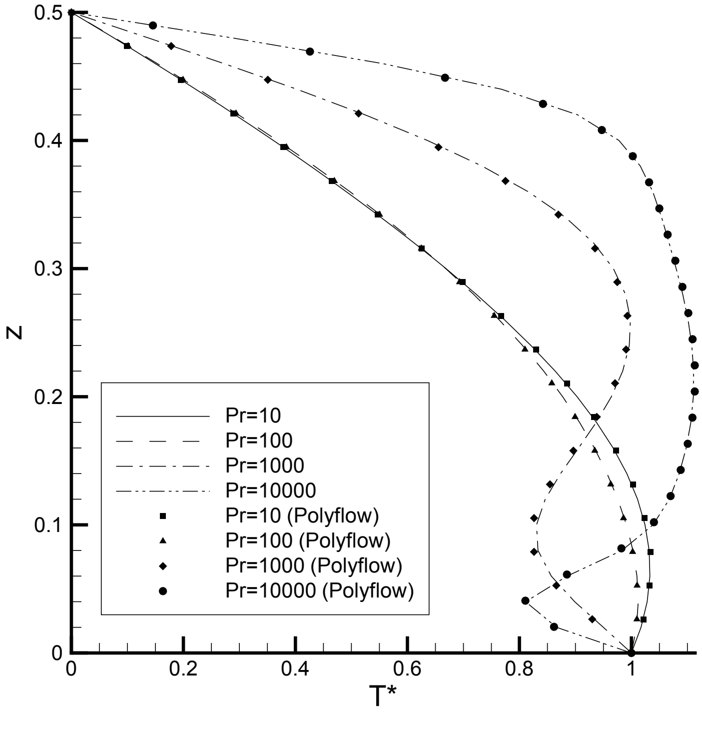

Figure 4.168. Temperature distributions on the vertical centerline for the Giesekus flow with the parameters of Re = 10.0, Br = 10, We = 1.0, $\delta = 0.5$, $\beta = 0.5$, $\alpha = 0.1$ and $\alpha_s = 0.02$

example problem with the parameters of; Re $= 10.0$, Pr $= 1000$, Br $= 20$, $\delta = 0.5$, $\beta = 0.5$, $\alpha = 0.1$ and $\alpha_s = 0.02$. The Weissenberg numbers of 0, 0.25, 0.5, 1, 5 and 10 are simulated where the non-dimensional temperature of the rotating disc is selected as 1 and the stationary edges are taken as 0. Figures 4.169 through 4.174 show the temperature contours for this problem where the maximum temperature is decreasing with the increasing Weissenberg numbers. The decrease in the maximum temperature can be explained by the reduced velocities in the r-z plane because of the increased Weissenberg numbers. When the velocities decrease, the effect of the viscous dissipation reduces and in consequence the maximum temperatures decrease. Figures 4.175 and 4.176 show the temperature distributions for the same problem where the temperatures on the centerlines of the RDCE are decreasing with the increasing Weissenberg numbers conveniently to the Figures 4.169 - 4.174.

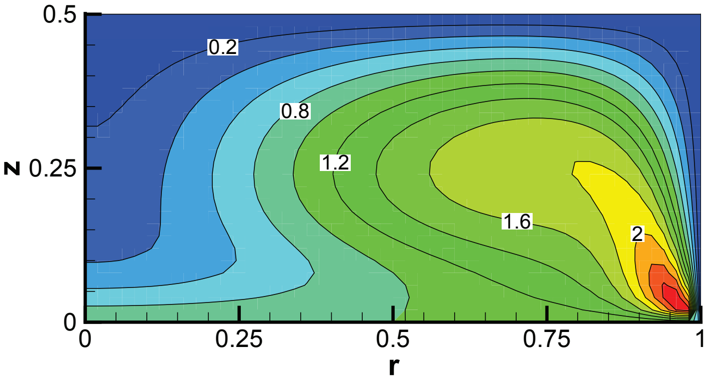

Figure 4.169. Temperature contours for the Giesekus flow with the parameters of Re $= 10.0$, Pr $= 1000$, We $= 0.00$, Br $= 20.0$, $\delta = 0.5$, $\beta = 0.5$, $\alpha = 0.1$ and $\alpha_s = 0.02$

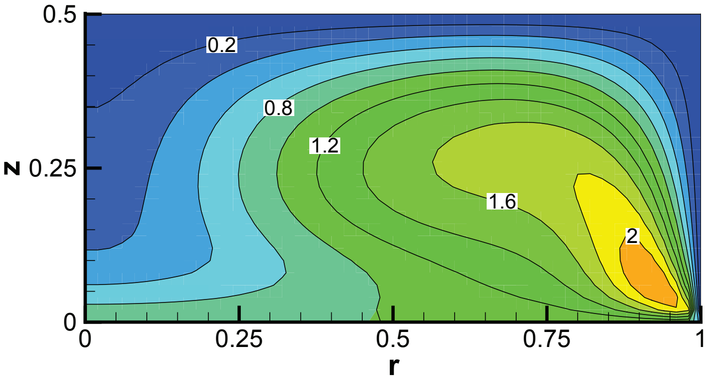

Figure 4.170. Temperature contours for the Giesekus flow with the parameters of Re $= 10.0$, Pr $= 1000$, We $= 0.25$, Br $= 20.0$, $\delta = 0.5$, $\beta = 0.5$, $\alpha = 0.1$ and $\alpha_s = 0.02$

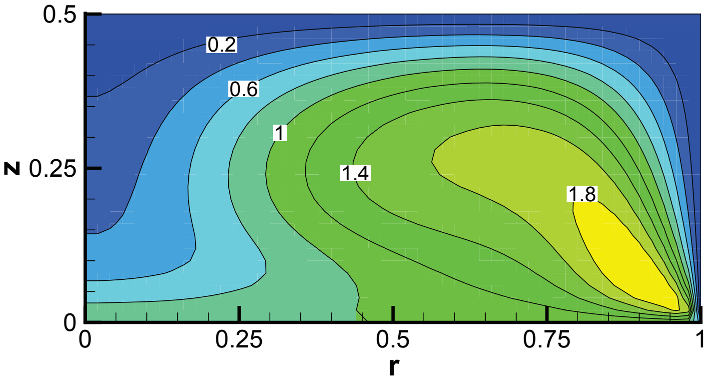

Figure 4.171. Temperature contours for the Giesekus flow with the parameters of $\mathrm{Re} = 10.0$, $\mathrm{Pr} = 1000$, $\mathrm{We} = 0.50$, $\mathrm{Br} = 20.0$, $\delta = 0.5$, $\beta = 0.5$, $\alpha = 0.1$ and $\alpha_s = 0.02$

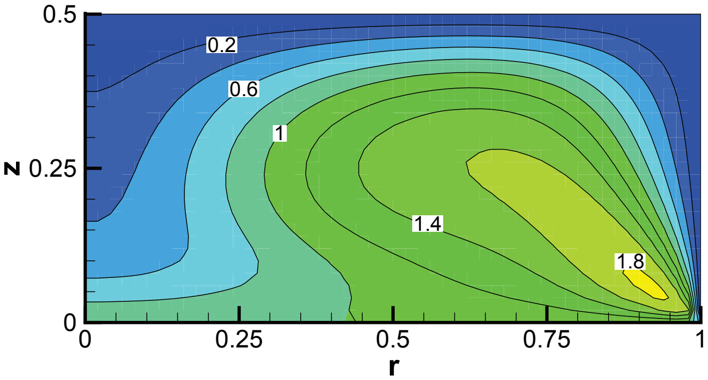

Figure 4.172. Temperature contours for the Giesekus flow with the parameters of $\mathrm{Re} = 10.0$, $\mathrm{Pr} = 1000$, $\mathrm{We} = 1.00$, $\mathrm{Br} = 20.0$, $\delta = 0.5$, $\beta = 0.5$, $\alpha = 0.1$ and $\alpha_s = 0.02$

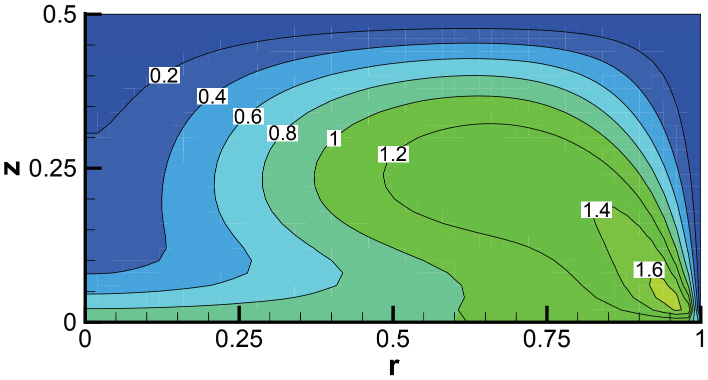

Figure 4.173. Temperature contours for the Giesekus flow with the parameters of $\mathrm{Re} = 10.0$, $\mathrm{Pr} = 1000$, $\mathrm{We} = 5.00$, $\mathrm{Br} = 20.0$, $\delta = 0.5$, $\beta = 0.5$, $\alpha = 0.1$ and $\alpha_s = 0.02$

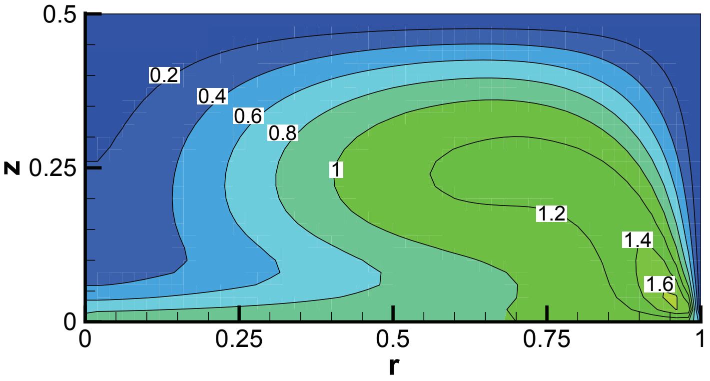

Figure 4.174. Temperature contours for the Giesekus flow with the parameters of Re = 10.0, Pr = 1000, We = 10.00, Br = 20.0, $\delta = 0.5$, $\beta = 0.5$, $\alpha = 0.1$ and $\alpha_s = 0.02$

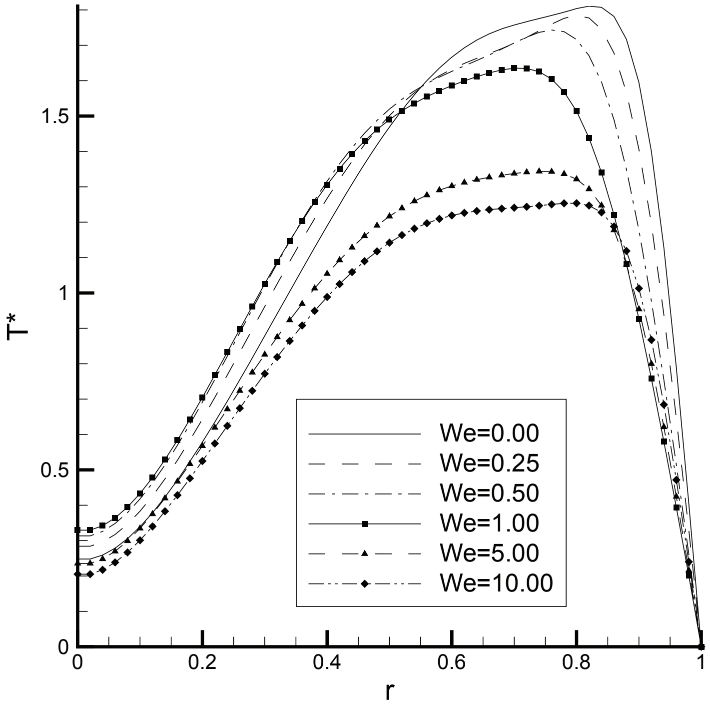

Figure 4.175. Temperature distributions on the horizontal centerline for the Giesekus flow with the parameters of Re = 10.0, Pr = 1000, Br = 20.0, $\delta = 0.5$, $\beta = 0.5$, $\alpha = 0.1$ and $\alpha_s = 0.02$

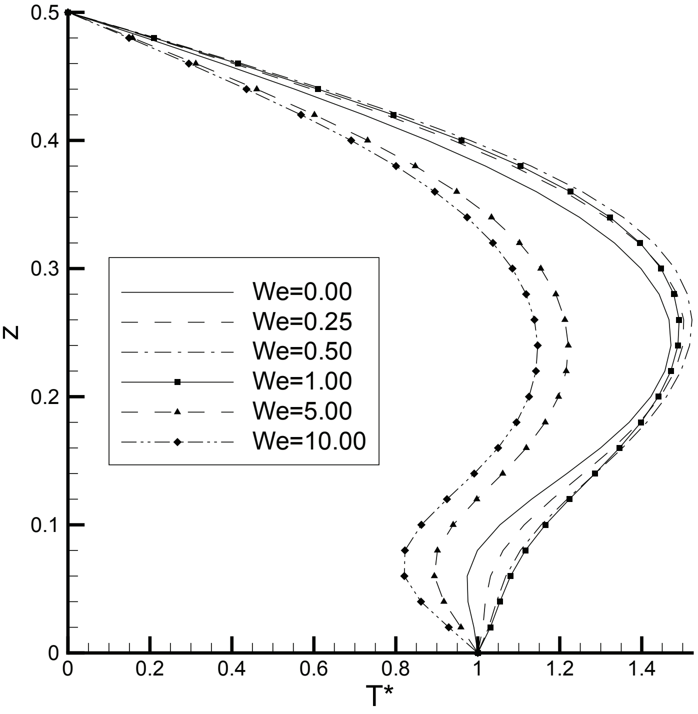

Figure 4.176. Temperature distributions on the vertical centerline for the Giesekus flow with the parameters of Re = 10.0, Pr = 1000, Br = 20.0, $\delta = 0.5$, $\beta = 0.5$, $\alpha = 0.1$ and $\alpha_s = 0.02$

5. CONCLUSIONS and FUTURE DIRECTIONS

In this thesis, the numerical investigations of the moving edge non-isothermal and non-Newtonian flows are simulated by using two example problems; lid driven cavity (LDC) and rotating disc in a cylindrical enclosure (RDCE) flows. The non-Newtonian behavior of the fluid is modeled by using three differential constitutive relations which are Upper Convected Maxwell, Oldroyd B and Giesekus models. The comparisons between these three models reveal that the Giesekus model is the most realistic one and the maximum Weissenberg number limit is higher compared to the others, therefore it should be preferred over UCM and Oldroyd B relations. Two separate solvers are used in the simulations; PETSc and IN-GMRES solvers. PETSc code is used as a solver for the Newtonian flows and a benchmark tool for the Krylov subspace methods and preconditioners. PETSc analyses reveal that BiCGStab with ILU(5) preconditioning is found out to be the most effective solver in the simulations of the Newtonian flows. IN-GMRES solver is used to simulate the non-isothermal and non-Newtonian flows and it is based on the matrix free preconditioned inexact Newton-Krylov methods. Additionally, in order to obtain higher Weissenberg number limits in the simulations, the numerical tools such as the continuation, the upwind differencing scheme, the higher order discretization schemes, the slanted stencils and similar others are implemented in this algorithm. In the non-isothermal part of the study, besides the advection and diffusion, the viscous dissipation is also included and it is understood that the viscous dissipation is very important in simulations of non-Newtonian flows. Moreover, the viscosity is modeled as temperature dependent by adopting the approximate Arrhenius formulation and it is realized that the viscosity changes can alter the flow field.

The importance of the study can be itemized as follows;

- Our study reveal that the Giesekus model is the most realistic one and the maximum Weissenberg number limit is higher compared to the others. Additionally, in order to obtain higher Weissenberg number limits in the simulations, the numerical tools such as the continuation, the upwind differencing scheme, the higher order discretization schemes (4th order), the slanted stencils and similar others are implemented in the IN-GMRES algorithm.

- In the non-isothermal part of the study, besides the advection and diffusion, the viscous dissipation is also included and it is understood that the viscous dissipation is very important in simulations of non-Newtonian flows. The viscosity is modeled as temperature dependent by adopting the approximate Arrhenius formulation and it is realized that the viscosity changes can alter the flow field. Moreover, the effects of the Reynolds number, the Weissenberg number, the Prandtl number, the Brinkman number, aspect ratio, some of the material parameters (such as viscosity ratio, mobility factor, sensitive coefficient of temperature and etc.) are documented within this study.
- The RDCE is selected because of a specific flow occurrence distinctive for non-Newtonian fluids within this geometry. This problem has two main fluid motions; the primary rotation in the $r-\theta$ plane and the secondary rotation in the $r-z$ plane. The primary motion, which is the outcome of the rotation of the disc, is always in the tangential direction. The secondary rotation differs according to the type of fluid inside the container. In the case of the Newtonian fluids, the secondary flow rotates radially outward from the disk. This motion is triggered by the angular velocity difference between the fluid particles near the rotating disc (large angular velocity) and the fluid particles near the container (small angular velocity). The fluid particles near the rotating disc experience large outward centrifugal forces and the flow rotates radially outward from the disc. For the non-Newtonian fluids, increasing elasticity - increased Weissenberg number in our simulations - generates growing normal stresses in the opposite direction of the centrifugal force. After a certain point depending on the problem, these stresses counterbalance the centrifugal force and generate a reversed flow field. The formation of the reversed flow fields can be observed in every simulation in this thesis.
- One of the most important findings of this research is the re-formation of the Newtonian-type flow for high Elasticity numbers. It is observed for the first time in the literature since Elasticity numbers of this magnitude can not be simulated

previously. This re-formation of the Newtonian-like flow appears because of the decreasing non-Newtonian stresses. The increase in the Elasticity number reduces the average velocity of the flow domain and consequently the stress values. Because of the reduced normal stresses the centrifugal forces due to the rotation of the disc become dominant again and the re-formation appears.

- The simulation of the energy equation is carried out in this research for both of the geometries. Knowing that the information on this part is very limited in the literature, understanding the effects of the parameters that governs the temperature field is very important. It is shown in this research that for the non-Newtonian fluids, the most important effect is the effect of the Brinkman number which is the coefficient of the viscous dissipation term. For a general non-Newtonian fluid the maximum temperature within the flow domain is nearly two times higher that the maximum temperatures of the boundaries for the Weissenberg numbers of the order 1. Since the viscosity is dependent on the temperature field, the viscous dissipation term alters the viscosity field and consequently the velocity field. Therefore it can be said that, simulating the non-Newtonian problems without the energy equation is shown to be inadvisable for the Weissenberg numbers of the order 1.
- Moreover, the effects of the other parameters such as The Reynolds number, the Prandtl number, the sensitive coefficient of the temperature and the temperature shift factor are investigated within this research.
- The solution strategies at the analyses in the literature are based on the time dependent solutions and there isn't any study utilizing Newton-Krylov type algorithms where in this thesis a steady, matrix free, preconditioned inexact Newton-Krylov algorithm is developed for the solutions.

As non-Newtonian flow is a hot topic in the academic and industrial areas, further studies concerning these types of flows should be carried out. The use of new and improved constitutive relations is always suggested in the area of this research. Additionally, since the degree of freedom is very high (ten for the RDCE flow), computations are getting more and more difficult with the increasing number of nodes. In order to pass around this difficulty, parallelization of the code is advised.

APPENDIX A: TENSOR OPERATIONS FOR THE LID DRIVEN CAVITY PROBLEM

$$\nabla = e_x \frac{\partial}{\partial x} + e_y \frac{\partial}{\partial y} \tag{A.1}$$

$$\nabla^2 = \left[\begin{array}{c} \frac{\partial^2 u}{\partial x^2} + \frac{\partial^2 u}{\partial y^2} \\ \frac{\partial^2 v}{\partial x^2} + \frac{\partial^2 v}{\partial y^2} \end{array} \right] \tag{A.2}$$

$$\mathbf{V}.\nabla\tau = \left[\begin{array}{cc} u\frac{\partial \tau_{xx}}{\partial x} + v\frac{\partial \tau_{xx}}{\partial y} & u\frac{\partial \tau_{xy}}{\partial x} + v\frac{\partial \tau_{xy}}{\partial y} \\ u\frac{\partial \tau_{xy}}{\partial x} + v\frac{\partial \tau_{xy}}{\partial y} & u\frac{\partial \tau_{yy}}{\partial x} + v\frac{\partial \tau_{yy}}{\partial y} \end{array} \right] \tag{A.3}$$

$$\left(\nabla\mathbf{V}\right)^T.\tau = \left[\begin{array}{cc} \tau_{xx}\frac{\partial u}{\partial x} + \tau_{xy}\frac{\partial u}{\partial y} & \tau_{xy}\frac{\partial u}{\partial x} + \tau_{yy}\frac{\partial u}{\partial y} \\ \tau_{xx}\frac{\partial v}{\partial x} + \tau_{xy}\frac{\partial v}{\partial y} & \tau_{xy}\frac{\partial v}{\partial x} + \tau_{yy}\frac{\partial v}{\partial y} \end{array} \right] \tag{A.4}$$

$$\tau.\nabla\mathbf{V} = \left[\begin{array}{cc} \tau_{xx}\frac{\partial u}{\partial x} + \tau_{xy}\frac{\partial u}{\partial y} & \tau_{xx}\frac{\partial v}{\partial x} + \tau_{xy}\frac{\partial v}{\partial y} \\ \tau_{xy}\frac{\partial u}{\partial x} + \tau_{yy}\frac{\partial u}{\partial y} & \tau_{xy}\frac{\partial v}{\partial x} + \tau_{yy}\frac{\partial v}{\partial y} \end{array} \right] \tag{A.5}$$

$$\tau.\tau = \left[\begin{array}{cc} \tau_{xx}^2 + \tau_{xy}^2 & \tau_{xx}\tau_{xy} + \tau_{xy}\tau_{yy} \\ \tau_{xx}\tau_{xy} + \tau_{xy}\tau_{yy} & \tau_{xy}^2 + \tau_{yy}^2 \end{array} \right] \tag{A.6}$$

APPENDIX B: TENSOR OPERATIONS FOR THE ROTATING DISC IN A CYLINDRICAL ENCLOSURE PROBLEM

$$\nabla = e_r \frac{\partial}{\partial r} + e_z \frac{\partial}{\partial z} \tag{B.1}$$

$$\nabla^2 = \begin{bmatrix} \frac{\partial^2 u}{\partial r^2} + \frac{1}{r}\frac{\partial u}{\partial r} + \frac{\partial^2 u}{\partial z^2} - \frac{u}{r^2} \\ \frac{\partial^2 v}{\partial r^2} + \frac{1}{r}\frac{\partial v}{\partial r} + \frac{\partial^2 v}{\partial z^2} - \frac{v}{r^2} \\ \frac{\partial^2 w}{\partial r^2} + \frac{1}{r}\frac{\partial w}{\partial r} + \frac{\partial^2 w}{\partial z^2} \end{bmatrix} \tag{B.2}$$

$$\mathbf{V}.\nabla\tau = \left[\begin{array}{c} u\frac{\partial \tau_{rr}}{\partial r} + w\frac{\partial \tau_{rr}}{\partial z} - \frac{2v}{r}\tau_{r\theta} \\ u\frac{\partial \tau_{r\theta}}{\partial r} + w\frac{\partial \tau_{r\theta}}{\partial z} + \frac{v}{r}\left(\tau_{rr} - \tau_{\theta\theta}\right) \\ u\frac{\partial \tau_{rz}}{\partial r} + w\frac{\partial \tau_{rz}}{\partial z} - \frac{v}{r}\tau_{\theta z} \end{array} \right.$$

$$\begin{array}{c} u\frac{\partial \tau_{r\theta}}{\partial r} + w\frac{\partial \tau_{r\theta}}{\partial z} + \frac{v}{r}\left(\tau_{rr} - \tau_{\theta\theta}\right) \\ u\frac{\partial \tau_{\theta\theta}}{\partial r} + w\frac{\partial \tau_{\theta\theta}}{\partial z} + \frac{2v}{r}\tau_{r\theta} \\ u\frac{\partial \tau_{\theta z}}{\partial r} + w\frac{\partial \tau_{\theta z}}{\partial z} + \frac{v}{r}\tau_{rz} \end{array}$$

$$\left. \begin{array}{c} u\frac{\partial \tau_{rz}}{\partial r} + w\frac{\partial \tau_{rz}}{\partial z} - \frac{v}{r}\tau_{\theta z} \\ u\frac{\partial \tau_{\theta z}}{\partial r} + w\frac{\partial \tau_{\theta z}}{\partial z} + \frac{v}{r}\tau_{rz} \\ u\frac{\partial \tau_{zz}}{\partial r} + w\frac{\partial \tau_{zz}}{\partial z} \end{array} \right] \tag{B.3}$$

$$\left(\nabla\mathbf{V}\right)^{T}.\tau = \begin{bmatrix} \tau_{rr}\frac{\partial u}{\partial r} + \tau_{rz}\frac{\partial u}{\partial z} - \tau_{r\theta}\frac{v}{r} & \tau_{r\theta}\frac{\partial u}{\partial r} + \tau_{\theta z}\frac{\partial u}{\partial z} - \tau_{\theta\theta}\frac{v}{r} & \tau_{rz}\frac{\partial u}{\partial r} + \tau_{zz}\frac{\partial u}{\partial z} - \tau_{\theta z}\frac{v}{r} \\ \tau_{rz}\frac{\partial v}{\partial r} + \tau_{zz}\frac{\partial v}{\partial z} + \tau_{\theta z}\frac{u}{r} & \tau_{r\theta}\frac{\partial v}{\partial r} + \tau_{\theta z}\frac{\partial v}{\partial z} + \tau_{\theta\theta}\frac{u}{r} & \tau_{rz}\frac{\partial v}{\partial r} + \tau_{zz}\frac{\partial v}{\partial z} + \tau_{\theta z}\frac{u}{r} \\ \tau_{rz}\frac{\partial w}{\partial r} + \tau_{zz}\frac{\partial w}{\partial z} & \tau_{r\theta}\frac{\partial w}{\partial r} + \tau_{\theta z}\frac{\partial w}{\partial z} & \tau_{rz}\frac{\partial w}{\partial r} + \tau_{zz}\frac{\partial w}{\partial z} \end{bmatrix} \tag{B.4}$$

$$\tau.\nabla\mathbf{V} = \begin{bmatrix} \tau_{rr}\frac{\partial u}{\partial r} + \tau_{rz}\frac{\partial u}{\partial z} - \tau_{r\theta}\frac{v}{r} & \tau_{rr}\frac{\partial v}{\partial r} + \tau_{rz}\frac{\partial v}{\partial z} + \tau_{r\theta}\frac{u}{r} & \tau_{rr}\frac{\partial w}{\partial r} + \tau_{rz}\frac{\partial w}{\partial z} \\ \tau_{r\theta}\frac{\partial u}{\partial r} + \tau_{\theta z}\frac{\partial u}{\partial z} - \tau_{\theta\theta}\frac{v}{r} & \tau_{r\theta}\frac{\partial v}{\partial r} + \tau_{\theta z}\frac{\partial v}{\partial z} + \tau_{\theta\theta}\frac{u}{r} & \tau_{r\theta}\frac{\partial w}{\partial r} + \tau_{\theta z}\frac{\partial w}{\partial z} \\ \tau_{rz}\frac{\partial u}{\partial r} + \tau_{zz}\frac{\partial u}{\partial z} - \tau_{\theta z}\frac{v}{r} & \tau_{rz}\frac{\partial v}{\partial r} + \tau_{zz}\frac{\partial v}{\partial z} + \tau_{\theta z}\frac{u}{r} & \tau_{rz}\frac{\partial w}{\partial r} + \tau_{zz}\frac{\partial w}{\partial z} \end{bmatrix} \tag{B.5}$$

$$\tau.\tau = \begin{bmatrix} \tau_{rr}^2 + \tau_{r\theta}^2 + \tau_{rz}^2 & \tau_{rr}\tau_{r\theta} + \tau_{r\theta}\tau_{\theta\theta} + \tau_{rz}\tau_{\theta z} & \tau_{rr}\tau_{rz} + \tau_{r\theta}\tau_{\theta z} + \tau_{rz}\tau_{zz} \\ \tau_{rr}\tau_{r\theta} + \tau_{r\theta}\tau_{\theta\theta} + \tau_{rz}\tau_{\theta z} & \tau_{r\theta}^2 + \tau_{\theta\theta}^2 + \tau_{\theta z}^2 & \tau_{r\theta}\tau_{rz} + \tau_{\theta\theta}\tau_{\theta z} + \tau_{\theta z}\tau_{zz} \\ \tau_{rr}\tau_{rz} + \tau_{r\theta}\tau_{\theta z} + \tau_{rz}\tau_{zz} & \tau_{r\theta}\tau_{rz} + \tau_{\theta\theta}\tau_{\theta z} + \tau_{\theta z}\tau_{zz} & \tau_{rz}^2 + \tau_{\theta z}^2 + \tau_{zz}^2 \end{bmatrix} \tag{B.6}$$

REFERENCES

1. Ghia, U., K.N. Ghia and C.T. Shin, ”High-Re Solutions for Incompressible Flow Using the Navier-Stokes Equations and a Multigrid Method” *Journal of Computational Physics*, Vol. 48, pp. 387-411, 1982.

2. Neofytou, P., ”A 3rd Order Upwind Finite Volume Method for Generalized Newtonian Fluid Flows” *Advances in Engineering Software*, Vol. 36, pp. 664-680, 2005.

3. Griller, A.M., B. Yang, B. Khomami and E.S.G. Shaqfeh, ”Modeling of Viscoelastic Lid Driven Cavity Flow Using Finite Element Simulations” *Journal of Non-Newtonian Fluid Mechanics*, Vol. 88, pp. 99-131, 1999.

4. Renardy, M., ”Stress Integration for the Constitutive Law of the Upper Convected Maxwell Fluid Near the Corners in a Driven Cavity” *Journal of Non-Newtonian Fluid Mechanics*, Vol. 112, pp. 77-84, 2003.

5. Fattal, R. and R Kupferman, ”Time-Dependent Simulation of Viscoelastic Flows at High Weissenberg Number Using the Log-Confirmation Representation” *Journal of Non-Newtonian Fluid Mechanics*, Vol. 126, pp. 23-37, 2005.

6. Surana, K.S., A. Mohammed, J.N. Reddy and P.W. TenPas, ”k-Version of Finite Element Method in 2D-Polymer Flows: Oldroyd-B Constitutive Model” *International Journal for Numerical Methods in Fluids*, Vol. 52, pp. 119-162, 2006.

7. Surana, K.S., S. Bhola, J.N. Reddy and P.W. TenPas, ”k-Version of Finite Element Method in 2D-Polymer Flows: Upper Convected Maxwell Model” *Computers and Structures*, Vol. 86, pp. 1782-1808, 2008.

8. Belblidia, F., H. Matallah, B. Puangkird and M.F. Webster, ”Alternative Subcell Discretizations for Viscoelastic Flow: Stress Interpolation” *Journal of Non-Newtonian Fluid Mechanics*, Vol. 146 , pp. 59-78, 2007.

9. Pakdel, P., S.H. Spiegelberg and G.H. McKinley, "Cavity Flows of Elastic Liquids: Two-Dimensional Flows" *Physics of Fluids*, Vol. 11, pp. 3123-3140, 1997.

10. Pao, H.P., "A Numerical Computation of a Confined Rotating Flow" *Transactions of ASME: Journal of Applied Mechanics*, Vol. 37, pp. 480-487, 1970.

11. Pao, H.P., "Numerical Solution of the Navier-Stokes Equations for Flows in the Disk-Cylinder System" *Physics of Fluids*, Vol. 15, pp. 4-11, 1972.

12. Lopez, J.M., "Flow Between a Stationary and a Rotating Disk Shrouded by a Co-Rotating Cylinder" *Physics of Fluids*, Vol. 8, pp. 2605-2613, 1996.

13. Saci R. and PG Bellamy-Knights, "Diffusion Driven Rotating Flow in a Cylindrical Container" *Acta Mechanica*, Vol. 126, pp. 45-57, 1998.

14. Kaptan, Y., A. Ecder and K. Atalık, "Computational Parametric Analysis of Rotating Surface Flow" *Proceedings of the Institution of Mechanical Engineers, Part C: Journal of Mechanical Engineering Science*, Vol. 229, pp. 889-899, 2009.

15. Moroi, T., M. Itoh and H. Toda, "Numerical Simulation of Viscoelastic Flow due to a Rotating Disc Enclosed in a Cylindrical Casing" *Proceedings of the* 13th *Australian Fluid Mechanics Conference*, 3-18 December 1998, pp. 313-316, Melbourne, 1998.

16. Moroi, T., M. Itoh, K. Fujita and H. Hamasaki, "Viscoelastic Flow due to a Rotating Disc Enclosed in a Cylindrical Casing (Influence of Aspect Ratio)" *JSME International Journal, Series B*, Vol. 44, No. 3 pp. 465-473, 2001.

17. Itoh, M., M. Suzuki and T. Moroi, "Swirling Flow of a Viscoelastic Fluid in a Cylindrical Casing" *Transactions of ASME: Journal of Fluids Engineering*, Vol. 128, pp. 88-94, 2006.

18. Tamano, S., M. Itoh, Y. Ide and K. Yokota, "Vortex Shedding in Confined Swirling Flow of Polymer Solutions" *Physics of Fluids*, Vol. 19, No. 023103, pp. 1-8, 2007.

19. Tamano, S., M. Itoh, M. Yoshida and K. Yokota, "Confined Swirling Flows of Aqueous Surfactant Solutions due to a Rotating Disk in a Cylindrical Casing" *Transactions of ASME: Journal of Fluids Engineering*, Vol. 130, No . 081502, pp. 1-8, 2008.

20. Stokes, J.R., L.J.W. Graham, N.J. Lawson and D.V. Boger, "Swirling Flow of Viscoelastic Fluids. Part 1. Interaction Between Inertia and Elasticity" *Journal of Fluid Mechanics*, Vol. 429, pp. 67-115, 2001.

21. Stokes, J.R., L.J.W. Graham, N.J. Lawson and D.V. Boger, "Swirling Flow of Viscoelastic Fluids. Part 2. Elastic Effects" *Journal of Fluid Mechanics*, Vol. 429, pp. 117-153, 2001.

22. Xue, S.C., N. Phan-Thien and R.I. Tanner, "Fully Three-Dimensional, Time-Dependent Numerical Simulations of Newtonian and Viscoelastic Swirling Flows in a Confined Cylinder Part I. Method and Steady Flows" *Journal of Non-Newtonian Fluid Mechanics*, Vol. 87, pp. 337-367, 1999.

23. Groisman, A. and V. Steinberg, "Elastic Turbulence in a Polymer Solution Flow" *Letters to Nature*, Vol. 405, pp. 53-55, 2000.

24. Groisman, A. and V. Steinberg, "Elastic Turbulence in Curvilinear Flows of Polymer Solutions" *New Journal of Physics*, Vol. 6, No. 29, pp. 1-48, 2004.

25. Xianhong, H. and X. Li, "An Iterative Stabilized CNBS-CG Scheme for Incompressible Non-Isothermal Non-Newtonian Flow" *International Journal of Heat and Mass Transfer*, Vol. 50, pp. 847-856, 2007.

26. Wachs, A. and J.R. Clermont, "Non-Isothermal Viscoelastic Flow Computations in an Axisymmetric Contraction at High Weissenberg Numbers by a Finite Volume Method" *Journal of Non-Newtonian Fluid Mechanics*, Vol. 95, pp. 147-184, 2000.

27. Yesilata, B., "Effect of Viscous Dissipation on Polymeric Flows Between Two Ro-

tating Coaxial Parallel Discs" *International Communications in Heat and Mass Trasnfer*, Vol. 29, No. 5, pp. 589-600, 2002.

28. Crochet, M.J., A.R. Davies and K. Walters, *Numerical Simulation of Non-Newtonian Flow*, Elsevier, Amsterdam, 1991.

29. Owens, R.G. and T.N. Phillips, *Computational Rheology*, Imperial College Press, London, 2005.

30. Tasai, C.C. and T.J. Liu, "Comparison of Three Solvers for Viscoelastic Fluid Flow Problems" *Journal of Non-Newtonian Fluid Mechanics*, Vol. 60, pp. 155-177, 1995.

31. Kim, J.M., C. Kim, K.H. Ahn and S.J. Lee, "An Efficient Iterative Solver and High-Resolution Computations of the Oldroyd-B Fluid Flow Past a Confined Cylinder" *Journal of Non-Newtonian Fluid Mechanics*, Vol. 123, pp. 161-173, 2004.

32. Howell, J.S., "Computation of Viscoelastic Fluid Flows Using Continuation Methods" *Journal of Computational and Applied Mathematics*, Vol. 225, pp. 187-201, 2009.

33. Baaijens, F.P.T., "An iterative solver for the DEVSS/DG method with application to smooth and non-smooth flows of the upper convected Maxwell fluid" *Journal of Non-Newtonian Fluid Mechanics*, Vol. 75, pp. 119-138, 1998.

34. Kawabata, N., M. Tachibana and I. Ashino, "A Numerical Simulation of Fluid Flow in a Two-Dimensional Channel (Application of Lax's Scheme to the Constitutive Equation)" *Transactions of the Japan Society of Mechanical Engineers B*, Vol.56 , pp. 601-608, 1990

35. Saad, Y. and M.H. Schultz, "GMRES: A generalized minimal residual algorithm for solving nonsymmetric linear systems" *, SIAM Journal on Scientific and Statistical Computing*, Vol. 7, No. 3, pp. 856-869, 1986.

36. Van der Vorst, H., "Bi CGSTAB: A fast and smoothly converging variant of BiCG

for the solution of nonsymmetric linear systems" *SIAM Journal on Scientific and Statistical Computing*, Vol. 13, pp. 631-644, 1992.

37. Brown, P.N. and Y. Saad, "Hybrid Krylov methods for nonlinear-systems of equations" *SIAM Journal on Scientific and Statistical Computing*, Vol. 11, pp. 450-481, 1990.

38. Qin, N., Ludlow, D.K. and S.T. Shaw, "A matrix-free preconditioned Newton/GMRES method for unsteady Navier Stokes equations" *International Journal for Numerical Methods in Fluids*, Vol. 33, pp. 223-248, 2000.

39. Freund, R.W. and N.M. Nachtigal, "QMR - A Quasi-Minimal Residual Method for Non-Hermitian Linear-Systems" *Numerische Mathematik*, Vol. 60, pp. 315-339, 1991.

40. Freund, R.W., "A Transpose-Free Quasi-Minimal Residual Algorithm for Non-Hermitian Linear Systems" *SIAM Journal on Scientific and Statistical Computing*, Vol. 14, pp. 470-482, 1993.

41. Kelley, C.T., *Solving Nonlinear Equations with Newton's Method*, SIAM, Philadelphia, 2003

42. Cai, X. and D.E. Keyes, "Nonlinearly Preconditioned Inexact Newton Algorithms" *SIAM Journal of Scientific Computing*, Vol. 24, pp. 183-200, 2002.

43. Saad, Y., *Iterative Methods for Sparse Linear Systems, Second Edition*, SIAM, Philadelphia, 2003.

44. Barrett, R., M. Berry, T.F. Chan, J. Demmel, J. Donato, J. Dongarra, V. Eijkhout, R. Pozo, C. Romine and H. Van der Vorst, *Templates for the Solution of Linear Systems: Building Blocks for Iterative Methods,2nd Edition*, SIAM, Philadelphia, 1994.

45. Chen, K., *Matrix Preconditioning Techniques and Applications*, Cambridge Uni-

versity Press, Cambridge, 2005.

46. Balay, S., K. Buschelman, W.D. Gropp, D. Kaushik, M.G. Knepley, L.C. McInnes, B.F. Smith and H. Zhang, *PETSc Web Page*, http://www.mcs.anl.gov/petsc/petsc-as/, 2009.

47. Hoffmann, K.A. and S.T. Chiang, *Computational Fluid Dynamics, Fourth Edition*, EES Books, Kansas, 2000

48. Hou, S., Q. Zou, S. Chen, G. Doolen and A. Cogley, "Simulation of Cavity Flows by the Lattice Boltzmann Method" *Journal of Computational Physics*, Vol. 118, pp. 329-347, 1995.

49. Vanka, S.P., "Block-Implicit Multigrid Solution of Navier-Stokes Equations in Primitive Variables", *Journal of Computational Physics*, Vol. 65, pp. 138-158, 1986.

50. Bird, R.B. and O. Hassager, *Dynamics of Polymeric Liquids, Volume 1, Fluid Mechanics*, Wiley, Canada, 1987.